



UNIVERSITÉ DE STRASBOURG

THESE de l'université de Strasbourg

Présentée
Pour l'obtention du grade de

DOCTEUR DE L'UNIVERSITE DE STRASBOURG
Discipline Chimie

par

Youssef EL KHOURY

Mid and far infrared spectroelectrochemical studies on the
metal–ligand interactions in respiratory chain enzymes

Thèse soutenue le 23 Septembre 2010 devant la commission d'examen

Prof. Petra HELLWIG

Directrice de thèse

Prof. Bernd LUDWIG

Rapporteur externe

Prof. Boniface KOKOH

Rapporteur externe

Prof. Helena SAVINOVA

Examinatrice

i. Table of contents	I
ii. List of figures	III
iii. List of abbreviation	XI
iv. The twenty amino acids	XII
v. List of publications	XIV
vi Abstract	XVI
vii Résumé	XVIII
viii Acknowledgments	XX

Table of contents

1. Introduction	1
1.1. Metals in biology	1
1.1.1. Sodium and potassium	1
1.1.2. Calcium	2
1.1.3. Magnesium	2
1.1.4. Manganese.....	2
1.1.5. Zinc.....	3
1.1.6. Nickel	3
1.1.7. Iron	4
1.1.8. Cobalt	5
1.1.9. Copper	6
1.1.10. Toxicity of metals.....	7
1.2. Respiratory chain proteins.....	9
1.2.1. Role, localization and organization	9
1.2.2. Complex I.....	10
1.2.3. Complex II.....	14
1.2.4. Complex III	16
1.2.5. Complex IV	19
1.2.6. Complex V	22
1.3. Iron–sulfur proteins	23
1.3.1. Rubredoxin	23
1.3.2. Ferredoxins.....	24
1.3.3. The Rieske protein	24
1.4. Infrared spectroscopy.....	26
1.4.1. Physical background	26
1.4.2. Infrared spectroscopy of proteins	29
1.5. The aim of the thesis	35
2. Materials and methods	37
2.1. Sample preparation	37
2.1.1. The copper coordination.....	37
2.1.2. The Rieske protein samples.....	38
2.1.3. Rubredoxin samples	38
2.1.4. Ferredoxin samples	38
2.1.5. NADH dehydrogenase fragment	39
2.1.6. The cytochrome <i>bc</i> ₁ complex.....	41
2.1.7. The cytochrome <i>c</i> oxidase.....	42
2.1.8. LFA–I domain of integrins	42
2.1.9. PLL and PLA	42
2.2. Spectroscopy.....	43
2.2.1. The Fourier transform infrared spectrometer	43
2.2.2. UV–Vis spectroscopy	46
2.3. Electrochemistry	47
3. Results and discussion.....	50
3.1. The copper coordination	50
3.1.1. The copper coordination by PLH	50
3.1.2. The copper coordination by amyloid–beta 16.....	63
3.2. The inhibitory effects of Zn cations on the cytochrome <i>bc</i>₁ complex	97

3.2.1. Introduction	97
3.2.2. Difference spectroscopy of the wild-type bc_1 complex.....	98
3.2.3. Difference spectroscopy of the Glu295Val mutant bc_1 complex.....	107
3.2.4. Difference spectroscopy of the subcomplex of the bc_1 complex	113
3.2.5. Conclusion.....	117
3.3. The inhibitory effect of Zn cations on the cytochrome c oxidase.....	120
3.3.1. Introduction	120
3.3.2. Difference spectroscopy of the wild-type CcO	122
3.3.3. Difference spectroscopy of the Glu78Ala CcO.....	131
3.3.4. Conclusion.....	136
3.4. Far infrared spectroscopy	138
3.4.1. Introduction and development of the method	138
3.4.2. Amide VI.....	140
3.4.3. Far infrared electrochemically induced FITR difference spectroscopy	148
3.4.4. Far infrared hydrogen bonding signature	168
4. Summary	174
5. References	177
6. Appendix	194

List of figures

Figure 1.1.1. Chemical structure of the chlorophyll A.....	2
Figure 1.1.2. Structure of the zinc finger protein–DNA complex (PDB code 1TF6). The zinc finger protein is presented as magenta cartoon, the DNA double helix as green cartoon and zinc atoms as blue sphere.....	3
Figure 1.1.3. Structure of the iron–protoporphyrin IX.	4
Figure 1.1.4. Chemical structure of the Vitamin B ₁₂	6
Figure 1.1.5. The active site of tyrosinase as example of type 3 copper–containing enzyme. The coordinating histidines are presented as sticks, the Cu atoms as orange balls, and the water molecule as red sticks (PDB code 2ZMX). ⁴³	7
Figure 1.2.1. The classical model of the mitochondrial respiratory chain and the ATP synthase. The structures are based on the following PDB codes: 3M9S (NADH:ubiquinone oxidoreductase); 1QLB (Fumarate reductase); 1ZRT (cytochrome <i>bc</i> ₁ complex); 3HB3 (CcO); 1BMF (F ₁ part of the ATP synthase).	9
Figure 1.2.2. Chemical structure of (A) ubiquinone, (B) menaquinone and (C) phylloquinone.	10
Figure 1.2.3. The decline of standard potentials of the redox cofactors of the mitochondrial respiratory chain as electron pairs flow down the respiratory chain to oxygen. The blue arrows denote the difference in standard potentials between each step. The NAD stands for Nicotine Adenine Dinucleotide, Q stands for quinol, <i>b</i> , <i>c</i> and <i>a</i> stand for the corresponding heme type.	11
Figure 1.2.4. (A) Overall architecture of the hydrophilic domain of the complex I from <i>T. thermophilus</i> and (B) the organization of the redox cofactors. The FMN is colored in blue and presented as sticks; the iron and sulfur atoms are colored in red and yellow, respectively and presented as spheres. The arrows present the electron transfer between the cofactors (PDB code 3I9V).	12
Figure 1.2.5. Architecture of the complex I and the proposed coupling mechanism. ⁵⁹ FMN is presented magenta balls, the Fe–S clusters are presented in yellow and red and the quinone is presented in blue. The blue arrows indicate the electron transfer pathway and the black ones indicate the proton pathways. The helices which undergo a conformational movement in the hydrophilic part are the Nqo4 (green cylinders) and Nqo6 (red cylinder). In the membrane domain, the HL helix is colored in magenta and the discontinuous helices are colored in red. ⁵⁹	13
Figure 1.2.6. (A) Crystal structure of the QFR from <i>Wolinella succinogenes</i> (PDB code 1QLB) and (B) the organization of redox cofactors where the FAD and the hemes are presented as sticks and the Fe–S clusters as spheres. The arrows indicate the electron transfer pathway from the hemes to the fumarate presented as red sticks.	15
Figure 1.2.7. (A) Crystal structure of the <i>bc</i> ₁ from <i>Rhodobacter capsulatus</i> (PDB code 1ZRT). (B) The organization of the redox cofactors and schematic presentation of the Q–cycle. The <i>b</i> _H hemes are presented as sticks and colored in orange, the <i>b</i> _L in blue, the cytochrome <i>c</i> ₁ in red. The Rieske [2Fe–2S] clusters are presented as spheres. Q and H ₂ Q represent quinone and quinol, respectively. The orange arrows indicate the electron transfer pathway and the red arrow indicates the proton translocation pathway.	17

Figure 1.2.8. (A) The release of the first proton from the Q_o site via the His156. (B) The release of the second proton via the Glu295. ¹⁰⁰ The heme b_L is presented in green sticks, the PEWY motif is colored in yellow, the Rieske [2Fe–2S] cluster is presented as spheres and the coordinating amino acids are presented as sticks. The H_2Q and Q are presented as cyan sticks.....	18
Figure 1.2.9. (A) Structure of the CcO from <i>P. denitrificans</i> . (B) Schematic presentation of the electron and proton uptake pathways. The hemes a and a_3 are presented as sticks and colored in orange and magenta, respectively. The Cu atoms are presented as spheres and colored in dark yellow, Ca in green and Mg/Mn in clear blue. The D124, E278 and K354 amino acids are presented as sticks. The dashed red arrows indicate the proton pathways (PDB code 3HB3). The orange arrows indicate the electron transfer.	20
Figure 1.2.10. (A) The active site of the CcO. The heme a_3 is colored in magenta. The Cu_B is presented as a sphere and the coordinating His325 and His326 are presented as yellow sticks. The crosslinking residues Tyr280 and His276 are presented in green and blue, respectively. (B) The catalytic turnover of the active site. The black arrows indicate the transition between the different states and the orange dashed arrows represent the proton pumping steps (for details see text). ¹⁰⁷	21
Figure 1.3.1. Representation of the most common Fe–S clusters (A) [2Fe–2S] (PDB code 1RIE), (B) [3Fe–4S] (PDB code 1FRF), (C) [4Fe–4S] (PDB code 1FRE) and (D) [7Fe–7S] (PDB code 1MIN. Iron atoms are presented as orange balls, Sulfur atoms are yellow balls. The coordinating amino acids are presents as sticks.....	23
Figure 1.4.1. Normal mode vibrations.	27
Figure 1.4.2. The harmonic oscillator model.	27
Figure 1.4.3. Absorbance spectra of the CcO in the oxidized state (blue trace) and in the reduced state (red trace).....	31
Figure 1.4.4. Schematic presentation of the OTTLE cell. The red arrow indicates the beam path through the cell. ¹⁴⁴	31
Figure 1.4.5. Fully oxidized minus fully reduced difference spectrum of the CcO from <i>P. denitrificans</i> recorded at pH 8.0. The positive signals (blue) are arising from the oxidized protein and the negative ones (red) from the reduced protein.....	32
Figure 1.4.6. Attenuated Total Reflection unit and an enlarged view of the evanescent wave.....	33
Figure 2.1.1. Typical UV absorbance spectrum of the A β 16 peptide. The dashed line represents the absorption used to determine the concentration.	38
Figure 2.1.2. Chromatography profiles on Fractogel EMD of the purification of both NDF from <i>E. coli</i> . The black line displays the NaCl gradient, the blue line shows the absorbance at 280 nm and the red line displays the NADH/ferricyanide oxidoreductase activity. The panel A shows the data for the unlabelled (⁵⁶ Fe) sample and the panel B shows the data for the ⁵⁴ Fe-labelled sample.	40
Figure 2.1.3. Chromatography profiles on the affinity (StrepTag)–Sepharose. (A) For the unlabelled NDF and (B) for the ⁵⁴ Fe-labelled NDF. The blue line displays the absorbance at 280 nm, the red line displays the NADH/ferricyanide oxidoreductase activity.	40

Figure 2.1.4. SDS-PAGE of the preparation of (A) unlabelled NDF and (B) ⁵⁴ Fe-labelled NDF. The bands were assigned to the individual subunits due to their apparent molecular weight using the etalon scale (C).....	41
Figure 2.2.1. (A) The main optical parts of a conventional FTIR spectrometer. (B) The shape of a typical interferogram. (C) A typical protein spectrum obtained after the transformation of its corresponding interferogram.....	43
Figure 2.3.1. Schematic presentation of the three-electrode setup. WE stands for the working electrode, Ref for the reference electrode and CE for the counter-electrode. The potential is controlled between the WE and the Ref while the current is controlled between the WE and the CE.	47
Figure 2.3.2. Schematic representation of the modified gold grid. The cysteamine is colored in black, the 3-mercaptopropionic acid in red and the gold grid in yellow.	48
Figure 3.1.1. The four possible protonation state of the imidazole ring of His. N ^π is the one close to the CH ₂ and N ^ε is the one far from the CH ₂ . (A) N ^ε is protonated, (B) N ^π is protonated, (C) both nitrogens are protonated and (D) the Im ring is deprotonated.	50
Figure 3.1.2. UV-Vis spectra of: (A) the Cu-Im and (B) the Cu-PLH complexes at pD 2.0 (Black), at pD 7.0 (Blue) and pD 9.5 (magenta).	51
Figure 3.1.3. MIR spectra of the Im and Cu-Im-D ₄ complexes. (A) at pD 2.0, (B) at pD 7.0 and (C) at pD 9.5. The right panel shows the chemical structure of the Im-D ₄	52
Figure 3.1.4. MIR spectrum of the CuSO ₄ -Im-H ₄ sample recorded at pH 2.0.....	53
Figure 3.1.5. FIR absorbance spectra of the free and Cu-bound deuterated Im. (A) at pD 2.0, (B) at pD 7.0 and (C) at pD 9.5.	54
Figure 3.1.6. FIR spectrum of the Cu-Im-H ₄ complex at pH 7.0.....	55
Figure 3.1.7. MIR spectra of the PLH and Cu-PLH complexes. (A) at pD 2.0, (B) at pD 7.0 and (C) at pD 9.5.	57
Figure 3.1.8. FIR absorbance spectra of the PLH and Cu-bound PLH. (A) at pD 2.0, (B) at pD 7.0 and (C) at pD 9.5.....	60
Figure 3.1.9. Schematic presentation of the healthy brain neurons and AD patient brain. The tangles are colored in black and the Aβ are colored in blue.....	63
Figure 3.1.10. The coordination modes of Cu ²⁺ by Aβ16 at physiological pH. Component I at pH 6.50 and component II at pH 9.0. ¹⁸⁵ The coordinating Asp1 is colored in red, His are colored in green and magenta and the alanine in orange.	65
Figure 3.1.11. Global view of the spectra of the free unlabelled and isotopically labelled peptides recorded at pH 6.50 in the 1800-700 cm ⁻¹ infrared range. The spectra are colored in black (unlabelled), red (H6), blue (H13), green (H14) and magenta (Asp1).	66
Figure 3.1.12. Enlarged view of the 1600-1200 cm ⁻¹ spectral region.....	67
Figure 3.1.13. Spectrum of 0.5 % w/v of TFA at pH 12 recorded in the region 1800-700 cm ⁻¹	68
Figure 3.1.14. Global view of the spectra of the Cu ²⁺ -Aβ16 peptides recorded at pH 6.50 in the 1800-900 cm ⁻¹ infrared range.	69
Figure 3.1.15. Global view of the spectra of the Aβ16 peptides recorded at pD 6.50 in the 1800-900 cm ⁻¹ infrared range.....	70
Figure 3.1.16. Enlarged view of the spectra of the Aβ16 peptides recorded at pD 6.50 in the 1750-1350 cm ⁻¹ infrared range.....	71

Figure 3.1.17. Enlarged view of the spectra of the A β 16 peptides recorded at pD 6.50 in the 1100–900 cm ⁻¹ infrared range.....	72
Figure 3.1.18. Global view of the spectra of the Cu ²⁺ -A β 16 complexes recorded at pD 6.50 in the 1800–900 cm ⁻¹ infrared range.	73
Figure 3.1.19. Enlarged view of the spectra of the Cu ²⁺ -A β 16 complexes recorded at pD 6.50 in the 1750–1350 cm ⁻¹ infrared range.....	74
Figure 3.1.20. Enlarged view of the spectra of the Cu ²⁺ -A β 16 complexes recorded at pD 6.50 in the 1100–900 cm ⁻¹ infrared range.....	74
Figure 3.1.21. Global view of the spectra of the A β 16 peptides recorded at pH 9.0 in the 1800–900 cm ⁻¹ infrared range.	75
Figure 3.1.22. Global view of the spectra of the Cu ²⁺ -A β 16 complexes recorded at pH 9.0 in the 1800–900 cm ⁻¹ infrared range.	76
Figure 3.1.23. Enlarged view of the spectra of the Cu ²⁺ -A β 16 complexes recorded at pH 9.0 in the 1750–1350 cm ⁻¹ infrared range.....	77
Figure 3.1.24. Global view of the spectra of the A β 16 peptides recorded at pD 9.0 in the 1800–900 cm ⁻¹ infrared range.	78
Figure 3.1.25. Enlarged view of the spectra of the A β 16 peptides recorded at pD 9.0 in the 1750–1350 cm ⁻¹ infrared range.....	79
Figure 3.1.26. Enlarged view of the spectra of the A β 16 peptides recorded at pD 9.0 in the 1100–900 cm ⁻¹ infrared range.....	80
Figure 3.1.27. Global view of the spectra of the Cu ²⁺ -A β 16 complexes recorded at pD 9.0 in the 1800–900 cm ⁻¹ infrared range.	80
Figure 3.1.28. Enlarged view of the spectra of the Cu ²⁺ -A β 16 complexes recorded at pD 9.0 in the 1750–1350 cm ⁻¹ infrared range.....	81
Figure 3.1.29. Enlarged view of the spectra of the Cu ²⁺ -A β 16 complexes recorded at pD 9.0 in the 1100–900 cm ⁻¹ infrared range.....	82
Figure 3.1.30. Global view of the spectra of the A β 16 free peptides recorded at pH 11.0 in the 1800–900 cm ⁻¹ infrared range.	83
Figure 3.1.31. Enlarged view of the spectra of the A β 16 free peptides recorded at pH 11.0 in the 1800–700 cm ⁻¹ infrared range.	84
Figure 3.1.32. Enlarged view of the spectra of the A β 16 free peptides recorded at pH 11.0 in the 1100–900 cm ⁻¹ infrared range.	85
Figure 3.1.33. Global view of the spectra of the Cu ²⁺ -A β 16 complexes recorded at pH 11.0 in the 1800–900 cm ⁻¹ infrared range.	85
Figure 3.1.34. Enlarged view of the spectra of the Cu ²⁺ -A β 16 complexes recorded at pH 11.0 in the 1750–1350 cm ⁻¹ infrared range.....	86
Figure 3.1.35. Enlarged view of the spectra of the Cu ²⁺ -A β 16 complexes recorded at pH 11.0 in the 1100–900 cm ⁻¹ infrared range.....	87
Figure 3.1.36. Global view of the spectra of the A β 16 peptides recorded at pD 11.0 in the 1800–900 cm ⁻¹ infrared range.....	87
Figure 3.1.37. Enlarged view of the spectra of the A β 16 peptides recorded at pD 11.0 in the 1750–1350 cm ⁻¹ infrared range.....	88
Figure 3.1.38. Enlarged view of the spectra of the A β 16 peptides recorded at pD 11.0 in the 1100–900 cm ⁻¹ infrared range.....	88
Figure 3.1.39. Global view of the spectra of the Cu ²⁺ -A β 16 complexes recorded at pD 11.0 in the 1800–900 cm ⁻¹ infrared range.	89
Figure 3.1.40. Enlarged view of the spectra of the Cu ²⁺ -A β 16 complexes recorded at pD 11.0 in the 1750–1350 cm ⁻¹ infrared range.....	89
Figure 3.1.41. Enlarged view of the spectra of the Cu ²⁺ -A β 16 complexes recorded at pD 11.0 in the 1100–900 cm ⁻¹ infrared range.....	90

Figure 3.1.42. Electrochemically induced FTIR difference spectrum of the Cu-A β 16 complex recorded in the 1800-1000 cm ⁻¹ range at pH 6.50.	92
Figure 3.1.43. Electrochemically induced FTIR difference spectrum of the Cu-A β 16 complex recorded in the 1800-1000 cm ⁻¹ range at pH 9.0.	93
Figure 3.1.44. Electrochemically induced FTIR difference spectrum of the Cu-A β 16 complex recorded in the 1800-1000 cm ⁻¹ range at pH 9.0.	94
Figure 3.1.45. Electrochemically induced FTIR difference spectrum of the Cu-A β 16 complex recorded in the 1800-1000 cm ⁻¹ range at pH 9.0 (black) and pD 9.0 (red).....	94
Figure 3.1.46. Proposed coordination modes of Cu cations by A β 16 at: pH 6.50 (left), pH 9.0 (middle) and pH 11.0 (right).	95
Figure 3.2.1. Zn cations binding site within the <i>bc</i> ₁ of <i>R. capsulatus</i> (PDB code 1ZRT). Zinc cations are blue, the binding partners are colored in red, the heme <i>b</i> _L is in yellow and the hemes <i>b</i> _H and <i>c</i> ₁ are in black.	97
Figure 3.2.2. UV-Vis difference spectra of the wild-type <i>bc</i> ₁	99
Figure 3.2.3. UV-Vis difference spectra of the wild-type <i>bc</i> ₁ in presence of 200 μ M of Zn ²⁺	99
Figure 3.2.4. Ox-red FTIR difference spectra in the region 1800–800 cm ⁻¹ of the wild-type <i>bc</i> ₁ before (black) and after the inhibition (red).	100
Figure 3.2.5. Enlarged view of the 1775–1600 cm ⁻¹ spectral region of the FTIR difference spectra of the wild-type <i>bc</i> ₁ (black) and Zn ²⁺ -inhibited enzyme (red).	101
Figure 3.2.6. Enlarged view of the 1600–1100 cm ⁻¹ spectral region of the FTIR difference spectra of the wild-type <i>bc</i> ₁ (black) and Zn ²⁺ -inhibited enzyme (red).	102
Figure 3.2.7. The chemical structure of the heme. The symbols of the carbon atoms of the porphyrin ring are also indicated.	103
Figure 3.2.8. Enlarged view of the 1000–800 cm ⁻¹ spectral region of the FTIR difference spectra of the wild-type <i>bc</i> ₁ (black) and Zn ²⁺ -inhibited enzyme (red).	104
Figure 3.2.9. Ox-red FTIR difference spectra recorded at pD 8.0 in the region 1800–800 cm ⁻¹ of the wild-type <i>bc</i> ₁ before (black) and after the inhibition (red).	105
Figure 3.2.10. Ox-red spectrum of the native enzyme minus ox-red Zn-poisoned enzyme recorded at pD 8.0.	106
Figure 3.2.11. Titration curves of the <i>bc</i> ₁ in the native form (left panel) and in presence of Zn cations (right panel).	107
Figure 3.2.12. UV-Vis difference spectra of the Glu295Val <i>bc</i> ₁	108
Figure 3.2.13. UV-Vis difference spectra of the Glu295Val <i>bc</i> ₁ in presence of 200 μ M of Zn ²⁺	108
Figure 3.2.14. Ox-red FTIR difference spectra in the region 1800–800 cm ⁻¹ of the Glu295Val <i>bc</i> ₁ before (black) and after the inhibition (red).	109
Figure 3.2.15. Enlarged view of the 1775–1600 cm ⁻¹ spectral region of the FTIR difference spectra of the Glu295Val <i>bc</i> ₁ (black) and Zn ²⁺ -inhibited enzyme (red).	109
Figure 3.2.16. Enlarged view of the 1600–1100 cm ⁻¹ spectral region of the FTIR difference spectra of the Glu295Val <i>bc</i> ₁ (black) and Zn ²⁺ -inhibited enzyme (red).	110
Figure 3.2.17. Enlarged view of the 1000–800 cm ⁻¹ spectral region of the FTIR difference spectra of the Glu295Val <i>bc</i> ₁ (black) and Zn ²⁺ -inhibited enzyme (red).	112

Figure 3.2.18. UV-Vis difference spectra of the subcomplex.....	113
Figure 3.2.19. UV-Vis difference spectra of the subcomplex in presence of 200 μM of Zn^{2+}	113
Figure 3.2.20. Ox-red FTIR difference spectra in the region 1800–800 cm^{-1} of the subcomplex before (black) and after the inhibition (red).	114
Figure 3.2.21. Enlarged view of the 1775–1600 cm^{-1} spectral region of the FTIR difference spectra of the subcomplex (black) and Zn^{2+} -inhibited enzyme (red).....	115
Figure 3.2.22. Enlarged view of the 1600–1100 cm^{-1} spectral region of the FTIR difference spectra of the subcomplex (black) and Zn^{2+} -inhibited enzyme (red).....	116
Figure 3.2.23. Enlarged view of the 1000–800 cm^{-1} spectral region of the FTIR difference spectra of the subcomplex (black) and Zn^{2+} -inhibited enzyme (red).....	117
Figure 3.2.24. The proposed mechanism of inhibition of the bc_1 by Zn cations. Panels A and B show the release of the second proton from the Q_o site. Panels C and D show the binding of Zn cations.....	119
Figure 3.3.1. The proton pathways in the CcO from <i>P. denitrificans</i> (PDB code 3HB3). The D-pathway is colored in blue, the K-pathway in green and the exit pathways in cyan. The water molecules are shown as black balls, the hemes as sticks and the metals as spheres.	120
Figure 3.3.2. High affinity binding site of Cd (or Zn) cations within the CcO from <i>R. sphaeroides</i> (PDB code 2GSM). The Glu101 and His96 are in magenta sticks. The Cd cation is shown as a blue sphere. The shown subunits are I (green) and II (yellow). The proton uptake pathways are represented as red arrows.	122
Figure 3.3.3. UV-Vis difference spectra of the CcO at pH 8.0.....	123
Figure 3.3.4. UV-Vis difference spectra of the CcO in presence of 200 μM of Zn^{2+} at pH 8.0.	123
Figure 3.3.5. Ox-red FTIR difference spectra in the region 1800–1000 cm^{-1} of the CcO before (black) and after the inhibition (red).	124
Figure 3.3.6. Enlarged view of the ox-red FTIR difference spectra in the region 1775–1600 cm^{-1} of the CcO before (black) and after the inhibition (red).....	125
Figure 3.3.7. Enlarged view of the ox-red FTIR difference spectra in the region 1600–1200 cm^{-1} of the CcO before (black) and after the inhibition (red).....	125
Figure 3.3.8. Double difference spectrum in the 1800–1000 cm^{-1} range of the inhibited CcO minus the native CcO at pH 8.0.	126
Figure 3.3.9. Comparison between the oxidized minus reduced difference spectra of the wild-type CcO recorded at pH 8.0 (black) and at pD 8.0 (red).	128
Figure 3.3.10. Ox-red FTIR difference spectra in the region 1800–1200 cm^{-1} of the CcO recorded at pD 8.0 before (black) and after the inhibition (red).....	128
Figure 3.3.11. Enlarged view of the ox-red FTIR difference spectra in the region 1800–1200 cm^{-1} of the CcO recorded at pD 8.0 before (black) and after the inhibition (red).	129
Figure 3.3.12. The neo-classical model of the anti-cooperativity of the heme centers of CcO. The left site is the a_3 site and the right site is the a site. E_m stands for the midpoint potential, R for the reduced state and O for the oxidized state. The letter in parenthesis shown for each E_m indicate the redox state of each center not undergoing a redox reaction.	130

Figure 3.3.13. Titration curves of the wild-type CcO in the native form (left panel) and in presence of Zn cations (right panel).	131
Figure 3.3.14. UV-Vis difference spectra of the Glu78Ala CcO at pH 8.0.	132
Figure 3.3.15. UV-Vis difference spectra of the Glu78Ala CcO in presence of Zn cations at pH 8.0.	132
Figure 3.3.16. Ox-red FTIR difference spectra in the region 1800–1200 cm ⁻¹ of the Glu78Ala CcO recorded at pH 8.0 before (black) and after the inhibition (red).	133
Figure 3.3.17. Double difference spectrum of the wild-type CcO minus Glu78Ala CcO recorded at pH 8.0. The difference spectra were normalized to the δ_{42} vibration of the hemes.	134
Figure 3.3.18. Double difference spectrum of the inhibited Glu78Ala CcO minus the native Glu78Ala at pH 8.0. The difference spectrum was normalized to the δ_{42} vibration of the hemes.	134
Figure 3.3.19. Titration curves of the Glu78Ala CcO in the native form (left panel) and in presence of Zn cations (right panel).	136
Figure 3.4.1. Typical contribution found in the FIR spectrum of a metalloprotein (Rieske).	139
Figure 3.4.2. FIR-ATR absorbance spectra of the NDF (black) and the MES buffer (red). ..	140
Figure 3.4.3. FIR ATR absorbance spectrum of the NDF in 20 mM MES buffer at pH 6.0 containing 20 mM KCl.	140
Figure 3.4.4. Amide I/amide I' and amide VI/amide VI' band of PLL in H ₂ O (Black), in D ₂ O (Red), at pH 11.20 (Blue) and at pD 11.20 (Magenta).	142
Figure 3.4.5. Amide I and amide VI band of: PLA at pD 9.0 (Black) and PLH at pD 7.0 (Red).	145
Figure 3.4.6. Amide I and amide VI bands of: the CcO (Black), the bc_1 (Red) and the Rieske protein (Blue).	146
Figure 3.4.7. Structure of the horse heart cytochrome <i>c</i> (PDB code 1HRC). The heme is colored in white, the coordinating His in blue and the coordinating Met in yellow.	149
Figure 3.4.8. (A) Reduced minus oxidized difference spectrum of the horse heart cytochrome <i>c</i> obtained in the ANKA synchrotron facility and (B) obtained in the laboratory in Strasbourg.	149
Figure 3.4.9. FIR ATR absorbance spectrum of liquid water.	150
Figure 3.4.10. Optical setups for the electrochemically induced FIR difference spectroscopy. (A) The setup developed by Berthomieu <i>et al.</i> , (B) the setup used at ANKA and (C) the setup developed in our laboratory.	150
Figure 3.4.11. Iron-sulfur clusters of (A) Rb from <i>C. pasteurianum</i> , (B) Fd from spinach, (C) Rieske from <i>T. thermophilus</i> and (D) Fd from <i>C. pasteurianum</i>	151
Figure 3.4.12. Crystal structure of Rb from <i>C. pasteurianum</i> (PDB code 1FHH). The iron is presented as a sphere and the coordinating Cys are in red.	151
Figure 3.4.13. FIR absorbance spectrum of the Rb from <i>C. pasteurianum</i> at pH 7.4.	152
Figure 3.4.14. Electrochemically induced difference spectrum of the Rb from <i>C. pasteurianum</i> at pH 7.4 in the 450–100 cm ⁻¹ spectral range.	153
Figure 3.4.15. Crystal structure of Fd from spinach (PDB code 1A70). The iron atoms are in orange, the sulfur in yellow and the coordinating Cys in red.	154
Figure 3.4.16. FIR absorbance spectrum of the Fd from Spinach at pH 7.5.	155
Figure 3.4.17. Electrochemically induced FTIR difference spectrum of the Fd from Spinach at pH 7.5 in the 450–100 cm ⁻¹ spectral range.	156

Figure 3.4.18. Solution structure of the Fd from <i>C. pasteurianum</i> (PDB code 1CLF). The iron atoms are in orange, the sulfur in yellow and the coordinating Cys in red.	157
Figure 3.4.19. FIR absorbance spectrum of the Fd from <i>C. pasteurianum</i> at pH 7.5.	157
Figure 3.4.20. Electrochemically induced FTIR difference spectrum of the Fd from <i>C. pasteurianum</i> at pH 7.5 in the 450–100 cm ⁻¹ spectral range.	158
Figure 3.4.21. Crystal structure of the Rieske protein from <i>T. thermophilus</i> (PDB code 1NYK). The iron atoms are in orange, the sulfur in yellow, the coordinating Cys in red and the coordinating His in blue.	159
Figure 3.4.22. Absorbance spectra of the Rieske protein in the 600–50 cm ⁻¹ spectral range for pH 6.0 (black), 8.0 (red), 10.2 (blue) and in pure water (green).	160
Figure 3.4.23. Electrochemically induced difference spectra of the Rieske from <i>T. thermophilus</i> at pH: 10.2 (black), 8.0 (red) and 6.0 (blue) in the 450–100 cm ⁻¹ spectral range.	164
Figure 3.4.24. The Fe–S clusters of the NDF. The backbone is in light grey, the Fe–S clusters are in balls, the coordinating His residue is in blue and the Cys residues in red.	165
Figure 3.4.25. FIR absorbance spectra of the ⁵⁶ Fe–NDF (black) and of the ⁵⁴ Fe–labelled NDF (red).	165
Figure 3.4.26. MIR electrochemically induced difference spectra of the ⁵⁶ Fe–NDF (black) and of the ⁵⁴ Fe–labelled NDF (red).	166
Figure 3.4.27. FIR electrochemically induced difference spectra of the ⁵⁶ Fe–NDF (black) and of the ⁵⁴ Fe–labelled NDF (red).	166
Figure 3.4.28. Cartoon view of the closed I-domain taken from the low affinity structure (PDB code 1LFA). The MIDAS magnesium ion is shown as a magenta sphere. The α 7 helix is colored in red.	170
Figure 3.4.29. FIR temperature dependent spectra of the LFA-I domain at pH 7.4 in presence of (A) Mg, (B) Mn, (C) Ca and (D) Fe cations.	172

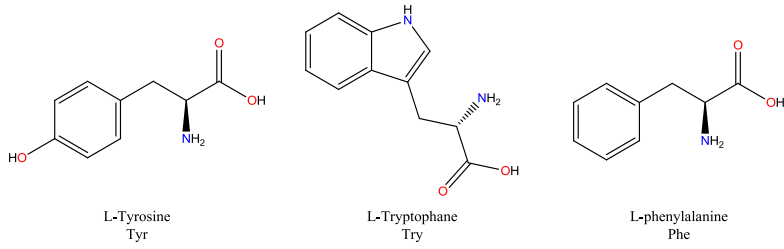
List of abbreviations

A β 16	Amyloid- β 16
Abs	Absorbance
ADP	Adenosine Diphosphate
ATP	Adenosine Triphosphate
ATR	Attenuated Total Reflection
<i>bc</i> ₁	Cytochrome <i>bc</i> ₁ complex
CcO	Cytochrome <i>c</i> oxidase
CHES	N-Cyclohexyl-2-aminoethanesulfonic acid
<i>C. Pasteurianum</i>	<i>Clostridium pasteurianum</i>
DDM	n-Dodecyl- β -maltoside
dTGS	Deuterated Triglycine sulfate
E _m	Midpoint potential
FAD	Flavine adenine dinucleotide
Fd	Ferredoxin
FIR	Far Infrared
FMN	Flavine mononucleotide
FTIR	Fourier transform infrared
H ₂ Q	Quinole
Im	Imidazole
KDa	Kilo Daltons
MCT	Mercury Cadmium Telluride
MES	2- (N-morpholino)ethanesulfonic acid
MIR	Mid infrared
NADH	Nicotine adenine dinucleotide
OTTLE	Optically Transparent Thin-Layer Electrochemical cell
<i>P. denitrificans</i>	<i>Paracoccus denitrificans</i>
PLA	Poly-L-alanine
PLH	Poly-L-histidine
PLL	Poly-L-lysine
Q	Quinone
<i>R. capsulatus</i>	<i>Rhodobacter capsulatus</i>
Rd	Rubredoxin

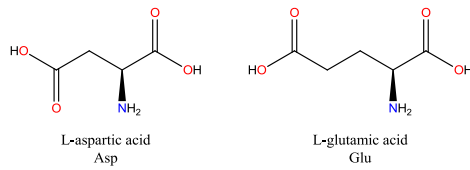
SHE	Standard Hydrogen Electrode
<i>T. Thermophilus</i>	<i>Thermus thermophilus</i>
THz	Terahertz
Tris	tris(hydroxymethyl)aminomethane
UV-Vis	Ultraviolet–Visible
ν	Stretching vibration
$\nu^{\text{“s”}}$	Symmetric stretching vibration
$\nu^{\text{“as”}}$	Antisymmetric stretching vibration
δ	Bending vibration
δ_{ip}	In–plane deformation
δ_{op}	Out–of–plane deformation
δ_{def}	Deformation vibration
γ	Wagging vibration

The twenty amino acids

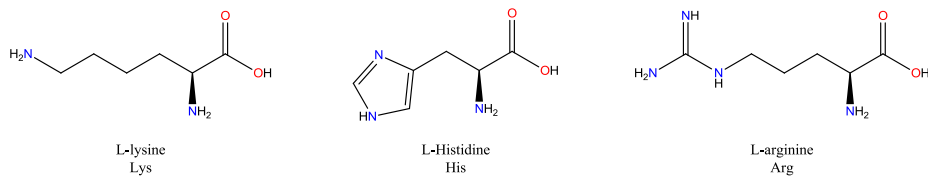
Aromatic amino acids



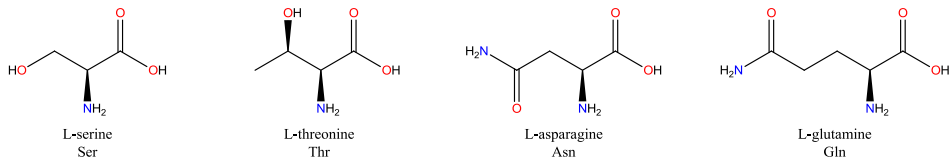
Acidic amino acids



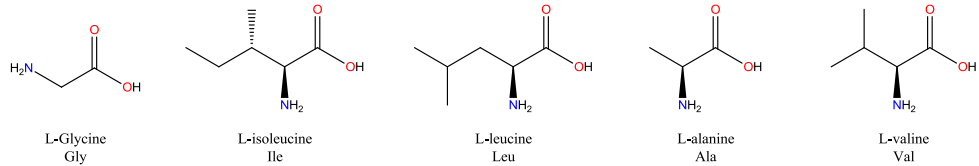
Basic amino acids



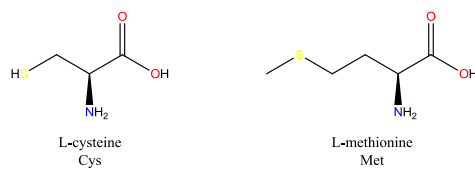
Hydrophilic amino acids



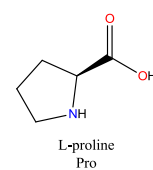
Hydrophobic amino acids



Sulfur containing amino acids



Special structure amino acid



List of publications

Published

El Khoury, Y., Hielscher, R., Voicescu., M, Gross, J., and Hellwig, P. On the Specificity of the Amide VI band for the Secondary Structure of proteins. *Vibr Spectrosc.* Submitted.

El Khoury, Y., Trivella, A., Gross, J., and Hellwig, P. Probing the hydrogen bonding structure in the Rieske protein by means of redox induced mid infrared spectroscopy and temperature derived far infrared spectroscopy. *ChemPhysChem.* Accepted.

Voicescu, M., **El Khoury, Y.**, Martel, D., Heinrich, M. and Hellwig, P. Spectroscopic Analysis of Tyrosine Derivatives: On the Role of the Tyrosine - Histidine Covalent Linkage in Cytochrome c Oxidase (2009) *J Phys Chem B.* **113**(40), 13429-36.

El Khoury, Y., and Hellwig, P. Infrared Spectroscopic Characterization of Copper-Polyhistidine from 1800-50 cm^{-1} : Model Systems for the Cu Coordination (2009) *Biol Inorg Chem.* **14**(1):23-34.

In preparation

El Khoury, Y., and Hellwig, P. Electrochemically induced far infrared difference spectra of iron-sulfur clusters.

El Khoury, Y., Dorlet, P., Faller, P., and Hellwig, P. New insights into the coordination of copper by the amyloid-beta 16 peptide from FTIR spectroscopy and isotopic labelling.

Lee, D. W., **El Khoury, Y.**, Daldal. F., and Hellwig, P. The inhibition of the proton pumping of the cytochrome bc_1 complex from *Rhodobacter capsulatus* by Zn cations.

Conference publications

El Khoury, Y., Lee, D. W., Daldal. F., and Hellwig, P. The Zn^{2+} cations inhibitve effects on the cytochrome bc_1 complex from *Rhodobacter capsulatus* as revealed by the FTIR difference spectroscopy. *Biochem Biophys Acta* (2010) **1797**, 13-14.

Trivella, A., **El Khoury, Y.**, Gaillard, T., Stote, R. H., Merino, N., Francisco J. Blanco, F. J., and Hellwig, P. Temperature Dependence of the Far Infrared Signature of Internal Hydrogen Bonds in Proteins as Probed for Integrins. *AIP Conf Proc* (2010) **1214**(1), 3-6.

Hellwig, P., **El Khoury, Y.**, and Hielscher, R. Far infrared spectroscopic studies on hydrogen bonding features in proteins from the respiratory chain. *Biochem Biophys Acta* (2008) **1777**, S92-S92.

Abstract

FTIR spectroscopy is a powerful analytical tool to investigate biological molecules. In the mid infrared domain, valuable information about the backbone reorganization and information at the level of individual amino acids side chain absorptions can be obtained. Importantly, the far infrared domain includes metal–ligand vibrations as well as the hydrogen bonding motions. This spectral range is currently being developed for biological molecules.

The thesis includes three main parts. First, the copper complexes vibrations have been probed in the mid and far infrared range. Copper is the cofactor of several proteins and most of the time it is coordinated by histidine residues. It is thus critical to understand the coordination modes of copper. In order to do so, the mid and far infrared absorption spectra of copper–poly–L–histidine complexes were investigated as a function of pH. The study allowed the observation of the backbone reorganization of the poly amino acid as well as the observation of metal–ligand vibrations in the far infrared domain. The copper binding to the amyloid–beta–16 is suggested to be a key step in the development of Alzheimer’s. The copper–amyloid–beta–16 complexes were studied in the mid infrared domain at different pH values. Combined with the isotopically labelled amyloid–beta–16, the mid infrared FTIR absorption spectroscopy allowed determining the coordination modes of copper.

In the second part of the thesis, we used the technique to study enzymes from the respiratory chain. The respiratory complexes are transmembrane proteins found in the inner mitochondrial membrane of eukaryotic cells and in the plasma membrane of prokaryotic cells. The respiratory complex I, III and IV couple the electron transfer reactions to the proton pumping across the membrane, creating thus the protonmotive force required for the synthesis of ATP. Zn cations are known to inhibit the proton pumping by the respiratory enzymes. In order to better understand the inhibitive effects of Zn on the respiratory complex III and IV, the electrochemically induced FTIR difference spectroscopy was used. The binding of Zn cations is shown to take place via the Glu295 of the heme–*b* subunit of the complex III. The complex IV seems to have more than one binding site for Zn. One binding site was shown to involve the Glu78 residue of subunit II while another one is suggested to inhibit the protons exit.

Finally, in the last part of the thesis, the far infrared was developed, including an electrochemical approach. The far infrared range offers a tool to observe the metal–ligand

vibrations, the amide VI signature as well as the signature of the hydrogen bonding. The far infrared absorbance spectra of several iron–sulfur proteins are recorded. Interestingly, it was found that the far infrared spectra of proteins showed a broad band below 300 cm^{-1} which arose from the hydrogen bonding collective motions. The hydrogen bonding signature of the [2Fe–2S] Rieske protein was probed for different pH values at low temperatures. The study pointed towards the effect of the protonation state of the coordinating histidines on the overall structure of the protein and the hydrogen bonding signature.

Résumé

La spectroscopie IRTF est un outil analytique important pour l'étude de molécules biologiques. En utilisant le moyen infrarouge, des informations importantes concernant la réorganisation de la chaîne peptidique de même que des informations concernant l'absorption des chaînes latérales des acides aminés peuvent être obtenues. Le domaine du lointain infrarouge contient les vibrations métal–ligand et les vibrations des liaisons hydrogène. Ce domaine spectral est en cours de développement pour les molécules biologiques.

La thèse contient trois parties principales. Les vibrations de complexes de cuivre ont été étudiées en moyen et lointain infrarouge. Le cuivre est le cofacteur de plusieurs protéines, et souvent, sa coordination a lieu via des résidus histidines. Il est donc critique de comprendre les modes de coordinations du cuivre. Pour cela les spectres des complexes cuivre–poly–L–histidine ont été enregistrés en fonction du pH en moyen et lointain infrarouge. Cette étude a permis d'observer la réorganisation de la chaîne peptidique. De même, les vibrations métal–ligand ont été observées dans le lointain infrarouge. La coordination du cuivre par l'amyloïde–beta–16 est une étape déterminante dans l'apparition de la maladie d'Alzheimer. Les complexes cuivre– amyloïde–beta–16 ont été étudiés dans le moyen infrarouge à différentes valeurs de pH. L'utilisation d'échantillons marqués isotopiquement pour cette étude a permis de déterminer les modes de coordination du cuivre.

Dans la deuxième partie de la thèse, nous avons utilisé le moyen infrarouge pour étudier des protéines de la chaîne respiratoire. Les complexes de la chaîne respiratoire sont des protéines transmembranaires qu'on trouve dans la membrane interne des mitochondries des cellules eucaryotes ou dans la membrane plasmique des cellules procaryotes. Les complexes respiratoires I, III et IV couplent les réactions de transfert d'électrons au pompage de protons à travers la membrane, créant ainsi un gradient de protons nécessaire pour la production d'ATP. Les cations Zn^{2+} sont connus pour leur pouvoir inhibiteur vis-à-vis du pompage de protons par les enzymes respiratoires. Pour mieux comprendre l'effet de l'inhibition par le Zn sur les complexes III et IV, la spectroscopie différentielle IRTF induite par l'électrochimie a été utilisée. L'étude montre que la chélation du Zn par le complexe III a lieu via le résidu Glu295 appartenant à la sous-unité des heme–*b*. L'inhibition du complexe IV se fait probablement dans deux sites de chélation. On a montré que le résidu Glu78 de la sous-unité

Il intervient dans la chélation du Zn. Cependant on propose qu'un deuxième site de chélation est présent dans les chemins de sortie des protons.

Enfin, dans la dernière partie de la thèse, le lointain infrarouge a été développé, y compris une approche électrochimique. Le domaine du lointain infrarouge offre un outil pour observer les vibrations métal–ligand, la signature amide VI et la signature des liaisons hydrogène. Les spectres d'absorbance de plusieurs protéines à centres fer–soufre ont été enregistrés. On a trouvé qu'une bande large apparaît en dessous de 300 cm^{-1} . Ce signal contient les vibrations des liaisons hydrogène. La signature des liaisons hydrogène de la protéine Rieske à [2Fe–2S] a été étudiée en fonction du pH à basses températures. L'étude a permis de discuter l'effet de l'état de protonation des histidines qui coordinent le centre fer–soufre sur la structure de la protéine de même que sur la signature des liaisons hydrogène.

Acknowledgments

I am grateful to Prof. Petra Hellwig for giving me the opportunity to join her laboratory three years ago. I am also grateful for her excellent supervision of my Ph.D studies. I would like also to say that I learned a lot from the discussions we had during the thesis. Besides, I am also thankful for her patience and kindness.

I would like to thank all my colleagues who supported me all these years. Thank you Frédéric, Mariana, Ruth, Aurélien, Yashvin, Nésrine and Julien.

Special thanks to Aurélien for his help in the temperature dependent measurements and to Ruth for helping me in the preparation of the NDF samples.

I am thankful to Frédéric Melin and Richard Bou Aoun for their critical reading of the manuscript.

I would like to thank Christiane Moster for her help concerning the administrative issues during the past four years.

I am grateful to Prof. Thorsten Friedrich and his team for the excellent collaboration and for giving me the opportunity to prepare the NDF samples in his laboratory.

I am indebted for my collaborators, Prof. Fevzi Daldal (University of Pennsylvania), Prof. Peter Faller (University of Toulouse), Dr. Pierre Dorlet (CEA), Pr. Francisco Blanco (Derio, Spain) and Pr. Bernd Ludwig (Goethe-Universität) for providing the samples and for the valuable discussions.

I am also thankful for Dr. Ulrich Shade for the excellent support at the BESSY II synchrotron facility and for Dr. David Moss, Dr. Yves-Laurent Mathis and Mr. Michael Süepfle for their excellent support at the ANKA synchrotron facility.

I would like to acknowledge the University of Strasbourg, The Agence Nationale de la Recherche “chair d’excellence”, The Centre National de la Recherche Scientifique and the French-German university for the financial support.

Finally, I am thankful to all my family members who always loved me and supported. Thanks also to my friends, especially Laure and Wissam for being there whenever I needed help.

1. Introduction

1.1. Metals in biology

Metal cations are present everywhere in the biosphere and are involved in innumerable vital biological processes. Few metals are considered as essential for Life (Na^+ , K^+ , Mg^{2+} , Ca^{2+} , Zn^{2+} , Mn^{2+} , Ni^{2+} , Cu^{+2+} , $\text{Fe}^{2+/3+}$, $\text{Co}^{2+/3+}$). Most of the time these trace elements are bound to proteins.¹ The other metals are considered to be toxic to a large extent.² The ability of a given protein to bind a specific metal comes from being capable of fulfilling the metal ions requirements. Indeed, the selectivity for a specific metal is mainly governed by its charge, ionic radius and the architecture of the metal binding pocket.³

Oxygen, nitrogen and sulfur are the most important donors in metalloproteins. Depending on the properties of the cation, the binding can occur via oxygen, nitrogen and/or sulfur donors. Most of the time metals are bound to the side chain of amino acids and rarely to an oxygen or nitrogen atoms of the backbone. Oxygen is offered by Asp, Glu or Tyr. Nitrogen is offered by His, Asn, Gln or Pro. Sulfur can be offered by Cys or Met. His is by far the most important amino acid regarding metal ligation in metalloprotein since it binds metals in a large number of metalloproteins.⁴

1.1.1. Sodium and potassium

These essential metal cations are charged ions, and thus they cannot access the cell on their own through the hydrophobic plasma membrane lipid bilayer. Highly specific channels are present in the cell walls allowing the cations to access the inside of the cell; this is the case for example of Na^+ , K^+ and Ca^{2+} . In fact Na^+ and K^+ play a central role in the regulation of cardiac impulse, as well as in the electrical signaling in the nervous system.⁵ The regulation mechanism is based on the ratio between Na^+ and K^+ concentration in the cells. This ratio is governed by Na^+ and K^+ channels, which are transmembrane proteins capable of discriminating between these two cations to a large extent.^{6,7} The permeability of the membrane to these cations is directly related to the membrane potential.⁵

1.1.2. Calcium

Ca^{2+} is a critical element to all living cells. It is involved in a wide range of biological processes such as the cellular signaling, gene expression regulation and metabolism.⁸ Keeping the normal level of Ca^{2+} in the cell requires a complex extrusion mechanism where Ca^{2+} can be pumped in or out of the cell.⁹

1.1.3. Magnesium

Mg^{2+} is involved in the regulation of Ca^{2+} and Na^+ transport as well as in a variety of cellular functions such as the signal transduction, enzyme activities, energy metabolism, nucleic acid and protein synthesis.¹⁰ Mg^{2+} is used by the photosynthetic species to produce chlorophylls (**Figure 1.1.1**), the key molecules for sunlight absorption and energy conversion.

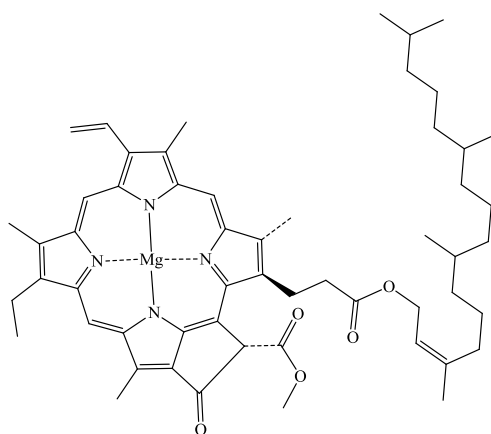


Figure 1.1.1. Chemical structure of the chlorophyll A.

1.1.4. Manganese

Mn can exist in the oxidation states (II), (III) and sometimes (IV). In light of its multiple oxidation states, Mn is employed by many biological systems as a redox cofactor as well as a structural support for proteins. In photosynthesis, Mn has an important role since a Mn cluster is used as the redox cofactor of the photosystem II.¹¹ It is also the cofactor of the manganese superoxide dismutase, oxidizing water to produce O_2 . In other cases, Mn helps maintaining some proteins in specific conformations without being involved as a cofactor. This is the case of the pyruvate carboxylase that binds tightly one Mn atom and many metallohydrolases.¹²

1.1.5. Zinc

Zn^{2+} transport towards the cytoplasm can be observed via two families of Zn-transporters, ZnT and Zip proteins.¹³ The regulation of the Zn^{2+} concentration in the cytoplasm is ruled out by metallothioneine which is a cysteine-rich protein and can coordinate up to seven Zn^{2+} cations. The tightly bound Zn^{2+} can be released by the oxidation of the cysteines.^{14 15} Zinc can be found in a significant number of proteins, hence it is involved in numerous vital biological mechanisms. Zn^{2+} is a cofactor in many oxidoreductases, protein kinases, superoxide dismutases, phosphatases, aminopeptidases...¹⁶ The so-called Zinc finger proteins superfamily are probably the most studied Zn-containing systems. These proteins are DNA binding transcription factors (**Figure 1.1.2**).¹⁷ Most of the time, Zn is bound in a tetrahedral coordination mode to four proteins by their side chains. This binding mode facilitates the interaction between the zinc finger proteins and DNA.¹⁸

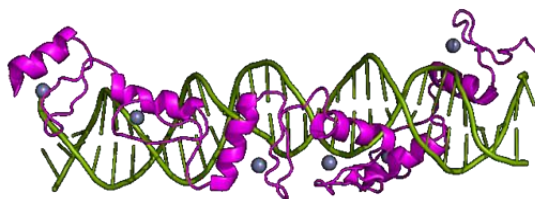


Figure 1.1.2. Structure of the zinc finger protein–DNA complex (PDB code 1TF6). The zinc finger protein is presented as magenta cartoon, the DNA double helix as green cartoon and zinc atoms as blue sphere.

1.1.6. Nickel

There are eight different Ni containing enzymes; glyoxylase I, acireductone dioxygenase, nickel superoxide dismutase, urease, NiFe hydrogenase, CO dehydrogenase, acetyl-CoA synthase and methyl-CoM reductase. The nickel center can perform redox reactions in a potential range up to 1.5 V.¹⁹ This is the result of the highly flexible coordination mode of Ni. Despite the fact that Ni-containing enzymes are crucial for the growth and development of many species, Ni is toxic to the cells. The synthesis of the Ni-containing enzymes is a delicate process, where Ni is meticulously transported to the cell and delivered to the adequate apoprotein with the help of specific metallochaperones.²⁰ Although Ni is an essential element for many plants and bacteria, its utility for humans is far from being certain. Ni is toxic at different levels for humans and animals. Beside of causing multiple biological alteration and diseases, it seems that Ni may disturb the generation of reactive oxygen species (ROS) that serve as signal transduction messengers in controlling

gene expression. The toxicity of Ni comes also from its ability to induce DNA damage and inhibiting DNA repair system.²¹

1.1.7. Iron

Iron need to be transferred with the help of specific Fe–chelators. In animals, plants and microorganisms, iron is stored in large specialized proteins, called ferritin in which up to 2500 iron atoms can be stored.^{22,23} The Fe atoms can be then delivered to the cell via a protein called transferrin. It should be noted that the soluble form of Fe, namely Fe^{2+} is easily oxidized by O_2 and that the highly insoluble form of Fe, Fe^{3+} becomes the major source of Fe. In microorganisms a family of molecules called siderophores plays the role of delivering the Fe atoms to the cell. These organic molecules show a very high affinity to Fe^{3+} with formation constant up to 10^{30} .²² The Fe^{3+} complex can be dissociated in the cell by several mechanisms; protonation of the Fe^{3+} binding ligands, reduction of the Fe^{3+} to Fe^{2+} , or chelation via ligand exchange.²⁴ Once the Fe atom is released, it can be used by the cellular machinery.

The free $\text{Fe}^{2+/3+}$ can be toxic to the cell since they can easily react with O_2 and produce free radicals, believed to be responsible of serious cellular damaging.²⁵ In order to avoid such a dramatic scenario, Fe is inserted into prosthetic groups such as protoporphyrin, where Fe cations are pentacoordinated or hexacoordinated most of the time. This coordination mode prevents O_2 to bind to the Fe cations. A wide variety of enzymes can be produced by introducing the iron–protoporphyrin based cofactor (**Figure 1.1.3**) into an apoprotein. Depending on the hosting protein, hemoglobin or myoglobin can be produced. These proteins are of small size and specialized in O_2 binding and transfer in the blood.²⁶

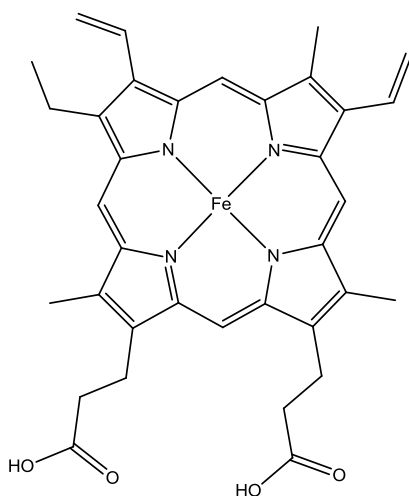


Figure 1.1.3. Structure of the iron–protoporphyrin IX.

Beside the O₂ transfer, the iron cofactor plays a crucial role in the electron transfer. Thanks to the variable oxidation state of the Fe atom, it can play the role of an electron acceptor as well as of an electron donor. Similar to the O₂ transport, the electron transport requires heme-type cofactors, where hemes are iron–protoporphyrin based cofactors covalently bound to a fatty ester.

The heme-containing proteins are for example present in mitochondria where the oxidative phosphorylation occurs. Different types of hemes exist; some are covalently bound to the apoprotein, such as the heme *c*. The corresponding protein is the cytochrome *c*. Other hemes can be maintained inside the apoprotein without being covalently bound such as the *a*-type, *b*-type and *o*-type hemes.²⁷

Besides, Fe can be bound to S to produce inorganic Fe complexes, so-called Fe–S clusters. The insertion of the Fe–S cluster into an apoprotein leads to the generation of a metalloprotein.^{28,29} These Fe metalloproteins are known to be implicated in many important biological functions. Among these functions we can cite the respiration, the ribosome biogenesis and the regulation of gene expression.¹ The ratio Fe/S atoms in the Fe–S cluster is tuned by its function.³⁰ Despite the existence of many synthetic analogues of Fe–S clusters,³¹ the most common natural Fe–S clusters are [2Fe–2S], [3Fe–4S] or [4Fe–4S] (Also see **3.4 Far infrared spectroscopy**).

Fe can also be found in the active site of hydrogenases. The superfamilies of Fe-only and Fe–Ni hydrogenases catalyze the reversible reduction of H⁺ into H₂. The evolution of the equilibrium between H⁺ and H₂ can be modified to increase or decrease the number of reducing equivalents of H⁺.³²

1.1.8. Cobalt

Co³⁺ is the central metal in the vitamin B₁₂, also called cobalamin (**Figure 1.1.4**).³³ The Vitamin B₁₂ is a water soluble vitamin that can be transferred to the cell by transcobalamin II, a plasma protein in charge of binding this vitamin and delivering it to the cell. The delivery process involves the formation of a complex between the transcobalamin II and a specific receptor. Eventually, the vitamin is released inside the cell by a complex endocytosis mechanism.^{34,35}

The cobalamin exists as a coenzyme in the cell, methylcobalamin, and adenosylcobalamin. The methylcobalamin is produced by the methylation of the cobalamin via a methyltransferase enzyme. This enzyme transfers methyl groups from the N⁵-methyl-

tetrahydrofolate to homocysteine, thereby forming tetrahydrofolate and methionine. The disproportion between the homocysteine, the Vitamin B₁₂ and folate is generally associated to poor cognitive functions.³⁶ The particularity of the synthesized cobalamin coenzymes is that one of the six Co³⁺ ligands is either a methyl group or a 5'-deoxy-5'-adenosyl moiety.³⁵

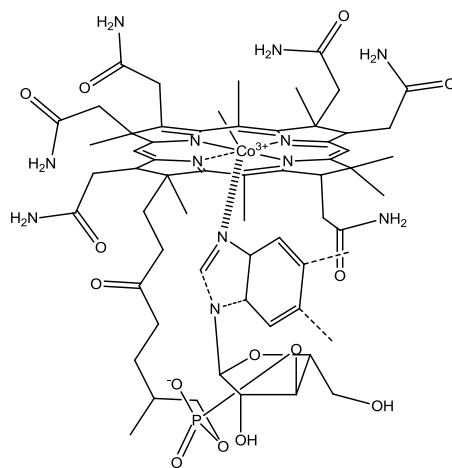


Figure 1.1.4. Chemical structure of the Vitamin B₁₂.

Both, the Vitamin B₁₂ and folate are involved in the transfer of methyl groups to DNA also in proteins synthesis.³⁷ Besides the Vitamin B₁₂, Co is the cofactor of several enzymes such as methionine aminopeptidase, prolidase, nitrile hydratase.³⁸

1.1.9. Copper

Copper is an ion essential to all living organisms. The redox state of Cu can be either in the stable Cu(II) state or in the instable Cu(I) state. The Cu(II)/Cu(I) couple allows the copper-containing proteins to perform a single-electron transfer, crucial to many biological functions.

As many transition metals cited above, the free Cu can be toxic to the cell since it can also be at the origin of the production of free radicals, responsible of damaging nearby proteins, DNA, phospholipids and other biological molecules.^{2,25} Copper chaperons are required to introduce the Cu cations into the cell without exposing them to oxygen to avoid the production of free radicals. In order to do so, the free Cu(II) present outside the membrane is reduced to Cu(I) and inserted to the cell by a transmembrane protein. The Cu uptake as Cu(I) by the chaperons can take place, then it can be transferred to the target protein.³⁹

Proteins containing a single copper atom can be classified according to their absorption in the visible range. Type-1 copper proteins also called 'blue copper proteins', have an intense

absorption band near 600 nm. Many type-1 copper proteins are known, as for example azurins, plastocyanins or amicyanins.⁴⁰ These proteins play the role of shuttling an electron from an electron donor and delivering it to an electron acceptor. Type-2 copper proteins have a weak absorption in the visible range. Most of time the type-2 copper proteins coordinate Cu by four N or O atoms and one coordination site remains empty. This coordination mode allows these proteins to play catalytic roles as in the copper amine oxidase, nitrite reductase and Cu-Zn superoxide dismutase.⁴¹

Proteins containing two antiferromagnetically coupled Cu bridged by molecular oxygen or a hydroxyl belong to the type-3 copper proteins (**Figure 1.1.5**). The active site of these proteins consists of a Cu_A and a Cu_B sites. Tyrosinase, catecholoxidase as well as hemocyanin bind oxygen and thus catalyze the oxidation of organic compounds such as phenol and catechol.⁴²

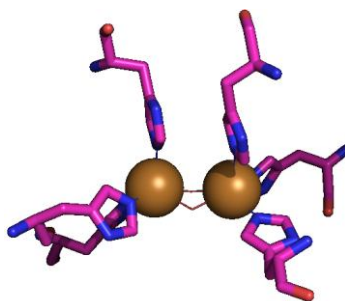


Figure 1.1.5. The active site of tyrosinase as example of type 3 copper-containing enzyme. The coordinating histidines are presented as sticks, the Cu atoms as orange balls, and the water molecule as red sticks (PDB code 2ZMX).⁴³

Moreover, enzymes like laccase, ascorbate oxidase, or ceruloplasmin contain multiple copper centers and combine type-1, type-2 and type-3 copper centers.⁴⁴ These proteins are oxidases that couple the electrons transfer to the reduction of O₂ to water. Besides the naturally occurring copper containing protein, a new copper protein was obtained artificially, the so-called type-zero copper protein, which absorbs around 800 nm.⁴⁵

1.1.10. Toxicity of metals

It is obvious that nature uses transition metals from the first row in order to build metalloproteins required to accomplish pivotal biological function. Besides the free radicals that might be produced from the essential elements themselves, other toxicity comes from the replacement of an essential metal, in a given cofactor, by another essential metal or by a “toxic” metal. This is the reason why well-defined metal uptake, transfer and insertion pathways are required to make sure that the right metal cations get into the right proteins.⁴⁶ In

fact, the biological media is more or less rich with the required transition metals as well as with other trace elements such as transition metals from the second and third row. These metals can bind to proteins in similar ways to many essential metals from the first row. Indeed, they can compete with these latter ones and replace them in the metalloproteins.

Under certain conditions, Co can produce oxidative stress during the biogenesis of iron–sulfur clusters and alters the cluster formation. Furthermore, Co can replace iron in the cluster before its insertion into the target protein thus inactivating pathways that depend on iron–sulfur clusters.⁴⁷

An example of the toxicity caused by replacing an essential metal by a toxic one is the replacement of Zn by Hg. The toxicity of Hg^{2+} is related to its binding mode, similar to Zn^{2+} . Hg^{2+} can be bound more tightly than Zn^{2+} and thus replace it in zinc–containing proteins.³

Other elements compete with other essential metals like Mg^{2+} which can be displaced by Al^{3+} thus leading to produce an inactive metalloprotein. Ln^{3+} inactivates Ca–containing proteins by removing the Ca^{2+} from its binding site.³ Besides the displacement of the active metal from its binding site, the coordination of a nonnative metal may lead to the aggregation of the metalloprotein.

The aggregation phenomenon is widely accepted as the origin of multiple neurodegenerative diseases such as Alzheimer's, Parkinson's, Huntington's, amyotrophic lateral sclerosis and prion.⁴⁸ Large aggregates are produced by amyloid deposition, a peptide with a β -sheet conformation also called amyloid- β peptide ($\text{A}\beta$ peptide). The $\text{A}\beta$ peptide derives from the cleavage of a protein called “amyloid precursor protein”.⁴⁹ The toxicity of the $\text{A}\beta$ peptides arises from their ability to bind transition metals such as Cu and Zn which induce the aggregation of $\text{A}\beta$ peptides. Furthermore, the binding of a redox metal ion such as Cu is also supposed to induce neuronal dysfunction by the production of ROS.⁵⁰

1.2. Respiratory chain proteins

1.2.1. Role, localization and organization

The cellular respiration is the hallmark of the modern bioenergetics. The respiratory chain enzymes contain many cofactors such as Fe–S clusters, cytochromes and copper centers. It is indeed a good representative of the importance of metal ions in biology.

Respiration is the biochemical process where an aerobic cell produces its own energy by oxidizing molecules such as sugar, fatty acids, or amino acids by molecular oxygen. A series of chemical reactions are undertaken in the cell in order to accomplish the respiration.

The respiratory chain is located in the inner membrane of the mitochondria of eukaryotes and in the plasma membrane of photosynthetic bacteria and the closely related respiratory bacteria. Similarly, the respiratory chain is located inside the thylakoides, functional analogues of mitochondria in plants. Beyond the classical model of the respiratory chain (**Figure 1.2.1**), the respiratory chain complexes are organized as supercomplexes, which may consist of two copies of the complex I, one copy of the complex III and two copies of the complex IV.⁵¹ The complex II is not observed in the supercomplexes, probably because of its involvement in the citric acid cycle.

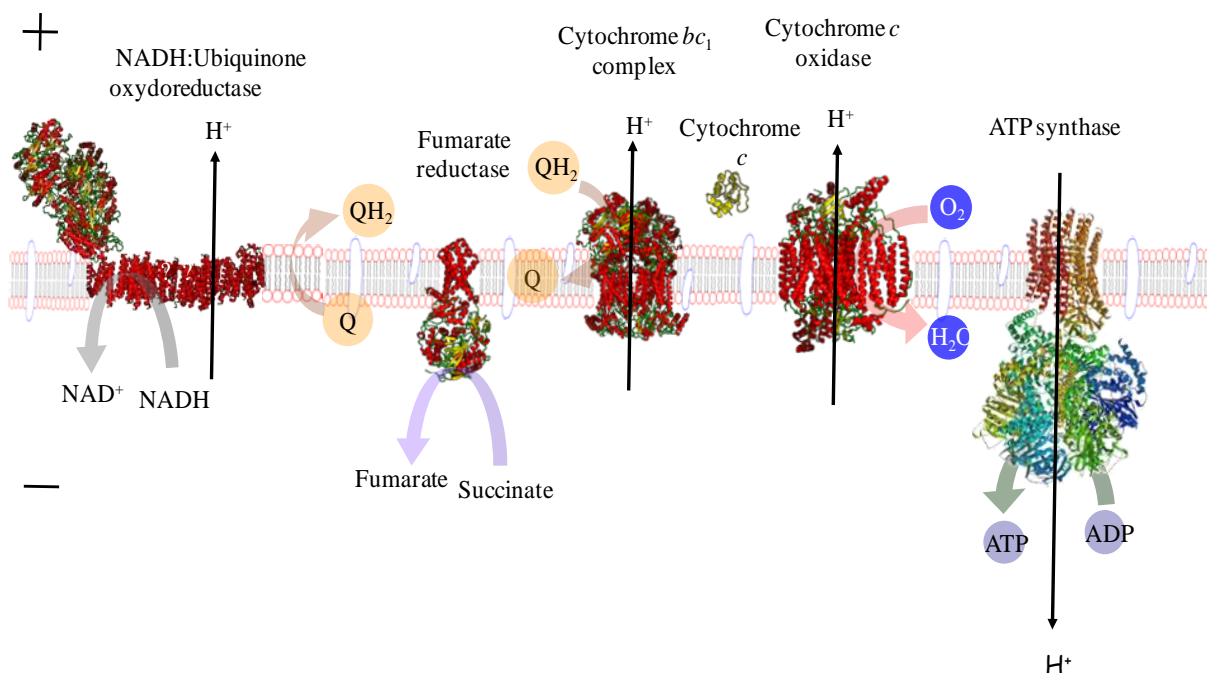


Figure 1.2.1. The classical model of the mitochondrial respiratory chain and the ATP synthase. The structures are based on the following PDB codes: 3M9S (NADH:ubiquinone oxidoreductase); 1QLB (Fumarate reductase); 1ZRT (cytochrome *bc*₁ complex); 3HB3 (CcO); 1BMF (F₁ part of the ATP synthase).

This organization is not common to all organisms, where the number of copies of each complex varies from an organism to another. The complex V, the ATP-synthase can be active as a monomer, dimer,⁵² or assembled into large oligomeric chains.⁵¹

1.2.2. Complex I

The first step of respiration starts when for example sugar is oxidized to produce the Acetyl-CoA. The second step is the entry of the Acetyl-CoA into the citric acid cycle during which Nicotinamide Adenine Dinucleotide (NAD^+) intermediate molecules are produced. The third step is the electron transport and the oxidative phosphorylation. The link between the second step and the third step of the respiration process is done by the respiratory complex I, also called NADH:ubiquinone oxidoreductase, by coupling the proton pumping across the membrane to the oxidation of NADH to the reduction of ubiquinone, a biological electron carrier deriving from quinone.⁵³ In mitochondria ubiquinones, in prokaryotes menaquinones and in plants phylloquinones are typically found (**Figure 1.2.2**).

Complex I catalyzes the electron transfer to the next member of the respiratory chain, the complex II also called fumarate reductase. The complex II couples the oxidation of succinate to fumarate to the reduction of ubiquinone to ubiquinol, derivatives of the coenzyme Q.

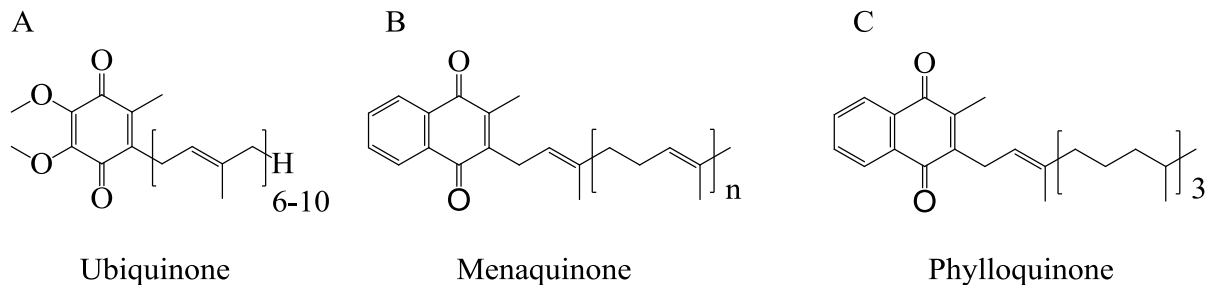


Figure 1.2.2. Chemical structure of (A) ubiquinone, (B) menaquinone and (C) phylloquinone.

Complex III, also called the cytochrome bc_1 complex (bc_1) couples the proton pumping across the membrane to the electron transfer from the coenzyme Q derivatives towards a c -type cytochrome which binds to the complex IV, the cytochrome c oxidase (CcO). Molecular oxygen binds to the CcO that couples the reduction of molecular oxygen to water to the proton pumping across the membrane.⁵³

The proton pumping by the complexes I, III and VI generates a proton gradient that can be used by the ATP-synthase to accomplish the oxidative phosphorylation. The successive

electron transfer steps in the respiratory chain and the production of ATP can be correlated to the standard redox potentials of each respiratory complex (**Figure 1.2.3**).⁵³

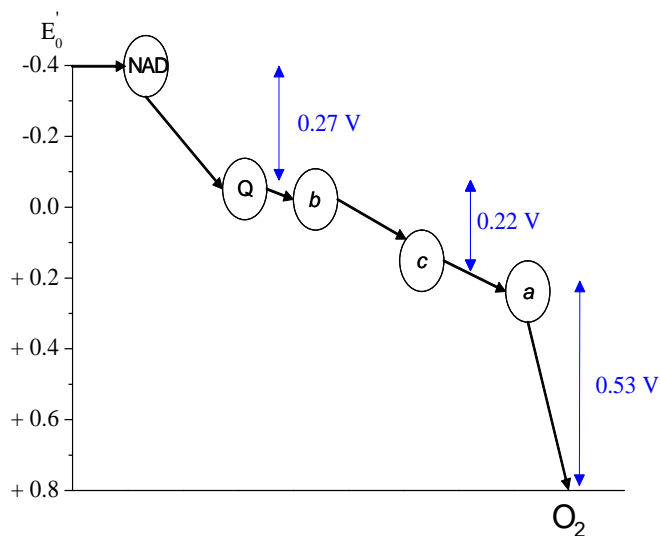


Figure 1.2.3. The decline of standard potentials of the redox cofactors of the mitochondrial respiratory chain as electron pairs flow down the respiratory chain to oxygen. The blue arrows denote the difference in standard potentials between each step. The NAD stands for Nicotine Adenine Dinucleotide, Q stands for quinol, *b*, *c* and *a* stand for the corresponding heme type.

The structure–to–function relationship in the mitochondrial and bacterial respiratory complexes is far from being fully understood. Furthermore, the mechanism by which the respiratory complexes couple the redox reactions of their corresponding substrates to the proton translocation is constantly debated. Several studies have been performed on the different complexes isolated from different organisms.

The NADH:ubiquinone oxidoreductase is by far the largest respiratory chain complex with a molecular weight of 980 kDa in mitochondria⁵⁴ and 520 kDa in the prokaryotic cells.⁵⁵ Electron microscopy revealed the architecture of the complex I; a boot–like shape enzyme containing two domains, a soluble and membrane bound domains.⁵⁶ Three different types of complex I are known so far and the classification is made according to their sensitivity to rotenone, a quinone structural analogue inhibitor.⁵⁷ Hence, the type–I and type–II complex I are the rotenone sensitive and insensitive complex I, respectively. However, the sensitivity to rotenone is not the same for all the species, e.g. the complex I from *Escherichia coli* (*E. coli*) is rotenone insensitive.⁵⁸ The type–III complex I pumps Na^+ instead of protons and it is known as the Na^+ –pumping NADH:quinone oxidoreductase (NQR), including a completely different set of cofactors.

The crystal structure of the hydrophilic domain of the complex I from *Thermus thermophilus* (*T. thermophilus*) (**Figure 1.2.4A**) has been resolved with a resolution of 3.3 Å (PDB code

3I9V) and recently the complete structure of the complex I was determined with a resolution of 4.5 Å.⁵⁹ The hydrophilic domain contains all the cofactors of the complex I, namely one flavin–mononucleotide (FMN) and up to nine Fe–S clusters (**Figure 1.2.4B**).

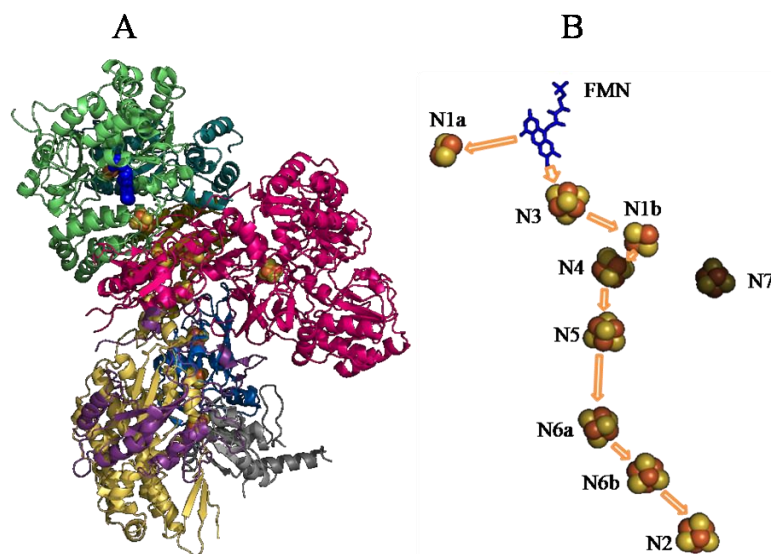


Figure 1.2.4. (A) Overall architecture of the hydrophilic domain of the complex I from *T. thermophilus* and (B) the organization of the redox cofactors. The FMN is colored in blue and presented as sticks; the iron and sulfur atoms are colored in red and yellow, respectively and presented as spheres. The arrows present the electron transfer between the cofactors (PDB code 3I9V).

The complex I is the entry point of electrons into the respiratory chain. The NADH binding site is located in the hydrophilic part of the complex I, close to the FMN (redox potential of -340 mV vs. the Standard Hydrogen Electrode at pH 7.0 (SHE')) binding site and the N3 Fe–S cluster.⁵⁵ The oxidation of NADH (redox potential of -320 mV vs. SHE') to NAD^+ reduces the FMN to FMNH_2 releasing thus two electrons, each by a one electron transfer step.⁶⁰ The same redox reaction is known to induce a conformational changing of the complex I.⁶¹ The transfer of the released electrons starts by the reduction of the N3 Fe–S cluster (redox potential of -100 mV vs. SHE') followed by the reduction of the Fe–S clusters chain until reaching the quinone binding site. It should be noted that the N1a Fe–S cluster has the lowest redox potential among the Fe–S of the complex I (-380 mV vs. SHE') which prevents the direct electron transfer from the FMN. Furthermore, the N1a cluster is conserved in all the versions of the complex I found in different species. The role of the N1a Fe–S cluster is however, not clearly understood. In line with its low redox potential, the N1a Fe–S cluster was found to accept one of the two electrons from the reduced flavosemiquinone limiting thus the formation of ROS.⁶²⁻⁶⁴

The electron flow arriving to the N2 Fe–S cluster reduces the quinone (redox potential of +110 mV vs. SHE') into quinol. The quinone reduction is believed to be the key step in the proton pumping mechanism since the redox potential of the N2 Fe–S cluster is pH dependent.⁶⁵ These findings support the hypothesis of the direct coupling between the electron transfer and the proton pumping mechanism (**Figure 1.2.5**).⁶⁶

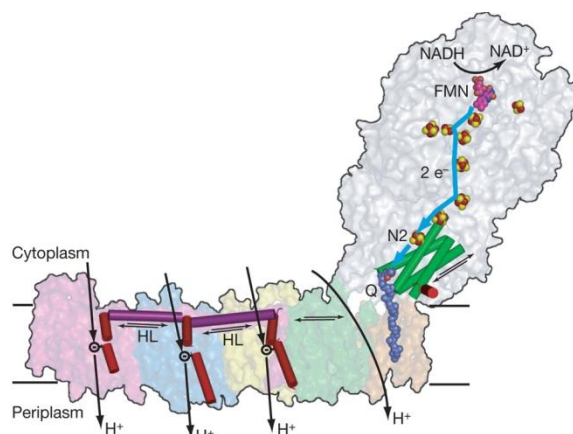


Figure 1.2.5. Architecture of the complex I and the proposed coupling mechanism.⁵⁹ FMN is presented magenta balls, the Fe–S clusters are presented in yellow and red and the quinone is presented in blue. The blue arrows indicate the electron transfer pathway and the black ones indicate the proton pathways. The helices which undergo a conformational movement in the hydrophilic part are the Nqo4 (green cylinders) and Nqo6 (red cylinder). In the membrane domain, the HL helix is colored in magenta and the discontinuous helices are colored in red.⁵⁹

The complete structure of the complex I shows some unexpected features which may clarify the proton pumping mechanism. In fact, the membrane part is constituted by 63 transmembrane helices among them one helix (HL) is oriented sideways instead of being extended over the surface of the membrane (**Figure 1.2.5**). Three discontinuous helices were also resolved in the hydrophilic part of the enzyme and two positively charged amino acids, Glu144 and Lys234, are conserved in the three helices.⁵⁹ Previous site-directed mutagenesis investigations showed that the mutation at the level of these amino acids inhibits the proton pumping activity.⁶⁷

A model of the coupling mechanism (**Figure 1.2.5**) has been proposed based on previous studies and the recently resolved structure of the entire complex I at 4.5 Å (ref. ⁵⁹ and references therein). The reduction of FMN leads to the oxidation of NADH into NAD⁺ which donates two electrons delivered to the N2 cluster via the Fe–S clusters chain to finally reach the quinone binding site near the N2 site. The quinone present in the site moves out of the membrane by about 10 Å during its reduction. Meanwhile, the first proton is pumped at the interface between the hydrophilic and hydrophobic domains (**Figure 1.2.5**) and redox induced difference spectroscopy showed that the Glu⁶⁷ residue, which belongs to the NuoB subunit

protonates upon the oxidation of the N2 Fe–S cluster.⁶⁸ Besides Glu67, two Tyr residues, namely Tyr114 and Tyr139 were shown to be involved in the proton translocation process by combining the site directed mutagenesis and the FTIR difference spectroscopy.⁶⁹ These data are supported by EPR studies which show the involvement of quinone and semiquinone in the proton translocation process.^{70,71} It should be noted that EPR spectroscopy is one of the best methods to follow the reaction of the complex I since the cofactors (FMN and Fe–S clusters) have overlapping and broad absorption bands in optical spectroscopy.⁷² It is worth to mention that EPR spectroscopy is capable of detecting the metal centers with unpaired electrons. Thus, all the Fe–S clusters of the complex I are detectable in the reduced state while flavin and quinone are detectable in the free radical state.

In line with FTIR data (reviewed in ref. ⁷³), the redox reaction is coupled to conformation movements in the soluble part of the complex which are then transmitted to the hydrophobic part. The helix HL moves then backward and forward. As a result the, three discontinuous helices undergo tilting movement which modifies the environment of the conserved charged residues in the three proton channels resulting in the pumping of three protons (**Figure 1.2.5**).⁵⁹

Unlike the quinone structural analogues inhibitors blocking the redox reaction itself, Zn²⁺ cations do not affect the quinone reduction neither the NADH oxidation but they inhibit the proton translocation across the membrane.⁷⁴ In a zinc–poisoned complex I of the bovine heart mitochondria a ratio of one Zn²⁺ cation to one flavin was found. Despite the identification of the four ligands that trap the Zn²⁺, namely two His and two Cys residues, the location of the binding site remains elusive due to the lack of structural information about the bovine heart complex I.⁷⁵

1.2.3. Complex II

The succinate:quinone oxidoreductase (SQR), the complex II of the aerobic respiratory chain, is also a member of the citric acid cycle. It couples the oxidation of succinate to fumarate to the reduction of quinone to quinol and also catalyses the reverse reaction without translocating protons across the membrane. The complex II of the anaerobic respiratory chain is the quinol:fumarate oxidoreductase (QFR). Unlike its aerobic analogue SQR, the QFR couples the reduction of fumarate into succinate to the oxidation of quinol without being involved in a proton translocation process. The superposition of the structures of both SQR and QFR shows high similarities.

The crystal structure of the complex II from *E. coli* was recently resolved with a resolution of 2.4 Å (PDB code 2WDQ).⁷⁶ The highest resolution available so far is the one from *Wolinella succinogenes* with a resolution of 2.2 Å (PDB code 1QLB).⁷⁷ The crystal structure of the QFR from *Wolinella succinogenes* is shown in the **Figure 1.2.6A** and the organization of the redox cofactors in the **Figure 1.2.6B**.

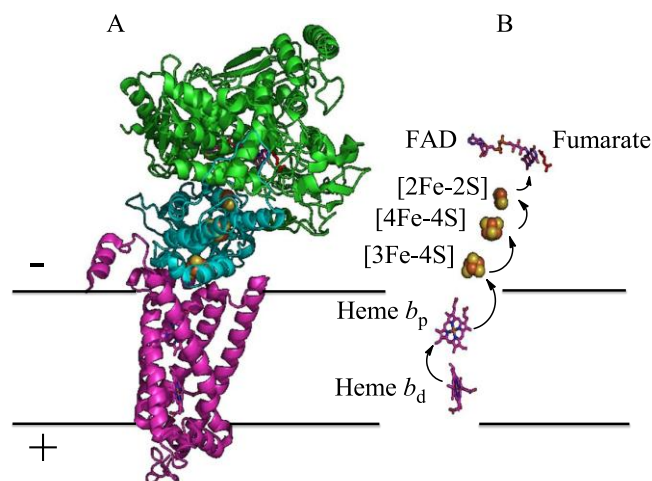


Figure 1.2.6. (A) Crystal structure of the QFR from *Wolinella succinogenes* (PDB code 1QLB) and (B) the organization of redox cofactors where the FAD and the hemes are presented as sticks and the Fe–S clusters as spheres. The arrows indicate the electron transfer pathway from the hemes to the fumarate presented as red sticks.

The QFR is the terminal respiratory complex of fumarate respiration where fumarate is the terminal electron acceptor. It consists of three different subunits. The subunit A carries one covalently bound Flavin Adenine Dinucleotide (FAD), the subunit B carries three Fe–S clusters (one [2Fe–2S] one [3Fe–4S] and one [4Fe–4S] clusters) and the subunit C carries two type-*b* hemes, namely heme b_p (high-potential) for the “proximal” and heme b_d (low-potential) for the “distal” heme *b*.^{77,78}

Fumarate reduction suggested to be catalyzed via Van der Waals interaction between FAD and the fumarate molecule where efficient electron transfer can take place. In contrast, the electrons required to reduce fumarate are produced by the oxidation of menaquinol within the membrane domain of the QFR, in the “proximal” and “distal” menaquinol binding sites. In both cases, the generated electrons are delivered to the fumarate reduction site through the Fe–S clusters wire traveling thus an unusual long distance of about 27 Å.⁷⁷

The protons required to achieve the reduction of fumarate into succinate are delivered via the “E-pathway”, named so after the highly conserved Glu180 of the subunit C. The “E-pathway” hypothesis⁷⁹ suggests a cotransfer of one proton per electron across the membrane. Upon oxidation of menaquinol into menaquinone, two other protons are released

in the periplasm. Since the QFR does not contribute to the generation of the proton gradient membrane, the two protons released in the periplasm are compensated via the coupling of the electron transfer through the hemes to the translocation of two protons from the periplasm by the intermediate of the ring C propionate of the heme b_d and the amino acid Glu180 until reaching the cytoplasm. The released protons in the cytoplasm compensate those used for the reduction of fumarate.

1.2.4. Complex III

The complex III, also called the bc_1 , is the third enzyme of the respiratory chain before the CcO. It couples the electron transfer to the proton translocation across the membrane. The crystal structure of the mitochondrial bc_1 from bovine heart was the first to be resolved⁸⁰ and the complete structure of the enzyme is constituted by eleven subunits that bear the prosthetic groups of the enzymes.⁸¹ The enzyme is a dimer that contains two low potential hemes (heme b_L), two high potential hemes (heme b_H), two cytochromes c_1 as well as two copies of the high potential Rieske iron–sulfur protein.^{80,81} The midpoint potentials as well as the absorption maxima in the visible range of each cofactor are presented in the **Table 1.2-1**.⁸² The Rieske protein was found at varying positions in the structure of the bc_1 from chicken, suggesting a long–range movement of the Rieske during the catalytic turnover.⁸³

Cofactor	Midpoint potential vs SHE'	λ_{\max}
Heme b_L	−90/−115 mV	558/565
Heme b_H	+50/+60 mV	560.5
Rieske [2Fe–2S]	+270 /+460 mV	460 ^(*)
Cytochrome c_1	+290/+340 mV	552

Table 1.2-1. Midpoint potential and absorption maxima in the visible range of the cofactors determined for the bc_1 from *Rhodobacter capsulatus*.^(*) The UV-Vis maxima are those of the oxidized Rieske from *T. Thermophilus*.

Crystal structures of the bc_1 from the yeast *Saccharomyces cerevisiae*,⁸⁴ the photosynthetic bacteria *Rhodobacter capsulatus* (*R. capsulatus*)⁸⁵ and *Rhodobacter sphaeroides*,⁸⁶ as well as the bc_1 homologous, the cytochrome b_6f complex from the chloroplast of *Mastigocladus laminosus* were resolved.⁸⁷

bc_1 is a dimer and its enzymatic turnover can be explained by the protonmotive Q–cycle first proposed by Mitchell^{88,89} and modified later.^{90,91} The mechanism of the enzyme remains

debated including the discussion whether it is a functional monomer or dimer.^{92,93} More recently, data from different laboratories support the hypothesis of the functional dimer which accounts for the intermonomer communication.^{94,95} The bc_1 is a dimer where two (Q_o) quinone binding site exist at the interface between the subunit bearing the b -type hemes and the Rieske iron–sulfur protein as well as two (Q_i) quinol binding sites (**Figure 1.2.7A**).

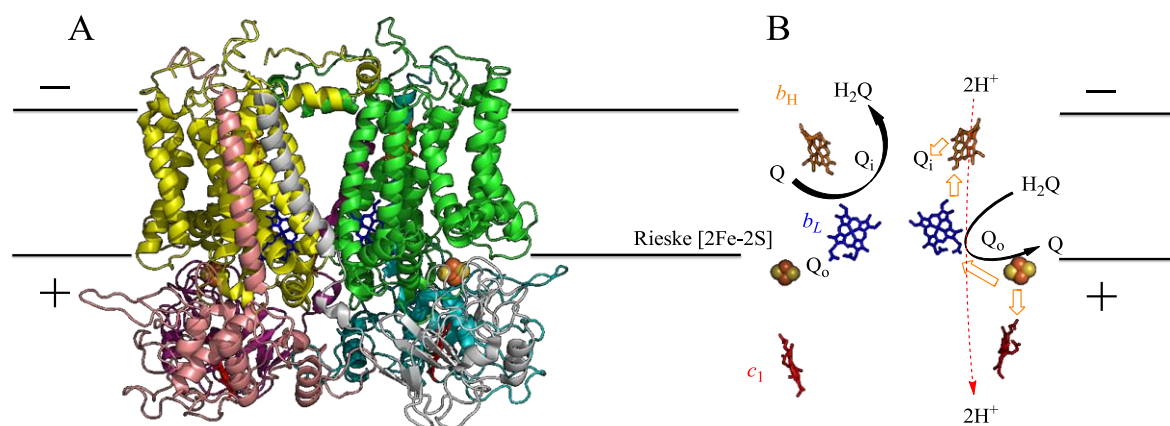


Figure 1.2.7. (A) Crystal structure of the bc_1 from *Rhodobacter capsulatus* (PDB code 1ZRT). (B) The organization of the redox cofactors and schematic presentation of the Q-cycle. The b_H hemes are presented as sticks and colored in orange, the b_L in blue, the cytochrome c_1 in red. The Rieske [2Fe-2S] clusters are presented as spheres. Q and H_2Q represent quinone and quinol, respectively. The orange arrows indicate the electron transfer pathway and the red arrow indicates the proton translocation pathway.

According to the heterodimeric aspect of the bc_1 presented in ref.⁹⁴ (**Figure 1.2.7B**), the catalytic cycle starts when a quinol molecule binds at the Q_o site of one monomer where it is oxidized to yield a quinone molecule, two protons and two electrons.

Following a bifurcated mechanism, the Rieske protein delivers one electron to the heme b_H by passing through the heme b_L and undergoes a macro movement toward the cytochrome c_1 transferring thus another electron. The cytochrome c_1 is then reduced and delivers on its turn the electron to an external c -type cytochrome.

Meanwhile, a quinone molecule enters the Q_i binding site of the other monomer where it is reduced to yield a stable semiquinone. At that time, the Rieske protein of the first monomer cannot be docked in the Q_o site due to a physical shielding as long as a semiquinone is present at the Q_i site. A quinol molecule is then reduced at the Q_o site of the other monomer. After intermonomer equilibration at the level of the low potential heme b chain, the semiquinone free radical leads to the formation of one quinone and one quinol molecule at both Q_i sites. The return of one of the Rieske proteins to the Q_o sites becomes then possible and induces the start of the next enzymatic turnover. By the end of one Q-cycle, two protons are withdrawn from the negative side of the membrane and translocated across the membrane to the positive

side of the membrane, hence, contributing to the creation of the electrochemical proton gradient, the driving force of the ATP-synthase.⁹⁴ The Rieske protein is in charge of electron transfer, it plays also the role of delivering the released protons to the positive side of the membrane.

Stigmatellin is a quinol structural analogue which blocks the Q_o active site by interacting with the Glu295 from the highly conserved PEWY motif and the His156 (*R. capsulatus* numbering) that coordinate the [2Fe-2S] cluster.^{83,85,96} It is known that the midpoint potential of the Rieske protein is pH-dependent.^{97,98} Upon the oxidation of quinol, the reduced Rieske captures one proton via the His156 (

Figure 1.2.8A).

The oxidation of the Rieske by the cytochrome c_1 makes the His156 a weak base and favors the proton release.⁹⁹ Upon the dissociation of the electron donor complex formed by the PEWY motif, quinol and the Rieske protein, the Glu295 carries a proton and undergoes a rotational movement of 170° to face the propionate of the heme b_L (

Figure 1.2.8B) where the proton is released via a water molecule.

Subsequently, the proton is carried to the aqueous phase via a hydrogen bonded water chain stabilized by the residues from the cytochrome b subunit.^{99,100}

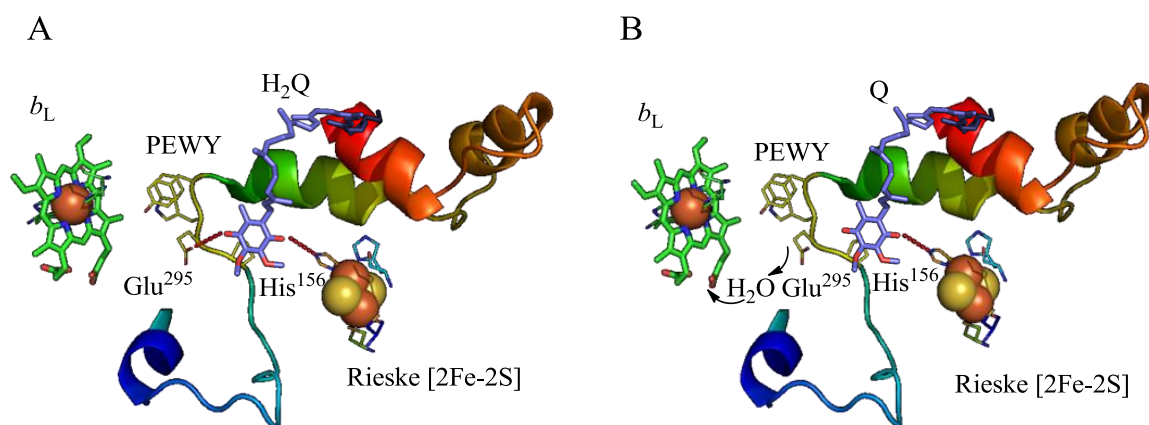


Figure 1.2.8. (A) The release of the first proton from the Q_o site via the His156. (B) The release of the second proton via the Glu295.¹⁰⁰ The heme b_L is presented in green sticks, the PEWY motif is colored in yellow, the Rieske [2Fe-2S] cluster is presented as spheres and the coordinating amino acids are presented as sticks. The H_2Q and Q are presented as cyan sticks.

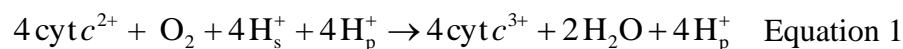
Heavy metals cations such as Zn^{2+} are capable of inhibiting the bc_1 in a pH-dependent manner. The X-ray structure of the Zn^{2+} -poisoned bc_1 from chicken revealed two binding sites for Zn^{2+} cations in each monomer and the data showed that one of the two Zn^{2+} binding site may interfere with the Q_o site while the other one is located in the hydrophobic channel between the Q_o site and the bulk lipid phase; the latter binding site, however, is not certain.¹⁰¹

The X-ray absorption studies of the Zn^{2+} binding sites in the bc_1 from bovine heart mitochondria, chicken and *R. capsulatus* showed similar binding patterns that include protonable acidic residues reflecting thus the competition between Zn^{2+} and protons.¹⁰²

1.2.5. Complex IV

The complex IV, also called the CcO, is the terminal enzyme of the respiratory chain where the reduction of molecular oxygen to water takes place. The mammalian enzyme is composed of 13 subunits and its molecular weight is about 200 kDa.¹⁰³ The enzyme couples efficiently the electron transfer to the proton pumping across the membrane. The crystal structure of the CcO from *P. denitrificans* (aa_3 -type oxidase) has been resolved^{104,105} and the enzyme consists of four subunits, namely subunit I, II, III and IV (**Figure 1.2.9A**). The subunits I and II bear all the prosthetic groups: The Cu_A binuclear site, the heme *a*, the heme a_3 - Cu_B binuclear site. The structure reveals also the presence of one Ca^{2+} and one Mg^{2+} or Mn^{2+} (**Figure 1.2.9B**).

The reduced cytochrome *c* delivers one electron to the CcO via the Cu_A center. The electron is then transferred to the heme a_3 - Cu_B binuclear site via the heme *a*. The active site of the CcO ensures the cleavage of the O–O bond. The formation of two water molecules requires four protons which can be delivered to the active site by the D and K-pathways, named after the highly conserved Aspartic acid124 (D124) and the Lysine354 (K354), respectively (**Figure 1.2.9B**).^{106,107} The free energy produced by the reduction of molecular oxygen into water is used to pump protons via the D- and K-pathways. The protons exit pathway is not well characterized. A complete turnover of the CcO can be summarized by the equation 1:¹⁰⁷



The protons denoted by the subscript “s” are substrate protons, used in the production of water and those denoted by the subscript “p” are the pumped protons.

The proton pathways can be blocked by micromolar concentrations of Zn^{2+} or Cd^{2+} . The crystal structure of the CcO from *Rhodobacter sphaeroides* with Cd^{2+} bound revealed the existence of four binding site that alter the proton transfer from the D and the K-pathways as well as the possible backflow from the exit pathway.¹⁰⁸

A third proton pathway (the “H–pathway”) was proposed in the mitochondrial CcO from bovine heart.¹⁰³ However, a similar pathway is far from being functional in the bacterial CcOs.¹⁰⁹

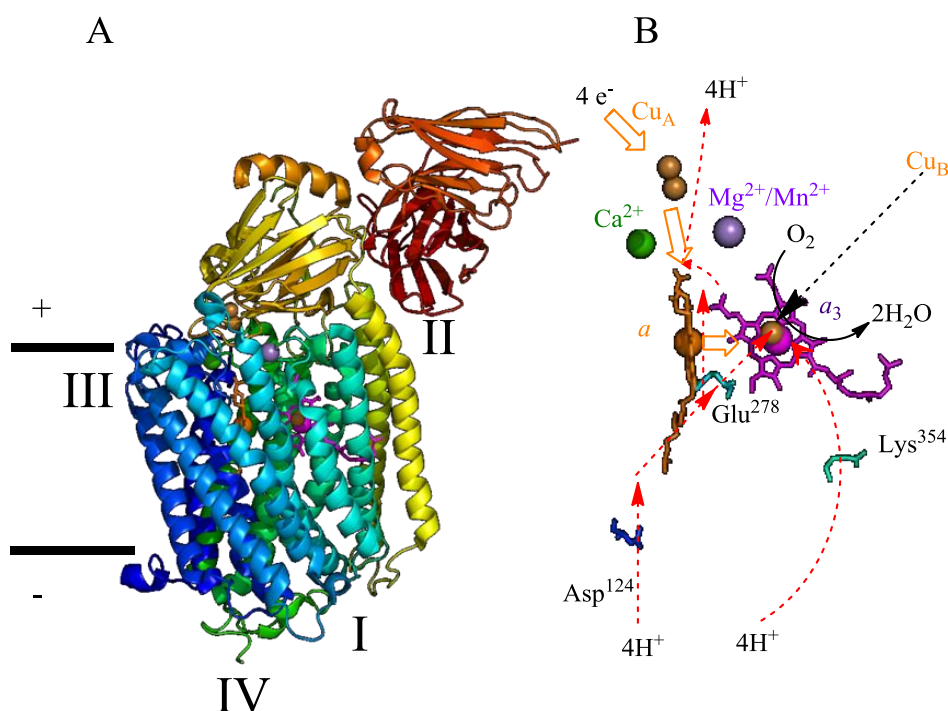


Figure 1.2.9. (A) Structure of the CcO from *P. denitrificans*. (B) Schematic presentation of the electron and proton uptake pathways. The hemes a and a_3 are presented as sticks and colored in orange and magenta, respectively. The Cu atoms are presented as spheres and colored in dark yellow, Ca in green and Mg/Mn in clear blue. The D124, E278 and K354 amino acids are presented as sticks. The dashed red arrows indicate the proton pathways (PDB code 3HB3). The orange arrows indicate the electron transfer.

In order to better understand the complex catalytic activity of the CcO several approaches were used including the site–directed mutagenesis, the inhibition of the oxygen reduction by carbon monoxide as well as by nitrogen monoxide.^{110–112} Site–directed mutagenesis was successful in identifying crucial amino acid involved in the proton translocation mechanism in both proton pathways.^{113–118} In addition, the combination between FTIR difference spectroscopy, site directed mutagenesis and the isotopic labeling of the heme propionates allowed to elucidate the protonation states of the propionate rings in the course of the enzymatic turnover.^{119,120}

The catalytic turnover^{104,121–123} of the active site of the CcO begins with the R state where the heme a_3 is in the ferrous state, the Cu_B is in the cuprous state and the Tyr of the Tyr280–His276 crosslink (**Figure 1.2.10A**) is in the protonated state. The binding of molecular oxygen to the heme a_3 leads to the A state (**Figure 1.2.10B**). At this level of the catalytic turnover, the O–O bound scission can be done. Two facultative states can then be

reached depending on the redox state of the heme *a* when reducing O_2 . When the heme *a* is reduced, the state P_R is reached, if it is oxidized, the state P_M is reached. It should be noted that the reduction of O_2 requires four electrons and four protons. For the P_M , the reaction proceeds by oxidizing the covalently bound Tyr280 which also donates one proton. By the end of this reaction, the O–O bond is broken and one oxygen atom is bound to the iron atom of the heme *a*₃ in the ferryl state (Fe^{IV}), the Cu_B is oxidized and bound a hydroxyl radical and the Tyr280 is in the radical state.

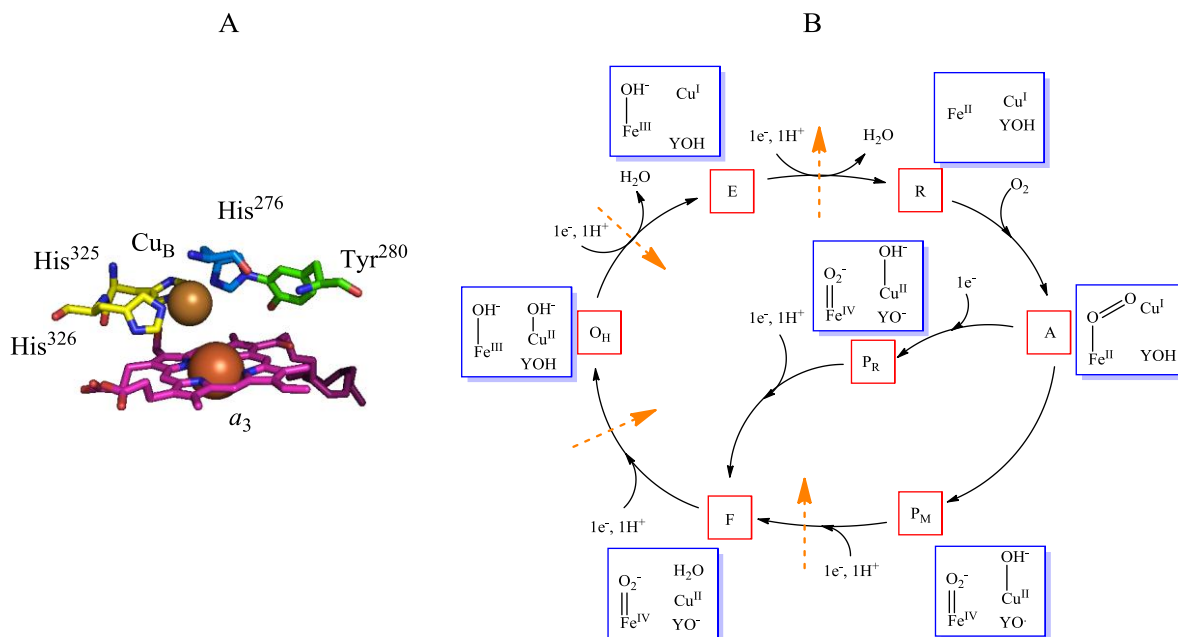


Figure 1.2.10. (A) The active site of the CcO. The heme *a*₃ is colored in magenta. The Cu_B is presented as a sphere and the coordinating His^{325} and His^{326} are presented as yellow sticks. The crosslinking residues Tyr^{280} and His^{276} are presented in green and blue, respectively. (B) The catalytic turnover of the active site. The black arrows indicate the transition between the different states and the orange dashed arrows represent the proton pumping steps (for details see text).¹⁰⁷

The formation of the P_R state requires the uptake of one electron from the heme *a* instead of the Tyr^{280} which presumably donates one proton and becomes a tyrosinate state which is the only difference between the P_R and the P_M states (**Figure 1.2.10B**). The redox states of the heme *a*₃ and the Cu_B are conserved during the formation of the F state. During the formation of the F state two protons are uptaken from the negative side of the membrane, one of them is used for the formation of a water molecule whereas the other one is translocated across the membrane. The oxidized catalytic site is reached after the uptake of one electron and one proton. It is designated as the O_H state in which both the Fe^{III} and Cu^{II} atoms are bound to hydroxyl groups and the Tyr^{280} comes back to its neutral state. In addition, the formation of the O_H state is coupled to the pumping of one proton across the membrane. Once in the fully

oxidized state, the reduction process of the catalytic site begins by the uptake of one electron and proton leading to the formation of the E state. The first one is required for the reduction of the Cu_B to Cu_B^I while the latter one is required to the formation of one water molecule. The transition between the O_H state and the E state is coupled to the translocation of one proton across the membrane. The final step of the catalytic turnover consists of the transition between the E state and the R state during which the heme a_3 is reduced to the Fe^{II} state. This step requires also one electron and one proton and it is coupled to the translocation of one proton across the membrane (**Figure 1.2.10B**).¹⁰⁷

1.2.6. Complex V

The ATP-synthase, also called complex V, is a large multisubunit protein acting as a molecular engine. The proton gradient generated by the respiratory complexes I, III and IV is consumed by the ATP-synthase in order to undergo a rotational movement essential to the catalysis of ATP synthesis. The reaction also produces inorganic phosphate and simultaneously protons are pumped back to the negative site of the membrane.¹²⁴

1.3. Iron–sulfur proteins

The iron–sulfur proteins play a ubiquitous biological role mainly as electron transfer agents and they are also involved in various catalytic and sensing activities.³² A large number of proteins containing Fe–S clusters exist, however, only a small number of Fe–S clusters are known so far. The Fe–S clusters have the particularity to exchange ligands within the protein.³⁰ Most of the time the Fe–S clusters are held within proteins by the coordination of the Fe atoms by Cys via the thiolate groups. The ligation by His, Ser, Asp or a backbone amide occurs less frequently.¹²⁵

Fe–S proteins have been extensively studied by a survey of techniques such as EPR spectroscopy, NMR, Mössbauer, Raman spectroscopy as well as by FTIR spectroscopy. In addition, synthetic Fe–S clusters were also produced in order to mimic the active sites of several Fe–S proteins.³¹ Thus, the Fe–S proteins are well–characterized and their functions are well understood compared to more complex proteins. Indeed, the wealth of the data available for Fe–S proteins makes them good candidates to develop new approaches to study proteins such as the low temperature and redox induced FIR spectroscopies.

1.3.1. Rubredoxin

The simplest Fe–S cluster is the cofactor of Rubredoxin (Rb), it contains one Fe atom whereas the more complex ones contain two, three, four or eight Fe atoms (**Figure 1.3.1**). Rb are soluble low–weight proteins and the crystal structures of several Rb have been solved.^{126–129} The high–spin Fe^{III} coordinated to four Cys residues undergoes a reversible one–electron reduction in a pH independent manner at around -50 mV vs. SHE’.

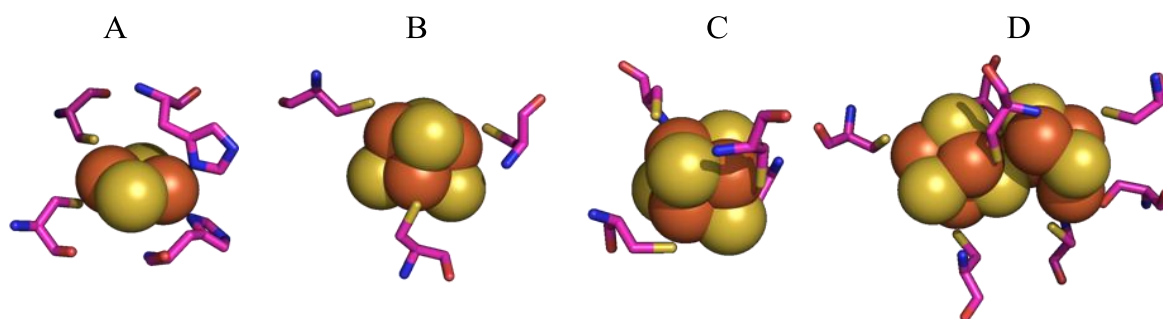


Figure 1.3.1. Representation of the most common Fe–S clusters (A) [2Fe–2S] (PDB code 1RIE), (B) [3Fe–4S] (PDB code 1FRF), (C) [4Fe–4S] (PDB code 1FRE) and (D) [7Fe–7S] (PDB code 1MIN. Iron atoms are presented as orange balls, Sulfur atoms are yellow balls. The coordinating amino acids are presents as sticks.

1.3.2. Ferredoxins

Ferredoxins (Fd) are small proteins containing Fe–S clusters. According to their prosthetic groups, Fd can be classified as type–I and type–II. The type–I Fd are usually found in plants and algae (plant–type Fd) and they bear a [2Fe–2S] cluster (**Figure 1.3.1C**).¹³⁰ The type–I Fd are mainly involved in photosynthesis. The type–II Fd contain one or two [4Fe–4S]¹³¹ cluster (or one or two [3Fe–4S])¹³² (**Figure 1.3.1**); they are also called bacterial–type Fd and they are mainly involved in anaerobic processes. The type–I Fd have a low–potential (around -400 mV vs. SHE') whereas the type–II Fd can be of low (-700 to -150 mV vs. SHE') or high–potentials (+50 to +400 mV vs. SHE').¹³³ The latter ones can be mainly found in photosynthetic purple bacteria having a reaction center–bound cytochrome.¹³⁴

Under physiological conditions, the [2Fe–2S] cluster can be found in two oxidation states, +II and +I. The [4Fe–4S] cluster can also switch between two oxidation states, namely +II and +I, the higher oxidation states (+III and +II) are exclusive for the high–potential [4Fe–4S] clusters. In contrast, the [3Fe–4S] cluster has three possible oxidation states, +I, 0 and –II. In the latter oxidation state, all the Fe atoms are in the ferrous state and the stabilization of this state requires the uptake of three protons.¹³⁵ These Fe–S cluster can undergo mutual interconversion in model systems as well as in proteins under physiological conditions. The most common example is the interconversion of the [4Fe–4S] cluster into [3Fe–4S] under mild oxidizing conditions when one of the coordinating amino acids is not a Cys.¹³³

1.3.3. The Rieske protein

The Rieske protein contains a [2Fe–2S] cluster coordinated by two His and two Cys (**Figure 1.3.1A**). It is a part of the bc_1 as well as of its chloroplastal analogue, the b_6f complex. In contrast to the above cited Fe–S proteins, the Rieske protein couples the redox reaction of the cluster to the protonation/ deprotonation process of the coordinating His. This particularity explains also the high–potential of the Rieske protein required for the mechanism of the bc_1 . The Rieske protein from the extremophilic organism *T. thermophilus* does not form a subunit of the bc_1 ; however, its midpoint potential is high and pH–dependent (+140 mV vs. SHE').⁹⁸ The Rieske protein undergoes a redox transition between the +II and the +I oxidation state. The all ferrous state of the Rieske protein from bovine can be reached and stabilized by

protonation.¹³⁶ In addition, the hydrogen bonding between the Fe–S cluster and neighboring amino acids were shown to affect the midpoint potential of the Rieske protein.^{137,138}

1.4. Infrared spectroscopy

1.4.1. Physical background

The absorption of light by a given molecule leads to an energetic transition from an initial state to a final state of higher energy. Depending on the energy of the absorbed light, the transition can occur for example at the electronic or vibrational levels. According to Lambert–Beer's law, the intensity of an absorption band is related to the concentration of the sample, the pathlength as well as the absorption coefficient.

$$A = \text{Log} \frac{I_0}{I} = \epsilon l C \quad \text{Equation 2}$$

Where:

A is the absorbance

I_0 is the intensity of the initial beam

I is the intensity of the transmitted light

ϵ is the absorption coefficient ($\text{Mol}^{-1} \cdot \text{L} \cdot \text{cm}^{-1}$)

l is the pathlength (cm)

C is the samples' concentration ($\text{Mol} \cdot \text{L}^{-1}$)

Infrared spectroscopy is an analytical technique based on the absorption of infrared light by molecules since chemical bonds can rotate or vibrate at specific frequencies. The vibrational frequencies depend on the nature of the functional groups present in a given molecules. They also depend on the properties of the chemical bond as well as on the mass of the atoms.

The transition from an initial state (i) to a final state (f) of higher energy requires the absorption of one photon of energy equal to ΔE , (Equation 3) which gives rise to an absorption signal.

$$\Delta E = hc \left(\frac{1}{\lambda_i} - \frac{1}{\lambda_f} \right) \quad \text{Equation 3}$$

Where:

ΔE is the energy of transition (J)

h is the Planck's constant (6.626×10^{-34} J.s)

c is the speed of light (3×10^{10} cm.s⁻¹)

λ is the wavelength in cm

For a non-linear molecule of N atoms, there are $3N-6$ normal vibrational modes. A normal vibrational mode is infrared active if dipole moment changing takes place during the course of

the vibration. Several vibrational modes can be observed by infrared spectroscopy such as the stretching vibrations which involve the chemical bond length, the bending vibrations which involve the modification of the bond angle as shown in Figure 1.4.1.

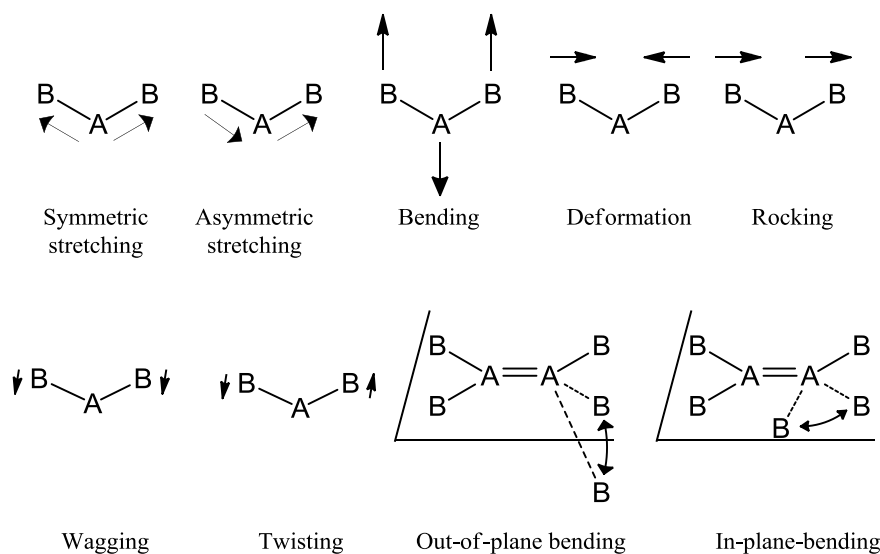


Figure 1.4.1. Normal mode vibrations.

The infrared frequencies of the molecular vibrations can be predicted and the easiest way to do so is to use the harmonic oscillator model where the atoms can be considered as point-like masses and the chemical bond as a spring (Figure 1.4.2). For a diatomic molecule, the atoms M1 and M2 are of m_1 and m_2 mass, respectively. The application of the harmonic oscillator requires the assumption that both molecules move in phase and at the same amplitude during the vibration.

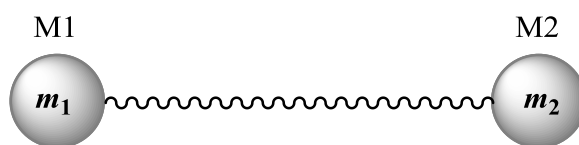


Figure 1.4.2. The harmonic oscillator model.

The stretching of the spring, which represents the chemical bond, can be described by the equation 4:

$$F = -kx \quad \text{Equation 4}$$

Where:

F is the restoring force of the spring (in N)

k is the force constant of the spring (N/cm)

x is the displacement of the spring from its equilibrium position (cm).

The mass of the diatomic molecule M1–M2 can be represented by the reduced mass μ as in the equation 5:

$$\mu = \frac{m_1 m_2}{m_1 + m_2} \quad \text{Equation 5}$$

The kinetic and potential energies of the molecule can be written as below:

$$E_k = \frac{1}{2}(m_1 \dot{x}_1^2 + m_2 \dot{x}_2^2) \quad ; \quad E_p = \frac{1}{2}(kx_1 - kx_2)^2$$

Where:

E_k is the kinetic energy

E_p is the potential energy

\dot{x} is the derivative of x .

In classic mechanics, the harmonic oscillator can be studied using Lagrange's equations:

$$\frac{d}{dt} \left(\frac{\partial E_k}{\partial (\Delta \dot{x})} \right) + \frac{\partial E_p}{\partial (\Delta x)} = 0$$

$$m_1 \ddot{x}_1 - k(x_2 - x_1) = 0 \quad ; \quad m_2 \ddot{x}_2 + k(x_2 - x_1) = 0$$

In order to resolve the equations system, we set:

$$x_1 = A_1 \cos(\omega t + \psi_1) \quad ; \quad x_2 = A_2 \cos(\omega t + \psi_2)$$

Where:

A is a constant

ω is the pulsation

φ is the phase

Two solutions are possible:

$$\omega = 0 \quad ; \quad \omega = \sqrt{\frac{k}{\mu}} = 2\pi\nu$$

The first solution corresponds to a translational movement while the second one corresponds to a vibrational frequency. Indeed the equation relating the vibrational frequency to the reduced mass can be written (Equation 6):

$$\nu = \frac{1}{2\pi c} \sqrt{\frac{k}{\mu}} \quad \text{Equation 6 where } \nu \text{ is given in } \text{cm}^{-1}.$$

Thus the frequency of the infrared vibration depends on two molecular parameters, the force constant k of the chemical bond and the reduced mass μ of the atoms. Molecules with a large

force constant will absorb at higher frequencies and molecules formed of heavy atoms will absorb at lower frequencies.

Consequently, the isotopic labeling would shift the frequency of the absorption bands and can be useful to accurately assign the vibrational modes in an infrared spectrum. It should be noted that the absorption shifts are exclusively due to the mass effect because the force constant determined by electronic motions does not change when an isotopic labeling is performed. Examples about the isotopic labeling on the absorption frequencies of some functional groups are collected in **Table 1.4-1**.

Bond	Vibrational mode	Frequency (cm ⁻¹)
C–H; C– ² H (<i>D</i>)	$\nu(\text{C–H}); \nu(\text{C–}^2\text{H})$ (<i>D</i>)	3000; 2120
¹² C=O; ¹³ C=O	$\nu(^{12}\text{C=O}); \nu(^{13}\text{C=O})$	1700; 1650
¹⁴ NH ₂ ; ¹⁵ NH ₂	$\nu(^{14}\text{N–H}); \nu(^{15}\text{N–H})$	3400; 3000
N– ⁵⁶ Fe; N– ⁵⁴ Fe	$\nu(\text{N–}^{56}\text{Fe}); \nu(\text{N–}^{54}\text{Fe})$	350; 356

Table 1.4-1: The impact of the isotopic labeling on the vibrational frequencies of some functional groups.

The infrared spectra of large molecules are significantly more complicated than the one of diatomic molecules. Hence, the harmonic oscillator model is not sufficient to determine the infrared active normal vibrational modes. Another mathematical approach is available and is based on the group theory which allows the study of the molecular symmetry and by the same allows the determination of the infrared active normal vibrational modes. Moreover, the normal mode analysis of macromolecules such as proteins cannot be undertaken with the help of the group theory due to the very important number of atoms.

1.4.2. Infrared spectroscopy of proteins

The mid infrared (MIR) absorbance spectra of proteins are dominated by the so-called amide bands which arise from the polypeptide backbone vibrations (**Table 1.4-2**). In the FIR domain (below 400 cm⁻¹), the backbone vibrations overlap with the metal–ligand vibrations as well as with the hydrogen bonding signature.

Among the amide bands observed in the absorbance spectrum of a protein, the amide I band is the most sensitive to the secondary structure organization of the protein. In order to analyze the secondary structure of proteins, the amide I band needs to be deconvoluted. Model compounds¹³⁹ as well as proteins of known secondary structure were analyzed.¹⁴⁰ A correlation between the amide I band position and secondary structures elements is generally

accepted (**Table 1.4-3**) and it allows the estimation of the secondary structure of a protein using the infrared spectroscopy.

Designation	Frequency range (cm^{-1})	Assignment
Amide A	~3300	$\nu(\text{N-H})$
Amide B	~3100	$\nu(\text{N-H})$ in resonance with first amide II overtone
Amide I	1690–1610	80 % $\nu(\text{C=O})$; 10 % $\nu(\text{C-N})$; 10 % $\delta(\text{N-H})$
Amide II	1575–1480	60 % $\delta(\text{N-H})$; 40 % $\nu(\text{C-N})$
Amide III	1320–1220	30 % $\delta(\text{C-N})$; 30 % $\delta(\text{N-H})$; 10 % $\nu(\text{C=O})$; 10 % $\delta(\text{O=C-N})$; coupled and overlapped with other modes
Amide IV	765–625	40 % $\delta(\text{O=C-N})$; 60 % other modes
Amide V	800–625	$\delta_{\text{op}}(\text{N-H})$
Amide VI	605–635	$\delta(\text{C=O/C-C-N})$
Amide VII	~200	Skeletal torsion

Table 1.4-2: designation, frequencies and assignments of the absorption bands of proteins backbone.^{141,142}

H_2O (cm^{-1})	D_2O (cm^{-1})	Assignment
1624–1642	1624–1637	β -sheet
1648	1645	Random coils
1656	1653	α -helix
1663	1641	3_{10} -helix
1667–1685	1663–1671/1683–1689	β -tuns
1691–1696	1675	β -sheet

Table 1.4-3: Assignment of protein secondary structure elements by the amide I band deconvolution.¹⁴³

The amide I band analysis is a fast method to obtain the secondary structure of a protein. However, it remains limited by the high absorption of the water in the amide I region. The amino acids side chain absorption may overlap with the amide I modes. In addition, the analysis itself requires some data manipulation such as the baseline correction. These factors taken together make the analysis of the amide I band less accurate; the typical error is of 5–10 %.

1.4.2.1. Transmission mode

The absorbance spectrum can provide information about the secondary structure of a protein, but it does not give information concerning the function of the protein, which is the scope of studying proteins. In other words, the absorbance spectra of a given protein recorded for

two different states (redox states in the case of the respiratory chain enzymes) are almost identical (Figure 1.4.3).

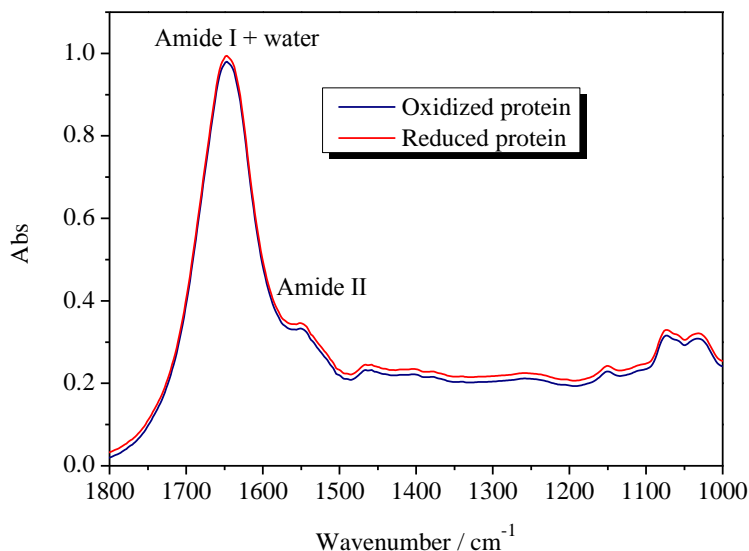
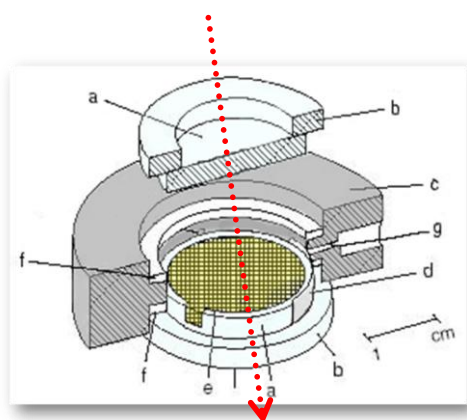


Figure 1.4.3. Absorbance spectra of the CcO in the oxidized state (blue trace) and in the reduced state (red trace).

In order to get insight into the protein mechanism by infrared spectroscopy, a differential spectroscopic technique was developed to visualize subtle changes taking place during the course of the protein reaction. The technique is based on recording the spectrum of the protein in a well-defined state (e.g. oxidized state) and then recording a spectrum of the protein in another state (e.g. reduced state). The subtraction of the spectra one from the other leads to a difference spectrum of the protein (oxidized minus reduced difference spectrum). The redox-induced difference spectrum can be obtained with the help of the OTTLE cell (Figure 1.4.4), developed in the early 1990's.¹⁴⁴ It consists of an electrochemical cell with a small pathlength to avoid the high absorption of the water.



- a. Optically transparent windows
- b. Plexiglass
- c. PVC
- d. Platinum counter-electrode
- e. Gold grid working electrode
- f. O ring
- g. Reference electrode Ag/AgCl 3M KCl

Figure 1.4.4. Schematic presentation of the OTTLE cell. The red arrow indicates the beam path through the cell.¹⁴⁴

The analysis of the difference spectrum can be undertaken with the help of infrared data obtained for individual amino acids, isolated cofactors as well as model compounds.

The difference spectrum can then reveal key events taking place during the redox reaction of the protein. The protonation–deprotonation process of acidic amino acids can be detected in the spectral region $1750\text{--}1700\text{ cm}^{-1}$, modifications of the secondary structure of the protein can be detected in the amide I region ($1690\text{--}1610\text{ cm}^{-1}$). Signals arising from the environmental modifications around the cofactors can also be detected in the $1600\text{--}1500\text{ cm}^{-1}$ region for example (**Figure 1.4.5**). Although the difference spectrum shows only the signals arising from the protein component involved in the reaction, the accurate assignments of the signals cannot be easily done. Most of the time the side chain absorption of amino acids overlaps with the absorption of backbone vibrations as well as the cofactors signals. The accurate assignment can be done by following different strategies: (i) The H–D exchange of the labile protons in the protein induces important shifts in the backbone vibrations, especially the amide II band. In addition, the signals arising from the solvent–exposed amino acids would downshift because of the H–D exchange; solvent–inaccessible amino acids would not exchange their protons. Indeed, the H–D exchange can bring information about the location of amino acids involved in the proteins reaction. The method is particularly efficient toward protonated acidic residues.¹⁴⁵ (ii) The specific labeling of the cofactors is also a successful method to differentiate between the “apoprotein” signals and the cofactors themselves.¹²⁰

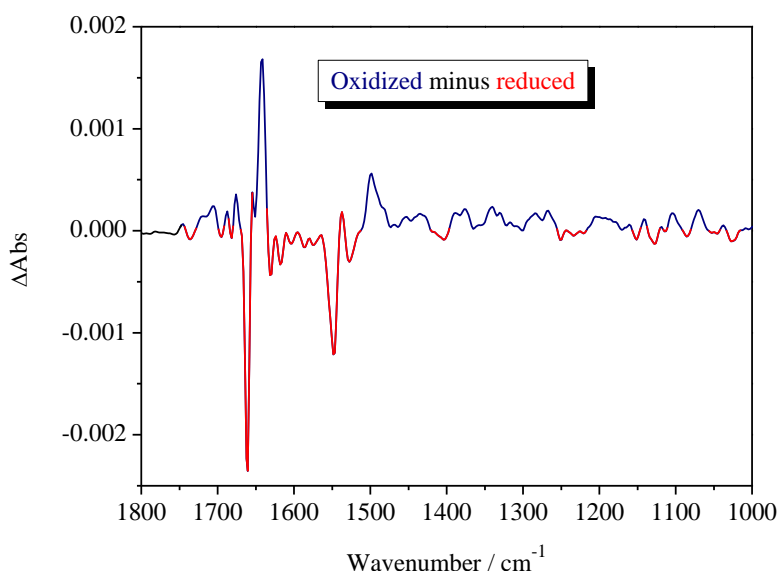


Figure 1.4.5. Fully oxidized minus fully reduced difference spectrum of the CcO from *P. denitrificans* recorded at pH 8.0. The positive signals (blue) are arising from the oxidized protein and the negative ones (red) from the reduced protein.

The specific labeling amino acids (e.g. Tyr residues of the *CcO* of *P. denitrificans*) helped for assigning the signals arising from these amino acids.¹⁴⁶

(iv) Finally, The comparison between the spectra of the wild-type protein and site-directed mutants is a powerful tool to determine the crucial amino acids required for the protein activity.¹⁴⁷

The ability of the infrared difference spectroscopy to detect subtle changes taking place within the protein with a high signal-to-noise ratio makes it a powerful tool to investigate proteins.

1.4.2.2. Attenuated total reflection mode

The ATR unit is an optical setup where the infrared beam undergoes multiple reflections on the surface of an internal reflection element (Diamond, Silicon, ZnSe...). The infrared beam is focused at the end of the internal reflection elements and enters it where it is reflected several times along the crystal. At each reflection, an evanescent wave of infrared light penetrates a short distance from the internal reflection element into the sample (**Figure 1.4.6**). Details about the ATR-FTIR spectroscopy can be found in ref.^{148,149}

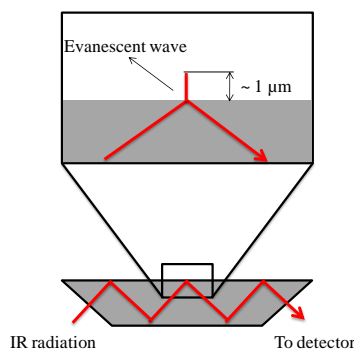


Figure 1.4.6. Attenuated Total Reflection unit and an enlarged view of the evanescent wave.

An infrared spectrum can be recorded using an ATR setup under two conditions: (i) the sample must be in contact with the prism because of the short pathlength of the evanescent wave ($\sim 1 \mu\text{m}$). (ii) The prism must have a greater refracting index than the samples because the depth of the evanescent wave depends on both refracting indexes as shown in the equation 7.¹⁵⁰

$$d_p = \frac{\lambda/n_1}{2\pi \sqrt{(\sin^2 \theta - (n_2/n_1)^2)}} \quad \text{Equation 7}$$

Where:

d_p is the depth of the evanescent wave

θ is the incident angle

n_1 is the refracting index of the prism

n_2 is the refracting index of the sample

λ is the wavelength

The ATR–FTIR spectroscopy is a useful method to study proteins and has some advantages when compared to the transmission mode. (i) It requires fewer amounts of sample (1–2 μL) than the transmission mode (6–8 μL). (ii) The multiple reflections allow the evanescent wave to pass through the sample several times; indeed the signal is increased leading to improve the signal–to–noise ratio. On the other hand, several inconveniences appear such as the sample orientation effect on the spectra recorded with two different ATR prisms (Diamond and silicon). The ATR yield is not always the same; indeed, the relative intensities are not the same when spectra are recorded for the same sample during two different experiments.

As for the transmission mode, the ATR–FTIR reaction–induced spectroscopy was also developed. An electrochemical cell was developed to combine ATR measurements with electrochemistry. Furthermore, perfusion measurements can be performed using an ATR setup combined with a dialysis kit. The sample is placed in contact with the ATR crystal which must be hydrophobic enough to interact with the protein and prevents it from being washed away when the perfusion is performed.¹⁵¹ The perfusion itself allows modifying the protein environment *in situ*. The method is particularly successful in exchanging buffers where information about the pH–dependent signals can be obtained. Furthermore, H–D exchange kinetics can also be followed by perfusion to learn more about the solvent accessibility to the protein.¹⁵²

1.5. The aim of the thesis

The research presented in this thesis is mainly concerned with four aspects of the coordination of metals within biologically important molecules as well as within proteins of the respiratory chain by means of FTIR spectroscopy.

- The copper coordination

Copper ions are present in many proteins and often its coordination takes place via His residue. It is indeed important to study model Cu-complexes. To better understand the copper coordination, the copper-PLH complexes were investigated as a model compound. The study of such model compounds in the FIR range would be useful to observe the metal-ligand vibrations.

The amyloid-beta-16 (A β 16) is a peptide constituted of a sequence of 16 amino acids and it binds tightly transition metals cations such as Cu²⁺ and Zn²⁺. These complexes are found as aggregates in the brain tissues of Alzheimer's patients and are thought to initiate the disease by producing reactive oxygen species. Using the FTIR spectroscopy, we aim to better understand the coordination of copper by the A β 16 in a pH dependent manner.

- The interaction of the respiratory enzymes with Zn²⁺

Three of the four respiratory enzymes are proton-pumping machines which produce an electrochemical proton gradient that can be used by the ATP-synthase. Protons cross the membrane from the negative side to the positive side via proton pathways constituted by highly conserved amino acids as well as wires of water molecules. In presence of Zn²⁺, the proton pumping is inhibited to a large extent. The effect of the Zn²⁺ binding to the respiratory chains complexes III and IV is studied at the molecular level by a redox-induced difference spectroscopic approach.

- The study of metals as cofactors

The electrochemically-induced FTIR difference spectroscopy in MIR domain is useful to observe the modification occurring at the level of the backbone as well as individual amino acids. On the other hand, the method does not allow the observation of modifications taking place at the level of metal-ligand vibrations. The FIR domain offers the possibility to obtain information about the metal-ligand vibrations. In order

to determine the redox signature of the cofactors themselves, the electrochemically-induced FTIR spectroscopic technique was adapted to the FIR range where metal-ligand vibrations occur.

The electrochemically-induced FTIR spectroscopy in the FIR range offered the opportunity to observe the redox signature of the metal-ligand vibrations of several small Fe-S containing proteins. These signatures can be useful in analyzing the FIR signature of more complex proteins such as the soluble fragment of the complex I.

- The hydrogen bonding signature

Beside of the metal-ligand vibrations, the internal hydrogen bonding signature of proteins can be observed in the FIR domain. The investigations concern the understanding of the effect on the metal environment in tuning the whole tertiary structure of metalloproteins.

The analysis of the hydrogen bonding in a temperature and pH-dependent manner of the Rieske protein shows different patterns at the level of the phase transition at different pH values. These results point towards the effect of the [2Fe-2S] cluster environment on the mechanism of the protein.

The LFA-I domain of integrins can bind metal cations such as Ca^{2+} , Fe^{2+} , Mn^{2+} and Mg^{2+} . The protein is only active when Mg^{2+} is bound. The protein was studied in a temperature-dependent manner.

2. Materials and methods

2.1. Sample preparation

2.1.1. The copper coordination

The poly-L-histidine (PLH) peptide (Sigma) was dissolved in D₂O (Aldrich 99.9%) or in milliQ water. The final PLH concentration was 5 mM. Imidazole and deuterated imidazole (Aldrich) were dissolved in milliQ water or in D₂O to a final concentration of 200 mM. CuCl₂·2H₂O (Riedel-de Haën) was dissolved in distilled water or D₂O to a final concentration of 100 mM.

CuSO₄·5H₂O (Carlo Erba Reactifs) was dissolved in water to a final concentration of 100 mM. In the Cu-containing samples, the final concentrations of Im and PLH were 100 mM and 2.5 mM, respectively. All products were used without further purification. The pH (pD) adjustment was done using HCl (DCI) or NaOH (NaOD).

Unlabelled Aβ-16 peptides were purchased from GENEPEP (Prades-le-Lez, France). It was synthesized chemically. The labelled amino-acids were purchased from Eurisotop (St-Aubin, France) and sent to GENEPEP for synthesis of the labelled-peptides.

For the ATR spectroscopy, the peptides were dissolved in pure water or in D₂O to a final concentration of 5 mM. The final concentration of Cu when added was 5 mM. The pH/ pD was controlled by the addition of small amounts of HCl/ (DCI) or NaOH/ (NaOD). 2 μL of each sample were dried on the ATR crystal to form a thin film. The final concentration of the peptide was determined by measuring the Tyr absorption at 275 nm ($\epsilon=1410 \text{ Mol}^{-1} \cdot \text{L} \cdot \text{cm}^{-1}$) (**Figure 2.1.1**) of a 700 times diluted sample of the mother solution used for the FTIR spectroscopy.

For the electrochemically induced difference spectroscopy of the Cu-Aβ-16 complexes the concentration of the peptide as well as Cu cations was of 10 mM. The medium was buffered with 50 mM phosphate buffer for pH 6.50 and 9.0 and with 50 mM CHES buffer for pH 11.0. All the buffers contained 50 mM of KCl as a supporting electrolyte.

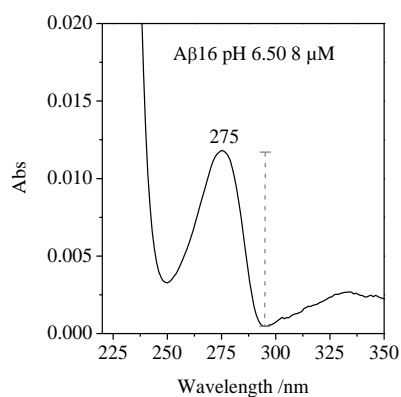


Figure 2.1.1. Typical UV absorbance spectrum of the Aβ16 peptide. The dashed line represents the absorption used to determine the concentration.

2.1.2. The Rieske protein samples

The *T. thermophilus* Rieske protein was prepared in the laboratory of Prof. B. Ludwig (Institute of Biochemistry, Molecular Genetics, Biocenter Goethe–Universität, Frankfurt, Germany). For the FIR electrochemistry, the protein was transferred in the following buffer solutions, each of 100 mM: MES pH 6.0, Tris–HCl pH 8.0 and CHES pH 10.2. All the buffers contained 100 mM KCl as a supporting electrolyte. For the FIR absorption measurements, the protein was equilibrated in the following buffer solutions each, 20 mM MES, pH 6.0; Tris, pH 8.0 or CHES, pH 10.2. The protein concentration used was typically 2.5 mM as determined using UV–Vis spectroscopy.¹⁵³ 2 μL of each sample were dried on the ATR crystal for the ATR and 5 μL were dried on polyethylene substrate for the temperature dependent measurements.

2.1.3. Rubredoxin samples

Clostridium pasteurianum (*C. pasteurianum*) Rb protein samples (Sigma) were received in 50 mM Tris–HCl buffer. For the electrochemistry measurements the buffer was exchanged against 50 mM Tris–HCl buffer pH 7.4 containing 100 mM KCl as a supporting electrolyte. The protein final concentration was about 4 mM.

2.1.4. Ferredoxin samples

C. pasteurianum Fd protein samples (Sigma) were received as lyophilized powder (39 % Fd). For the electrochemistry measurements the protein was dissolved in Tris–HCl buffer

50 mM pH 7.5 containing 100 mM KCl as a supporting electrolyte. The protein final concentration was about 4 mM.

The *Spinacia oleracea* (spinach) Fd protein samples (Sigma) were received in 150 mM Tris-HCl buffer pH 7.5. The protein concentration was 1–3 mg/mL. For the electrochemistry measurements the buffer was exchanged against 50 mM Tris-HCl pH 7.5 buffer containing 100 mM KCl as a supporting electrolyte. The protein final concentration was about 15 mM.

2.1.5. NADH deshydrogenase fragment

The NADH dehydrogenase fragment (NDF) samples were prepared in the laboratory of Prof. Thorsten Friedrich, Institute of Organic Chemistry and Biochemistry at Albert-Ludwigs-Universität in Freiburg, Germany.

The *E. coli* strain BL21(DE3) and the plasmid pET11a (AGS, Heidelberg) were used as described in ref.¹⁵⁴. Ampicillin was added to 100 µg/mL. All enzymes used for recombinant DNA techniques were from Pharmacia, Freiburg or Biolabs, Schwalbach. For the overexpression of the NADH dehydrogenase fragment, the protocol is described in ref.¹⁵² with some modification of the medium where a minimal M9 medium was used.¹⁵⁵ The cells were broken by a single pass through a French pressure cell at 110 MPa. Cell debris and the cytoplasmic membranes were removed by ultracentrifugation at 250000 g for 60 min. The cytosol was applied to a 50 mL anion exchange chromatography column (Fractogel, EMD, Merck) equilibrated with 50 mM MES/NaOH, 50 mM NaCl, pH 6.0, 30 µM PMSF and 5 mM DTT. The column was washed with the same buffer until the absorbance at 280 nm decreased. Proteins were eluted with a 300 mL linear salt gradient from 50 to 300 mM NaCl in 50 mM MES/NaOH, pH 6.0 using a flow rate of 5 mL/min. Fractions exhibiting NADH/ferricyanide reductase activity were pooled and adjusted to pH 6.6 with 200 mM NaOH (see profiles in **Figure 2.1.2**).

The total concentration of the proteins was determined using the biuret test, where samples of 400 µL of protein were mixed with biuret in presence of ferricyanide. The activity of the protein was controlled by following the NADH oxidoreductase activity against ferricyanide at 410 nm. The concentration of the harvested proteins was 11.7 (100 µL) and 14.4 mg/ mL (108 µL) for the native and labelled preparations, respectively. The samples were then applied to a 10 mL Strep-Tactin Sepharose column (0.4 x 1.6 cm, IBA) equilibrated with 50 mM MES/NaOH, 50 mM NaCl, pH 6.6, 30 µM PMSF and 5 mM DTT at a flow rate of 0.8

mL/min. The NADH dehydrogenase fragment was eluted with 2.5 mM D–desthiobiotine in 50 mM MES/NaOH, 50 mM NaCl, pH 6.0.

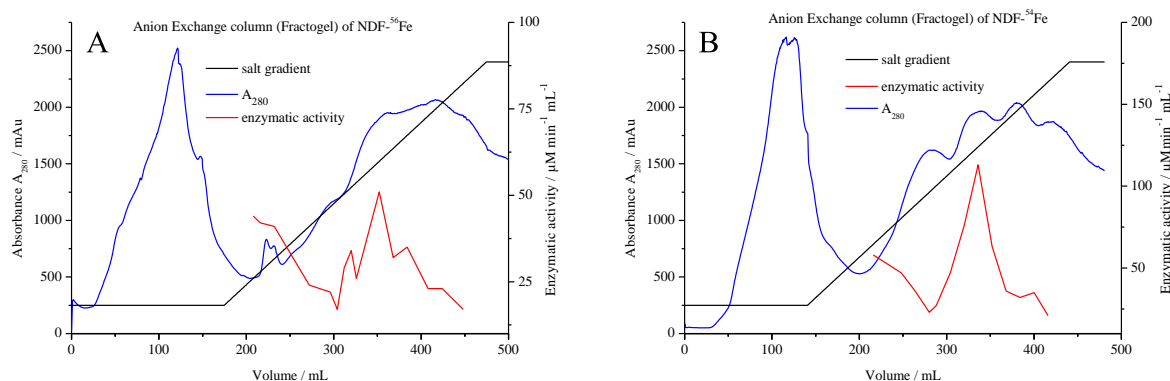


Figure 2.1.2. Chromatography profiles on Fractogel EMD of the purification of both NDF from *E. coli*. The black line displays the NaCl gradient, the blue line shows the absorbance at 280 nm and the red line displays the NADH/ferricyanide oxidoreductase activity. The panel A shows the data for the unlabelled (^{56}Fe) sample and the panel B shows the data for the ^{54}Fe –labelled sample.

The fractions with NADH/ferricyanide reductase activity were pooled (See profile in **Figure 2.1.3**). By the end of the preparation, 7.1 and 8.0 mg of unlabelled and ^{54}Fe labelled NDF, respectively, were obtained. The samples were concentrated by ultrafiltration (100 kDa MWCO Amicon, Millipore), shock frozen in liquid nitrogen and stored at $-80\text{ }^{\circ}\text{C}$ until use.

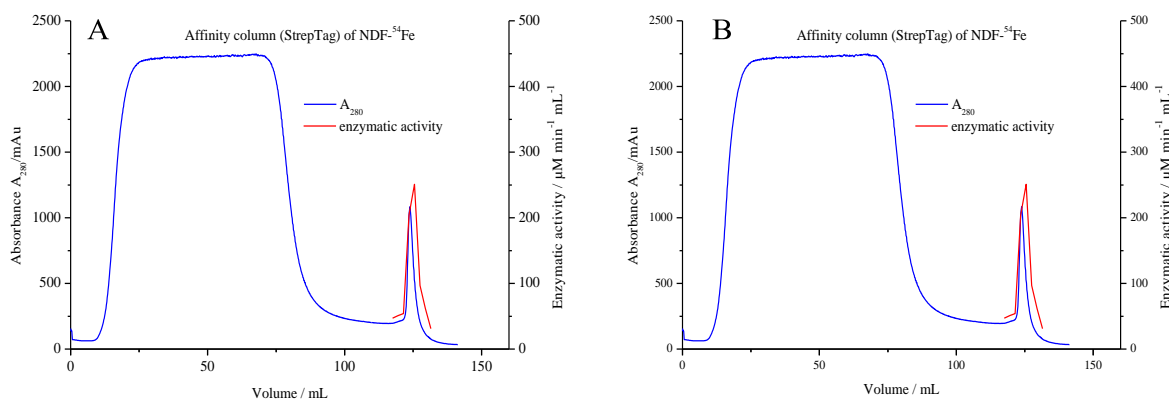


Figure 2.1.3. Chromatography profiles on the affinity (StrepTag)–Sepharose. (A) For the unlabelled NDF and (B) for the ^{54}Fe –labelled NDF. The blue line displays the absorbance at 280 nm, the red line displays the NADH/ferricyanide oxidoreductase activity.

The presence of the three subunits (NuoF, NuoE and NuoG) was confirmed by SDS-PAGE gel filtration¹⁵⁶ performed on small samples of the unlabelled and labelled samples ($\sim 5\mu\text{g}$ of protein for each sample) (**Figure 2.1.4**). The ATR absorbance spectra of the NDF were recorded in presence of 20 mM MES buffer pH 6.0 containing 20 mM KCl. The

electrochemically induced difference spectra were recorded in 50 mM MES buffer pH 6.0 containing 50 mM KCl. For, FITR spectroscopy, the sample concentration was ~1 mM.

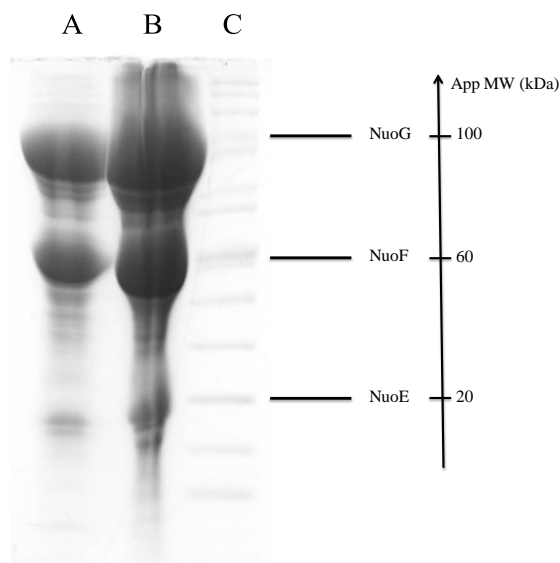


Figure 2.1.4. SDS-PAGE of the preparation of (A) unlabelled NDF and (B) ⁵⁴Fe-labelled NDF. The bands were assigned to the individual subunits due to their apparent molecular weight using the etalon scale (C).

2.1.6. The cytochrome *bc*₁ complex

The wild-type *R. capsulatus bc*₁, the Glu295Val mutant enzyme and the *bc*₁ lacking the Rieske protein (subcomplex) samples were prepared in the laboratory of Prof. Fevzi Daldal (Department of biology, university of Pennsylvania, USA) as previously reported.^{94,157,158} The samples contained the protein in a final concentration of 7 mg / mL. The buffer concentration was 100 mM Tris-HCl buffer pH 8.0 containing 350 mM KCl and 0.05 % n-dodecyl β-D- maltoside (DDM). The samples were concentrated using membranes of 100 kDa MWCO Amicon purchased from Millipore; simultaneously the buffer was exchanged against 100 mM Tris-HCl buffer pH 8.0 containing 100 mM KCl and 0.05 % DDM (AppliChem). The ZnSO₄·H₂O 99.99 % (Sigma-Aldrich) was dissolved in the same buffer as the protein sample to a final concentration of 2 mM. The final concentration of the Zn cations, when mixed to the protein sample, was 200 μM. The ZnSO₄ was added to the sample on ice 15 hours before the measurements in order to maximize the filling of the high affinity Zn binding site within the protein.

2.1.7. The cytochrome *c* oxidase

The wild-type *Paracoccus denitrificans* (*P. denitrificans*) CcO as well as the Glu78Gln mutant samples were prepared in the laboratory of Pr. Bernd Ludwig (Institute of Biochemistry, Molecular Genetics, Biocenter Goethe-Universität, Frankfurt, Germany). The protein samples were concentrated using membranes of 50 kDa MWCO Amicon purchased from Millipore; simultaneously the buffer was exchanged against 100 mM Tris-HCl buffer pH 8.0 containing 100 mM KCl and 0.05 % DDM (AppliChem). The Zn inhibition procedure is the same as described for the *bc*₁ samples. For spectroscopy, the final concentration of the protein is ~0.5 mM.

2.1.8. LFA-I domain of integrins

The LFA-I domain was purified according to the previously reported method.¹⁵⁹ The samples were dissolved in PBS buffer pH 7.4 (137 mM NaCl, 10 mM sodium phosphate, 2.7 mM KCl and 2 mM potassium phosphate) with one of the following salts (at a final concentration of 10 mM): MgSO₄, CaCl₂, MnCl₂ or FeSO₄.

2.1.9. PLL and PLA

PLL 45 kDa and PLA 1076 Da were purchased from Sigma. The samples were prepared in an ice bath to avoid the spontaneous aggregation. The pH and the pD value was adjusted by adding small amounts of 0.1 M NaOH (NaOD) or HCl (DCl).

2.2. Spectroscopy

This thesis deals mainly with infrared and UV–Vis spectroscopies. This part contains a general description of the optics of the used infrared spectrometer in the MIR and FIR ranges.

2.2.1. The Fourier transform infrared spectrometer

2.2.1.1. Main optical elements

The infrared spectra are recorded with the help of FTIR spectrometers. They are equipped with different infrared sources for different spectral domains. The infrared light is transformed to an interferogram by the Michelson interferometer and then the light goes into the sample compartment and finally reaches the detector which also depends on the spectral range used. The **Figure 2.2.1** shows the main parts of an infrared spectrometer. The Michelson interferometer consists of a beamsplitter, two mirrors, M1 and M2. The latter one is a mobile (**Figure 2.2.1A**). The infrared light comes from the source to the beamsplitter which reflects 50 % of the initial beam to the mirror M1, the remaining 50 % continue to hit the mirror M2. The beams coming back from both mirrors pass then through the sample to the detector.

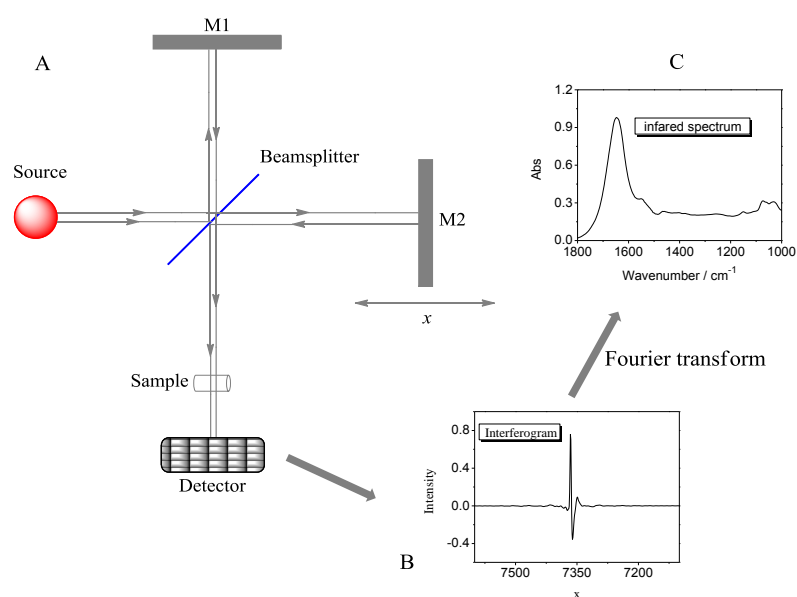


Figure 2.2.1. (A) The main optical parts of a conventional FTIR spectrometer. (B) The shape of a typical interferogram. (C) A typical protein spectrum obtained after the transformation of its corresponding interferogram.

The movement of the mirror M2 makes unequal the optical paths of the two beams, indeed interference occurs and it is detected by the detector (**Figure 2.2.1B**). The interferogram represents the intensity (y axis in the **Figure 2.2.1B**) as a function of the mirror M2 displacement (x axis in the **Figure 2.2.1B**). If the mirror movement is uniform, the x axis in the **Figure 2.2.1B**) represents the time scale rather than the mirror displacement x . The Fourier transform (Equation 8) allows the transformation of the interferogram to a spectrum (**Figure 2.2.1C**).

$$B(\tilde{\nu}) = \int_{-\infty}^{+\infty} I(\delta) \cos(2\pi\delta\tilde{\nu}) d\delta \quad \text{Equation 8}$$

Where B is the intensity of the signal in the spectrum, I is the intensity in the interferogram, $\tilde{\nu}$ is the frequency (cm^{-1}) and δ is the optical path difference of the two beams (δ is equal to twice the velocity of the M2 mirror).

The FT requires the integration between $-\infty$ and $+\infty$, however, it is physically impossible to scan the interferogram in this domain. It is indeed necessary to restrict the scan domain to fixed limits, $-L$ and $+L$. The resolution of an infrared spectrum depends on this restricted domain and it is given by the equation 9 where $2L$ is the optical retardation.

$$\Delta\tilde{\nu} = \frac{1}{2L} \quad \text{Equation 9}$$

In addition, the intensity of a given infrared signal (Equation 10) is correlated to the intensity of the incident radiation I_0 , to $B(\tilde{\nu})$, the absorption coefficient of the sample and to $\tilde{\omega}$, the angular modulation of light.

$$I \propto \frac{I_0 B(\tilde{\nu})}{\tilde{\omega}} \quad \text{Equation 10}$$

It should be noted that $\tilde{\omega}$ is the product of the mirror rate V and the infrared frequency $\tilde{\nu}$ and is described as $\tilde{\omega} = 4\pi V\tilde{\nu}$. It is indeed obvious that the high scan rate yields signals of low intensity and vice versa.

2.2.1.2. Optical elements by spectral range

In order to obtain the spectrum of a sample in a given infrared range, the optics needs to be adequately chosen. The modification concerns the source, the detector, the beamsplitter, as well as the sample compartment material (windows). The appropriate optics for each spectral range is listed in the **Table 2.2-1**.

Three spectrometers were used during the thesis, all of them from Bruker Optics, Karlsruhe. The vertex 70 was used to perform the redox induced FTIR–difference spectroscopy of the bc_1 and the CcO. The source was the globar source; the difference spectra in the 1800–1000 cm^{-1} range were recorded using CaF_2 (Korth Kristalle GMBH) as window material. In the range 1800–700 cm^{-1} ZnSe windows (Korth Kristalle GMBH) were used.

Source	Beamsplitter	Detector	Cell window	Spectral range (cm^{-1})	Preferred scan velocity (kHz)
Globar	Ge covered KBr	MCT	CaF_2	4000–1000	40–10
			BaF_2	4000–800	
			ZnSe	4000–700	
			Diamond*	4000–700	
Hg vapor	Si; 6 μm Mylar–Si**	dTGS Bolometer**	Diamond	700–50	2.5–1.6
			Si		
			Polyethylene		
			Diamond*		
Hg vapor	Si; 6 μm Mylar–Si**	dTGS Bolometer**	Si	700–30	5–1.6
			Polyethylene		

Table 2.2-1. The appropriate optics for each infrared spectral range. *The ATR unit is equipped with diamond crystal. ** The 6 μm Si–Mylar beamsplitter and bolometer were used at the ANKA and BESSY II synchrotron facilities.

The redox induced FTIR MIR spectra of the NADH deshydrogenase fragment were recorded with the help of an IFS 28 spectrometer. The detector was the room temperature–dTGS, the scan velocity was 10 kHz and the window material was ZnSe.

The redox induced FIR spectra of the Rieske protein from *T. thermophilus* as well as for the Fd from *C. pasteurianum* were obtained at the ANKA facility, using an IFS 66/v spectrometer equipped with helium cooled bolometer and Hg vapor source. The scan velocity was 5 kHz and the windows were 2 mm Si (Korth Kristalle GMBH). At least 20 redox cycles (64 scans each) with 4 cm^{-1} spectral resolution were averaged to obtain the difference spectrum of one sample. The FIR data of the Rieske protein from *T. thermophilus* and the Fd from *C. pasteurianum* were reproduced in the laboratory with the help of the vertex 70 spectrometer equipped with Hg vapor source and a room temperature dTGS detector. The scan velocity was 2.5 kHz and the windows were 1 or 2 mm Si (Korth Kristalle GMBH). At least 40 redox cycles (2 x 64 scans (ox) and 2 x 64 scans (red) of 4 cm^{-1} spectral resolution for each cycle) were averaged to obtain the difference spectrum of each sample. The FIR redox induced

spectra of the Rb from *C. pasteurianum*, the Fd from spinach and the NADH deshydrogenase fragment were obtained in the laboratory as described above for the Rieske and the Fd. The redox cycling parameters were the same as above.

The MIR and FIR spectra of the Cu-PLH and the Cu-A β 16 samples were obtained with the help of the vertex 70 spectrometer equipped with the Harrick-ATR unit. The source was the globar and the detector was the liquid nitrogen cooled MCT for the MIR domain. For the FIR domain the detector was the room temperature dTGS. In the MIR range the scan velocity was 40 kHz while in the FIR range the scan velocity was 1.6 kHz. The second derivatives of the spectra were used to determine the exact position of each signal.

The low-temperature studies on integrins were carried at the BESSY II synchrotron facility at the IRIS beamline which is equipped with IFS 66/v spectrometer and He-cooled cryostat. The source was the synchrotron radiation and substrate material was 1 mm of polyethylene. The data were reproduced in the laboratory using the vertex 70 spectrometer, the globar source, the dTGS detector, 1 mm polyethylene window and He-cooled cryostat (Advanced Research System, Inc). The scan rate was 2.5 kHz. At least five spectra of 128 scans for each sample were averaged to obtain one spectrum.

The low temperature data of the Rieske protein from *T. thermophilus* were obtained in the laboratory as described for the integrins.

Typically 256 scans were used to record a spectrum in the MIR range whereas 128 or 64 scans were used to record a spectrum in the FIR range.

2.2.2. UV-Vis spectroscopy

The UV-Vis spectra presented here were recorded on a Varian Carry 300 spectrometer. The absorbance spectra were recorded with the help of quartz cuvette (Helma) of 1 cm pathlength. The redox induced UV-Vis spectra were recorded on the same spectrometer with the help of the OTTLE cell. The windows were 4 mm thick CaF₂.

The UV-Vis titrations of the *bc*₁ samples as well as the CcO samples were performed by following the evolution of the Soret band of the hemes absorbance during oxidative titration. The absorbance values are then plotted vs. the applied potential. The obtained curves were then fitted with the sum of Nernst equations:

$$A(p) = \sum \frac{A_{max}}{1 + \exp\left(\frac{(p-E_m)nF}{RT}\right)} \quad \text{Equation 11}$$

Where A_{max} is the maximal change in the absorbance
 p is the applied potential
 E_m is the midpoint potential of the cofactor
 n is the number of the transferred electrons
 F is the constant of Faraday
 R is the universal gas constant
 T is the temperature in K

2.3. Electrochemistry

The electrochemistry was performed with the help of the OTTLE cell which consists of a conventional three electrodes setup (**Figure 2.3.1**). The reference electrode was Ag/AgCl 3M KCl and its potential is + 208 mV vs. SHE'. The counter-electrode was a platinum foil and the working electrode was a gold grid of 4–6 μm thickness (Precision Eforming, New York, USA). The potential of the working electrode was controlled with the help of a homemade potentiostat.

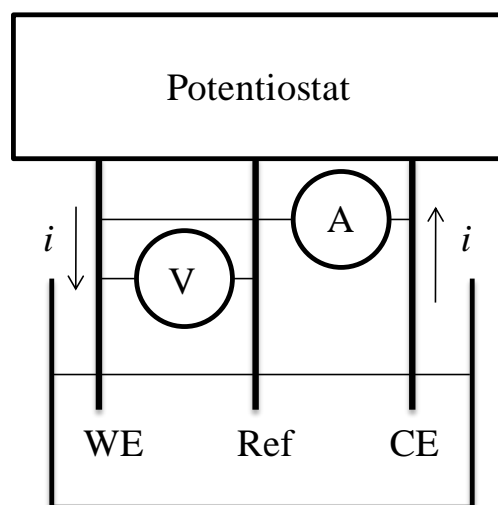


Figure 2.3.1. Schematic presentation of the three-electrode setup. WE stands for the working electrode, Ref for the reference electrode and CE for the counter-electrode. The potential is controlled between the WE and the Ref while the current is controlled between the WE and the CE.

The working electrode was chemically modified in order to prevent the protein denaturation (**Figure 2.3.2**). The chemical modifiers used for this purpose were cysteamine and the 3-mercaptopropionic acid. The modification of the working electrode was achieved by immersing it in a solution containing the modifiers at a concentration of 2 mM for an hour at room temperature.

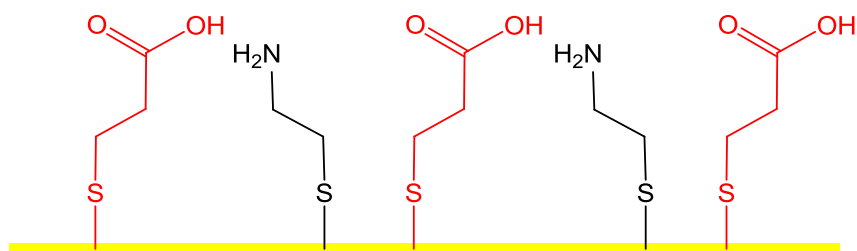


Figure 2.3.2. Schematic representation of the modified gold grid. The cysteamine is colored in black, the 3-mercaptopropionic acid in red and the gold grid in yellow.

The respiratory chain enzymes are large molecules and most of the time the cofactors are embedded deep in the protein structure. Indeed, the electron transfer rates between the cofactors and the working electrode are slow. In order to overcome this problem, a cocktail of 19 electrochemical mediators was added to each protein sample. The mediators were adequately chosen to cover the potential range of the respiratory chain cofactors, i.e., from ~ -600 mV to $\sim +600$ mV vs. Ag/AgCl 3M KCl (**Table 2.3-1**).

Name	E_m (mV) vs. Ag/AgCl 3M KCl	Purchased from	Solvent
Ferrocenylmethyltrimethylammoniumiodide	607	Strem chemicals	ethanol
1,1'-ferrocenedicarboxylic acid	436	Fluka	ethanol
Potassiumhexacyanoferrate(II) trihydrate	212	Riedel-de-Haën	water
1,1'-dimethylferrocene	133	Aldrich	ethanol
Quinhydrone	70	Fluka	ethanol
Tetrachloro-1,4-benzoquinone (<i>p</i> -Chloranil)	72	Aldrich	acetone
N,N,N',N'-tetramethyl- <i>p</i> -phenylenediamine dihydrochloride	62	Fluka	water
2,6-dichlorophenolindophenol sodium salt hydrate	9	Biochemika	ethanol
Hexaammineruthenium(III)chloride	-8	Aldrich	water
Anthraquinone-2-sulfonic acid sodium salt	-23	Aldrich	water
1,4 naphthoquinone hydrate	-63	Aldrich	ethanol
Anthraquinone	-108	Aldrich	ethanol
5-hydroxy-1,4-naphthoquinone	-158	Aldrich	ethanol
Duroquinone	-198	Sigma	ethanol
Menadione	-220	Sigma	acetone
2-hydroxyl-1,4 naphthoquinone	-333	Sigma	ethanol
9,10-antraquinone-2,6-disulfonic acid disodium salt	-433	Sigma	ethanol
Neutral Red	-515	Sigma-Aldrich	ethanol
Methyl viologen dichloride hydrate	-628	Aldrich	water

Table 2.3-1. List of the 19 mediators used in the electrochemistry and their respective midpoint potentials.

The final concentration of each mediator was 13 μM . This low concentration of the mediators was used to prevent their contribution to the infrared difference spectrum of the studied protein.

3. Results and discussion

3.1. The copper coordination

3.1.1. The copper coordination by PLH

3.1.1.1. Introduction

The metal–ligand vibrations occur in the FIR spectral range and Raman spectroscopy has been widely used to determine the coordination of metals complexes.¹⁶⁰⁻¹⁶³ Besides, FIR spectroscopy of proteins is starting to gain more attention and the metal–ligand vibrations of heme proteins and their model compounds were investigated.¹⁶⁴⁻¹⁶⁶ Transition metals like Cu are redox cofactors of several proteins. Most of the time, the Cu cations are coordinated by His residues. This is the motivation behind the investigation of the Cu–PLH complexes by FTIR spectroscopy, especially in the FIR spectral range.

A complete study on the Cu–His compounds was done by Mesu *et al.*¹⁶² They used, among other techniques, Raman and IR spectroscopies and they proposed different molecular structures of Cu–His complexes in function of pH. In those structures, the amine nitrogen and the carboxylate entities were involved in the coordination, while in proteins and peptides the carboxylate function is not present. Indeed, the Cu–PLH complexes offer a more reliable mimic for the Cu coordination within proteins. It should be noted that the imidazole ring of His can adopt four different protonation states (Figure 3.1.1). The Cu–PLH complexes were studied in a pD–dependent manner by means of ATR–FTIR spectroscopy in the spectral range 1800–50 cm⁻¹.

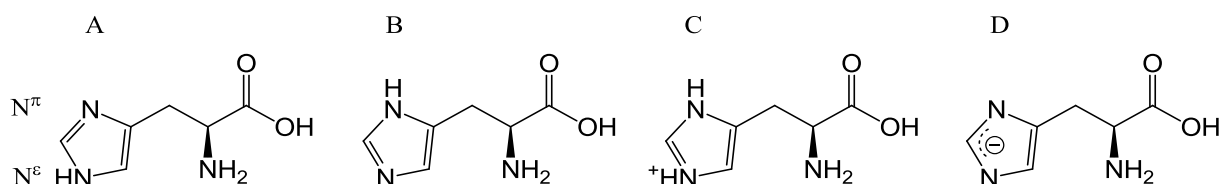


Figure 3.1.1. The four possible protonation state of the imidazole ring of His. N^ε is the one close to the CH₂, N^δ is the one far from the CH₂. (A) N^ε is protonated, (B) N^δ is protonated, (C) both nitrogens are protonated and (D) the Im ring is deprotonated.

3.1.1.2. UV–Visible spectroscopy

The UV–Vis spectra of the Cu–imidazole (Cu–Im) and Cu–PLH complexes were recorded at three pD values (**Figure 3.1.2**). At pD 2.0, where the nitrogen atoms of the Im ring are protonated (deuterated), the maximum of the d–d transition band are 798 nm for Cu–Im solution and 794 nm for Cu–PLH solution, suggesting the presence of the $[\text{Cu}(\text{D}_2\text{O})_6]^{2+}$ aquo complex. At acidic pD no coordination effects from the Cu are expected for Im or PLH due to the protonation of the ring.

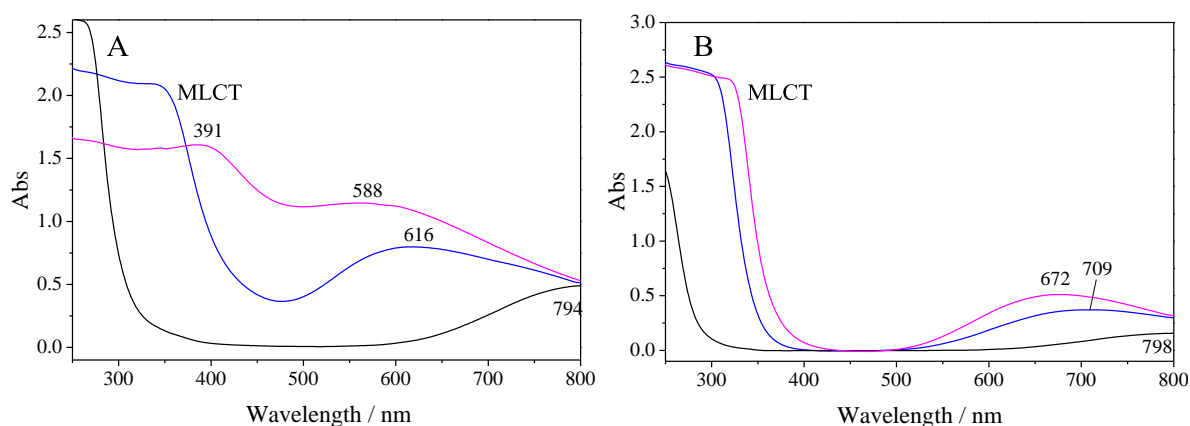


Figure 3.1.2. UV–Vis spectra of: (A) the Cu–Im and (B) the Cu–PLH complexes at pD 2.0 (Black), at pD 7.0 (Blue) and pD 9.5 (magenta).

At neutral pD, a blue shift is seen that could be explained by the Cu complexation by the nitrogen atoms of the Im ring. In the case of the Cu–PLH complex, the blue shift and intensity increase of the d–d transition from 794 nm at pD 2.0 to 616 nm at pD 7.0 is important due to the formation of the Cu–PLH complex and the involvement of nitrogen in the complexation.

Once the pD is at 9.5, the d–d transition band of the Cu–Im shifts further down and the intensity increases based on the increase of the metal–ligand bonding. Also for this pD the d–d transition of the Cu–PLH complex exhibits a larger downshift. At pD 9.5, the nitrogen atoms of the Im ring and the Im ring of the PLH are unprotonated and could be involved in the coordination of Cu. Besides, nitrogen atoms of the backbone and chloride anions are also possible candidates for the coordination.¹⁶⁷

In fact, the downshift of the d–d transition band below 600 nm in the case of the Cu–PLH complex was previously explained by the participation of the amine nitrogen in the Cu coordination.^{167,168} Furthermore, the amide group absorption in the UV domain could not be observed since it was overlapped by the MLCT band occurring in the same spectral region and no information about the protonation state of the amide group could directly be extracted. On the other hand, the observed MLCT band shifts to a higher wavelength upon pD increase

(data not shown). The maximum of this band is observed at 391 nm for the sample at pD 9.5 indicating that the amine nitrogen is involved in the coordination. This band position was previously observed for synthetic peptides used as Cu ligands and studied by circular dichroism.¹⁶⁹ As expected, the visible spectroscopy clearly reveals that a comparable behavior is observed for Im and PLH in the presence of Cu in function of pH.

3.1.1.3. FTIR spectroscopy of the Cu–imidazole complexes

Prior to the characterization of the Cu–PLH complexes the spectra of deuterated Im (Im–D₄) in the MIR spectral domains in presence and absence of Cu²⁺ have been recorded (**Figure 3.1.3**).

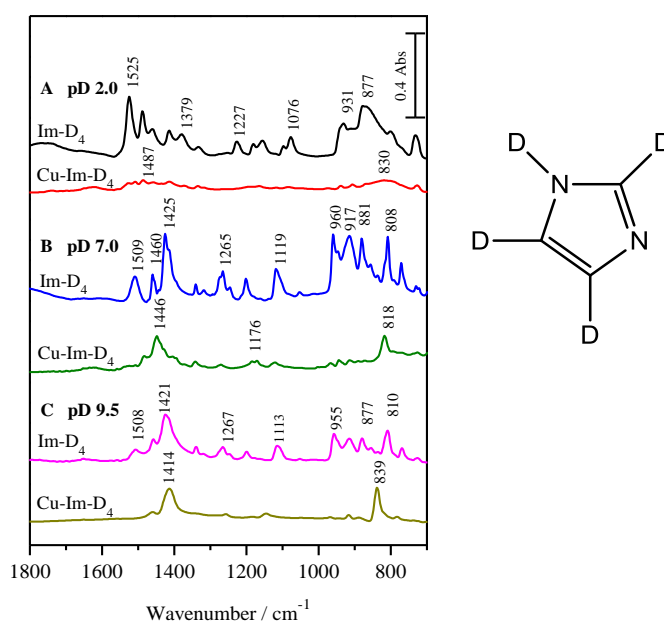


Figure 3.1.3. MIR spectra of the Im and Cu–Im–D₄ complexes. (A) at pD 2.0, (B) at pD 7.0 and (C) at pD 9.5. The right panel shows the chemical structure of the Im–D₄.

At pD 2.0 (**Figure 3.1.3A**), no coordination could be observed since the Im ring is deuterated; however the Im–D₄ spectrum was largely affected upon the addition of Cu; Only three broad bands, centered at 1618, 1487 and 830 cm⁻¹, were discernable and most of the bands lost intensities. This is interesting since the Im molecules are protonated and no coordination sites are available. According to data obtained in the visible spectral range (see **Figure 3.1.2**), the Cu²⁺ ions are coordinated by D₂O molecules at pD 2.0. It was previously described, that the Cu–N complexation does not occur below pH 3.0.^{167,169,170} The modifications in the spectra upon Cu addition at low pD/pH could be explained by the interactions between chloride anions (CuCl₂) and the positively charged Im ring. In line with these observations we note

that chloride anions have been found to be bound to the protonated imidazole from PLH in HCl solution.¹⁷¹ The effect could indeed be reversed with control experiments with CuSO₄ (**Figure 3.1.4**). The vibrations summarized in the **Table 3.1-1** for the Cu–Im sample at pD 2.0 are thus exclusively assigned to metal–free Im.

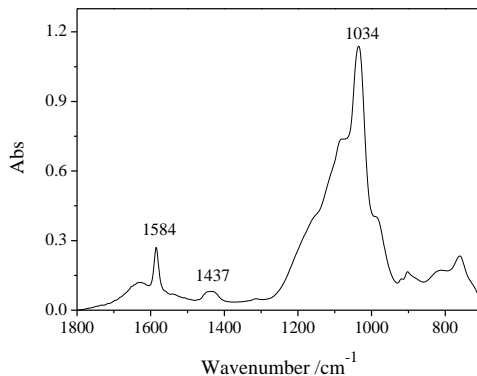


Figure 3.1.4. MIR spectrum of the CuSO₄–Im–H₄ sample recorded at pH 2.0.

The deuterated Im data at neutral pD (**Figure 3.1.3B**), obtained in the absence of Cu, showed new bands in direct comparison to pD 2.0 and some signals were shifted to lower wavenumbers. The band appearing at 1509 cm⁻¹ could be assigned to a $\nu(\text{C}_4=\text{C}_5)$ vibration.¹⁶⁸ The band that appeared at 1458 cm⁻¹ for the metal–free Im in acidic media was shifted to higher wavenumbers in neutral media. This band could be assigned to ring motion vibrations, more specifically the $\nu(\text{N}^\pi\text{--C}_2)$ vibration coupled to the $\delta(\text{C}_2\text{--D})$ vibration of the N^ε–deuterated Im.¹⁷² The sharp band at 1425 cm⁻¹ could be assigned to $\nu(\text{ring})$ vibration coupled to the $\delta(\text{N--D})$ vibration.¹⁷³

At 1265 cm⁻¹, a new band appeared that may be assigned to $\nu(\text{N}^\epsilon\text{--C}_4)$ vibration or $\nu(\text{C}_5\text{--N}^\pi)$ motions rising from N^ε–deuterated Im.^{173,174} The band observed at 881 cm⁻¹ could be assigned to the $\delta(\text{N--D})$ coupled to the $\delta(\text{ring})$ vibration¹⁷² and the signal appearing at 808 cm⁻¹ to the $\gamma(\text{N}^\pi\text{--D})$ vibration.¹⁷³ On the basis of the signals observed for the Im ring and as previously reported for solid state experiments,¹⁷³ indeed, the Im is deuterated only on the N^π site.

Upon Cu addition, significant changes are seen for the samples at pD 7 (**Figure 3.1.3B**). The sharp band at 1425 cm⁻¹ upshifts and gains intensity. A shoulder appeared at 1405 cm⁻¹ and another weak band appeared at 1393 cm⁻¹. Those two bands can arise from the Cu–N^π–D–Im complex.¹⁷⁵ The $\gamma(\text{N}^\pi\text{--D})$ vibration shifts from 808 to 818 cm⁻¹ upon Cu binding. This behavior indicated that the Cu is bound to the Im ring via the N^π atom while N^ε is deuterated.¹⁷⁵ This spectrum allows us to conclude that Im can coordinate the Cu by N^π while N^ε is deuterated (for detailed band assignments see **Table 3.1-1**).

At pD 9.5, the spectrum of Im is comparable to that at pD 7.0 indicating that the Im form at both pD values are comparable. In other words, the dominating form is the N^{ϵ} -deuterated form. The data obtained at pD 9.5 (**Figure 3.1.3C**) showed that the coordination mode is similar to that observed at pD 7.0. On the other hand, the same characteristic bands of the deprotonated Im ring appeared, leading to conclude that the addition of Cu^{2+} induces the deprotonation of few percents of the Im despite the relatively high pK_a of the Im ring.¹⁷⁰ The marker bands of the Im- D_4 deprotonation are observed at 1414 cm^{-1} and 839 cm^{-1} . The first one could be assigned to the $\nu(N^{\epsilon}-C_2)$ vibration of the imidazolate form. The latter one could be assigned to $\delta(\text{ring})$ vibration. Compared to its position at neutral and acidic pD, this vibration is upshifted by about 20 cm^{-1} probably because of symmetry changes upon deprotonation.

The FIR absorption spectra of the Im- D_4 and Cu-Im samples at pD 2.0 (**Figure 3.1.5A**) show, in contrast to the MIR, that the bands seem to lose intensity upon Cu addition. Since the study was performed with dried films, no clear statements about the intensities are possible. The $\gamma(N^{\pi}-D)$ or $(N^{\epsilon}-D)$ vibrations of the positively charged Im seen at 521 cm^{-1} ¹⁷² were found upshifted to 526 cm^{-1} and with smaller intensity. The weak band appearing from Im ring motions was seen at 307 cm^{-1} .

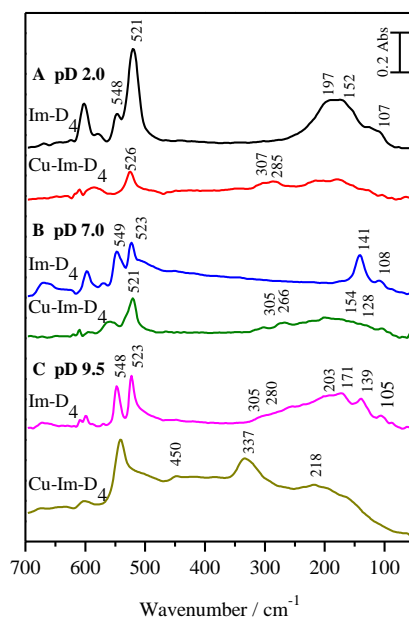


Figure 3.1.5. FIR absorbance spectra of the free and Cu-bound deuterated Im. (A) at pD 2.0, (B) at pD 7.0 and (C) at pD 9.5.

Upon Cu addition, a band appeared at 285 cm^{-1} . This band mainly includes contributions from the Im ring motions¹⁷², but also contributions from $\nu(\text{Cu}-\text{Cl})$ vibrations.¹⁶⁰ The replacement of CuCl_2 by CuSO_4 makes this signal disappears, thus confirming the origin of this vibration.

The spectrum of Im shows a broad band below 250 cm^{-1} and could be rising mainly from hydrogen bonding vibrations, breathing or doming modes (See ref. ¹⁶⁶ and references therein). Upon Cu addition the spectra show that the broad band typical of the hydrogen bonding structure disappears. In the control experiment where CuCl_2 was replaced by CuSO_4 , the broad band did not disappear. This behavior could indicate that CuCl_2 addition leads to the breaking of the hydrogen bonds between Im molecules by creating new bonds between chloride anions and the positively charged Im.¹⁷¹ As expected, vibrations arising from Cu–Im complex are not observed at pD 2.0 (for band assignments see **Table 3.1-1**).

In the Cu–Im spectrum observed for pD 7.0 (**Figure 3.1.5B**) the $\gamma(\text{Cu–Im})$ vibration of the $\text{Cu–N}^{\text{E}}\text{–Im}$ complex was found at 266 cm^{-1} .¹⁷⁵ The $\nu(\text{Cu–N})$ vibration coupled with $\nu(\text{Cu–Cl})$ motion may also contribute to this band.¹⁷⁶ Below 250 cm^{-1} the spectrum was affected by Cu addition and new bands appeared, such as the ones at 154 and 128 cm^{-1} . At 154 cm^{-1} the $\delta_{\text{def}}(\text{Cu–Im})$ of N^{π} –complex and the $\gamma(\text{Cu–Im})$ vibrational modes of the N_3 complex have been reported in a theoretical approach.¹⁷⁵ At 128 cm^{-1} The $\gamma(\text{Cu–Im})$ vibration of the N^{π} –complex and the $\delta_{\text{def}}(\text{Cu–Im})$ vibration of the N^{E} complex have been assigned on the same basis.¹⁷⁵ It should be noted that the signals below 250 cm^{-1} are weak and may be covered by the broad hydrogen bonding and respiration features. It should be noted that in this region, the signal are influenced by the salt polarizability.

At pD 9.5 (**Figure 3.1.5C**) the band at 523 cm^{-1} which was assigned above to wagging vibrations of N–D moieties disappeared indicating the presence of the negatively charged Im. The Cu coordination induced a deprotonation of the Im molecule at this pD value. The band at 450 cm^{-1} could be assigned to $\nu(\text{Cu–N})$ vibration.¹⁶⁰ A new intense band was found at 337 cm^{-1} and could be assigned to $\delta(\text{N–Cu–N})$ vibration.¹⁷⁶ The intensity directly depends on the CuCl_2 concentration and the involvement of Cu–Cl vibrations at this position is likely. In the control experiment with CuSO_4 the signal at 337 cm^{-1} was absent, while new signals were evident confirming that the origin of this vibration is the Cu–Cl bond (**Figure 3.1.6**).

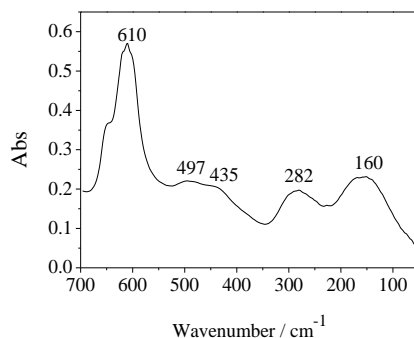


Figure 3.1.6. FIR spectrum of the Cu–Im– H_4 complex at pH 7.0.

In the data shown in **Figure 3.1.5C**, further new bands were seen below 250 cm^{-1} in the presence of Cu, namely at 197, 162, 146 and 128 cm^{-1} . Those bands could be arising from the Cu-Im complex where the Im ring is totally deprotonated. The signals and their shifts seen in the FIR due to Cu coordination in D_2O and H_2O are presented in **Table 3.1-1**. At neutral pH (D), only the vibration at 154 cm^{-1} remained in the same position and at pH (D) 9.5 the vibration at 128 cm^{-1} was only slightly affected.

Frequency (cm^{-1})						Assignments
pD 2.0		pD 7.0		pD 9.5		
Im-D ₄	Cu-ImD ₂	Im-D ₄	Cu-ImD ₂	Im-D ₄	Cu-ImD ₂	
1618	1618					$\nu(\text{C}_4=\text{C}_5)$
1525	1511					$\nu(\text{Ring})$
		1509	1497	1508		$\nu(\text{C}_4=\text{C}_5)$
	1458	1460		1421		$\nu(\text{N}^\pi-\text{C}_2) + \delta(\text{C}_2-\text{D})$
1446						$\nu(\text{N}^\epsilon-\text{C}_4)$
		1425	1425			$\nu(\text{Ring}) + \delta(\text{N}-\text{D})$
					1414	$\nu(\text{N}^\epsilon-\text{C}_2)$
			1405			$\nu(\text{N}^\epsilon-\text{C}_2) / \delta(\text{C}_2-\text{D})$
			1393			$\nu(\text{N}^\epsilon-\text{C}_2)$
	1372					$\nu(\text{C}_2\text{N}^\pi) / \nu(\text{N}^\pi\text{C}_4)$
		1265	1265	1267		$\nu(\text{N}^\pi-\text{C}_4) / \nu(\text{C}_5-\text{N}^\epsilon)$
1227		1119	1119	1113		$\delta(\text{C}_2-\text{D})$
1099						$\nu(=\text{C}-\text{N}) / \delta(=\text{C}-\text{N}^\pi)$
		960				$\nu(\text{Ring})$
				955		$\delta(\text{Ring}) + \nu(\text{N}^\pi-\text{C}_4)$
931		945			839	$\delta(\text{Ring})$
		917				$\delta_{\text{def}}(\text{C}_5-\text{D})$
877 br		881				$\delta(\text{N}-\text{D}) + \delta(\text{Ring}) /$ $\delta(\text{C}_5-\text{D})$
		808	818	810		$\gamma(\text{N}^\epsilon-\text{D})$
521	526			523		$\gamma(\text{N}-\text{D})$
			266		197	$\gamma(\text{Cu}-\text{Im})$
					162	$\gamma(\text{Cu}-\text{Im}) / \delta_{\text{def}}(\text{Cu}-\text{Im})$
			154		146	$\gamma(\text{Cu}-\text{Im}) / \delta_{\text{def}}(\text{Cu}-\text{Im})$
			128		128	$\gamma(\text{Cu}-\text{Im}) / \delta_{\text{def}}(\text{Cu}-\text{Im})$

Table 3.1-1. Detailed band assignments of the free deuterated Im and the Cu-bound deuterated Im at pD 2.0, 7.0 and 9.5.

3.1.1.4. FTIR spectroscopy of the Cu–PLH complexes

The FTIR signals of the PLH and Cu–PLH complexes can be separated into three categories, i.e. backbone signals, Im ring signals and metal–ligand signals.

- Backbone signals:

At pD 2.0 (**Figure 3.1.7A**), the amide I band at around 1650 cm^{-1} indicated an important α -helical contribution. The so-called amide II' band at 1433 cm^{-1} , that includes the CN vibrations, was found unperturbed upon Cu addition. The $\delta(\text{N-D})$ vibration appeared at 1082 cm^{-1} . The amide III $\delta(\text{N-D}) + \nu(\text{C-N})$ vibration exhibited a downshift from 1258 to 1244 cm^{-1} upon Cu addition. This downshift could be explained by variations of the secondary structure.^{141,143}

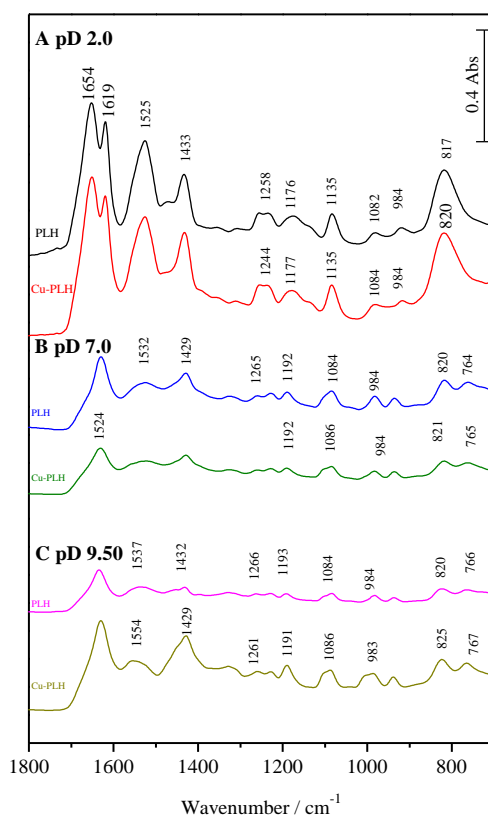


Figure 3.1.7. MIR spectra of the PLH and Cu–PLH complexes. (A) at pD 2.0, (B) at pD 7.0 and (C) at pD 9.5.

At pD 7.0 (**Figure 3.1.7B**), the amide I' band of PLH appeared at around 1630 cm^{-1} and the adopted conformation became mainly β -sheet (66%), α -helix (28%) with a small contribution of turns (6%) in direct comparison of pD 2.0 and pD 7.0. The Cu addition modified the adopted secondary structure and 15% of it became random coils, while 59% remained in the β -sheet conformation.

At pD 9.5 (**Figure 3.1.7C**) the amide I' band of PLH appeared at around 1634 cm^{-1} reflecting a β -sheet conformation. At this pD value, the relative contribution of β -sheet elements of 97% was found reduced to 87% upon Cu addition and 13% of turns became observable. The band appearing at 1537 cm^{-1} could be assigned to a fraction of unexchanged backbone protons leading to a residual amide II band.

- Imidazole ring:

The $\nu(\text{C}_4=\text{C}_5)$ vibrations of the deuterated Im ring (ImD_2^+) at pD 2.0, are seen as a sharp band at 1619 cm^{-1} .¹⁷⁷ This signal includes the antisymmetric bending vibration of the NH_3^+ group as well.¹⁷⁰ In agreement with previously published results this band disappears in neutral or basic media.⁹⁷ For pD 9.5 (**Figure 3.1.7C**) the assignment of the broad band at 1537 cm^{-1} to the $\nu(\text{C}_4=\text{C}_5)$ vibrational mode of the Im in both tautomeric forms was suggested according to Hasegawa *et al.*¹⁷² The shoulder at 1138 cm^{-1} was most likely arising from $\nu(\text{ring})$ vibration of the positively charged Im ring, this signal not being observable at pD 7.0 and 9.5 (For detailed band assignments see **Table 3.1-2**). The signal observed at 1082 cm^{-1} was probably arising from the ring motions coupled to the $\gamma(\text{N}^\pi\text{-D})$. This signal splits into two bands, namely at 1084 and 1103 cm^{-1} at pD 7.0 and 9.5 thus, indicating that both tautomeric forms are present at pD 7.0 and pD 9.5.¹⁷⁰

It is known that at pD 7.0 (**Figure 3.1.7B**), His can adopt 3 different tautomers and $\text{ND}^+\text{-N}$ crosslink the ring.¹⁷⁰ These tautomerisms lead to a broad band, seen at 1532 cm^{-1} in our measurements. It is possible that this signal may be partially covered by the amide II vibration seen at the same position. The band appearing at 765 cm^{-1} could be assigned to the $\delta(\text{ring})$ vibration.¹⁷³ Also for PLH no coordination effects were observed at a value of pD 2.0 and 7.0 (**Figure 3.1.7A, B**). At pD 9.5 (**Figure 3.1.7C**), the presence of Cu cations may have led to a deprotonation of the Im ring. The $\nu(\text{C}_4=\text{C}_5)$ vibration observed for N^ϵ coordinating the Cu of Cu-PLH complex, is observed at 1554 cm^{-1} .¹⁷⁵ An intense band appeared at 1429 cm^{-1} and signals observed in this domain were assigned to the $\nu(\text{C}=\text{O}) + \nu(\text{C}-\text{N}^-)$ vibrations of deprotonated amide groups.¹⁷⁴ Contributions from the amide II' band $\delta(\text{N}-\text{D})$ usually occur at this position. In addition, the vibration arising from Cu-Im complex was calculated at 1427 cm^{-1} and it is assigned to a vibration from Cu-Im complex, where N^ϵ is coordinating the Cu.¹⁷⁰ The Cu addition slightly modified the spectrum and a shoulder appeared at 1009 cm^{-1} , that could be directly related to the Cu coordination at this pD value. This signal was previously reported for data from L-His at pH 14 arising from the $\nu(\text{C}-\text{N})$ side chain¹⁷⁰ and seems characteristic for the N^ϵ -complex.¹⁷⁵ This observation led us to conclude that the

nitrogen atoms of the backbone participate in the Cu coordination in line with the data from the visible spectra (See Figure 3.1.2B). We note that no new bands appeared upon the Cu addition in the MIR spectral range. (For detailed band assignments see Table 3.1-2).

Frequency (cm ⁻¹)						Assignments
pD 2.0		pD 7.0		pD 9.5		
PLH	Cu-PLH	PLH	Cu-PLH	PLH	Cu-PLH	
1654	1650	1630	1632	1634	1632	Amide I
1619	1619					$\nu(\text{C}_4=\text{C}_5)$
1525	1525	1537	1532	1537	1554	Amide II / $\nu(\text{C}_4=\text{C}_5)$
1433	1430	1429	1427	1432	1429	Amide II'
1258	1244	1260	1264	1266	1261	Amide III'
1178	1177	1192	1192	1193	1191	$\nu(\text{C-N}) + \nu(\text{C-D})$
1138	1135					$\nu(\text{Ring})$
1082	1084	1084	1086	1084	1086	$\delta(\text{N-D}) / \gamma(\text{N}^\pi\text{-D})$ + Ring motions
984	984	984	984	984	983	$\delta(\text{Ring})$
917	919	935	935	939	939	$\delta_{\text{ip}}(\text{C-D})$
817	820	821	820	820	825	$\delta(\text{Ring})$
		764	765	766	767	$\delta(\text{ring})$
621	621	621		619		$\delta(\text{Ring})$
550	544	557	561	560	553	Amide IV'
524	517	530	536	545	537	Amide VI'
329	307					Amide VII'
					313	$\nu(\text{Cu}_2\text{-Im}^-) /$ $\delta(\text{N-Cu-N})$
299	285					Amide VII'
		278			276	$\tau(\text{Ring})$
			268			$\gamma(\text{Cu-Im})$
					162	$\gamma(\text{Cu-Im}^-)$
			154			$\gamma(\text{Cu-Im}) /$ $\delta_{\text{def}}(\text{Cu-Im})$
152	154					H-Bonds $\gamma(\text{Cu-Im}) /$ $\delta_{\text{def}}(\text{Cu-Im})$
			128			

Table 3.1-2. Detailed band assignments of the free PLH and the Cu-bound PLH at pD 2.0, 7.0 and 9.5.

The FIR spectra of the PLH and Cu-PLH complexes are presented in **Figure 3.1.8**. Below 250 cm⁻¹ hydrogen bonding vibrations, the so-called connectivity band^{178,179} and the amide

VII' band $\tau(\text{CONH})^{141}$ are expected. Signals due to the backbone, imidazole ring and metal–ligand vibrations will be discussed separately (**Table 3.1-2**).

The broad feature centered at 152 cm^{-1} may tentatively be assigned to the hydrogen bonding structures.¹⁸⁰

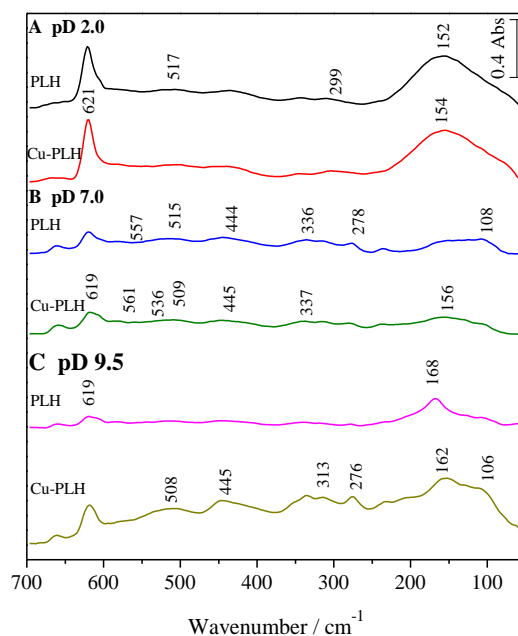


Figure 3.1.8. FIR absorbance spectra of the PLH and Cu–bound PLH. (A) at pD 2.0, (B) at pD 7.0 and (C) at pD 9.5.

At pD 2.0 the $\delta(\text{ring})$ vibration is observed at 621 cm^{-1} as a sharp band in spectra of PLH and Cu–PLH. Skeletal torsion vibrations are observed at two distinct positions, namely 299 and 328 cm^{-1} . The CuCl_2 addition led to a downshift of these two bands to 285 and 307 cm^{-1} respectively. At pD 7.0, the band intensities became smaller. The $\tau(\text{ring})$ vibration appearing at 278 cm^{-1} disappears upon Cu addition and a new band appears at 268 cm^{-1} . The $\gamma(\text{N}^\pi\text{--D})$ vibration appears at 515 cm^{-1} for the PLH and shifts to 509 cm^{-1} upon Cu addition. At pD 9.5 (**Figure 3.1.8C**), the $\delta(\text{ring})$ vibration at 619 cm^{-1} and the tentatively assigned Cu–Cl vibration at 337 cm^{-1} gain intensity upon Cu addition.

- Metal–ligands:

At pD 7.0 (**Figure 3.1.8B**), the band appearing at 268 cm^{-1} is assigned to $\gamma(\text{Cu–Im})$ vibration of the $\text{Cu–N}^\epsilon\text{–Im}$ complex.¹⁷⁵ The maximum of the broad feature below 250 cm^{-1} upshifts in the presence of Cu. The band at 154 cm^{-1} could be assigned to $\delta_{\text{def}}(\text{Cu–Im})$ vibration of the Cu–N^π complex or $\gamma(\text{Cu–Im})$ vibration of the Cu–N^ϵ complex. Furthermore, another new band appears at 128 cm^{-1} indicating a $\gamma(\text{Cu–Im})$ vibration of the Cu–N^π complex or the $\delta_{\text{def}}(\text{Cu–Im})$ vibration of the Cu–N^ϵ complex.

At pD 9.5 (**Figure 3.1.8C**), contributions from the $\nu(\text{Cu-N})$ vibrations appearing at 445 cm^{-1} may be involved despite the fact that the band was also observed for the sample lacking the Cu, as previously described by Torreggiani *et al.* for the Cu-Histamine complex at pH 9.0.¹⁶⁰ The approach of Hasegawa *et al.*,¹⁷⁵ however, concluded that no Cu-N vibrations could be expected in the region of 450 cm^{-1} . We suggest that this vibration rises from Cu-N vibration where the backbone nitrogen is the binding partner. This suggestion is in line with the results obtained from the visible spectrum of the Cu-PLH complex.

A new band is observed at 313 cm^{-1} and could be assigned to $\nu(2\text{Cu-Im}^-)$ vibration with the Cu cations coordinated to both nitrogen atoms of negatively charged Im ring.¹⁷⁵ Furthermore, the $\gamma(\text{Cu-Im}^-)$ vibration is tentatively attributed to the signal at 162 cm^{-1} .¹⁷⁵

3.1.1.5. Conclusion

The coordination sites within Cu-imidazole and PLH complexes have been characterized by means of an infrared spectroscopic approach in the MIR and FIR domains. Data recorded in the MIR domain indicate a higher variety of Cu-complexes possible for Im and for PLH. At pH (D) 7.0, the N^π atom, both, in Im and in PLH was found protonated. According to the MIR data, the Cu can be coordinated by one of the two nitrogen atoms of the Im ring and on the basis of the FIR the coordination with the N^ϵ atom was found to be likely. At pH (D) 9.5, the Cu addition leads to a complete deprotonation of the Im ring. At this level, both nitrogen atoms became available for the Cu coordination. The same interaction principle was observed for the PLH samples. The coordination of the Cu may include two nitrogen atoms of one His residue, two His residues or two His residues from neighboring PLH chains. Besides the Im ring nitrogen atoms, the visible and FIR spectroscopic studies revealed that the amine nitrogen atom of the backbone deprotonates at pD 9.5 and contributes to the Cu coordination. Interestingly the Cu coordination changes the secondary structure of the PLH as well as the so-called hydrogen bonding features in the FIR.

The characterization of Cu-PLH complexes in the FIR domain showed that new signals appear at 313 , 162 , 154 and 128 cm^{-1} upon Cu addition. These bands have been tentatively assigned to the $\nu(\text{Cu-Im})$, $\gamma(\text{Cu-Im})$ and $\delta_{\text{def}}(\text{Cu-Im})$ vibrational modes and will be used as marker bands in future studies for the identification of the metal-ligand vibrations in the spectra of metalloproteins. Furthermore we could show how the vibrational features of the coordinated histidine change in the presence of a metal ion and summarized the data in the

tables. This information is important for the analysis of, for example, reaction-induced data that is often performed by direct comparison to the isolated amino acid or polyamino acid.

3.1.2. The copper coordination by amyloid–beta 16

3.1.2.1. Introduction

Alzheimer is one of the several neurodegenerative diseases caused by protein aggregation where extra- and intracellular aggregates are involved.⁴⁸ The deposition of these aggregates leads to progressive loss of memory and altered behaviors. The intracellular aggregates are constituted by the microtubule-associated protein tau, also called neurofibrillary tangles while the extracellular aggregates are mainly constituted by A β peptide plaques^{48,181} (Figure 3.1.9).

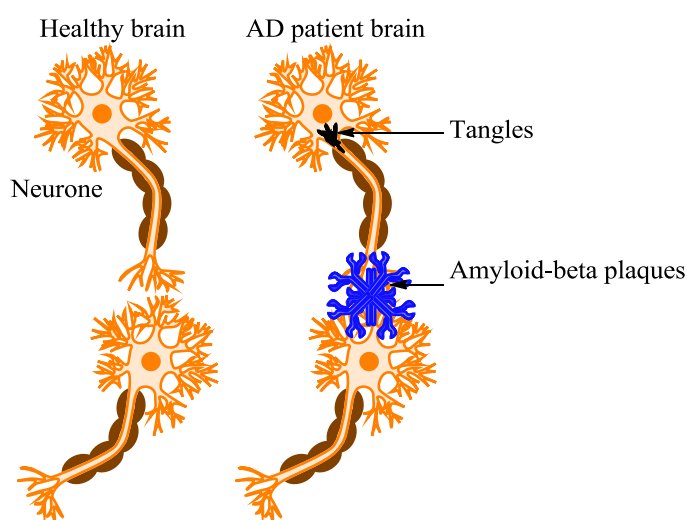


Figure 3.1.9. Schematic presentation of the healthy brain neurons and AD patient brain. The tangles are colored in black and the A β are colored in blue.

The A β peptides are produced in both, healthy brains as well as in Alzheimer's brain patients. The A β peptides carry this name for their β -sheet conformation, they aggregate as random coils. The neurotoxicity of the A β aggregates is related to the ROS production following the coordination of redox active transition metals such as Cu²⁺ and less frequently Fe³⁺. The coordination of Zn²⁺ leads to the aggregation of the A β peptides without inducing ROS production.^{50,181} The toxicity of Zn cations is not clear; it is probably related to different structures of the aggregates. In absence of metal ions A β aggregates form a monomer with a β -sheet structure. The coordination of Cu or Zn ions modifies the conformation of the A β , thus, the aggregation mode. The formation of A β oligomers can be catalyzed by the binding of Cu²⁺ through Tyr radicals chemistry.¹⁸² The deposited plaques are constituted of A β peptides of 39-43 amino acids long peptides. An increased ratio of A β 42/A β 40 is associated with the

development of Alzheimer disease. The most common A β peptide is the so-called 1-40 A β peptide and its sequence is the following:¹⁸¹

(1) ^+H_3N -Asp-Ala-Glu-Phe-Arg-His-Asp-Ser-Gly-Tyr-Glu-Val-His-His-Gln-Lys-Leu-Val-Phe-Phe-Ala-Glu-Asp-Val-Gly-Ser-Asn-Lys-Gly-Ala-Ile-Ile-Gly-Leu-Met-Val-Gly-Gly-Val-Val-COO $^-$ (40).

A significant effort has been made in order to determine the binding properties of Cu $^{2+}$ and Zn $^{2+}$ by the A β peptide and many aspects are still discussed (reviewed in ref.¹⁸¹). On the other hand and prior to the aggregation, Cu $^{2+}$ and Zn $^{2+}$ bind to the hydrophilic N-terminal portion, the so-called A β 1-16 (underlined in the sequence above) while the hydrophobic C-terminal part of the A β (1-42) peptide contains other binding sites for Cu $^{2+}$ of a much lower affinity than the ones present in the hydrophilic part. The main role of the hydrophobic part is to promote the helix-to-sheet transition, required for the aggregation.

The coordination of Cu $^{2+}$ and Zn $^{2+}$ by the native A β 42 was investigated and the results point toward a bridging His coordination mode (His-M $^{2+}$ -His), thought to play a crucial role in the aggregation.^{183,184} The coordination of Cu $^{2+}$ by truncated A β peptides has been extensively studied (See for example ref.¹⁸⁴⁻¹⁹¹). The A β 16 binds Cu $^{2+}$ in a pH-dependent manner¹⁸⁴ and the resulting Cu $^{2+}$ complex is very dynamic. Hence, the Cu $^{2+}$ exchanges binding partners within the single A β -16 peptide and more than one complex are present at a well-defined pH value. On the other hand, one binding mode dominates the other ones.¹⁸¹ The coordination of Zn $^{2+}$ is also known to promote the A β aggregation in a pH-dependent manner, different from that of Cu $^{2+}$. In fact, the binding of Cu $^{2+}$ induces the aggregation of A β peptides in a small pH range (6-7) while the binding of Zn $^{2+}$ induces the aggregation in a wide pH range (> pH 6).^{184,192}

Recently, Dorlet *et al.* used pulse EPR spectroscopy to determine the coordination sphere of Cu $^{2+}$ by the A β -16 under physiological pH.¹⁸⁵ The specific isotopic labeling of the coordinating amino acids allowed the characterization of two Cu $^{2+}$ -A β -16 complexes, namely component I and II (**Figure 3.1.10**). In the component I (pH 6.50), the Cu $^{2+}$ is coordinated by two His residues in the equatorial positions (His6 and His13 or His14), the backbone carbonyl of Ala2 as well as the NH $_2$ terminus Asp1. The carboxylate side chain contributes to the coordination at the axial position.

At pH 9.0 (component II), the amide nitrogen occupies an equatorial position in the binding mode of Cu $^{2+}$ and another equatorial position is occupied by the carbonyl of Ala2. The contribution of Asp1 to the coordination sphere of Cu $^{2+}$ remained the same while one His residue occupies an equatorial position instead of two for the component one.

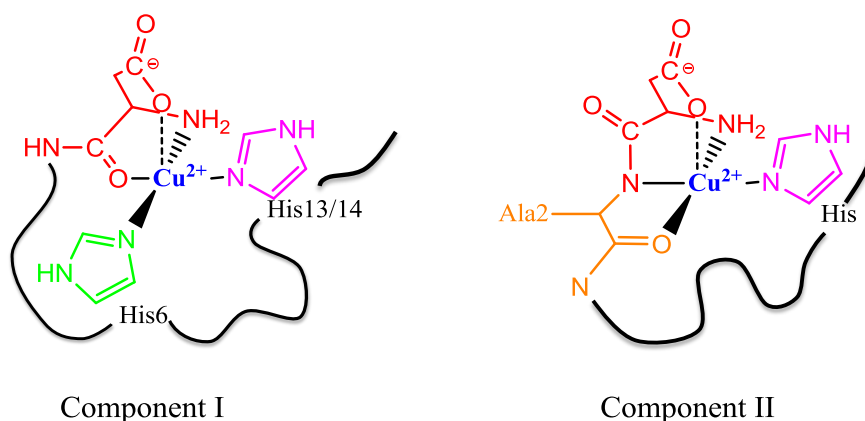


Figure 3.1.10. The coordination modes of Cu²⁺ by Aβ16 at physiological pH. Component I at pH 6.50 and component II at pH 9.0.¹⁸⁵ The coordinating Asp1 is colored in red, His are colored in green and magenta and the alanine in orange.

Pulse EPR spectroscopy suggested the coordination by the Asp1 via the NH₂ terminus and the carboxylate side chain. Furthermore, the pulse EPR data suggest the coordination by the His6 residue and either the His13 and His14. In component II, the pulse EPR spectra showed equivalent signals for all the ¹⁵N-labelled His, probably because the His are in equilibrium as ligands for Cu²⁺.¹⁸⁵ More recently, the coordination of Cu²⁺ within the component I and II was also investigated by means of EPR spectroscopy and the results are in line with those obtained by Dorlet *et al.* for the component I. On the other hand, the Aβ16 was shown to coordinate Cu²⁺ via the three His and the backbone carbonyl of the Ala2.¹⁹³

Here the FTIR spectroscopy was used in order to learn more about the coordination of Cu²⁺ within the Aβ16 at three pH values, namely pH 6.50, 9.0 and 11.0. The H-D exchange and the isotopic labeling of the His residues as well as the Asp1 were crucial for the accurate assignments of the infrared absorption bands of the free and the Cu²⁺-bound peptide. Concerning the His residues, the isotopic labeling was performed for all the nitrogen atoms, with ¹⁵N instead of ¹⁴N. Concerning the Asp1 residue, the isotopic labeling was performed for all the carbon atoms with ¹³C instead of ¹²C. In the Asp1 residue the nitrogen atoms were also labelled by replacing the ¹⁴N atoms by the ¹⁵N atoms. In a given labelled sample, only one amino acid was labelled.

The coordination of Cu⁺ is also of a great interest since the redox conversion between Cu²⁺ and Cu⁺ is suspected to produce ROS. The investigation of Cu⁺-Aβ complexes showed that the Cu⁺ was bound in a linear fashion by two His residues.^{189,194} It also seems that this binding mode is exclusive for Cu⁺ within Aβ peptides.¹⁹⁵

The electrochemical properties of Cu-Aβ complexes were previously determined and the redox potentials of these complexes were found to be in the range 181–268 mV vs.

SHE^{187,196} The effect of the electrochemical conversion within the Cu²⁺/Cu⁺ A β complexes was studied here by means of the redox induced FTIR spectroscopy at pH 6.50, 9.0 and 11.0. The unlabelled and the labelled samples were studied by ATR-FTIR spectroscopy. The spectra of the free and Cu²⁺-A β 16 dried films were recorded for pH 6.50, 9.0 and 11.0 in the infrared range 1800-700 cm⁻¹. The H-D exchange was also performed for all the samples in order to accurately assign the infrared signals.

3.1.2.2. Spectra of the A β 16 at pH 6.50

The MIR absorption spectra of the free A β 16 at pH 6.50 are presented in the **Figure 3.1.11**. The spectra were normalized to avoid the drying and the sample orientation effects on the intensities of the absorption bands.

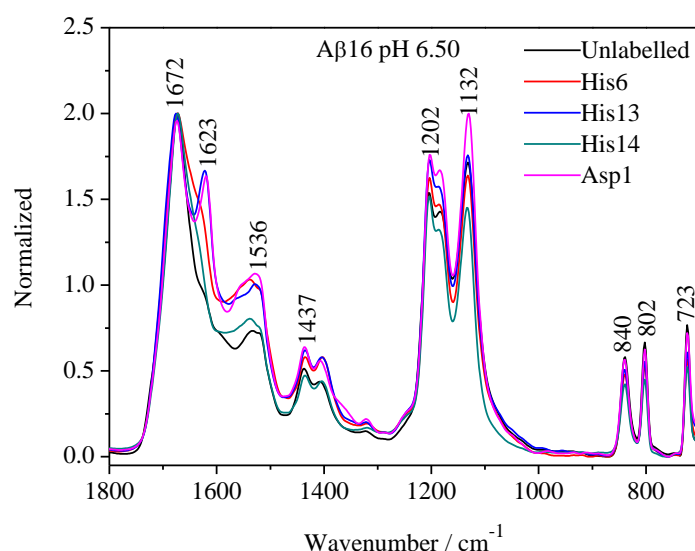


Figure 3.1.11. Global view of the spectra of the free unlabelled and isotopically labelled peptides recorded at pH 6.50 in the 1800–700 cm⁻¹ infrared range. The spectra are colored in black (unlabelled), red (H6), blue (H13), green (H14) and magenta (Asp1).

In the amide I region an intense signal can be seen at 1672 cm⁻¹ and a less intense one at 1623 cm⁻¹. The A β 16 contains one Arg residue, which would contribute in the amide I region with a high absorption coefficient at around 1675 cm⁻¹.¹⁷⁷ The latter one can be assigned to the $\nu(C_4=C_5)$ vibrations of the protonated His residues as well as to the side chain absorption of other amino acids (Tyr, Asp, Glu, Gln).¹⁷⁷ This signal is more or less intense depending on the studied sample, probably because of a different orientation on the ATR surface.

The **Figure 3.1.12** shows an enlarged view of the region between 1600 and 1200 cm⁻¹. The amide II band of the unlabelled sample appears as a broad band at 1536 cm⁻¹. The contribution of the His side chain as well as of Tyr, Asp and Glu are expected in this spectral

range. The shoulder at 1517 cm^{-1} can be assigned to the $\nu(\text{CC})$ vibrations of the Tyr ring in the neutral state (Tyr-OH).¹⁷⁷

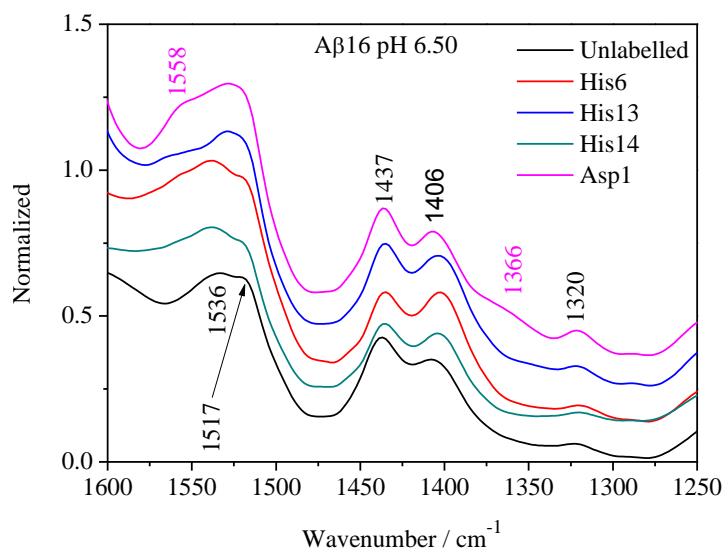


Figure 3.1.12. Enlarged view of the $1600\text{-}1200\text{ cm}^{-1}$ spectral region.

The amide II band of the ^{15}N -labelled His is larger than the one of the unlabelled sample and slightly shifted to higher wavenumbers. The upshift reflects the contribution of the $\nu(\text{C}_4=\text{C}_5)$ vibrations of the His residues to this large band. For the His13 labelled sample, the shift is more pronounced, a shoulder can be distinguished at 1566 cm^{-1} . Two signals are present in the amide II region of the ^{13}C - and ^{15}N -labelled Asp1. One signal is observed at 1558 cm^{-1} and the other one at 1525 cm^{-1} .

The $\nu(\text{COO}^-)^{\text{as}}$ vibrations of acidic residues are expected in the region $1570\text{-}1540\text{ cm}^{-1}$.¹⁷⁷ The ^{13}C -labeling of the Asp1 residue is expected to downshift the signal by about 20 cm^{-1} . Indeed, the signal appearing at 1558 cm^{-1} can be arising from the His side chain absorptions. The signal observed at 1406 cm^{-1} for the unlabelled sample remains almost in position for the ^{15}N -His labelled samples. This signal can be arising from the $\nu(\text{COO}^-)^{\text{s}}$ vibrations of acidic residues.¹⁷⁷ For the Asp1 labelled sample, the signal is still present, however an additional broad signal can be seen at 1366 cm^{-1} which can be assigned to the $\nu(\text{COO}^-)^{\text{s}}$ vibration of the Asp1 residue. The weak signal seen at 1320 cm^{-1} can be assigned to the amide III vibration. In the region below 1450 cm^{-1} the side chain absorption of His residues is expected to dominate the spectrum. Contributions from the Lys side chain are not excluded as well as from the side chain of deprotonated acidic residues. However, the signals below 1450 cm^{-1} are too intense to be assigned to the side chain absorptions alone. The A β 16 peptides are of

synthetic origin and purified by HPLC and eluted with trifluoroacetic acid (TFA). Indeed, TFA molecules can still be present in the lyophilized peptides.

The spectrum of TFA has been recorded in order to see if it contributes to the spectra of the A β 16 and unfortunately the spectrum showed that the studied spectral range is dominated by the high absorption of TFA (**Figure 3.1.13**).

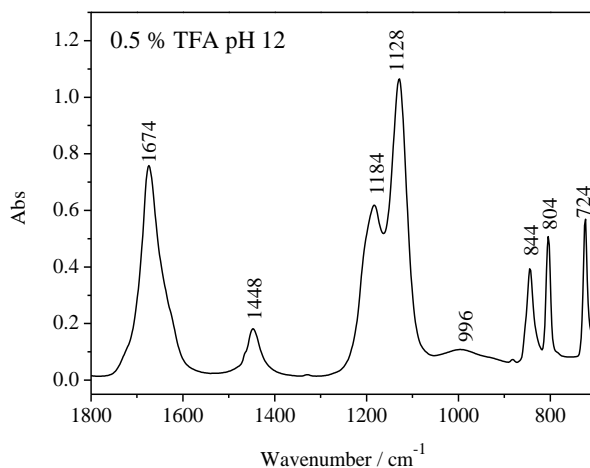


Figure 3.1.13. Spectrum of 0.5 % w/v of TFA at pH 12 recorded in the region 1800–700 cm^{-1} .

The amide I band overlaps with an intense absorption of TFA, hence the secondary structure modifications upon copper binding cannot be discussed based on the amide I shifts. Furthermore, the region specific of the His side chain absorptions is masked by the TFA signals. This is the reason why the analysis of the FTIR data is focused on the amide II region and the region between 1400 and 1200 cm^{-1} . The broad band of TFA centered at 996 cm^{-1} does not affect the analysis of the data in the spectral region around 1000 cm^{-1} . On the other hand, the signals arising from the peptide are too weak. Because of the signals arising from TFA below 900 cm^{-1} the spectra of the peptides are limited to the spectral region 1800–900 cm^{-1} . The overview of the band assignments in the free peptides is presented in the **Table 3.1-3**. This table also includes the assignments made in the later text.

Frequency (cm ⁻¹)	Assignments
1672	TFA / amide I / $\nu(\text{C}=\text{N})$ Arg
1645	Amide I
1623	$\nu(\text{C}_4=\text{C}_4)$ protonated His / $\nu(\text{NH}_3^+)^{\text{as}}$ Arg / $\nu(\text{C}=\text{C})$ Tyr—OH
1580	$\nu(\text{COO}^-)^{\text{as}}$ acidic residues / Amide II / $\nu(\text{C}_4=\text{C}_4)$ His
1536	$\nu(\text{COO}^-)^{\text{as}}$ acidic residues / Amide II
1437	TFA
1401	$\nu(\text{COO}^-)^{\text{s}}$ acidic residues
1323	Amide III / $\delta(\text{CH})$ non specific
1202	TFA
1132	TFA
1050	$\delta(\text{ring})$ N ^{π} -protonated His
1010	$\delta(\text{ring})$ N ^{ϵ} -protonated His
975	$\delta(\text{ring})$ His
840	TFA
802	TFA
723	TFA

Table 3.1-3. Detailed assignments of the free A β 16 peptides bands in the MIR. Depending on the studied samples, the band positions can be more or less shifted. For more details see text.

3.1.2.3. Spectra of the Cu²⁺-A β 16 complexes at pH 6.50

The infrared absorbance spectra of the Cu²⁺-A β 16 complexes were recorded for all the samples and the **Figure 3.1.14** shows an overview of the spectra in the infrared region 1800-700 cm⁻¹.

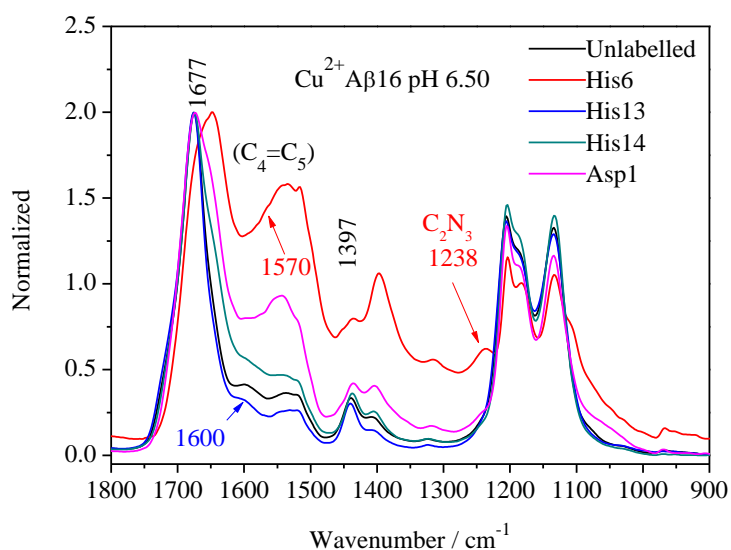


Figure 3.1.14. Global view of the spectra of the Cu²⁺-A β 16 peptides recorded at pH 6.50 in the 1800–900 cm⁻¹ infrared range.

The coordination of Cu²⁺ at pH 6.50 leads to the production of insoluble aggregates of the A β 16. Furthermore, the signals observed at 1623 cm⁻¹ for the free peptides disappear upon coordination which means that Cu²⁺ leads to the deprotonation of the His residues.

The signal appearing at 1600 cm^{-1} in the spectrum of the unlabelled, the ^{15}N -His13 and ^{15}N -His14 samples can be assigned to the $\nu(\text{C}_4=\text{C}_5)$ vibration of N^π coordinated His.¹⁷⁵ The fact that this signal is present for both H13 and H14 samples leads to conclude that this signal could be arising from one of these residues or from both residues.

The spectrum of the H6 sample shows a weak shoulder at 1570 cm^{-1} . This signal can be assigned to the N^ϵ coordinated form. The signature of the His in the amide II region shows that the coordination of Cu^{2+} by the His residues is taking place via N^π and N^ϵ . These observations are in line with the previously reported data suggesting the involvement of the N^ϵ metal binding in the aggregation of the A β peptides.¹⁸⁴

Additional signals can only be seen for the ^{15}N -His6 coordinated sample at 1238 cm^{-1} and 1103 cm^{-1} . These signals can be assigned to the $\nu(\text{C}_2\text{N}^\epsilon)$ and to the $\nu(\text{C}_5\text{N}^\pi)$ vibrations of the N^π bound His.¹⁷⁵ The spectrum of the Asp1 sample shows a band at 1547 cm^{-1} where the amide II and the $\nu(\text{COO}^-)^{\text{as}}$ vibration of acidic residues are expected. Hence, the discrimination between these two signals is not possible without the H-D exchange that is required to decouple the amide II vibration and shift it to lower frequencies.

3.1.2.4. Spectra of the A β 16 at pD 6.50

The spectra of the free A β 16 samples were recorded at pD 6.50 (**Figure 3.1.15**). In the amide I' region, two signals can be observed for the unlabelled sample at 1671 and at 1616 cm^{-1} .

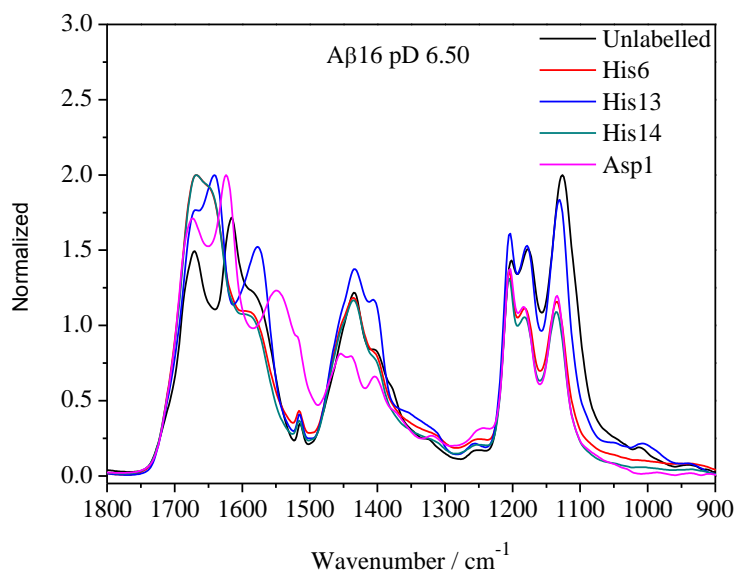


Figure 3.1.15. Global view of the spectra of the A β 16 peptides recorded at pD 6.50 in the $1800\text{--}900\text{ cm}^{-1}$ infrared range.

The first is most likely arising from the TFA absorption (**Figure 3.1.13**), the latter one can be arising from the backbone amide I' vibration as well as from the side chain absorptions of His, Tyr, Phe, Glu, Gln, or Asp. This signal is upshifted in the spectra of the isotopically labelled sample, which makes the accurate assignment of this signal difficult (**Figure 3.1.16**). The H-D exchange decouples the amide II vibration $\delta_{op}(\text{NH})$ coupled to the $\nu(\text{CN})$ vibrations which leads to a downshift from around 1550 cm^{-1} to around 1450 cm^{-1} of the $\nu(\text{CN})$ vibration (amide II') and to $1070\text{--}900\text{ cm}^{-1}$ the $\delta_{op}(\text{ND})$ vibration.¹⁹⁷ The signals appearing in the amide II' region are of higher intensities than the ones obtained before the H-D exchange. The amide II shifts allow better assigning the side chain absorptions overlapping with the amide II band in the spectra recorded at pH 6.50. The spectrum of the unlabelled sample shows a signal at 1580 cm^{-1} which is slightly shifted in the spectra of the ^{15}N -labelled His samples. The signal is downshifted to 1547 cm^{-1} in the spectrum of the ^{13}C - and ^{15}N -Asp1 labelled sample. Despite the overlapping with other vibrational modes in the spectra of the unlabelled sample and the ^{15}N -His labelled sample, this signal can be assigned to the $\nu(\text{COO}^-)^{\text{as}}$ vibration since it is downshifted upon labeling of the Asp1 residue. The Tyr residue is in the neutral form and gives rise to a signal at 1514 cm^{-1} in all the spectra of the free peptides recorded at pD 6.50. This signal is assigned to the $\nu(\text{CC})$ vibration of the Tyr ring (**Figure 3.1.16**).

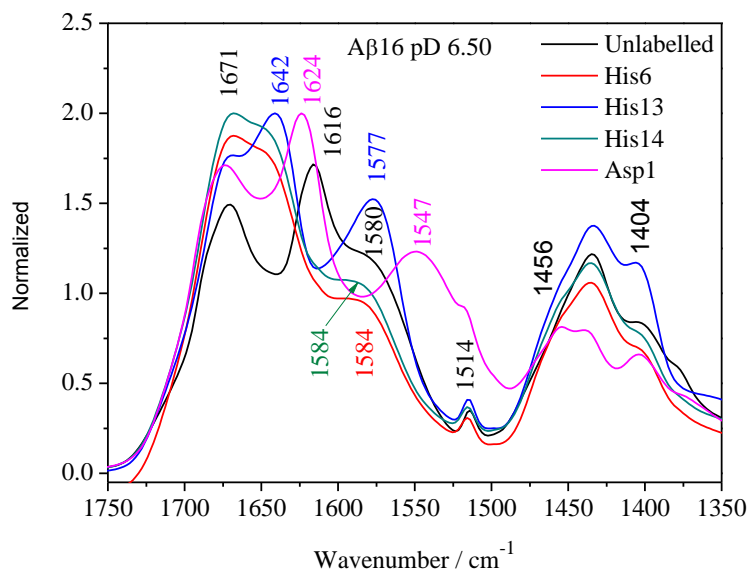


Figure 3.1.16. Enlarged view of the spectra of the A β 16 peptides recorded at pD 6.50 in the $1750\text{--}1350\text{ cm}^{-1}$ infrared range.

The signal observed at 1456 cm^{-1} can be arising from the absorption of TFA. The overlapping of the TFA absorption with other vibrational modes arising from the A β 16 peptide is not excluded. The backbone vibration of the amide II' band is expected in this region.¹⁹⁷ The signal observed at 1435 cm^{-1} is most likely arising from the aliphatic chains of several amino

acids (**Figure 3.1.16**). The weak signal observed at 1401 cm^{-1} in the spectrum of the unlabelled sample can be assigned to the $\nu(\text{COO}^-)^s$ vibration of acidic residues. A weak shoulder is detected at 1375 cm^{-1} which can be arising from the $\omega(\text{CH}_2)$ vibration of Tyr.¹⁷⁷ The intensities and the position of this signal are not conserved in all the spectra and this is probably caused by orientation and drying effects. In addition, the $\nu(^{13}\text{COO}^-)^s$ vibration of the Asp1 residue is expected in this region but the signal appearing at 1370 cm^{-1} in the spectrum of the Asp1 sample cannot be exclusively assigned to this mode since a similar feature is observed in the spectrum of the unlabelled sample.

Below 1300 cm^{-1} , the TFA absorptions predominates the spectra (**Figure 3.1.13** and **Figure 3.1.15**). Only the region around 1000 cm^{-1} can be useful to the data analysis and the weak signals appearing at 1012 cm^{-1} for the unlabelled sample can be arising from the Tyr side chain as well as from His ring motions (**Figure 3.1.17**).¹⁷⁷ On the other hand, this signal is downshifted in the spectrum of the His14 sample. Therefore this signal can be assigned to the $\delta(\text{ring})$ of the His14 residue where the N^π is protonated.

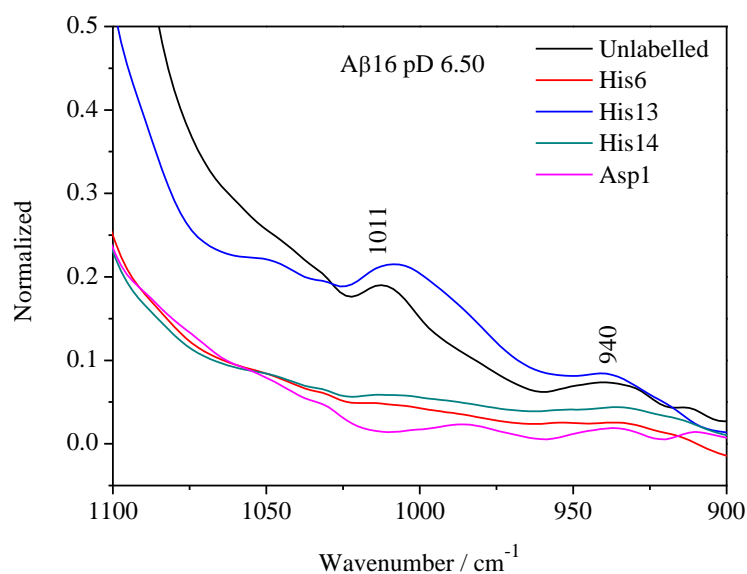


Figure 3.1.17. Enlarged view of the spectra of the Aβ16 peptides recorded at pD 6.50 in the 1100–900 cm^{-1} infrared range.

3.1.2.5. Spectra of the Cu^{2+} -Aβ16 complexes at pD 6.50

The spectra of the Cu^{2+} -Aβ16 complexes recorded in the region $1800\text{--}700\text{ cm}^{-1}$ at pD 6.50 are shown in the **Figure 3.1.18**. Two signals arise in the amide I' region, one appearing at 1673 cm^{-1} for all the samples and it is mainly arising from the absorption of TFA. The other signal appears at 1648 cm^{-1} and it can be arising from the backbone amide I' vibration as well as from the side chains absorptions of His, Tyr, Phe, Glu, Gln, or Asp.

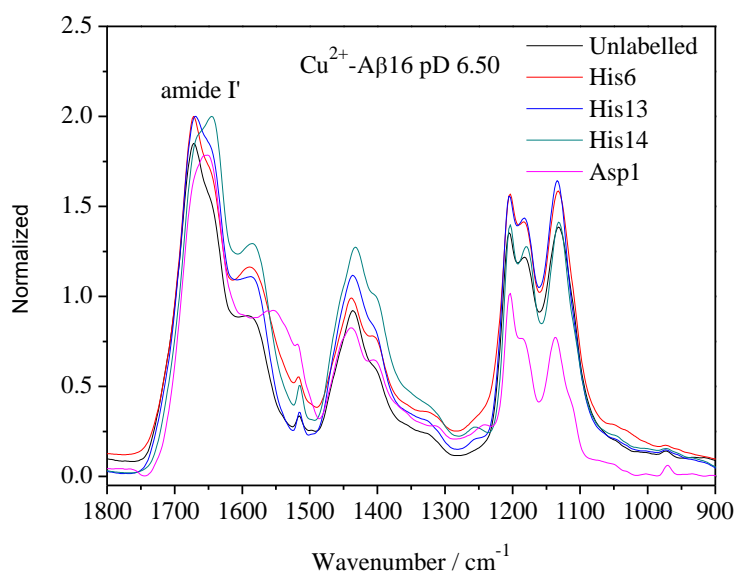


Figure 3.1.18. Global view of the spectra of the Cu^{2+} -A β 16 complexes recorded at pD 6.50 in the 1800–900 cm^{-1} infrared range.

The signal observed at 1590 cm^{-1} for the unlabelled sample remains in position of the His13 sample. On the other hand, this signal is downshifted towards 1586 cm^{-1} for the His6 and His14 samples. This signal can be assigned to the $\nu(\text{C}_4=\text{C}_5)$ vibration of the His residues (**Figure 3.1.19**).^{172,175} Compared to the free peptides, this signal upshifts upon copper coordination, indicating that the coordination by His residues takes place. The lower frequencies found for His6 and His14 indicate that these residues are bound to the copper at pD 6.50. On the other hand, the $\nu(\text{COO}^-)^{\text{as}}$ vibration occurs in the same spectral range and may overlap with the His motions. The copper binding to the carboxylate side chain of Asp1 residue can be monitored in the spectra of the free and the copper bound Asp1 sample. The signal observed at 1547 cm^{-1} in the spectrum of the free Asp1 sample was assigned to the $\nu(^{13}\text{COO}^-)^{\text{as}}$ vibration. The copper binding induces an upshift of this signal towards 1554 cm^{-1} (**Figure 3.1.19**). Indeed the coordination via the carboxylate side of the Asp1 at pD 6.50 is confirmed. Below the signature of the acidic residues, the Tyr contribution is observed at 1515 cm^{-1} . The signal appearing at 1434 cm^{-1} can be assigned to the aliphatic side chain of amino acids since it is not sensitive to the H-D exchange.

In addition to the TFA absorption bands present below 1300 cm^{-1} , the spectra of the bound peptides show a signal at 1047 cm^{-1} which is typical for N^π -deuterated His (**Figure 3.1.20**). The spectrum of the His6 sample shows an additional shoulder at 1030 cm^{-1} compared to the other spectra. Indeed, the His6 residue coordinates the copper via the N^ϵ atom while the N^π atom is deuterated. The signals seen at around 1005 cm^{-1} in the spectra of the coordinated peptides are assigned to the $\delta(\text{ring})$ vibration of the N^ϵ -protonated His.^{172,175}

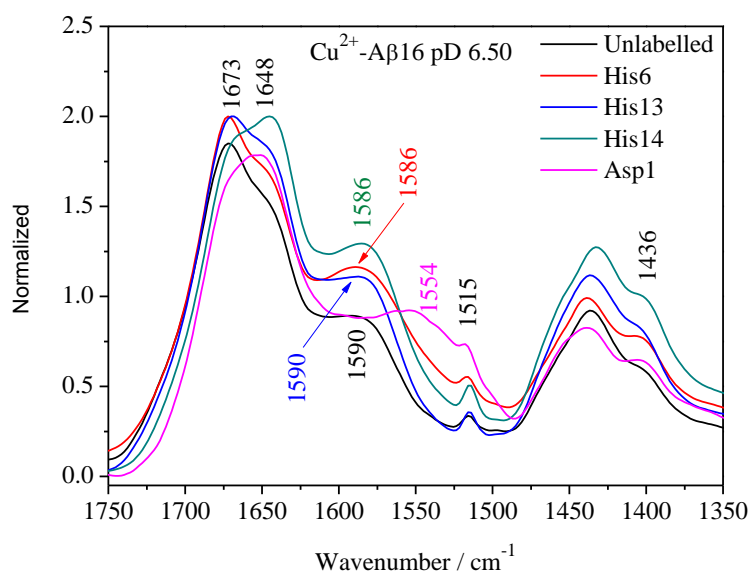


Figure 3.1.19. Enlarged view of the spectra of the Cu^{2+} -A β 16 complexes recorded at pD 6.50 in the 1750–1350 cm^{-1} infrared range.

The signal appearing at 972 cm^{-1} is present in all the spectra of the bound peptides. In addition, the isotopic labeling did not induce a shift of this signal; indeed, the signal cannot be specifically assigned to one of the three His. This signal can be assigned to the $\delta(\text{ring})$ vibration of the copper bound His where the ligation takes place via the N^{π} atom of the imidazole ring.¹⁷⁵ This observation leads us to conclude that the coordination of copper displaces the proton from the N^{π} to the N^{ϵ} atom of the coordinating His, most likely the His14 (See above).

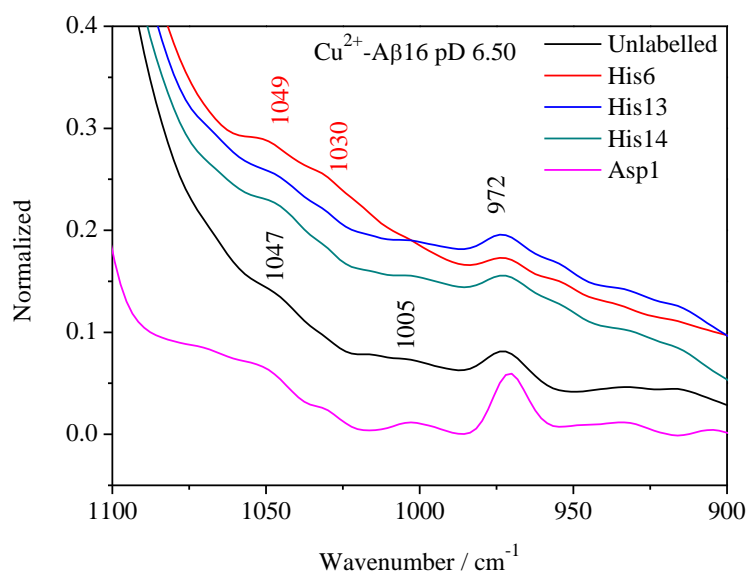


Figure 3.1.20. Enlarged view of the spectra of the Cu^{2+} -A β 16 complexes recorded at pD 6.50 in the 1100–900 cm^{-1} infrared range.

All together, the data recorded at pH/pD 6.50 allow concluding that the coordination by the carboxylate side chain of the Asp1 is taking place. The three His residues contribute to the coordination sphere of Cu; His6 coordinates via the N^ε, His13 and His14 via the N^π atoms. On the other hand, the coordination via the amine side chain of the Asp1 residue cannot be observed due to the overlapping of the amine signals with other modes of higher absorption coefficients.

It should be noted that the coordination via the N^ε of a His was previously reported to cause the aggregation of the Aβ peptides.¹⁸⁴ According to the data presented here, this coordination mode is most likely offered by the His6 residue.

3.1.2.6. Spectra of the Aβ16 at pH 9.0

The coordination of copper by the Aβ16 at pH 9.0 was recently studied by EPR spectroscopy.^{185,193} The data analysis led to controversial conclusions at the level of the nature and the number of His residues bound to copper; hence, the coordination mode at pH 9.0 is not completely elucidated.

The infrared spectra of the free Aβ16 were recorded at pH 9.0 and they are shown in Figure 3.1.21. The amide I band at 1672 cm⁻¹ overlaps with the TFA absorption. In the amide II region, two distinct signals are present in all the spectra. For the unlabelled sample, these signals occur at 1589 and 1537 cm⁻¹. The former one is too high to be arising from the amide II band. For the His labelled samples, this signal is observed at 1581, 1568 and 1575 cm⁻¹ for the His6, His13 and His14, respectively.

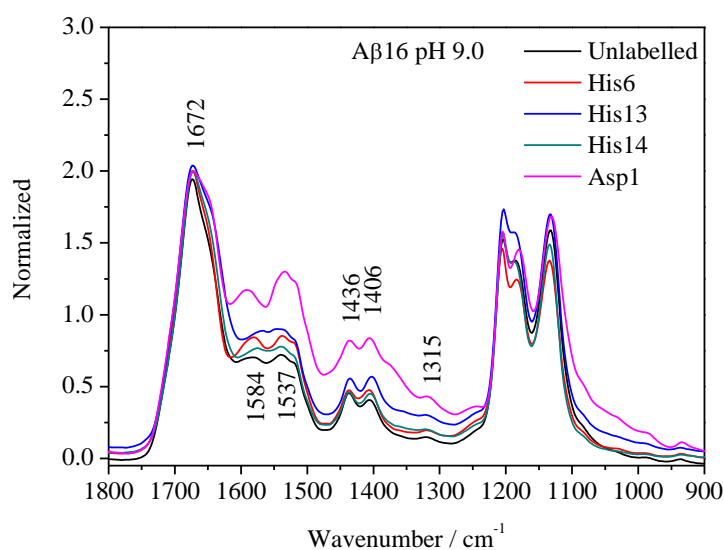


Figure 3.1.21. Global view of the spectra of the Aβ16 peptides recorded at pH 9.0 in the 1800–900 cm⁻¹ infrared range.

The downshift indicates that this signal contains the contribution of the His residues. In the spectrum of the Asp1 labelled sample, the signal appears at 1591 cm^{-1} , very close to the frequency observed in the spectrum of the unlabelled sample. Indeed, this signal can be assigned to the $\nu(\text{C}_4=\text{C}_5)$ vibration of the N^{e} protonated form of His.

The signal observed at 1537 cm^{-1} for the unlabelled sample remains almost in position in the spectra of the labelled samples except in the spectrum of the Asp1 sample where a slight downshift is observed towards 1533 cm^{-1} . Indeed this signal contains coordinates from the amide II band as well as from the $\nu(\text{COO}^-)^{\text{as}}$ vibration of the acidic residue, most likely of the Asp1 residue. The neutral Tyr (Tyr-OH) ring motion occurs at 1519 cm^{-1} in all the spectra.

Below the amide II region, the TFA contribution occurs at 1436 cm^{-1} . The signal appearing at 1406 cm^{-1} can be assigned to the $\nu(\text{COO}^-)^{\text{s}}$ vibration of acidic residue. The spectrum of the Asp1 labelled sample shows an additional shoulder at 1373 cm^{-1} compared to the other spectra. This signal can be assigned to the $\nu(^{13}\text{COO}^-)^{\text{s}}$ vibration of the Asp1 residue. The weak signal observed at 1315 cm^{-1} can be assigned to the amide III vibration. Below 1200 cm^{-1} , the TFA absorptions dominate the spectra. The region around 1000 cm^{-1} contains weak signals that can be mainly assigned to His ring motions.

3.1.2.7. Spectra of the Cu^{2+} -A β 16 complexes at pH 9.0

The coordination of copper at pH 9.0 modifies the spectra especially in the amide II region (**Figure 3.1.22**) where one band is observed instead of two in the spectra of the free A β 16.

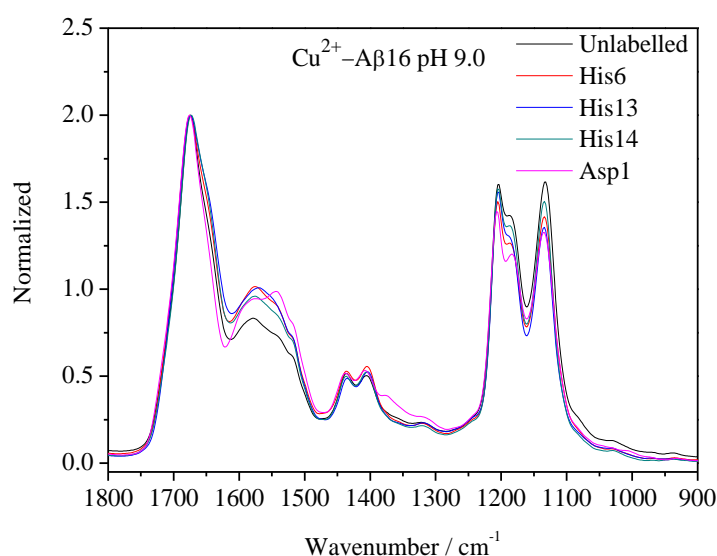


Figure 3.1.22. Global view of the spectra of the Cu^{2+} -A β 16 complexes recorded at pH 9.0 in the $1800\text{--}900\text{ cm}^{-1}$ infrared range.

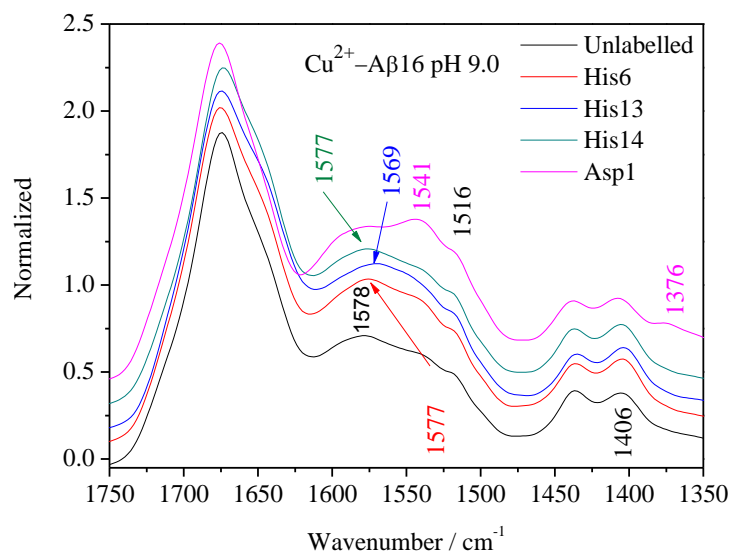


Figure 3.1.23. Enlarged view of the spectra of the Cu^{2+} -A β 16 complexes recorded at pH 9.0 in the 1750–1350 cm^{-1} infrared range.

In the spectrum of the unlabelled sample, the signal is observed at 1578 cm^{-1} and it remains almost in position in the spectra of the His6 and His14 samples. A downshift is observed for the His13 sample where the signal is observed at 1569 cm^{-1} (**Figure 3.1.23**). Compared to the spectra of the free peptides, the positions of these bands are shifted only by few wavenumbers. These slight shifts are not sufficient to conclude about which His residues are bound to the copper.

The spectrum of the Cu^{2+} -A β 16 complex obtained for the Asp1 labelled sample shows an additional shoulder compared to the other spectra which occurs at 1540 cm^{-1} . This signal can be arising from the $\nu(^{13}\text{COO}^-)^{\text{as}}$ vibrations of the Asp1 residue. On the other hand, this signal coincides with the amide II band. The signal appearing at 1406 cm^{-1} is mainly arising from the $\nu(\text{COO}^-)^{\text{s}}$ vibration of acidic residues. This signal remains in position for all the samples. The ring vibration of the neutral Tyr residue is observed at 1516 cm^{-1} . The spectrum of the Asp1 sample exhibits an additional shoulder appearing at 1376 cm^{-1} which can be assigned to the $\nu(^{13}\text{COO}^-)^{\text{s}}$ vibration (**Figure 3.1.23**). The direct comparison between the frequencies of the antisymmetric and symmetric stretching vibrations of the free and bound carboxylate side chain is a good indicator about the coordination mode of the carboxylate, which can bind the metal in a bidentate, monodentate, or in a pseudo-bridging mode. The relationship between the frequencies and the coordination modes are well documented in the milestone review by Deacon and Phillips¹⁹⁸ which can be resumed by the following:

$\Delta \nu_{\text{as-}\nu_{\text{s}}}$ (free)	>	$\Delta \nu_{\text{as-}\nu_{\text{s}}}$ (bound)	Bidentate
$\Delta \nu_{\text{as-}\nu_{\text{s}}}$ (free)	<	$\Delta \nu_{\text{as-}\nu_{\text{s}}}$ (bound)	Monodentate
$\Delta \nu_{\text{as-}\nu_{\text{s}}}$ (free)	\approx	$\Delta \nu_{\text{as-}\nu_{\text{s}}}$ (bound)	Pseudo-bridging

It should be noted that the quasi-monodentate or quasi-bidentate forms can be suggested when the difference between the Δ is greater than $\sim 20 \text{ cm}^{-1}$.

At pH 9.0, the frequencies of the free and bound carboxylate group of the Asp1 residue give the following values:

$$\Delta \nu_{\text{as-}\nu_{\text{s}}} \text{ (free)} = 1533 - 1373 = 160 \text{ cm}^{-1}$$

$$\Delta \nu_{\text{as-}\nu_{\text{s}}} \text{ (bound)} = 1541 - 1376 = 165 \text{ cm}^{-1}$$

Since the values are so close to each other, indeed the coordination mode is probably monodentate with a pseudo-bridging character.

In the region around 1000 cm^{-1} , the weak signals arising mainly from the His ring motions can be seen.

3.1.2.8. Spectra of the A β 16 at pD 9.0

The spectra recorded for the free and coordinated peptides are not enough to accurately assign the infrared signals, especially in the amide II region. Indeed, the H-D exchange is necessary to better assign the signals and hence, learn more about the copper coordination at pH 9.0. The spectra of the free A β 16 were recorded at pD 9.0 and they are shown in the **Figure 3.1.24**.

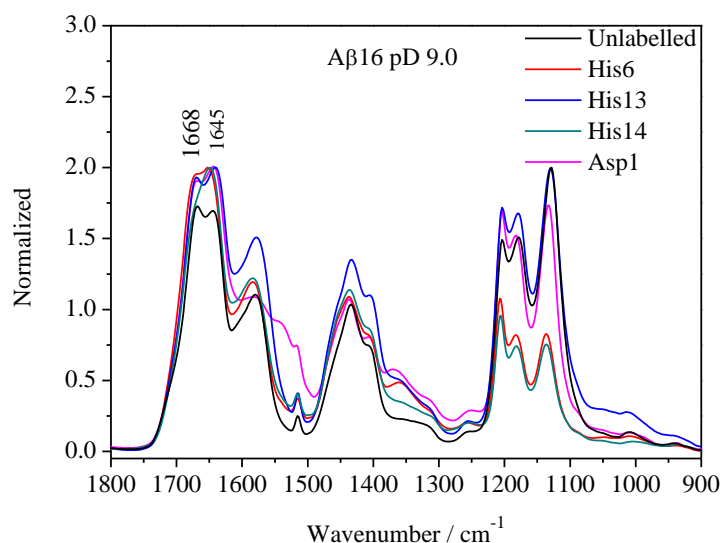


Figure 3.1.24. Global view of the spectra of the A β 16 peptides recorded at pD 9.0 in the $1800\text{--}900 \text{ cm}^{-1}$ infrared range.

In the amide I' region, the two signals appearing at 1668 and 1645 cm^{-1} for the unlabelled sample can be assigned to the TFA and the amide I' absorptions, respectively.

The region below the amide I' region contains the ring motion vibrations of the His residues as well as the antisymmetric stretching vibrations of the carboxylate groups that belongs to the acidic residues. The spectrum of the unlabelled sample shows a unique signal in this region appearing at 1580 cm^{-1} . This signal remains almost in position in all the spectra (Figure 3.1.25).

The spectrum of the Asp1 labelled sample shows an additional shoulder appearing at 1539 cm^{-1} which can be tentatively assigned to the $\nu(^{13}\text{COO}^-)^{\text{as}}$ vibration of the Asp1 residue. The neutral Tyr contributes at 1515 cm^{-1} . Below 1500 cm^{-1} , the TFA absorbs at around 1435 cm^{-1} and the $\nu(\text{COO}^-)^{\text{s}}$ vibration of the acidic residues appear at 1406 cm^{-1} . The Asp1 sample shows an additional shoulder at 1367 cm^{-1} compared to the other spectra. This shoulder is most likely arising from the $\nu(^{13}\text{COO}^-)^{\text{s}}$ vibration of the Asp1 residue. Surprisingly, the spectra of the His6 and His13 samples show similar shoulders as in the spectrum of the Asp1 sample but at lower frequencies (1360 cm^{-1}) than in the spectrum of the Asp1 sample (Figure 3.1.25). These signals can arise from the $\nu(\text{CN}^{\text{n}})$ and the $\nu(\text{CN}^{\text{c}})$ vibrations of the His residues. On the other hand, the appearance of these shoulders for the His6 and His13 samples cannot be the result of the ^{15}N -labelling of the His residues since the shifts caused by this labeling induce only small shifts.

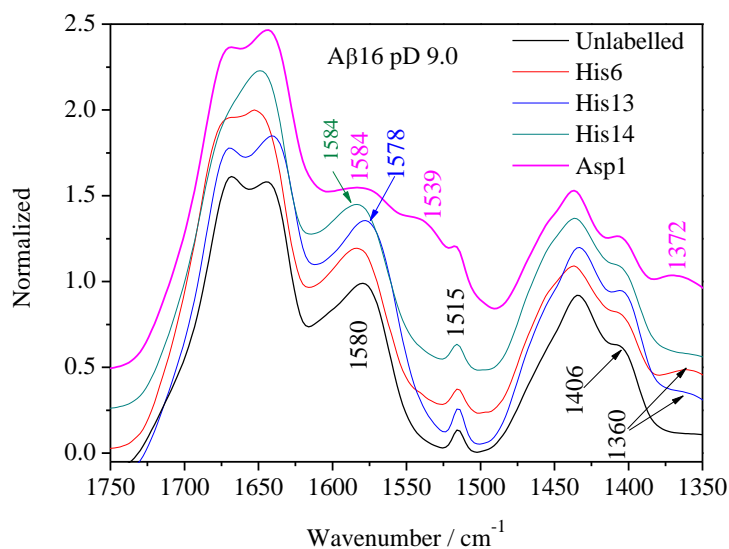


Figure 3.1.25. Enlarged view of the spectra of the A β 16 peptides recorded at pD 9.0 in the 1750–1350 cm^{-1} infrared range.

In the region below 1100 cm^{-1} (**Figure 3.1.26**), the ring deformation vibrations of the His residues occur. In the spectrum of the unlabelled sample, a weak signal appears at 1009 cm^{-1} .

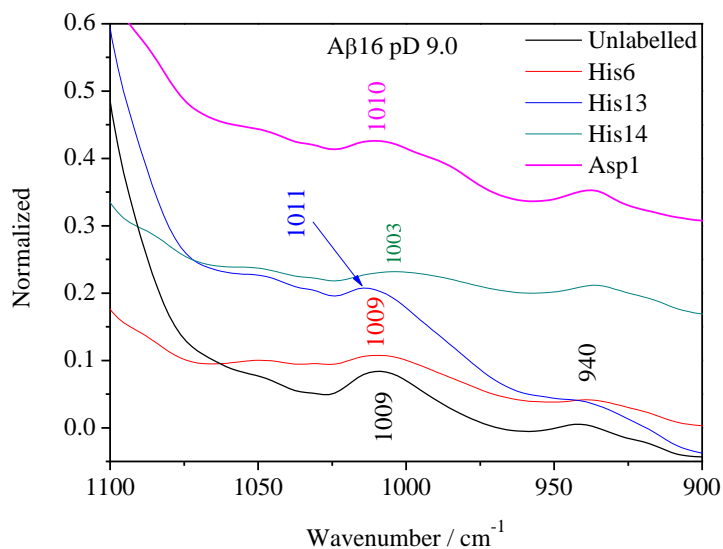


Figure 3.1.26. Enlarged view of the spectra of the A β 16 peptides recorded at pD 9.0 in the 1100–900 cm^{-1} infrared range.

This signal is characteristic of the N $^{\epsilon}$ deuterated form of His¹⁷² and it exhibits small shifts upon His labeling, except for the His14 sample where a downshift of 6 cm^{-1} occurs. Furthermore, the weak signals appearing around 940 cm^{-1} can be also assigned to the ring deformation vibration of the His residues. The spectral region below 900 cm^{-1} is dominated by the high TFA absorptions.

3.1.2.9. Spectra of the Cu²⁺–A β 16 complexes at pD 9.0

The spectra of the Cu²⁺–A β 16 complexes recorded at pD 9.0 are presented in the **Figure 3.1.27**. The signals observed in the amide I' region are not significantly affected by the copper binding.

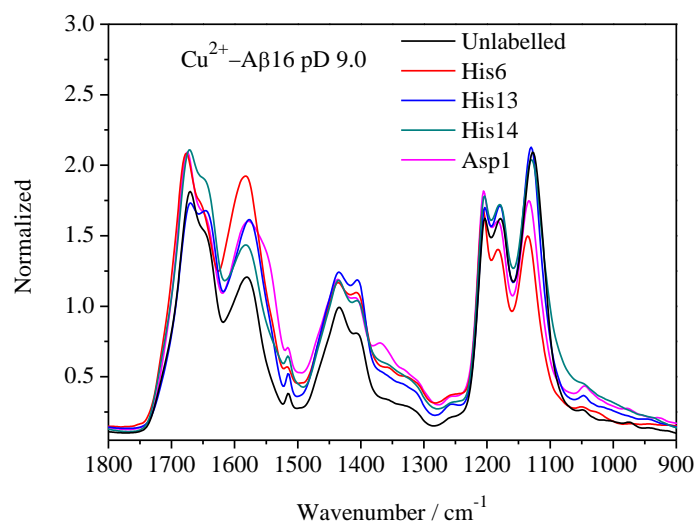


Figure 3.1.27. Global view of the spectra of the Cu²⁺–A β 16 complexes recorded at pD 9.0 in the 1800–900 cm^{-1} infrared range.

A signal appears at approximately 1580 cm^{-1} in the spectra of the free peptides. It remains at the same position after the copper binding. This behavior was not expected. Nonetheless, the high absorption coefficient of the carboxylate symmetric stretching vibration of the acidic residues may overlap with the His signatures. The downshift of the corresponding signal in the spectrum of the Asp1 sample upon copper binding from 1584 cm^{-1} towards 1577 cm^{-1} can support this suggestion (**Figure 3.1.28**).

The $\nu(^{13}\text{COO}^-)^{\text{as}}$ vibration of the Asp1 residue shifts from 1539 to 1548 cm^{-1} upon copper binding. The $\nu(^{13}\text{COO}^-)^{\text{s}}$ vibration shifts from 1372 to 1367 cm^{-1} . The frequency shifts of the $\nu(^{13}\text{COO}^-)^{\text{as}}$ and the $\nu(^{13}\text{COO}^-)^{\text{s}}$ in the spectra of the free and coordinated peptides allows the determination of the coordination mode by the carboxylate group of the Asp1 residue:^{198,199}

$$\Delta \nu_{\text{as}} - \nu_{\text{s}} (\text{free}) = 1539 - 1372 = 167\text{ cm}^{-1}$$

$$\Delta \nu_{\text{as}} - \nu_{\text{s}} (\text{bound}) = 1548 - 1367 = 181\text{ cm}^{-1}.$$

Since $\Delta \nu_{\text{as}} - \nu_{\text{s}}$ of the coordinating peptide is larger than the free one, the coordination type is suggested to be monodentate with a pseudo-bridging character.¹⁹⁸

The infrared region around 1000 cm^{-1} (**Figure 3.1.29**), can be useful to better understand the coordination by the His residues since the ring motion vibrations occurring at approximately 1580 cm^{-1} did not show significant modifications upon the copper binding.

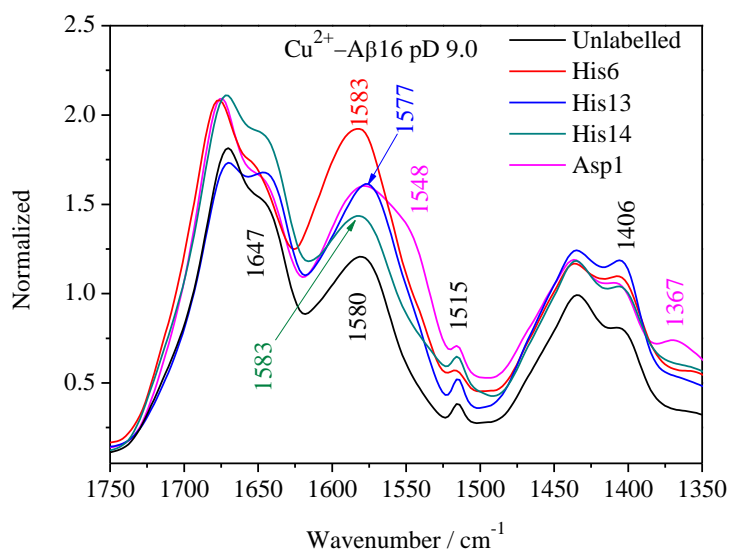


Figure 3.1.28. Enlarged view of the spectra of the Cu^{2+} -A β 16 complexes recorded at pD 9.0 in the 1750 – 1350 cm^{-1} infrared range.

The His ring deformation vibrations observed in the spectrum of the peptides at around 1010 cm^{-1} is upshifted in the spectra of the coordinated peptides to frequencies higher than 1045 cm^{-1} . This upshift points toward the coordination of copper by the N^{ϵ} atom of the His residue

while the N^π atom is protonated.¹⁷⁵ Indeed, the copper binding displaces the hydrogen (or deuterium) atom from the N^ϵ to the N^π atom.

The ^{15}N -isotopic labeling of the His6 residue induces the splitting of the signal into two signals, one remains at the same position like in the other spectra and the second is downshifted toward 1025 cm^{-1} . Thus, the His6 residue binds copper via the N^ϵ atom while the N^π is protonated. The signal split leads to two possibilities: (1) At least one other His residue bind copper via the N^ϵ atom. This suggestion is in line with the data previously reported where the three His are bound to the copper via the N^ϵ atoms.¹⁹³ (2) The His6 residue is the only His residue bound to copper and the N^π atoms of the other His residues became protonated due to environmental modifications caused by the copper binding. The fact that the downshift occurs only when the His6 residue is labelled makes the second suggestion the most plausible one. Otherwise, the spectra of the His13 and/or the His14 samples would show a similar downshift. The signal observed at 973 cm^{-1} in the spectrum of the unlabelled sample remains at the same position in the spectrum of the Asp1 labelled sample. This signal can be tentatively assigned to the ring deformation vibration of His residues bound to the copper via the N^ϵ atom while the N^π is deuterated.¹⁷⁵

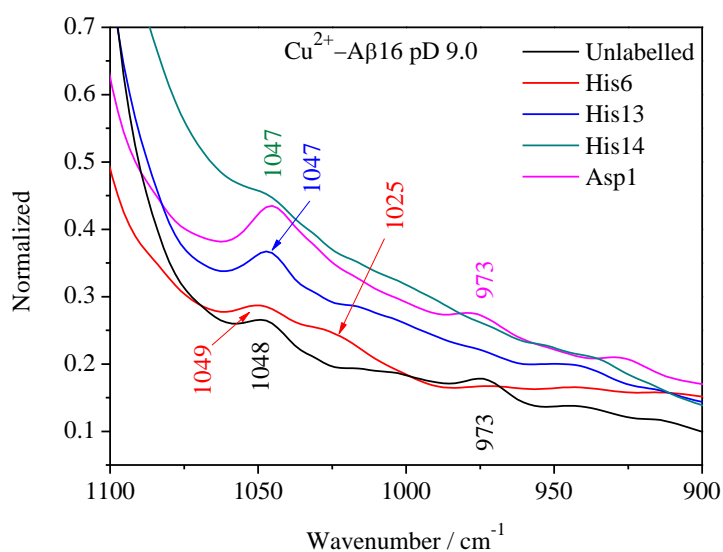


Figure 3.1.29. Enlarged view of the spectra of the Cu^{2+} -A β 16 complexes recorded at pD 9.0 in the 1100–900 cm^{-1} infrared range.

Finally, the coordination of copper by the side chain carboxylate Asp1 residue is taking place at pH (pD) 9.0 by a monodentate mode with a pseudo-bridging character. The isotopic labeling of the His residues revealed the effect of the copper coordination of the protonation state of these residues where copper binds to the N^ϵ atom by displacing the atom to the N^π

atom. The coordination via the backbone as well as by the amine side chain of the Asp1 residue was not observed here.

3.1.2.10. Spectra of the A β 16 at pH 11.0

The spectra of the free peptide show one signal in the amide I region at 1673 cm^{-1} which is mainly arising from the TFA absorption. The β -turns contributions coincide with the TFA absorption as well as with the side chain absorption of the Arg. The amide I band conserves the same shape for all the samples except for the Asp1 sample which exhibit a shoulder at 1648 cm^{-1} (**Figure 3.1.30**). This signal can be most likely assigned to the $\delta(^{15}\text{NH}_2)$ vibration of the Asp1 residue. In the amide II region, two signals can be distinguished at 1584 and 1537 cm^{-1} . The $\nu(\text{C}_4=\text{C}_5)$ vibrations of His residues as well as the $\nu(\text{COO}^-)^{\text{as}}$ vibration of the side chain of acidic residues are expected in this region. Furthermore, the amide II band contributes to the lower frequency signal.

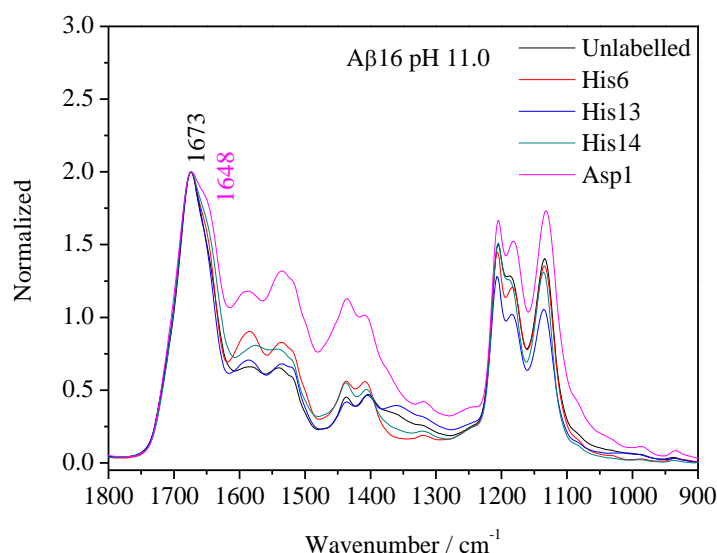


Figure 3.1.30. Global view of the spectra of the A β 16 free peptides recorded at pH 11.0 in the 1800–900 cm^{-1} infrared range.

If we look at the spectra of all the free samples at pH 11.0 we can notice that the signal observed at 1580 cm^{-1} in the spectrum of the unlabelled sample is downshifted towards 1575 cm^{-1} in the spectrum of the His14 sample (**Figure 3.1.31**). This downshift indicates that this signal is mainly arising from the $\nu(\text{C}_4=\text{C}_5)$ vibration of H14 residue. It should be noted that the frequency of the $\nu(\text{C}_4=\text{C}_5)$ vibration depends on the protonation state of the imidazole ring of the His. In other words, the His are in the N^π protonated form since the N^ϵ protonated form absorbs at approximately 1594 cm^{-1} .¹⁷²

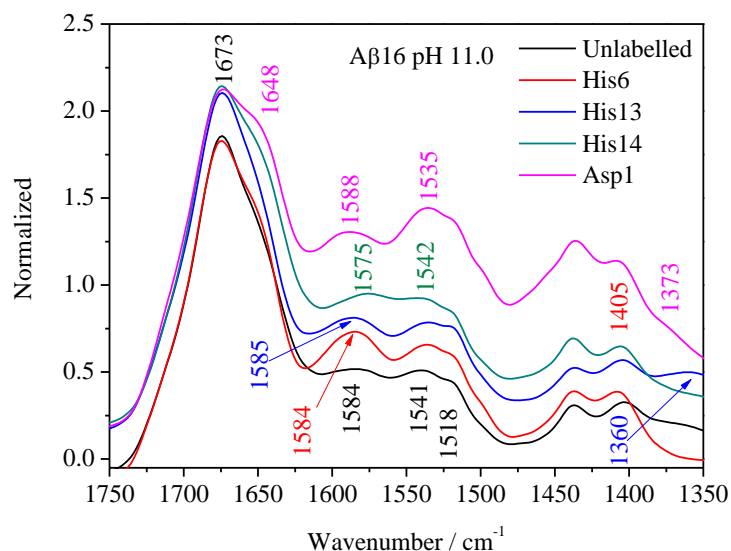


Figure 3.1.31. Enlarged view of the spectra of the A β 16 free peptides recorded at pH 11.0 in the 1800–700 cm^{-1} infrared range.

The signal appearing at 1541 cm^{-1} in the spectrum of the unlabelled sample is downshifted towards 1535 cm^{-1} in the spectrum of the Asp1 labelled sample. Despite the contribution of the amide II band to this signal, the downshift indicates the contribution of the $\nu(\text{COO}^-)^{\text{as}}$ vibration of the Asp1 residue. The H-D exchange would downshift the amide II contribution, leading thus to accurately assign this signal.

The weak shoulder at 1518 cm^{-1} can be assigned to the $\nu(\text{CC})$ ring vibration of the neutral form of Tyr. A signal appearing at 1405 cm^{-1} in all the spectra can be assigned to the $\nu(\text{COO}^-)^{\text{as}}$ vibration of acidic residues. The Asp1 sample exhibits an additional weak shoulder at 1373 cm^{-1} which can be assigned to the $\nu(^{13}\text{COO}^-)^{\text{s}}$ vibration of the Asp1 residue (**Figure 3.1.31**).

All the spectra exhibit a weak shoulder at around 1360 cm^{-1} and the most prominent ones are observed in the spectra of the unlabelled and the His13 labelled sample. This signal can be arising from the $\nu(\text{CN}^{\pi})$ and the $\nu(\text{CN}^{\epsilon})$ vibrations of the His residues.

In the spectral region around 1000 cm^{-1} where His ring deformation vibrations occur, the spectrum of the unlabelled sample shows three signals at 1031, 987 and 935 cm^{-1} . The signal with the highest frequency can be arising from the N^{ϵ} protonated form whereas the middle one can be arising from the N^{π} protonated form. The signal appearing at 935 cm^{-1} is common for both forms. The spectrum of the His13 sample shows only one large signal appearing at 1006 cm^{-1} instead of the two highest ones observed in the other spectra.

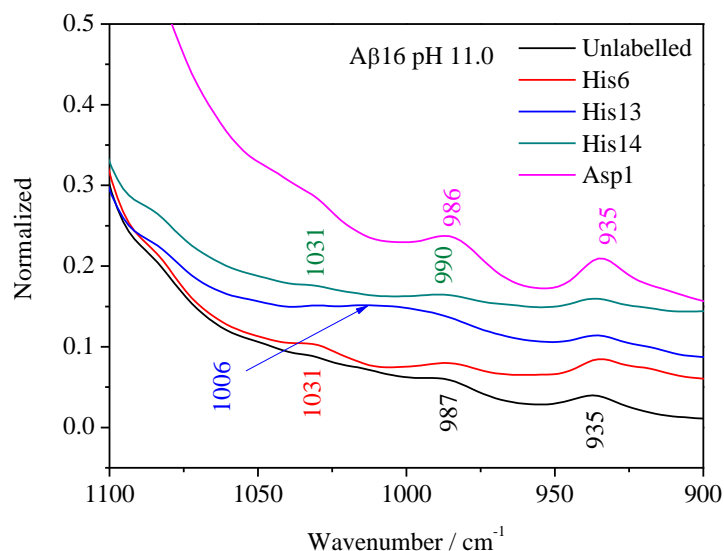


Figure 3.1.32. Enlarged view of the spectra of the A β 16 free peptides recorded at pH 11.0 in the 1100–900 cm^{-1} infrared range.

3.1.2.11. Spectra of the Cu^{2+} -A β 16 complexes at pH 11.0

The spectra of the Cu^{2+} -A β 16 complexes were recorded at pH 11.0 and they are presented in the **Figure 3.1.33**. The signal appearing in the amide I region is slightly upshifted upon copper coordination. The high TFA absorption prevents any secondary structure analysis.

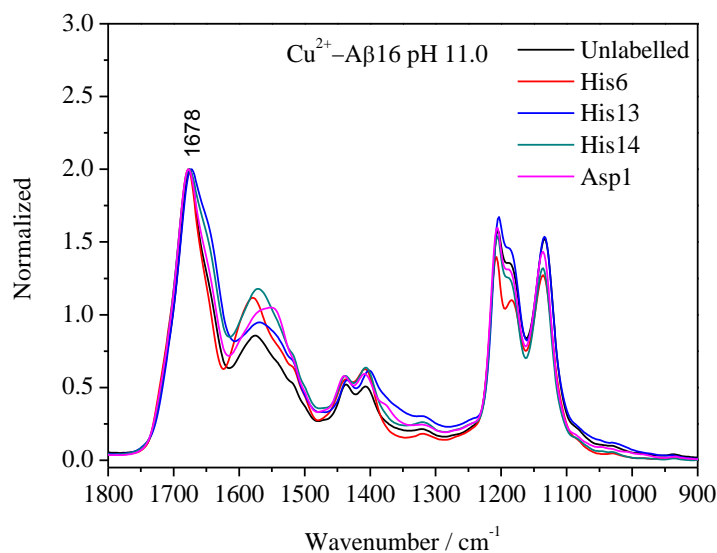


Figure 3.1.33. Global view of the spectra of the Cu^{2+} -A β 16 complexes recorded at pH 11.0 in the 1800–900 cm^{-1} infrared range.

The amide II region, where the side chain absorption of the His and the acidic residues are expected, is affected by the copper binding (**Figure 3.1.34**). The spectrum of the unlabelled sample shows a single band at 1576 cm^{-1} which shifts to higher frequencies in the spectrum of

the His6 labelled sample and to lower frequencies in the spectra of the His13 and His14 samples. Compared to the data obtained for the free peptides, a downshift occurs upon copper binding. The most pronounced downshift is observed when the His13 is labelled. Therefore, the His13 residue is most likely not bound to copper at pH 11.0 since the copper binding induces an upshift of the signal rather than a downshift.

The Asp1 signature can be recognized in the spectrum of the Asp1 labelled sample where a shoulder is observed at 1544 cm^{-1} which can be assigned to the $\nu(^{13}\text{COO}^-)^{\text{as}}$ vibration of the carboxylate side chain of the Asp1 residue. The neutral Tyr absorbs at 1517 cm^{-1} while the $\nu(^{13}\text{COO}^-)^{\text{s}}$ vibration of the side chain of acidic residues absorbs near 1408 cm^{-1} . This signal is observed at 1402 cm^{-1} and the shift is maybe due to the $\nu(\text{N}^{\pi}\text{C}_2)$ vibration of the His13 which also contributes in this spectral region.²⁰⁰

The weak shoulder appearing at 1376 cm^{-1} can be assigned to the $\nu(^{13}\text{COO}^-)^{\text{s}}$ vibration of the D1 residue. The frequency shifts of the $\nu(^{13}\text{COO}^-)^{\text{as}}$ and the $\nu(^{13}\text{COO}^-)^{\text{s}}$ in the spectra of the free and coordinated peptides at pH 11.0 allows the determination of the coordination mode by the carboxylate group of the Asp1 residue:^{198,199}

$$\Delta \nu_{\text{as}} - \nu_{\text{s}} (\text{free}) = 1535 - 1373 = 162 \text{ cm}^{-1}$$

$$\Delta \nu_{\text{as}} - \nu_{\text{s}} (\text{bound}) = 1544 - 1376 = 168 \text{ cm}^{-1}.$$

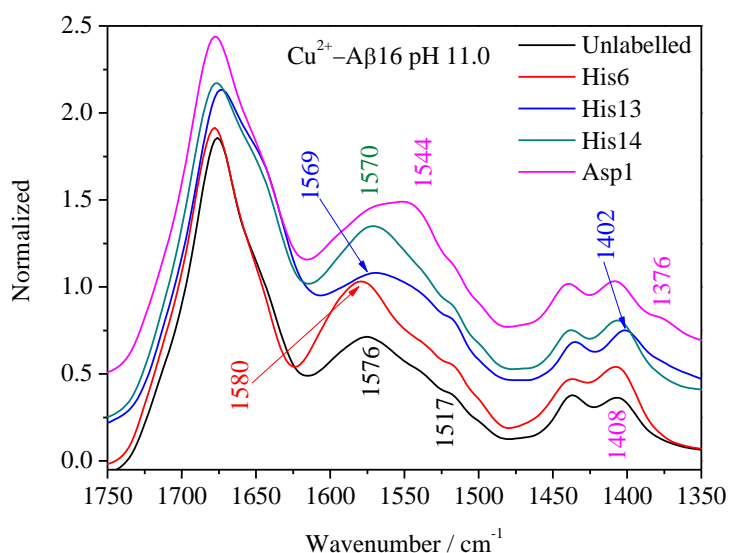


Figure 3.1.34. Enlarged view of the spectra of the Cu^{2+} - $\text{A}\beta 16$ complexes recorded at pH 11.0 in the 1750–1350 cm^{-1} infrared range.

Since $\Delta \nu_{\text{as}} - \nu_{\text{s}}$ of the coordinating peptide is larger than the free one, the coordination type is suggested to be monodentate. A pseudo-bridging character of this coordination can be also suggested since the difference between the two Δ is not too large.¹⁹⁸

The $\delta(\text{ring})$ vibrations of the His residues occurring below 1100 cm^{-1} can be seen in the **Figure 3.1.35**. The spectra show a signal at around 1030 cm^{-1} which remains in position compared to the spectra of the free peptides. However, the signal observed for the His13 sample is broader than the ones observed in the other spectra.

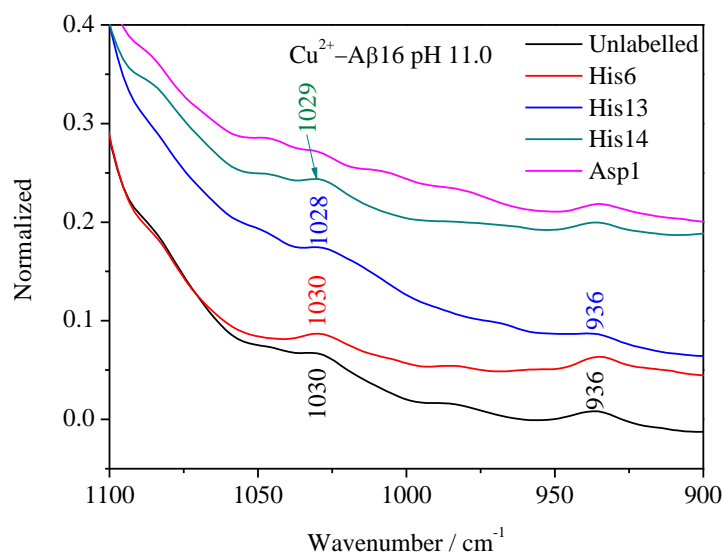


Figure 3.1.35. Enlarged view of the spectra of the Cu^{2+} -A β 16 complexes recorded at pH 11.0 in the $1100\text{--}900\text{ cm}^{-1}$ infrared range.

3.1.2.12. Spectra of the A β 16 at pD 11.0

The spectra of the free peptides were recorded at pD 11.0 to better assign the signals arising from the labelled residues. The **Figure 3.1.36** shows the spectra of all the peptides.

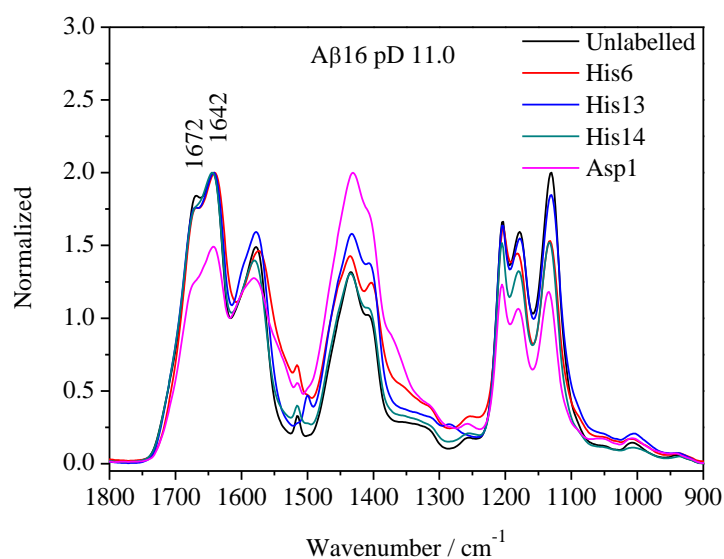


Figure 3.1.36. Global view of the spectra of the A β 16 peptides recorded at pD 11.0 in the $1800\text{--}900\text{ cm}^{-1}$ infrared range.

In the amide I' region two signals are present instead of one in the spectra of the free peptides recorded at pH 11.0. The one appearing at 1672 cm^{-1} is mainly arising from the absorption of TFA while the one appearing at 1642 cm^{-1} can be arising from the amide I' vibration. The $\nu(\text{C}_4=\text{C}_5)$ vibration appearing at 1578 cm^{-1} in the spectrum of the free unlabelled sample is slightly upshifted upon labeling of the His residues (**Figure 3.1.37**).

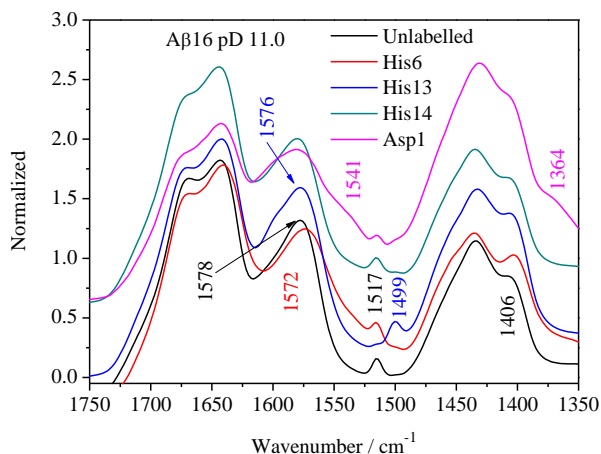


Figure 3.1.37. Enlarged view of the spectra of the A β 16 peptides recorded at pD 11.0 in the $1750\text{--}1350\text{ cm}^{-1}$ infrared range.

In the spectrum of the Asp1 sample, the $\nu(^{13}\text{COO}^-)^{\text{as}}$ vibration occurs at 1541 cm^{-1} while the $\nu(^{13}\text{COO}^-)^{\text{s}}$ vibration occur at 1364 cm^{-1} . The Tyr residue absorbs at 1515 and 1499 cm^{-1} for the neutral and negatively charged ring, respectively. This indicates that the side chain of the Tyr residue has a pK_a value very close to 11.0. The $\delta(\text{ring})$ vibrations of the His residues occurring below 1100 cm^{-1} can be seen in the **Figure 3.1.38** where the signals appearing at 1048 and 1008 cm^{-1} in the spectrum of the unlabelled sample remains almost in position in the spectra of the labelled samples. These signals can be assigned to the N^{π} and to the N^{ϵ} protonated (deuterated) form of His, respectively. Indeed both forms of His coexist in the free samples.

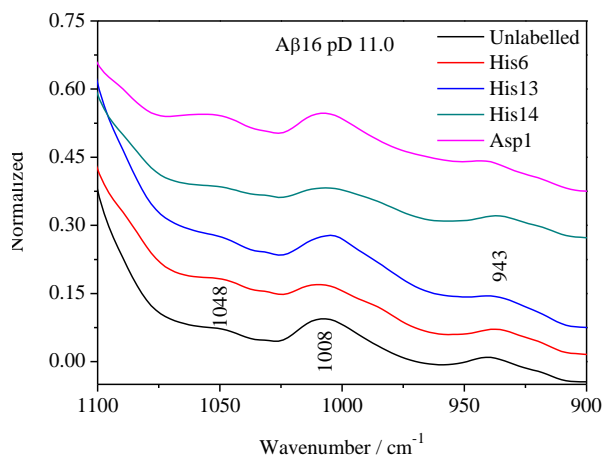


Figure 3.1.38. Enlarged view of the spectra of the A β 16 peptides recorded at pD 11.0 in the $1100\text{--}900\text{ cm}^{-1}$ infrared range.

3.1.2.13. Spectra of the Cu^{2+} -A β 16 complexes at pD 11.0

The spectra recorded at pD 11.0 for the Cu^{2+} -A β 16 complexes are presented in the **Figure 3.1.39**. The region of the amide I' band contains two signals, one arising from the TFA absorption at 1678 cm^{-1} and the other one from the amide I' band at 1645 cm^{-1} . The downshift of the amide II band by H-D exchange allows a better assignment of the side chain signals arising in the amide II region.

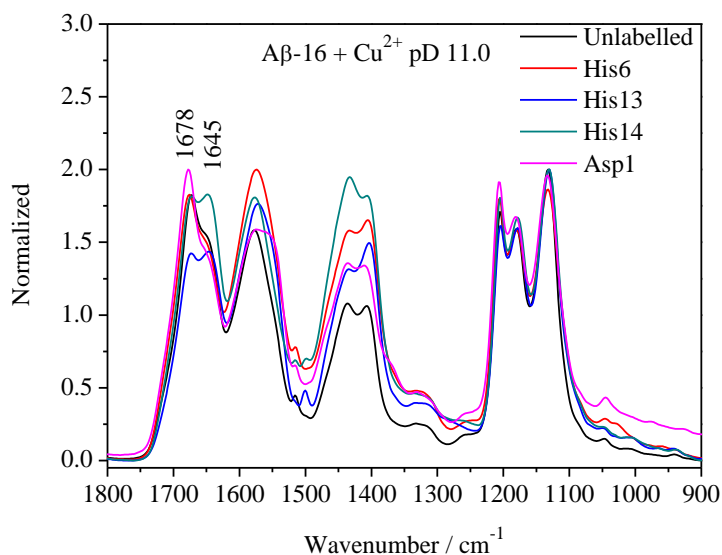


Figure 3.1.39. Global view of the spectra of the Cu^{2+} -A β 16 complexes recorded at pD 11.0 in the $1800\text{--}900\text{ cm}^{-1}$ infrared range.

The signal occurring at 1578 cm^{-1} in the spectrum of the free unlabelled sample remains in the same position after the copper binding (**Figure 3.1.40**). The same observation can be done for the His14 sample. On the other hand, the signal upshifts by few wavenumbers in the spectrum of the His6 sample which could be an indicator of the His6 binding to the copper.

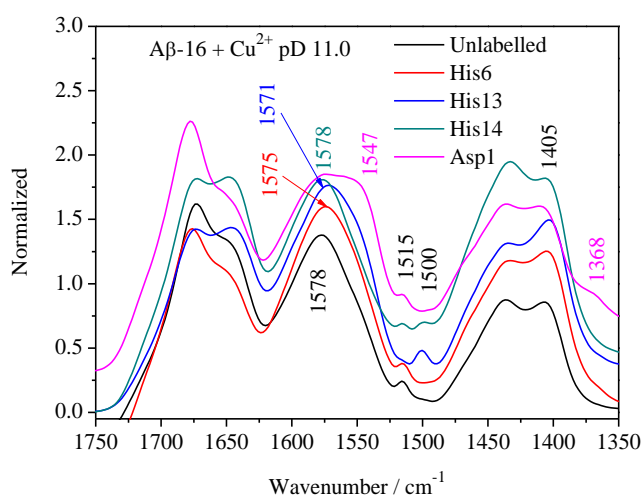


Figure 3.1.40. Enlarged view of the spectra of the Cu^{2+} -A β 16 complexes recorded at pD 11.0 in the $1750\text{--}1350\text{ cm}^{-1}$ infrared range.

The spectrum of the Asp1 sample shows an additional shoulder, which can be assigned to the $\nu(^{13}\text{COO}^-)^{\text{as}}$ vibration of the side chain of the Asp1 residue. The $\nu(^{13}\text{COO}^-)^{\text{s}}$ vibration occurs at 1368 cm^{-1} .

Calculating Δ :

$$\Delta \nu_{\text{as}} - \nu_{\text{s}} (\text{free}) = 1541 - 1364 = 177\text{ cm}^{-1}$$

$$\Delta \nu_{\text{as}} - \nu_{\text{s}} (\text{bound}) = 1547 - 1368 = 179\text{ cm}^{-1}$$

Since $\Delta \nu_{\text{as}} - \nu_{\text{s}}$ of the coordinated peptide is too close to the free one, the coordination type in a pseudo-bridging mode can be suggested.

The signals arising from the neutral and negatively charged Tyr are observed at 1515 and 1500 cm^{-1} , respectively (**Figure 3.1.40**).

The signal appearing at 1048 cm^{-1} gains intensity upon coordination while the signal at 1010 cm^{-1} loses intensity upon coordination. It is known that this couple of vibrations is sensitive to the protonation state of His, it is thus possible to find out how the His is bound to the Cu. In fact, the signal appearing at 1048 cm^{-1} is typical to the N^{π} -deuterated His and the one at 1010 cm^{-1} is typical to the N^{ϵ} -deuterated His. Since the former signal gains intensity upon coordination and the later one loses intensity, the coordination is occurring via the N^{ϵ} atom.

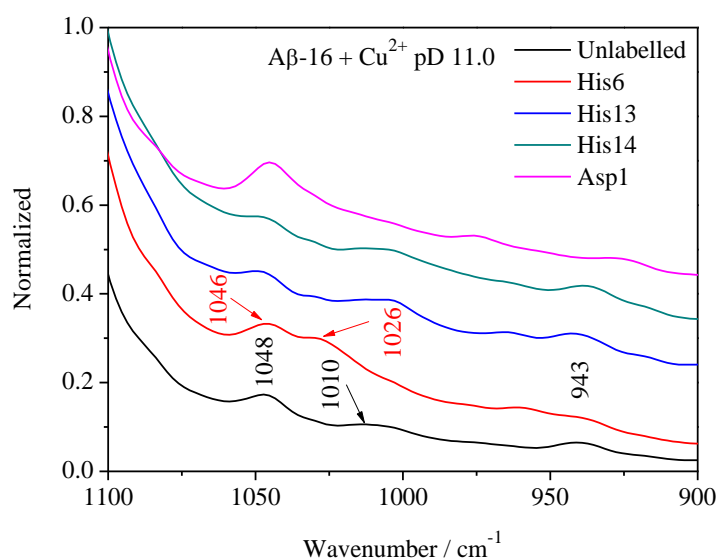


Figure 3.1.41. Enlarged view of the spectra of the Cu^{2+} - $\text{A}\beta 16$ complexes recorded at pD 11.0 in the 1100 – 900 cm^{-1} infrared range.

If we look at the spectra of the free and coordinated His6 samples, we notice that the free sample does not have similar features as the unlabelled one. Comparing the spectra of the coordinated His6 and unlabelled samples, we can see that the former one has an additional signal appearing at 1026 cm^{-1} . The His6 residue coordinates the copper via the N^{ϵ} atom. The

N atoms of the other His residues might be in one or another protonation state since both signals, at 1048 and 1010 cm^{-1} continue to coexist as in the spectra of free peptides.

To conclude about the coordination at pH (pD) 11.0 we can say that the coordination of copper by the side chain carboxylate Asp1 residue is taking place by a pseudo-bridging mode. The His6 residue is bound to copper via the N^{ϵ} atom. The coordination via the backbone as well as by the amine side chain of the Asp1 residue was not observed here.

3.1.2.14. Electrochemically induced FTIR difference spectroscopy

The ROS production by the Cu-A β 16 complexes comes from the redox conversion of copper. It is thus important to understand the coordination of Cu^+ by the A β 16 peptide. The midpoint potential of the redox couples formed by the Cu-A β 16 complexes was previously determined by cyclic voltammetry.¹⁹⁶ The electrochemical response of the complexes was found to be dependent on the A β 16 concentration under physiological pH which reflects the presence of equilibrium between different complexes.

The electrochemically induced FTIR difference spectroscopy is a powerful tool to show subtle changes in the FTIR spectra occurring upon the redox reaction. The oxidized-minus reduced difference spectra of the Cu-A β 16 complexes were recorded in order to gain insight into the effect on the redox transition of copper on the organization of the coordination sphere around the metal in both redox states. The method allows visualizing the capture and release of copper by a ligand upon the redox reaction, especially when the ligands are isotopically labelled. In addition, the electrochemically induced difference spectroscopy offers the possibility to overcome the high absorption of TFA observed in the absolute absorbance spectra.

Electrochemically induced FTIR difference spectra were recorded at pH 6.50, 9.0 and 11.0. At pH 6.50 (**Figure 3.1.42**), the difference spectrum shows a positive signal appearing at 1726 cm^{-1} which is typical for the $\nu(\text{C}=\text{O})$ vibration of protonated acidic residues, Asp and Glu. The fact that the signal is observed as a positive signal, means that at least one acid residue is protonated when the Cu^{2+} is bound. The deprotonation takes place upon the reduction of Cu^{2+} into Cu^+ and the signals arising from the deprotonated acidic residues are expected in the region of the amide II band, as well as around 1400 cm^{-1} . The negative signal appearing at 1655 cm^{-1} can be assigned to the amide I band, which reflects the backbone reorganization upon the redox reaction. The position of this signal is typical of α -helical secondary structure. The positive signal at 1610 cm^{-1} can be arising from the amine side chain

of several amino acids such as Lys, Gln, Asn. Furthermore, the ring $\nu(\text{CC})$ vibration of Phe and the $\nu(\text{C}_4=\text{C}_5)$ vibration of the bound His may overlap with this signal.

In the amide II region, an intense negative signal occurs at 1555 cm^{-1} which can be assigned to the amide II signal as well as to the side chain of the protonated acidic residues. H-D exchange was used to assign this signal.

The Tyr residue gives rise to a shoulder at 1520 cm^{-1} which points towards the conformational changing of this residue upon the redox reaction. In addition, the environmental changing around the Tyr could be at the origin of this signal. The region below 1500 cm^{-1} is dominated by signals arising from the side chains of Tyr as well as by the acidic residues. The intense negative signal appearing at 1401 cm^{-1} can be assigned to the side chain of acidic residues as well as the $\nu(\text{CN})$ vibration of deprotonated amide.

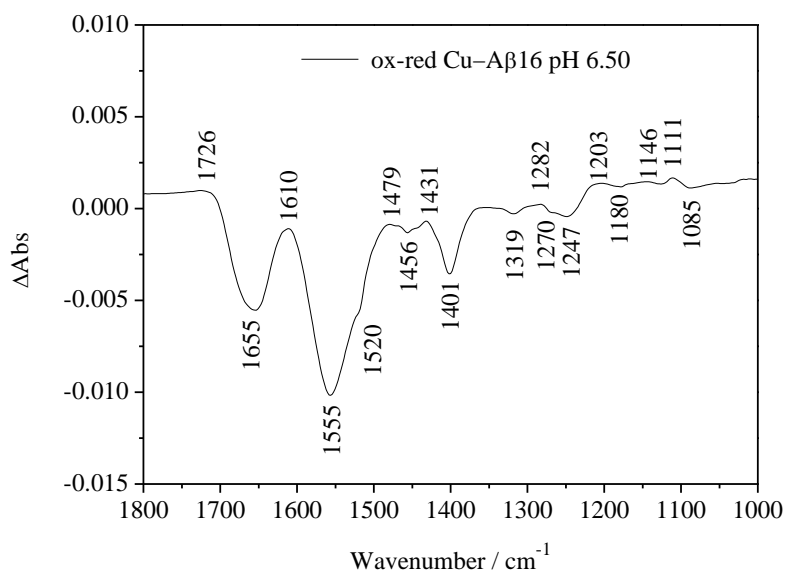


Figure 3.1.42. Electrochemically induced FTIR difference spectrum of the Cu-Aβ16 complex recorded in the $1800\text{-}1000\text{ cm}^{-1}$ range at pH 6.50.

The side chains of His and Tyr are expected to contribute below 1300 cm^{-1} . The side chain absorptions of the Tyr are of higher absorption coefficient than the His ones. Thus the electrochemically induced FTIR spectroscopy applied on the complexes formed with the isotopically labelled samples would lead to an accurate assignment in this region. It should be noted that the contribution of the phosphate buffer is expected between 1160 and 1000 cm^{-1} .

At pH 9.0 (**Figure 3.1.43**), the electrochemically induced difference spectrum of the Cu-Aβ16 complexes shows similar features to the one recorded at pH 6.50 where the amide I and the amide II bands are observed as negative signals. The amide I band is observed as a broad negative signal appearing at 1679 cm^{-1} , typical of the β -turns conformation. It should be noted that the Arg side has an intense absorption in the same region. The positive signal

appearing at 1610 cm^{-1} in the spectrum recorded at pH 6.50 is downshifted towards 1603 cm^{-1} at pH 9.0.

The amide II signal remains in position compared to the spectrum recorded at pH 6.50. The same observation can be done concerning the Tyr contribution at 1519 cm^{-1} . The signals appearing below 1500 cm^{-1} are affected by the pH increasing where the signal observed 1479 cm^{-1} loses intensity. Furthermore, the negative signal appearing at 1270 cm^{-1} in the spectrum recorded at pH 6.50 disappears.

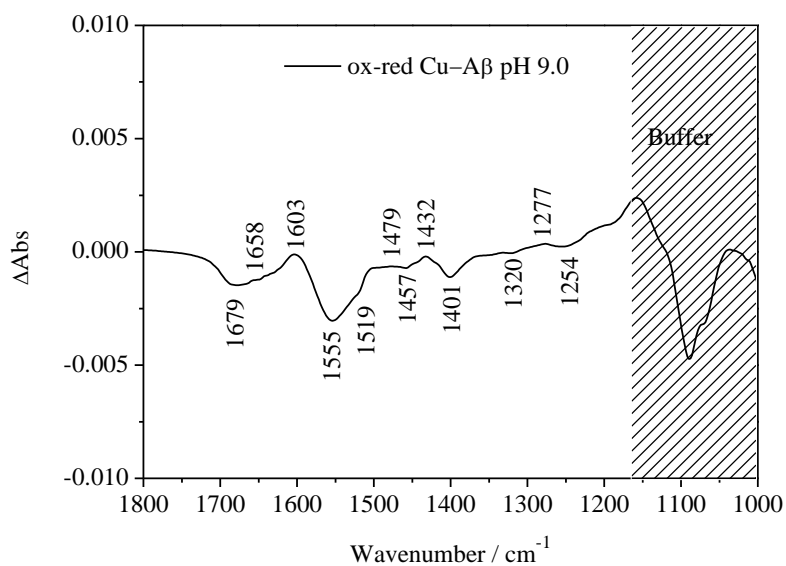


Figure 3.1.43. Electrochemically induced FTIR difference spectrum of the Cu-A β 16 complex recorded in the $1800\text{-}1000\text{ cm}^{-1}$ range at pH 9.0.

The electrochemically induced difference spectrum recorded at pH 11.0 is shown in **Figure 3.1.44**. The amide I region shows one negative signal at 1657 cm^{-1} . In the region around 1600 cm^{-1} , the positive signal appearing at lower pH values is conserved at pH 11.0. The amide II region is quite affected by the pH increase where an additional positive signal appears at 1575 cm^{-1} and the intense negative signal in the amide II region loses intensity and shifts to lower frequencies towards 1520 cm^{-1} .

Additional shifts are observed in the region below 1500 cm^{-1} . In addition, the negative signal appearing at around 1400 cm^{-1} gains intensity at pH 11.0 and downshifts towards 1393 cm^{-1} . The signals appearing below 1200 cm^{-1} could be arising from the CHES buffer.

In order to better assign the redox signals, the H-D exchange was performed at pH 9.0. Furthermore, the difference spectrum of the labelled Asp1 samples was recorded at pH 9.0.

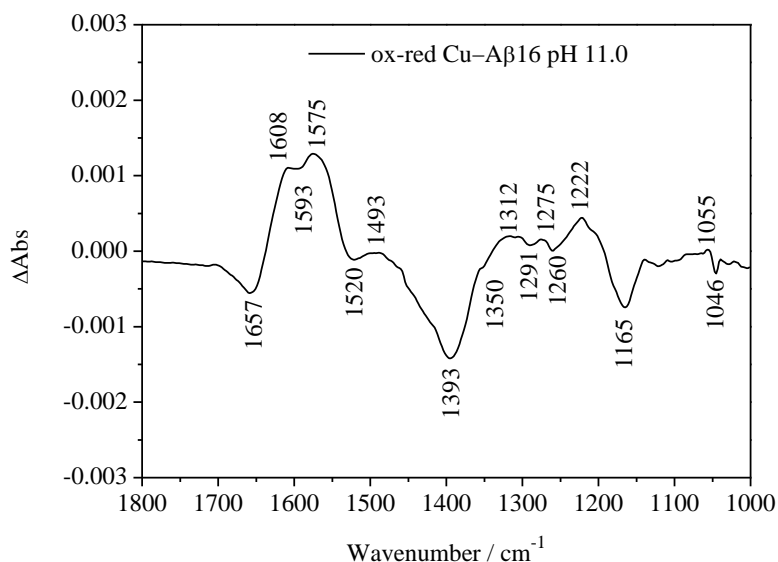


Figure 3.1.44. Electrochemically induced FTIR difference spectrum of the Cu-A β 16 complex recorded in the 1800-1000 cm^{-1} range at pH 9.0.

The **Figure 3.1.45** shows a direct comparison between the spectra of the unlabelled samples recorded at pH 9.0 and pD 9.0. The H-D exchange shows that the broad amide I signal shifts towards 1648 cm^{-1} , a frequency typical for random coil conformation. The negative signal observed at 1555 cm^{-1} belongs to the amide II contribution, which shifts towards 1450 cm^{-1} upon H-D exchange. The amide II shift to lower frequencies allows the observation of a negative signal at 1584 cm^{-1} , typical for the ring motions of His.

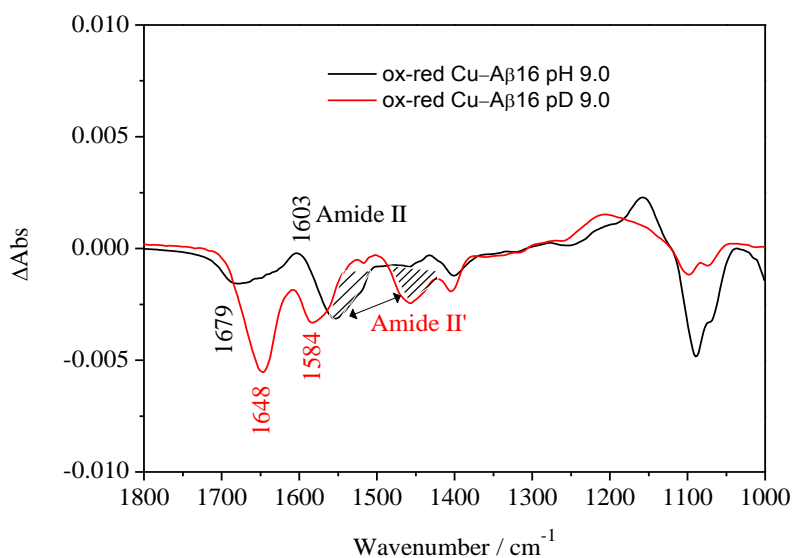


Figure 3.1.45. Electrochemically induced FTIR difference spectrum of the Cu-A β 16 complex recorded in the 1800-1000 cm^{-1} range at pH 9.0 (black) and pD 9.0 (red).

3.1.2.15. Conclusion

The ATR-FTIR spectroscopic study allowed a better understanding of the copper coordination by the A β 16 at three pH (pD) values, 6.5, 9.0 and 11.0. The data obtained by ATR-FTIR spectroscopy support the coordination by the carboxylate side chain of the Asp1 residue at all the pH values used here. At pH 6.50 and 9.0, the coordination takes place via a monodentate mode with a pseudo-bridging character while at pH 11.0 the pseudo-bridging mode is predominant. In addition, the contribution of all the His residues to the coordination at pH 6.50 is also supported, the His6 coordinates via the N $^{\epsilon}$, His13 and His14 via the N $^{\pi}$ atoms. At pH 9.0 and 11.0 the His6 residue is bound via the N $^{\epsilon}$ atom. Based on the results cited above and the FTIR data, the following coordination modes are proposed (**Figure 3.1.46**).

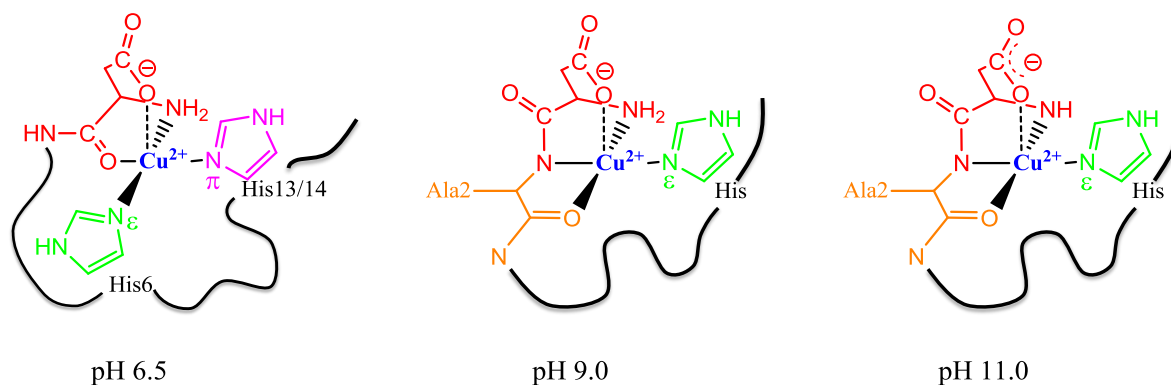


Figure 3.1.46. Proposed coordination modes of Cu cations by A β 16 at: pH 6.50 (left), pH 9.0 (middle) and pH 11.0 (right).

The strong absorption of TFA made the data analysis very difficult and the overlapping with the amide I mode prevented the analysis of the secondary structure modifications upon coordination, which is central for a better understanding of the aggregation at low pH value. FTIR spectroscopy is not sensitive to the position of the ligand within the coordination sphere; indeed, the discrimination between the axial and equatorial coordination partners is not possible.

The electrochemically induced spectra recorded as a function of pH show that backbone reorganization takes place upon the redox transition. These observations suggest different coordination modes of Cu $^{2+}$ and Cu $^{+}$ by the A β 16. The signals concomitant with the oxidized form (positive), show negligible intensity. Strong signals are found for the reduced form. This may be due to a noteworthy difference in absorption coefficient based on different interactions.

The low frequency region is a useful region to directly observe the metal–ligand vibrations. Combined with the isotopic labelling, the FIR spectroscopy would provide valuable information about the coordination. The FIR spectra of the free and copper-bound peptides were recorded, but unfortunately, the TFA absorption dominates the spectra and the metal–ligand vibrations are of weak intensities. Thus, the signals are very difficult to be accurately assigned.

3.2. The inhibitory effects of Zn cations on the cytochrome *bc*₁ complex

3.2.1. Introduction

The cytochrome *bc*₁ complex (*bc*₁) is a multisubunit membrane protein present in the respiratory chains of animals, plants and bacteria. It couples the redox reaction of quinol to proton pumping from the negative to the positive side of the membrane. The *bc*₁ of *R. capsulatus* has a molecular weight of 201.431 kDa. The enzyme is a dimer and each monomer is constituted of three different subunits; the heme *b* subunit, the heme *c* subunit and the Rieske protein. The *bc*₁ catalyzes the oxidation of quinol and the reduction of quinone molecules at two distinct binding sites, the Q_o and the Q_i sites, respectively.

Metal cations such as Zn²⁺ or Cd²⁺ are known to inhibit the proton translocation in the respiratory complex III. The mechanism by which these cations block the proton translocation is not fully understood. On the other hand, these cations are known to bind to protonated acidic residues. The Zn²⁺ binding site in the *bc*₁ from *R. capsulatus* was located with the X-ray absorption studies.¹⁰² The binding site is constituted of the His276, Asp278, Asn279, His291 and Glu295 residues (Figure 3.2.1).

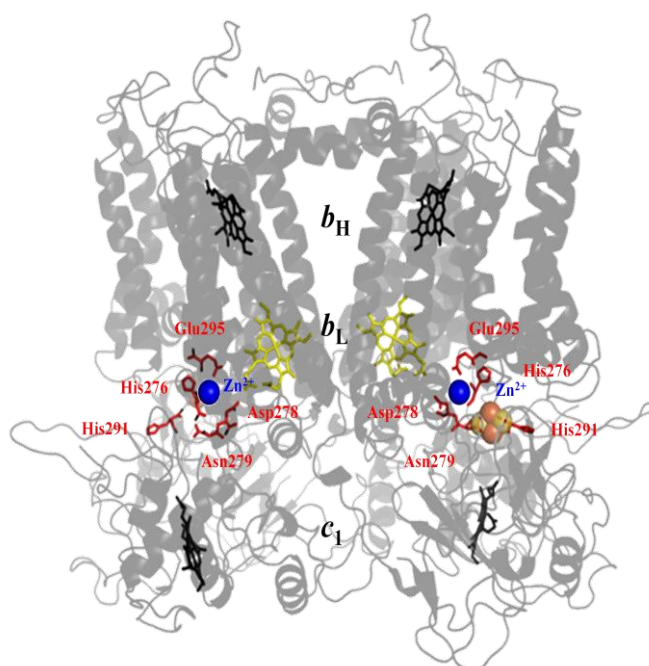


Figure 3.2.1. Zn cations binding site within the *bc*₁ of *R. capsulatus* (PDB code 1ZRT). Zinc cations are blue, the binding partners are colored in red, the heme *b*_L is in yellow and the hemes *b*_H and *c*₁ are in black.

All these amino acids belong to the heme b subunit. The Glu295 analogues in the bc_1 from other species are suggested to play a crucial role in the catalytic turnover.^{100,201,202} On the other hand, the Glu295Val mutation did not affect the FTIR difference spectra.¹⁵⁸

Here we studied the Zn^{2+} -inhibition of the wild-type bc_1 from *R. capsulatus*. In order to get insight into the binding of Zn cations to the enzyme, the Glu295V mutated enzyme and the enzyme lacking the Rieske protein were also inhibited and investigated. Hereafter the enzyme lacking the Rieske protein will be called the “subcomplex”.

3.2.2. Difference spectroscopy of the wild-type bc_1 complex

3.2.2.1. UV-Vis difference spectroscopy

UV-Vis difference spectroscopy was applied on the wild-type bc_1 in order to check the reaction times of the enzyme. In other words, the UV-Vis difference spectroscopy allows determining how long the enzyme takes to get fully oxidized or fully reduced. The difference spectra were recorded for the wild-type alone and in presence of 200 μ M of Zn cations. Furthermore, the UV-Vis difference spectroscopy allows the determination of the concentration of the enzyme. The UV-Vis difference spectra of the wild-type bc_1 are presented in the **Figure 3.2.2**. The γ -band (also called Soret band) is observed at 428 nm. It is constituted of the γ -bands of all the heme cofactors. The α -band (also called Q-band) is observed at 525, 552 and 559 nm. The signal at 525 nm arises from all the reduced hemes while the one at 552 nm arises mainly from the heme c_1 . The band at 559 nm contains overlapping signals from the b_L and b_H hemes.²⁰³ By following the evolution of the UV-Vis difference spectra as a function of time we can determine the time required to obtain the fully oxidized or the fully reduced enzyme. The **Figure 3.2.2** shows that the heme c_1 is the last cofactor to get oxidized. The fully oxidized state of the enzyme is reached 4 minutes after the application of the oxidizing potential. The fully reduced form of the enzyme is reached after 6 minutes from the application of the reducing potential.

The concentration of the enzyme was also determined using the signal at 559 nm, which has an absorption coefficient of 20 $\text{mM}^{-1}\cdot\text{cm}^{-1}$.²⁰³ Using the Lambert-Beer equation, the concentration of the sample is between 120 and 240 μ M. These values depend of the pathlength of the OTTLE cell, considered to be between 10 and 5 μ m.

The UV-Vis difference spectra of the Zn^{2+} -inhibited enzyme are presented in the **Figure 3.2.3**. The addition of Zn cations did not affect the spectral features of the enzyme. However, the inhibition by Zn cations slows down the redox reaction. The fully oxidized form is obtained after 6 minutes, the reduced form after 10 minutes. The fully ox-red and fully red-ox UV-Vis difference spectra of the wild-type are shown in the **Appendix 1**.

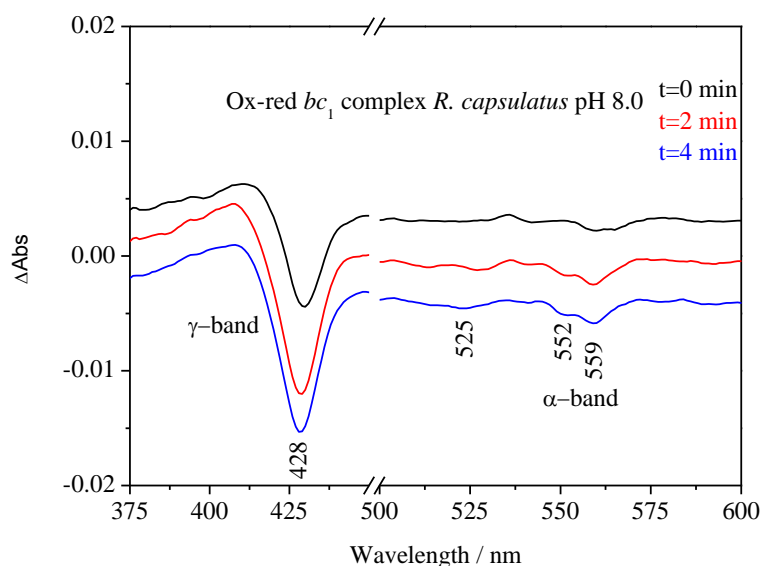


Figure 3.2.2. UV-Vis difference spectra of the wild-type bc_1 .

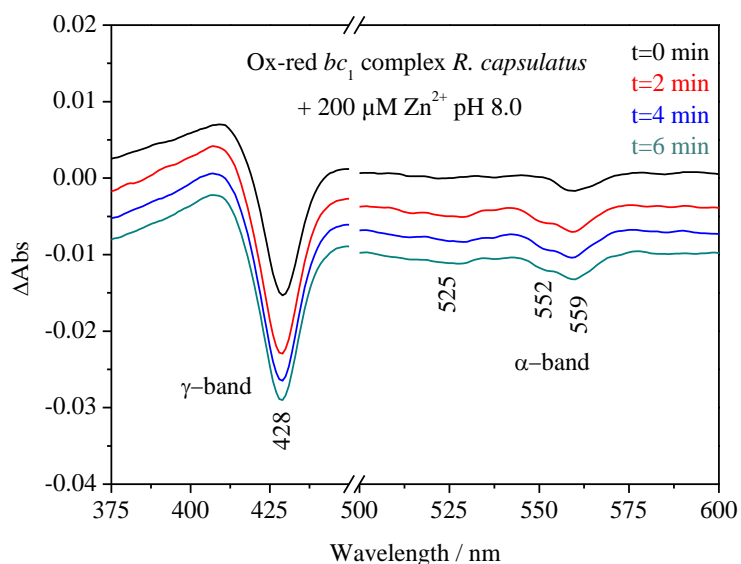


Figure 3.2.3. UV-Vis difference spectra of the wild-type bc_1 in presence of 200 μM of Zn^{2+} .

The concentration of the sample is between 8 and 16 μM . The concentration was determined as described for the wild-type alone. The determination of the reaction times is useful to know how long we should wait after applying the oxidizing and the reducing potentials to

obtain the fully oxidized and the fully reduced forms. Accordingly, the fully oxidized minus reduced FTIR difference spectra.

3.2.2.2. FTIR difference spectroscopy

The FTIR difference spectra of the *bc*₁ from *R. capsulatus* were recorded at pH 8.0 in the spectral region 1800–800 cm⁻¹. The spectra are mainly dominated by signals from the free and bound quinones as well as by the amide I and II bands (**Figure 3.2.4**). The detailed band assignments are shown in the **Appendix 2**.

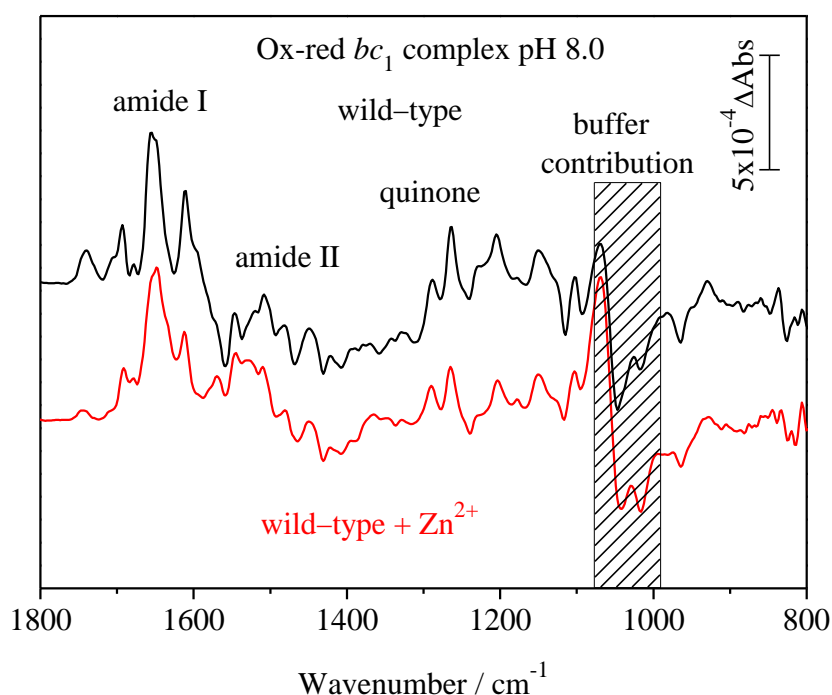


Figure 3.2.4. Ox-red FTIR difference spectra in the region 1800–800 cm⁻¹ of the wild-type *bc*₁ before (black) and after the inhibition (red).

In the region above 1700 cm⁻¹ the signature of the protonated acidic residues can be observed.^{145,204-206} The oxidation-induced protonation of acidic residues gives rise of a positive signal at 1740 cm⁻¹. This signal was previously assigned to the $\nu(\text{C}=\text{O})$ vibration of Asp278 and Glu295 residues in the *bc*₁.^{206,207} The negative signal observed at 1720 cm⁻¹ can be assigned to the $\nu(\text{C}=\text{O})$ vibration of protonated acidic residues.

The appearance of a couple of signals (+) 1740 cm⁻¹ and (-) 1720 cm⁻¹ is typical of the modification of the environment of redox active acidic residue upon the redox reaction. In fact, the higher the frequency, the more hydrophobic the environment of the acidic residue.

The downshift of the signal in the reduced form indicates that the acidic residue is more hydrogen bonded, or more exposed to the solvent. This behavior points toward a conformational change of the residue.

A positive signal can be seen at 1706 cm^{-1} . This signal was tentatively assigned to an acidic residue located in the heme *b* subunit of *P. denitrificans*.^{207,208} Furthermore, this signal can arise also from the $\nu(\text{C}=\text{O})$ vibration of the heme propionates. At lower frequencies, the $\nu(\text{C}=\text{O})$ vibration of the heme propionates can be observed at 1694 (+) / 1684 cm^{-1} (-). The former can also arise from the backbone reorganization of the Rieske protein (β -sheet). The positive signal appearing at 1679 cm^{-1} can be arising from the amide I contribution (β -turns). Furthermore, this signal may include contributions from the $\nu(\text{CN}_3\text{H}_5)^{\text{as}}$ vibration of redox active Arg residue as well as from the $\nu(\text{C}=\text{O})$ vibration of the side chain of Asn or Gln (See Appendix 2 for detailed assignments).

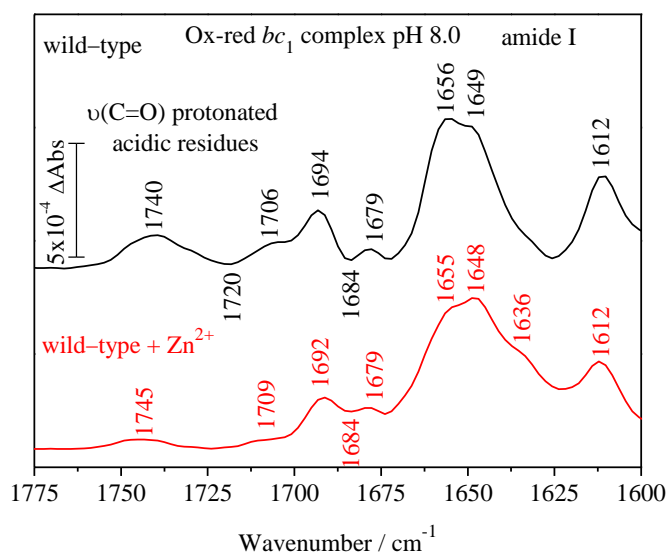


Figure 3.2.5. Enlarged view of the 1775–1600 cm^{-1} spectral region of the FTIR difference spectra of the wild-type *bc*₁ (black) and Zn^{2+} -inhibited enzyme (red).

The positive signal observed at 1656 cm^{-1} can be assigned to the $\nu(\text{C}=\text{O})$ vibration of the amide I band arising from the backbone reorganization of α -helices as well as of random coils. The $\nu(\text{C}=\text{O})$ vibration of free and bound quinones absorbs at 1649 cm^{-1} .^{206,208} The $\nu(\text{C}=\text{C})$ vibration of the quinone ring is observed at 1612 cm^{-1} .

Upon inhibition, the $\nu(\text{C}=\text{O})$ vibration of the acidic residue is much weaker than the in the difference spectrum of the wild-type enzyme alone. In addition, the signal is shifted to higher frequencies (1745 cm^{-1}). The negative signal previously assigned to the $\nu(\text{C}=\text{O})$ vibration of protonated acidic residue disappears in the Zn^{2+} -inhibited enzyme. Indeed, the Zn cations

interact with the redox active protonated acidic residue. This observation leads to suggest that: (1) The Zn cations weakly interact with the protonated acidic residue, leading thus to prevent its conformational movement upon the redox reaction. (2) The binding of Zn cations requires the deprotonation of the relevant protonated acidic residue. The positive signal observed at 1706 cm^{-1} in the difference spectrum of the wild-type enzyme alone loses intensity and shifts to higher frequencies upon inhibition (**Figure 3.2.5**). Indeed, the Zn cations interact with, at least, another protonated acidic residue in a more hydrophilic domain than the first one.

In the region of the amide I, the most important modification is the appearance of a shoulder at 1636 cm^{-1} . This signal can be arising from the amide I band (β -sheet) as well as from the $\nu(\text{C}=\text{O})$ vibration of the quinone. The appearance of this shoulder reflects the effect of Zn cations on the Q_o binding site where the quinol oxidation takes place. The binding of Zn cations may force the quinone to bind in a different orientation compared to the native wild-type.

The deprotonated heme propionates are involved in the amide II region (**Figure 3.2.6**), but they overlap with the side chain contribution of deprotonated acidic residues. It should be noted that these contributions can be seen as negative signals in the difference spectra at 1560 and 1536 cm^{-1} for the wild-type enzyme alone. The positive signal at 1547 cm^{-1} can be assigned to amide II signal as well as to the ν_{38} vibration ($\nu(\text{C}_\beta\text{C}_\beta)$ vibration) of the heme b_L (The chemical structure of the heme is shown in **Figure 3.2.7**. The discrimination between the amide II modes and the side chain contribution can be done with the help of the H-D exchange (See below)).

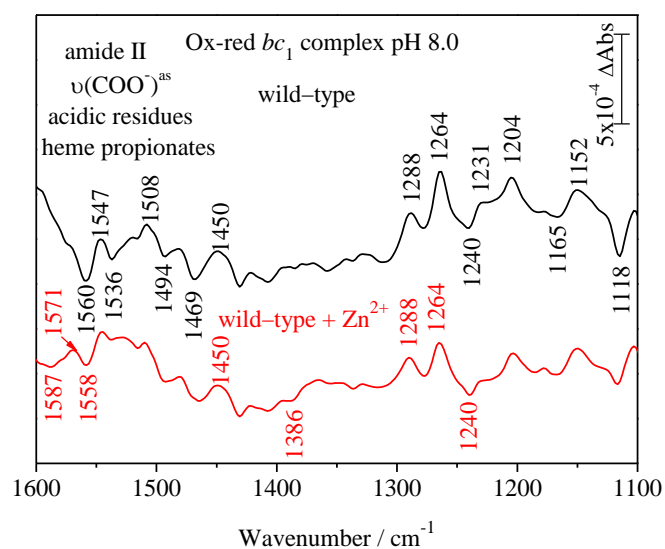


Figure 3.2.6. Enlarged view of the 1600–1100 cm^{-1} spectral region of the FTIR difference spectra of the wild-type *bc*₁ (black) and Zn^{2+} -inhibited enzyme (red).

The region below 1500 cm⁻¹ is dominated by negative signals arising from the quinone ring motions. The negative signal at 1385 cm⁻¹ may arise from the ring motions of quinones as well as from the $\nu(\text{COO}^-)^s$ vibrations of deprotonated acidic residues and the heme propionates of the *b*_H.

The positive signals appearing at 1288 and 1264 cm⁻¹ arise from the $\nu(\text{C}-\text{O})$ vibration of the methoxy group of the quinone ring. In the latter, a contribution of the ν_{42} vibration ($\delta(\text{C}_m-\text{H})$ vibration) of the hemes *b*_H and *c*₁ is also expected. Another negative signal at 1240 cm⁻¹ can also be assigned to the ν_{42} vibration of the hemes *b*_H and *c*₁. Detailed band assignments are presented in the Appendix 2.

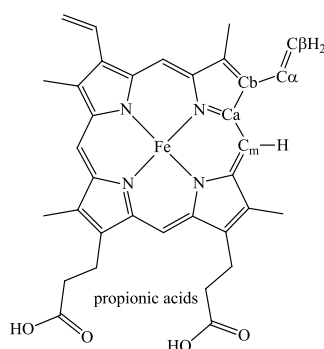


Figure 3.2.7. The chemical structure of the heme. The symbols of the carbon atoms of the porphyrin ring are also indicated.

The inhibition by Zn ions affects the difference spectrum of the enzyme, especially in the amide II region where a positive signal appears at 1571 cm⁻¹. This signal may be arising from the $\nu(\text{COO}^-)^{as}$ vibration of deprotonated acidic residues or from the $\nu(\text{COO}^-)^{as}$ vibration of the heme propionates. The analysis of the region of the $\nu(\text{C}=\text{O})$ vibration has already shown that the Zn ions interact with a protonated acidic residue and probably leads to its deprotonation. The positive signal at 1571 cm⁻¹ could then be arising from the acidic residues that bind Zn cations. The negative signal appearing at 1536 cm⁻¹ loses intensity upon inhibition. This signal can be assigned to the amide II modes of the Rieske protein as well as of the side chain of acidic residues or heme propionates. Since the amide II region also contains several side chain absorptions, none of these signals can be accurately assigned without the H-D exchange (See below).

Additional spectral modifications occur at 1386 cm⁻¹. This signal was previously assigned to the $\nu(\text{COO}^-)^s$ vibrations of deprotonated acidic residues and heme propionates that belong to the heme *b*_H. The inhibition affects also the intensity of the ν_{42} vibration of the hemes *b*_H and *c*₁ observed at 1240 cm⁻¹. The loss of intensity of this signal allows us to conclude that the

effect of the inhibition is extended from the binding site to long-range modifications in the bc_1 to reach either the heme b_H or c_1 . The spectral range between 1100 and 1000 cm^{-1} contains the Tris-HCl buffer contribution. The difference spectra of the Tris-HCl buffer at pH 8.0 in presence and absence of Zn cations are shown in the **Appendix 3**. The porphyrin ring motions can be observed between 1000 and 800 cm^{-1} (**Figure 3.2.8**). The difference spectrum of the wild-type contains a negative signal at 964 and a positive signal at 930 cm^{-1} . These signals were previously assigned to pH-sensitive motions of the porphyrin ring.^{165,209,210}

The positive signal appearing at 952 cm^{-1} for the oxidized form shifts toward 946 cm^{-1} upon reduction. This signal can be assigned to the $\nu(\text{ring})$ vibration of deprotonated His. The FTIR difference spectra of isolated Rieske protein from *R. capsulatus* show similar signals.⁹⁷ It is thus likely that the coordinating His of the Rieske protein give rise to these signals. Upon the addition of Zn cations, these signals disappear suggesting thus that the relevant His residue(s) is (are) not redox active anymore and probably binds Zn (See Appendix 2 for detailed assignments).

The redox sensitive signal appearing at 836 cm^{-1} is shifted towards 827 cm^{-1} upon reduction (**Figure 3.2.8**). This signal was previously assigned to the $\gamma(\text{C}_m\text{-H})$ vibration of the porphyrin ring. The frequency of the $\gamma(\text{C}_m\text{-H})$ vibration depends also on the pH. At high pH, the signal is found at high frequency (i.e. 836 cm^{-1}) and at low pH, the signal is found at low frequency (i.e. 827 cm^{-1}). This behavior indicates that the heme propionates are in the protonated state in the oxidized form and deprotonated in the reduced.

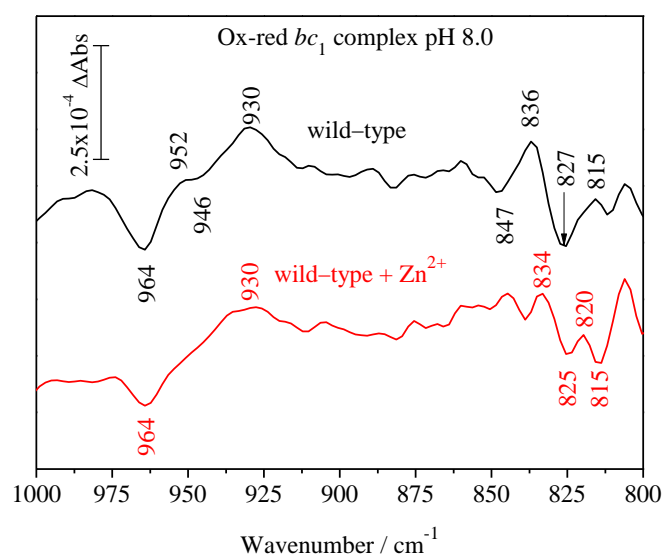


Figure 3.2.8. Enlarged view of the 1000–800 cm^{-1} spectral region of the FTIR difference spectra of the wild-type bc_1 (black) and Zn^{2+} -inhibited enzyme (red).

The inhibition induces the splitting of the negative signal into two signals at 825 and 815 cm^{-1} . Thus, the addition of Zn modifies the protonation state of the propionates. It should be noted that the proton pumping machinery of the *bc*₁ involves the heme propionates groups of the heme *b*_L. It is thus most likely that the porphyrin of the heme *b*_L gives rise to the additional negative signal at 815 cm^{-1} because of a different protonation state.

3.2.2.3. FTIR difference spectroscopy after the H–D exchange

The amide II region contains several signals arising from the backbone itself as well as from the side chains of several amino acids and the heme propionates. The data recorded at pH 8.0 suggests the deprotonation of the Glu295 and or the heme propionates. However, the overlapp of these signals with the amide II modes makes the suggestion speculative. The H–D exchange induces a large downshift of the amide II modes, making thus the assignments of the side chain absorptions easier. The spectra of the native and Zn–poisoned *bc*₁ recorded at pD 8.0 are shown in **Figure 3.2.9**. The difference spectra are similar to those previously reported.²⁰⁶ The $\nu(\text{C}=\text{O})$ vibrations of the acidic residues show a similar behavior to the one observed at pH 8.0. In other words, the signal decreases upon inhibition.

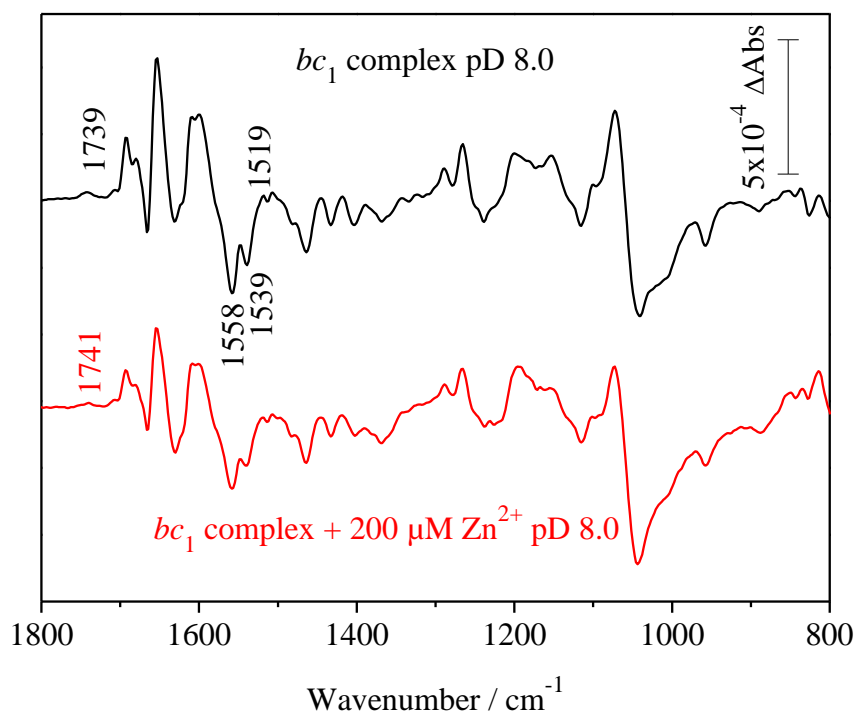


Figure 3.2.9. Ox-red FTIR difference spectra recorded at pD 8.0 in the region 1800–800 cm^{-1} of the wild-type *bc*₁ before (black) and after the inhibition (red).

In the amide II region, the negative signals are conserved after the H–D exchange. On the other hand, the positive signal appearing at 1536 cm⁻¹ at pH 8.0 is partially missing at pH 8.0. Thus the signal can be assigned to the amide II modes. In order to see the effect of the Zn cations binding on the protonation state of the acidic residues as well as the heme propionates clearer, the double difference spectrum is calculated and shown in **Figure 3.2.10**.

The evidence on the deprotonation of the acidic residue upon Zn binding can be seen in the region of the $\nu(\text{C}=\text{O})$ vibration of the protonated acidic residues. The double difference spectrum shows a negative signal at 1744 cm⁻¹. This behavior supports the binding of Zn cations to a protonated acidic residue. In addition, the amide II' region contains two positive signals at 1558 and 1540 cm⁻¹. These signals can be assigned to the $\nu(\text{COO}^-)^{\text{as}}$ vibrations of both, heme propionates and the side chain of acidic residues. This observation leads to conclude that the relevant acidic residue binds Zn cations via the carboxylate moiety. However, the double difference spectrum does not provide direct evidence on the deprotonation of the heme propionates.

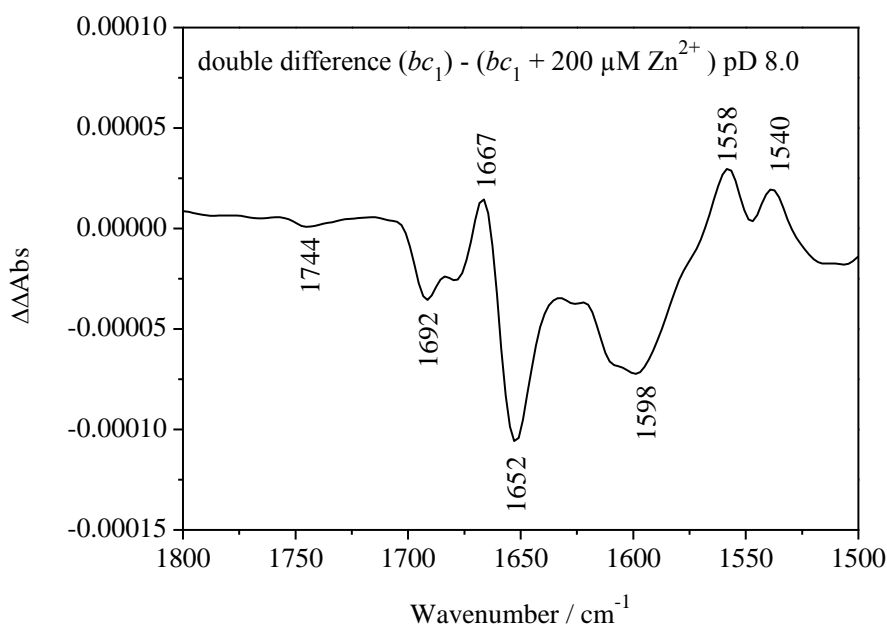


Figure 3.2.10. Ox-red spectrum of the native enzyme minus ox-red Zn-poisoned enzyme recorded at pD 8.0.

3.2.2.4. UV-Vis Titration of the *bc*₁ complex

In order to learn more about the effect of Zn binding on the hemes midpoint potentials, the UV-Vis titration was performed on the wild-type enzyme in presence and absence of Zn cations. The midpoint potentials were determined by fitting the absorbance of the Soret band

with the Nernst equation. The titration curves are shown in **Figure 3.2.11**. The data shows that the inhibition does not significantly affect the midpoint potentials of the b -type hemes. On the other hand, the midpoint potential of the heme c_1 seems to be more positive in presence of Zn cations. The spectra of the oxidative titration of the wild-type enzyme are shown in **Appendix 4**.

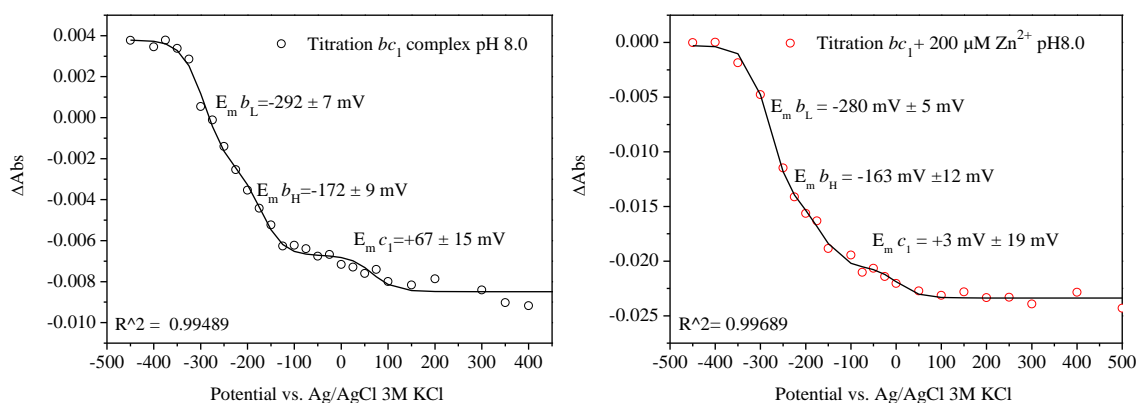


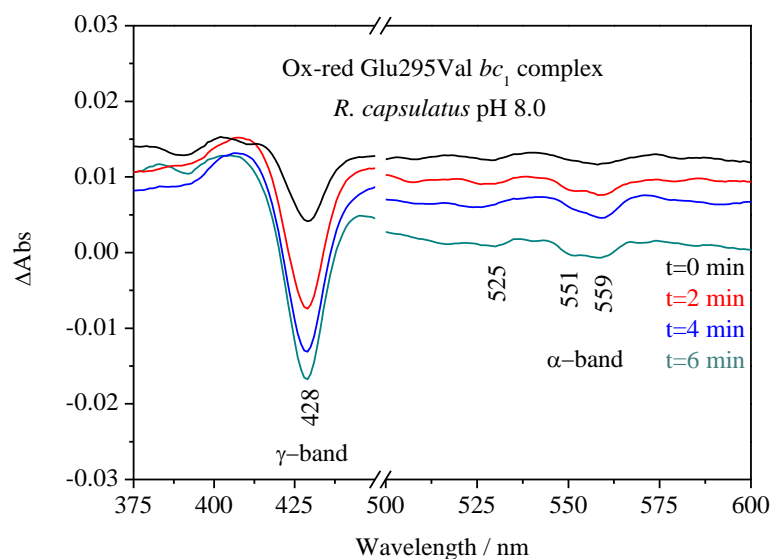
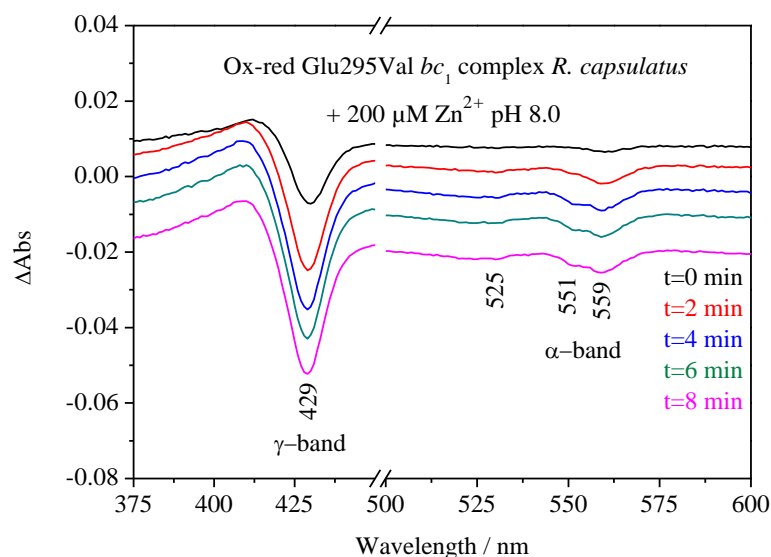
Figure 3.2.11. Titration curves of the bc_1 in the native form (left panel) and in presence of Zn cations (right panel).

However, the heme c_1 absorption does not fit well with the Nernst curve; heme c_1 is often difficult to fit. The titration following the Q band absorption is required to clarify the effect of Zn binding on the midpoint potential of the heme c_1 .

3.2.3. Difference spectroscopy of the Glu295Val mutant bc_1 complex

3.2.3.1. UV-Vis difference spectroscopy

The UV-Vis difference spectra of the Glu295Val mutant bc_1 are presented in **Figure 3.2.12**. The γ -band is observed at 429 cm^{-1} . The α -band is observed at 525, 551 and 559 nm. The fully oxidized state of the enzyme is reached 5 minutes after the application of the oxidizing potential. The fully reduced form of the enzyme is reached 7 minutes after from the application of the reducing potential. Upon inhibition (**Figure 3.2.13**), the reaction becomes slower. The fully reduced form is reached 10 minutes after the application of the reducing potential while the oxidation rate remains unaffected.

Figure 3.2.12. UV-Vis difference spectra of the Glu295Val bc_1 .Figure 3.2.13. UV-Vis difference spectra of the Glu295Val bc_1 in presence of 200 μM of Zn^{2+} .

3.2.3.2. FTIR difference spectroscopy

The FTIR difference spectra of the Glu295Val mutant in presence and absence of Zn cations are shown in **Figure 3.2.14**. Compared to the FTIR difference spectrum of the wild-type, the spectrum of the Glu295Val mutant shows weaker signals in the spectral region of the protonated acidic residues. Thus the Glu295 residue is probably responsible for signals observed at 1740 and 1720 cm^{-1} in the difference spectrum of the wild-type. On the other hand, the signals did not completely disappear (**Figure 3.2.15**).

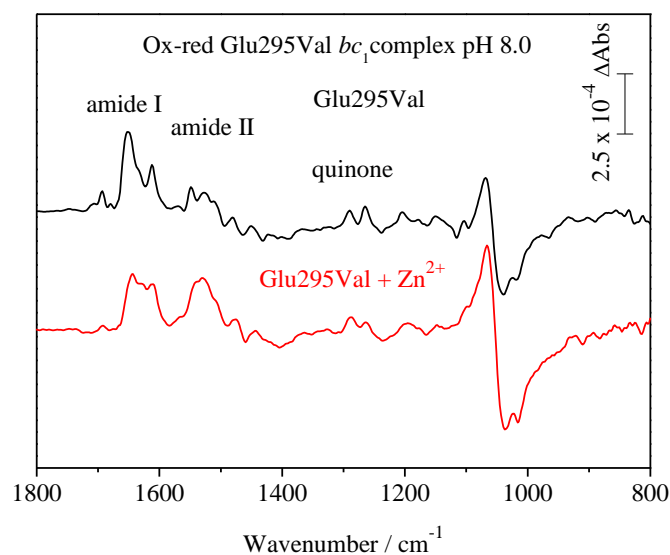


Figure 3.2.14. Ox-red FTIR difference spectra in the region 1800–800 cm^{-1} of the Glu295Val *bc*₁ before (black) and after the inhibition (red).

The contribution of other protonated acidic residues is indeed not excluded. The remaining positive signal is observed at higher frequency compared to the one observed for the wild-type. This behavior reflects a weaker hydrogen bonding or a more hydrophobic environment around the residues.

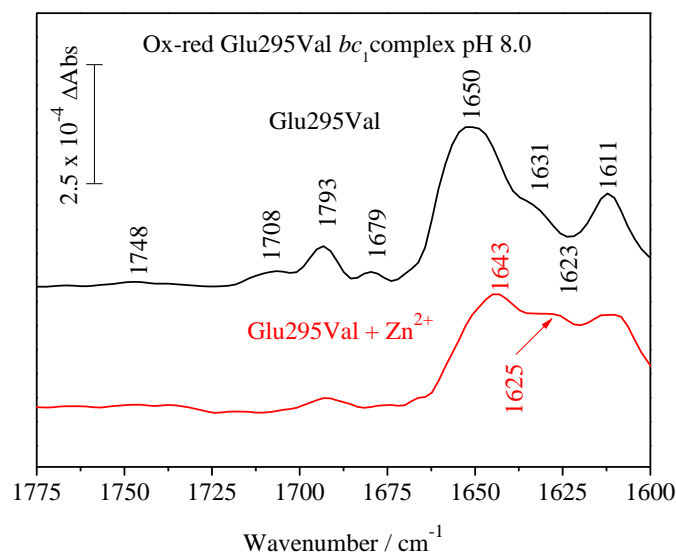


Figure 3.2.15. Enlarged view of the 1775–1600 cm^{-1} spectral region of the FTIR difference spectra of the Glu295Val *bc*₁ (black) and Zn^{2+} -inhibited enzyme (red).

The addition of Zn cations to the mutant sample showed no significant modifications on the 1748 cm^{-1} signal. However, the signal observed at 1708 cm^{-1} in the difference spectrum of the mutant disappears upon the addition of Zn cations. This signal was previously assigned to

redox active protonated acidic residues of the heme *b* subunit.²⁰⁶ Accordingly, Zn cations may still bind to the mutated enzyme via another protonated acidic residue when the Glu295 is not available. The amino acid suggested to be relevant is the Asp278 as it was shown by EXAFS studies to be a part of the binding site of Zn cations.¹⁰² The binding of Zn to the Asp278 may also explain the slower reaction rates observed in the UV-Vis range (**Figure 3.2.13**).

In the amide I region, the positive signals appearing at 1693 and 1679 cm⁻¹ lose intensity upon addition of Zn cations. These signals may arise from the backbone reorganization of the Rieske protein (β -sheet) or from the heme propionates of the *b*_L or *b*_H hemes. The contribution of the $\nu(\text{CN}_3\text{H}_5)^{\text{as}}$ vibration of Arg94 to the positive signal at 1679 cm⁻¹ is not excluded. In addition, the intense signal appearing at 1650 cm⁻¹ in the spectrum of the mutant enzyme downshifts towards 1643 cm⁻¹ upon inhibition. These signals may be arising from the amide I band as well as from the $\nu(\text{C}=\text{O})$ vibration of quinones. These spectral modifications point towards different reorganizations of the Q_o site in presence Zn.

In the amide II region (**Figure 3.2.16**), the difference spectrum of the mutant is similar to the wild-type. The negative signal observed at 1584 cm⁻¹ can be assigned to the $\nu(\text{COO}^-)^{\text{as}}$ vibration of protonated acidic residues side chains. Upon inhibition, the signal gains intensity. Thus, the deprotonation of additional acidic residue is taking place when Zn is added to the mutant. This observation is in line with the deprotonation of the Asp278 residue. However, the mutation of this residue is required to confirm its deprotonation.

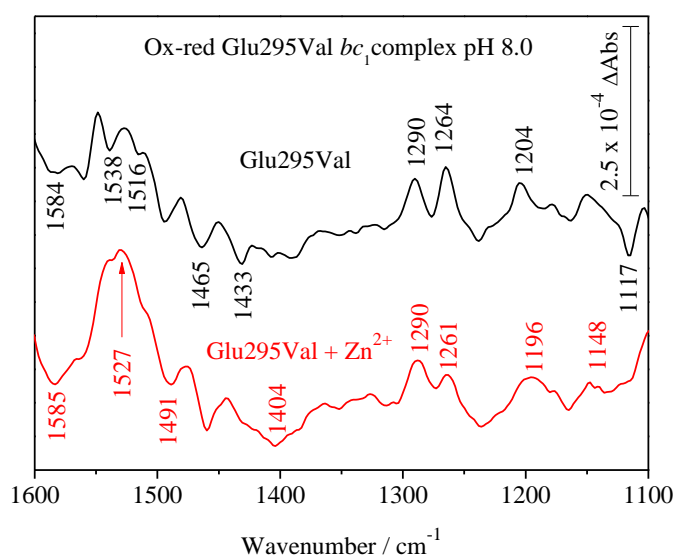


Figure 3.2.16. Enlarged view of the 1600–1100 cm⁻¹ spectral region of the FTIR difference spectra of the Glu295Val *bc*₁ (black) and Zn²⁺-inhibited enzyme (red).

Furthermore, the difference spectrum of the Zn-inhibited mutant shows a broad positive band at 1527 cm⁻¹ instead of the positive and negative signals observed in the difference spectrum of the mutant. This signal is too broad to arise from a single vibration. On the other hand, the absence of the negative signal at 1538 cm⁻¹ indicates that the heme propionates become redox inactive since the protonation of the propionates would give rise to a signal in the amide I region. This is not the case since the signal loses intensity upon inhibition. So far, we can conclude that the propionates of the heme *b*_L or *b*_H do not change protonation state when Zn cations are bound to the mutant enzyme.

The signals appearing at 1495, 1464 and 1433 cm⁻¹ are arising from the quinol ring motions. The frequency of these signals is lower in the difference spectrum of the inhibited enzyme. It is thus clear that the quinol oxidation within the Q_i binding site is affected.

The negative signal observed at 1433 cm⁻¹ can be assigned to the ring vibration of quinol. The addition of Zn cations leads to the appearance of a broad negative signal at 1404 cm⁻¹ which contains coordinates from the $\nu(\text{COO}^-)^{\delta}$ vibration of protonated acidic residues side chains as well as less intense contributions from the isoprenoid tail of the quinol.²⁰⁶

At lower frequencies, the $\nu(\text{C-O})$ vibration of the quinone methoxy group are observed at 1290, 1264 and 1204 cm⁻¹. The latter two bands contain overlapping signals from the quinones and the heme *c*₁. These signals are found at lower frequencies when the mutant is inhibited by Zn cations. Furthermore, the intensity of these signals gets weaker in presence of Zn. the heme *c*₁ reduces the Rieske protein after the quinol oxidation at the Q_o site. It is indeed possible that the low reactivity of the Rieske protein in presence of Zn cations affects the reactivity of the heme *c*₁. It should be noted that the sample may contain bound and unbound quinones. Indeed, signals arising from the free quinone are also visible in the difference spectra, however, contributing with a large C=O signal at ~ 1650 cm⁻¹.

The spectral region between 1000 and 800 cm⁻¹ is shown in the **Figure 3.2.17**. The difference spectrum of the mutant contains a negative signal at 964 and a positive signal at 933 cm⁻¹. These signals were previously observed in the difference spectrum of the wild-type enzyme. These signals may arise from pH-sensitive motions of the porphyrin ring.^{165,209,210}

The positive signal appearing at 952 cm⁻¹ in the spectrum of the wild-type enzyme is missing in the spectrum of the mutant. This signal can be assigned to the $\nu(\text{ring})$ vibration of deprotonated His. It is possible to conclude that the relevant His residue(s) is (are) involved in the proton pumping mechanism and the mutation of the Glu295 blocks the capture or release of protons by the concerned His residue(s). The concerned His residues can be the ones

directly involved in the binding of Zn cations or the ones that coordinate the $[2Fe-2S]$ cluster of the Rieske protein.

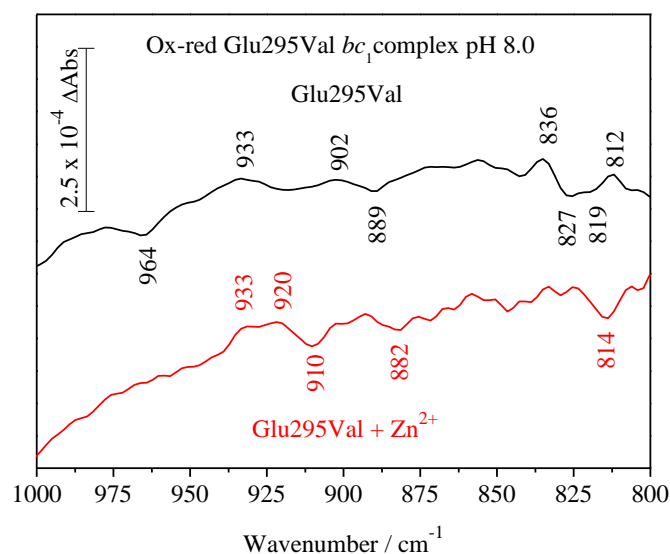


Figure 3.2.17. Enlarged view of the 1000–800 cm^{-1} spectral region of the FTIR difference spectra of the Glu295Val bc_1 (black) and Zn^{2+} -inhibited enzyme (red).

The porphyrin ring motion observed as a positive signal at 933 cm^{-1} in the difference spectrum of the mutant is not affected by the inhibition. On the other hand, an additional positive signal appears at 920 cm^{-1} which can be arising from His residues as well as from the ring motions of the porphyrins.

The $\gamma(\text{C}_m\text{-H})$ vibration of the porphyrin ring appearing at 836 cm^{-1} is splitted upon reduction into two signals at 827 and 819 cm^{-1} . This spectral feature is similar to the one observed in the difference spectrum of the inhibited wild-type bc_1 . Obviously the mutation of the Glu295 residue has a similar effect as the inhibition by Zn cations on the reactivity of the hemes. In addition, the difference spectrum of the inhibited mutant shows a different signature of the porphyrin ring vibrations where the positive and negative signals previously observed at 836 and 827 cm^{-1} are missing, in contrast to the wild-type. Furthermore, a negative signal appears at 814 cm^{-1} which can also be assigned to the $\gamma(\text{C}_m\text{-H})$ vibration of the porphyrin ring. This observation points towards the relationship between the proton translocation and the electron transfer by the hemes.

3.2.4. Difference spectroscopy of the subcomplex of the *bc*₁ complex

3.2.4.1. UV-Vis difference spectroscopy

The subcomplex of the *bc*₁ of *R. capsulatus* was previously reported to lack the Q_o binding sites. Indeed, no quinol oxidation can take place within the subcomplex. On the other hand, the Q_i binding sites and the midpoint potentials of the hemes are not affected.¹⁵⁷

The UV-Vis difference spectra of the subcomplex alone are shown in **Figure 3.2.18**. The reaction rates of the subcomplex alone are identical to those observed for the mutant alone, namely 5 minutes for the oxidation and 7 minutes for the reduction. The inhibition slows down only the reduction of the subcomplex since 10 minutes are now required to obtain the fully reduced inhibited subcomplex (**Figure 3.2.19**).

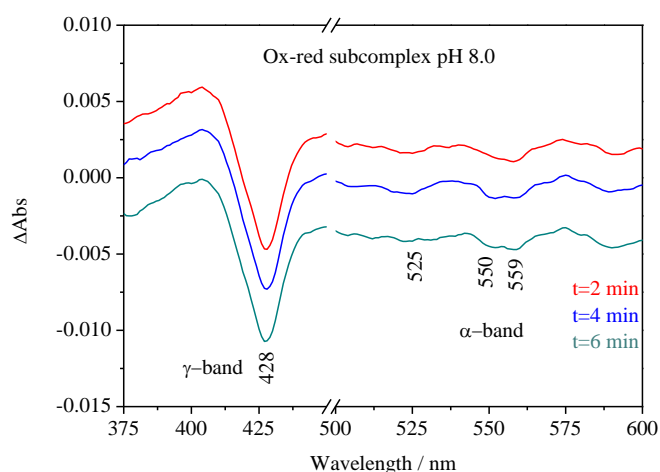


Figure 3.2.18. UV-Vis difference spectra of the subcomplex.

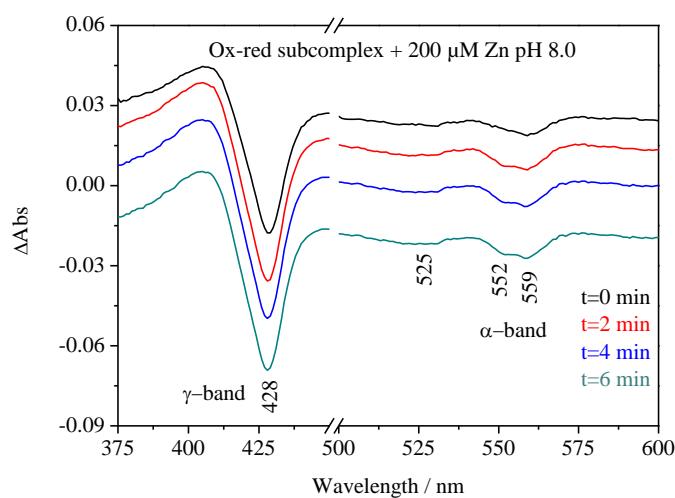


Figure 3.2.19. UV-Vis difference spectra of the subcomplex in presence of 200 μM of Zn²⁺.

3.2.4.2. FTIR difference spectroscopy

The FTIR difference spectra of the subcomplex before and after the inhibition by Zn cations are shown in **Figure 3.2.20**.

Compared to the difference spectrum of the wild-type, two positive signals can be observed in the region of the $\nu(\text{C}=\text{O})$ vibrations of protonated acidic residues instead of one (**Figure 3.2.21**). The frequencies of these signals are 1750 and 1735 cm^{-1} . These signals can arise from two different residues. The one with the higher frequency is arising from an amino acid with a more hydrophobic environment than the lower one. The data obtained from the mutant enzyme clearly show that the main contribution in this spectral region comes from the Glu295 residue. It is thus likely to assign one of these signals to the Glu295 residue.

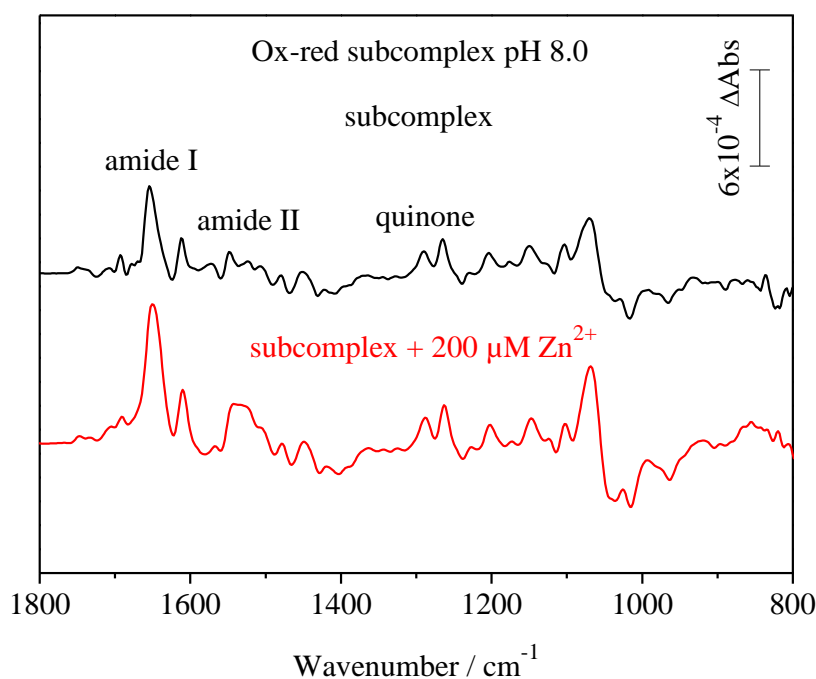


Figure 3.2.20. Ox-red FTIR difference spectra in the region 1800–800 cm^{-1} of the subcomplex before (black) and after the inhibition (red).

The crystal structure of the subcomplex is not available yet, however, the fact that the Rieske subunit is missing may affect the position of the *ef* loop containing the Glu295 residue. The removal of the Rieske protein is supposed to expose the Glu295 residue more to the solvent. Indeed, the frequency is expected to be lower than the one observed in the difference spectrum of the wild-type. However, the signal is splitted into two signals; one at higher frequency than the one observed for the wild-type (See **Figure 3.2.6**). Thus this residue adopts a different conformation as compared to the wild-type, probably in a more

hydrophobic environment than in the wild-type. The same observation can be done for the negative signal appearing at 1725 cm^{-1} .

The inhibition did not affect the intensities of these signals, only slight downshifts are observed. This behavior could be the result of structural changing of the *ef* loop making the Glu295 residue inaccessible to Zn cations. However, the UV-Vis difference spectroscopy showed a slower reduction rate in presence of Zn cations, hence, the Zn cations are still interacting with the subcomplex.

In the amide I region, the positive signals appearing at 1677 and 1670 cm^{-1} disappear upon inhibition (**Figure 3.2.21**). These signals were previously assigned to the backbone reorganization of the heme *b* subunit.²⁰⁶ On the other hand, these signals may arise from the side chain absorption of an Arg residue from the *b*_H subunit.²⁰⁸ Several Arg were previously suggested to construct salt bridges with the heme *b* propionates.²¹¹ The crystal structure of the *bc*₁ from *R. capsulatus* support the interaction between Arg side chains with the propionates (Arg94, Arg107 and Arg114).⁸⁵ Furthermore, the site-directed mutagenesis of the highly conserved Arg114 residue showed that the positively charged residue is crucial to the assembly of the enzyme.²¹²

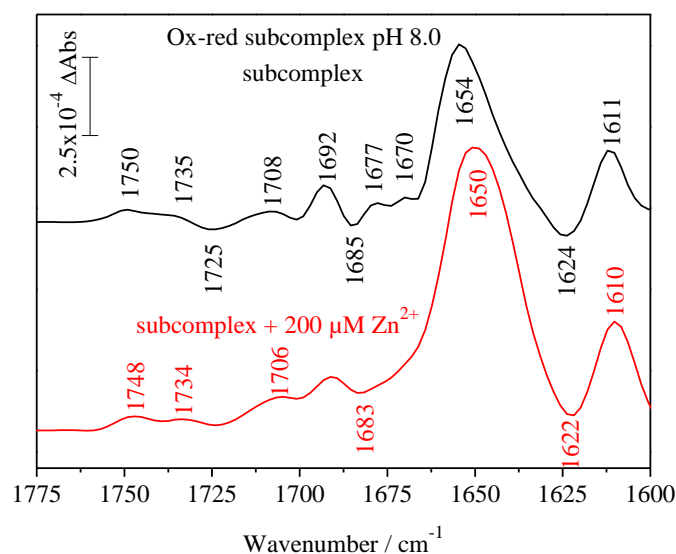


Figure 3.2.21. Enlarged view of the 1775–1600 cm^{-1} spectral region of the FTIR difference spectra of the subcomplex (black) and Zn^{2+} -inhibited enzyme (red).

The Arg signals are missing in the spectrum of the Zn-inhibited subcomplex. The direct interaction of Zn cations with the Arg94 (heme *b* subunit) or Arg107 (heme *c*₁ subunit) is the most likely since the Arg114 (heme *b* subunit) is the closest one to the Zn cations binding site.

This interaction may be the origin of the slower reaction rates observed by the UV-Vis difference spectroscopy.

The sharp signal appearing at 1654 cm^{-1} slightly downshifted upon the addition of Zn cations. This signal can be assigned to the $\nu(\text{C}=\text{O})$ vibrations of free quinones since the Q_o binding site is missing in the subcomplex.

The signals observed in the $1600\text{--}1100\text{ cm}^{-1}$ spectral range are similar to those observed for the wild-type. The addition of Zn cations modifies the spectral features in the amide II region where a broad positive signal appears at 1532 cm^{-1} (**Figure 3.2.22**). This behavior was observed in the difference spectra of the mutant. The absence of the heme propionates $\nu(\text{COO}^-)^{\text{as}}$ vibrations can result from a unique protonation state during the redox reaction.

These modifications in the heme propionates signature upon inhibition can be caused by the interaction of the Arg107 (of the heme *c*₁ subunit) with Zn cations. The lack of interaction between the propionates and the Arg114 is not excluded. These suggestions remain speculative due to the lack of site-directed mutagenesis of these residues and the crystal structure of the subcomplex.

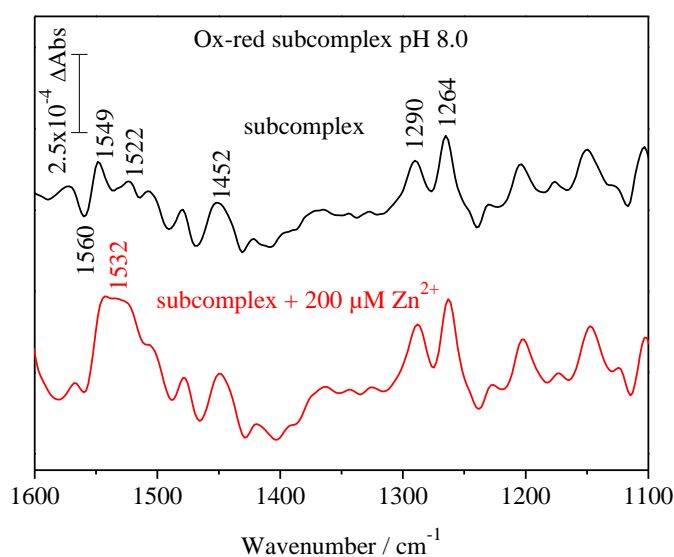


Figure 3.2.22. Enlarged view of the $1600\text{--}1100\text{ cm}^{-1}$ spectral region of the FTIR difference spectra of the subcomplex (black) and Zn^{2+} -inhibited enzyme (red).

The His ring motions as well as the porphyrin ring motions can be observed below 1000 cm^{-1} . The presence of the His ring motions excludes the contribution of the His residues of the Rieske protein. Thus the His residues giving rise to these signals are probably the His276 and His291.

The subcomplex alone shows similar features in this spectral range compared to the wild-type, except for the $\gamma(\text{C}_m\text{-H})$ vibration. Two negative signals are observed at 823 and 817 cm^{-1} instead of one in the spectrum of the wild-type. The splitting of the negative signal was also observed in the difference spectrum of the mutant. Thus, the removal of the Rieske protein and the mutation of the Glu295 residue have similar effects on the hemes environment.

The presence of Zn cations affects the difference spectrum of the subcomplex at the level of the porphyrin ring motions. The negative signal appearing at 890 cm^{-1} disappears. The $\gamma(\text{C}_m\text{-H})$ vibrations observed at 836, 827 and 817 cm^{-1} almost vanish upon inhibition. The binding of Zn cations to the subcomplex affects the redox reactions of the hemes, thus the communication between the different cofactors.

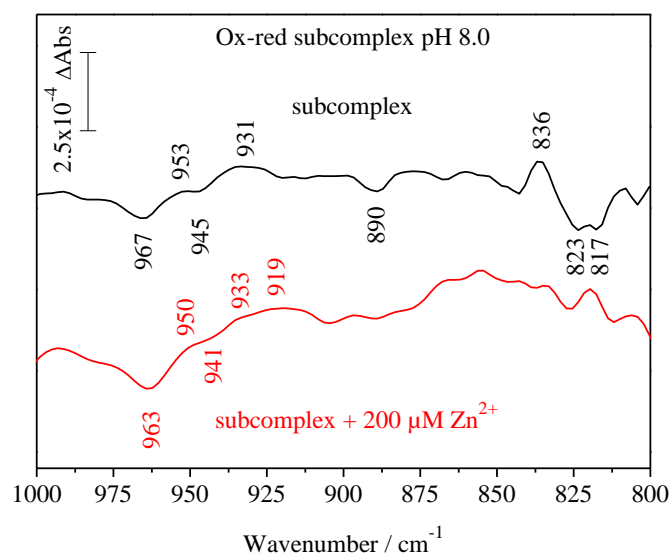


Figure 3.2.23. Enlarged view of the 1000–800 cm^{-1} spectral region of the FTIR difference spectra of the subcomplex (black) and Zn^{2+} -inhibited enzyme (red).

3.2.5. Conclusion

The inhibition effect of Zn cations towards the *bc*₁ from *R. capsulatus* was investigated by means of UV-Vis and FTIR difference spectroscopy. The data show that the reaction rates are drastically slowed down upon inhibition. Unlike one previously reported data,¹⁵⁸ but in line with several other studies,^{100,202,207,208} our data show that the Glu295 is a crucial residue to the proton translocation process of the enzyme. Furthermore, the Glu295 residue binds Zn cations via the carboxylate moiety. The deprotonation of the Glu295 results

in blocking the conformational movement of the side chain toward the propionate of the heme *b*_L. It prevents indeed the rapid release of protons from the Q_o site.

The slow electron transfer rates deduced from the UV-Vis difference spectra are supported by the modifications of the infrared signature of the porphyrin ring observed below 1000 cm⁻¹.

When Glu295 is replaced by Val, the porphyrin ring signature is similar to the one observed in the difference spectrum of the inhibited wild-type. This behavior shows that Glu295 is also crucial to the electron transfer within the Q_o site. The addition of Zn cations to this mutation induced slower reaction rates. The FTIR difference spectra showed that the inhibition led to the deprotonation of a protonated acidic residue in a more hydrophilic environment. According to the EXAFS studies,¹⁰² we suggest that the Asp278 is the relevant amino acid, also protonated in the *bc*₁ from *P. denitrificans*.²⁰⁷ In addition, the presence of Zn cations affected the signature of the porphyrin ring of the hemes. In other words, the binding of Zn cations to the mutation still affect the electron transfer at the Q_o binding site.

The removal of the Rieske protein blocks the accessibility of the Zn cations to the Glu295. The fact that the Q_o site lacks the Rieske protein is not supposed to modify the binding site of Zn cations, since the Rieske protein does not participate in the binding process. However, it is possible that the *ef* loop collapsed in absence of the Rieske protein, which induced a different conformation of the PEWY motif. Once in this conformation, the Glu295 residue is in a more hydrophobic environment and becomes inaccessible to Zn cations. Indeed, Zn cations seem to interact with Arg residue, most likely Arg107 of the heme *c*₁ subunit or the Arg94 (heme *b* subunit).

The determination of the midpoint potentials of the wild-type enzyme in the native form and in presence of Zn cations showed that the inhibition does not affect the midpoint potentials of the hemes. However, the fitting curves are not accurate for the heme *c*₁ potential. In addition, the absorption coefficients of the [2Fe-2S] cluster of the Rieske protein are too small compared to the heme ones. It is thus difficult to determine the midpoint potential of the Rieske protein by UV-Vis titration; however, it can be done by EPR spectroscopy.

According to the available data about the proton exist from the Q_o site,^{99,100} we propose a mechanism of inhibition on the *bc*₁ by Zn cations (**Figure 3.2.24**). In absence of inhibition, the quinone reduction to semiquinone leads to the release of the first proton via the His of the [2Fe-2S] cluster. The semiquinone rotates towards the Glu295 (**Figure 3.2.24A**). The dissociation of the reaction complex allows the rotation of the protonated Glu295 residue toward a water molecule which delivers the proton to the propionate of the heme *b*_L (**Figure**

3.2.24B). The propionate is hydrogen bonded to the Arg94 residue which is probably at the gate of the proton exit channel. The binding of Zn cations leads to the deprotonation of the Glu295 residue (**Figure 3.2.24C**). The rotation of the Glu295 cannot take place and thus the release of the second proton is prevented (**Figure 3.2.24D**).

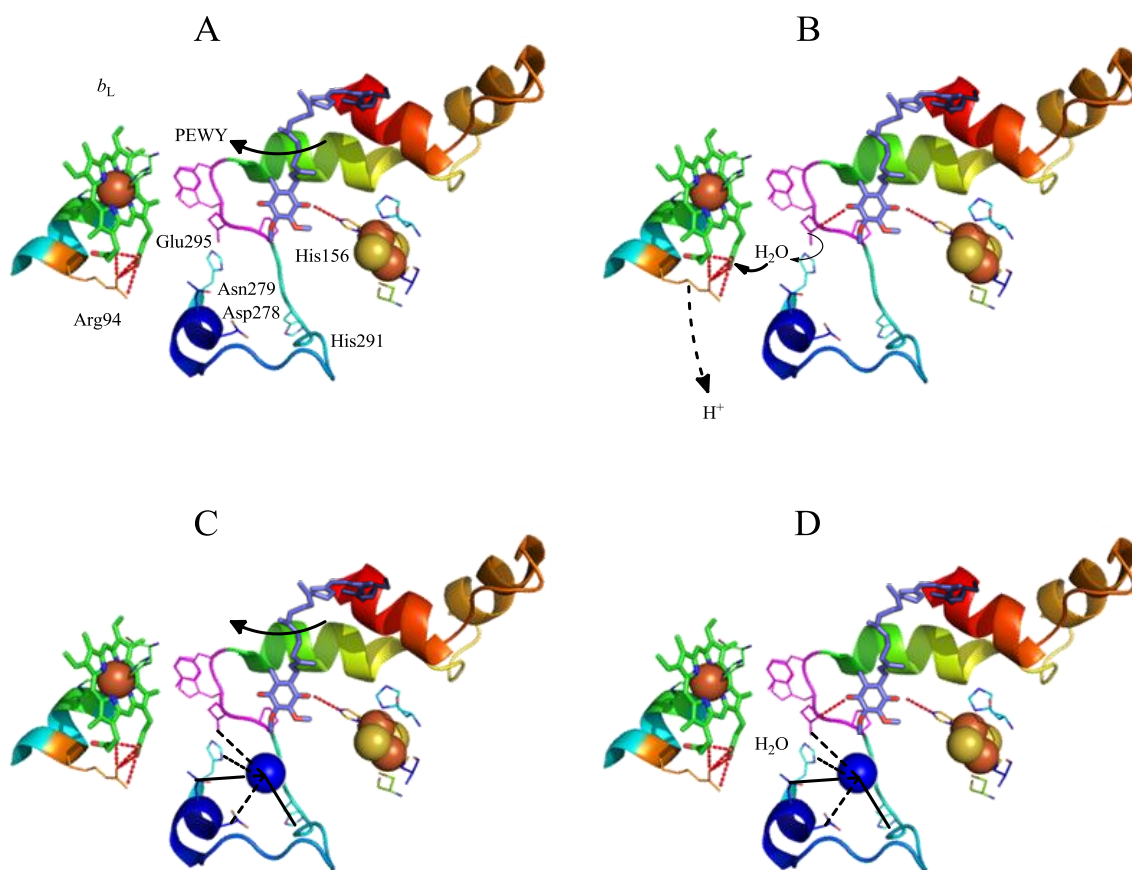


Figure 3.2.24. The proposed mechanism of inhibition of the *bc*₁ by Zn cations. Panels A and B show the release of the second proton from the Q_o site. Panels C and D show the binding of Zn cations.

3.3. The inhibitory effect of Zn cations on the cytochrome *c* oxidase

3.3.1. Introduction

The CcO is the terminal enzyme of the respiratory chain. The enzyme belongs to the superfamily of heme-copper oxidases. The CcO of the *P. denitrificans* bacterium has four different subunits and a molecular weight of 134.105 kDa. The enzyme catalyzes the reduction of molecular oxygen to water and couples the redox reaction to the proton pumping across the membrane (The mechanism is described in the Introduction cf. Complex IV).

The translocation of protons takes place via two proton pathways, namely the D- and K-pathways. Recently, high resolution crystal structure of the CcO from *P. denitrificans* has been reported.¹⁰⁴ The substrate protons that are required for water formation at the active site, travel along the K-pathway (**Figure 3.3.1**). This proton channel consists of several highly conserved residues and few water molecules. The entry site of protons to this channel is still under discussion. The Glu101 of the subunit II was previously suggested as the entry of point of the K-pathway in the CcO from *Rhodobacter sphaeroides*.¹¹⁸ However, the Glu78 of the subunit II of the CcO from *P. denitrificans* is not necessary for the proton input to the K-pathway.²¹³ It is thus not excluded that the water molecules near the Glu78 of the subunit II form the entry of the K-pathway (**Figure 3.3.1**).²¹⁴

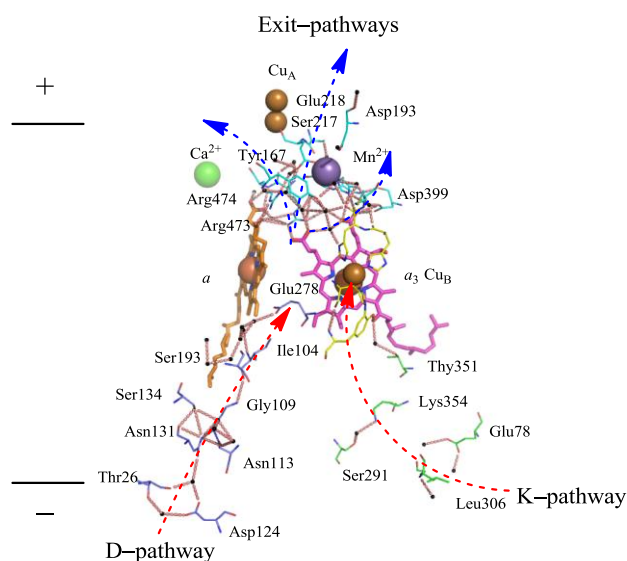


Figure 3.3.1. The proton pathways in the CcO from *P. denitrificans* (PDB code 3HB3). The D-pathway is colored in blue, the K-pathway in green and the exit pathways in cyan. The water molecules are shown as black balls, the hemes as sticks and the metals as spheres.

The pumped protons as well as some of the substrate protons need to cross the membrane via the D-pathway (**Figure 3.3.1**). The entry of protons to the channel is made by the Asp124.²¹⁵ Protons travel through the D-pathway from the entry point to the highly conserved Glu278.^{147,215} In between, highly conserved residues are hydrogen bonded to eleven water molecules to form a “wire” connecting between the entry point and the Glu278. When a proton arrives to Glu278, it can be transferred, to either, the active site via the propionate of the heme *a*₃ or to the exit-pathway (**Figure 3.3.1**).

Afterwards, the pumped protons reach the positive side of the membrane via the exit-pathways (**Figure 3.3.1**). Several possible exit points were proposed (See ref.¹⁰⁴ and references therein). However, the pumped protons and the water produced at the active sites exits are not well defined. Highly conserved residues such as His326 and Asp399 seem to play an important in the proton release. The highly conserved Arg473 and Arg474 form bridges with the propionates of both hemes. Together with a cluster of water molecules they may form a possible proton exit. However, the role of these Arg residues is still debated.²¹⁶⁻²¹⁸ In the presence of Zn cations, the proton pumping mechanism of CcO is inhibited.^{219,220} Bovine heart CcO was shown to bind Zn cations at both, the negative and positive side of the membrane. The high affinity binding site of Zn cations was found to be located at the entrance of the D-pathway. Furthermore, the binding of Zn cations to the bovine heart CcO drastically decreased the activity of the enzyme.^{219,220}

The binding of Zn cations to the bacterial CcO was also suggested to inhibit the proton uptake by the D-pathway.²²¹ In addition, the *Rhodobacter sphaeroides* CcO was co-crystallized with cadmium.¹⁰⁸ The structure revealed a high affinity binding site located at the entrance of the K-pathway where Cd cations interact with the Glu101 of the subunit II (equivalent to Glu78 of subunit II in *P. denitrificans* CcO) and with His96 of subunit II (equivalent to His73 of subunit II in *P. denitrificans* CcO) (**Figure 3.3.2**).^{108,222} On the other hand, the inhibition was also shown to affect the proton pumping by the D-pathway as well as the exit-pathway. The binding of Zn or Cd cations to the D-pathway was not evidenced; however, subunit III might offer a binding site close to the entry of the D-pathway.¹⁰⁸

The binding of Zn cations to the *P. denitrificans* CcO was investigated here by means of UV-Vis and FTIR difference spectroscopy. Although the Glu78 of the subunit II of the *P. denitrificans* CcO is known for not being crucial for the proton pumping via the K-pathway, its replacement by Ala decreased the activity to 50 % compared to the wild-type.²¹³

In order to learn more about the effect of the inhibition by Zn cations, the wild-type, as well as the Glu78Ala mutated enzymes were investigated.

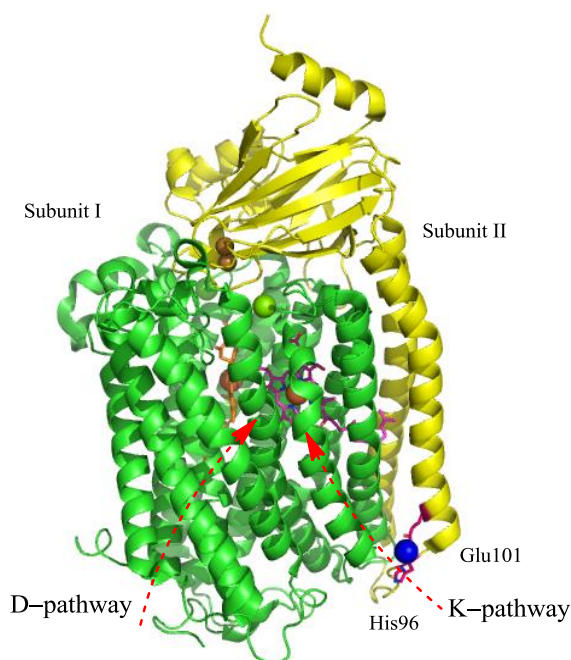


Figure 3.3.2. High affinity binding site of Cd (or Zn) cations within the CcO from *R. sphaeroides* (PDB code 2GSM). The Glu101 and His96 are in magenta sticks. The Cd cation is shown as a blue sphere. The shown subunits are I (green) and II (yellow). The proton uptake pathways are represented as red arrows.

3.3.2. Difference spectroscopy of the wild-type CcO

3.3.2.1. UV-Vis difference spectroscopy

The UV-Vis difference spectra of the wild-type CcO from *P. denitrificans* in the native form are shown in the **Figure 3.3.3**. The fully oxidized form is reached four minutes after application of the oxidizing potential, and the fully reduced one after six minutes. The difference spectra are similar to those previously reported.²²³ The γ - and α -bands occur at 446 and 607 nm, respectively.

The difference spectra of the inhibited CcO are identical to those obtained for the CcO alone. However, the reaction rate is decreased. The fully oxidized form is reached six minutes after the applications of the oxidizing potential. The reduced form is reached after ten minutes (**Figure 3.3.4**).

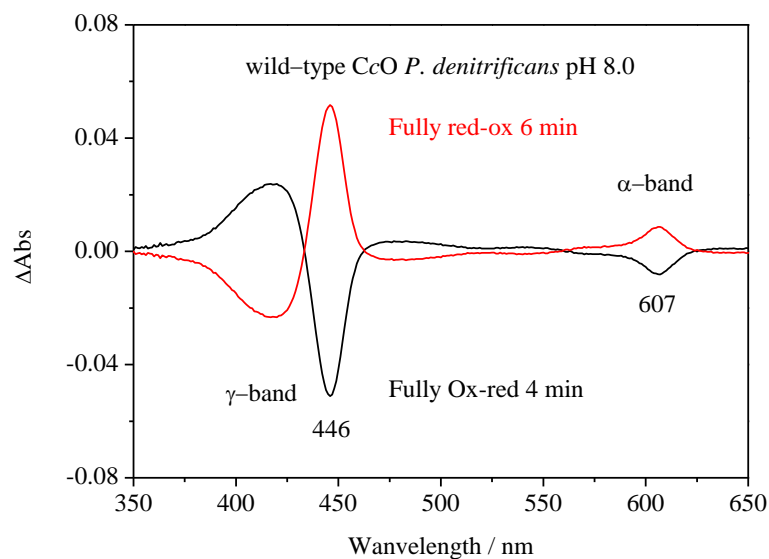
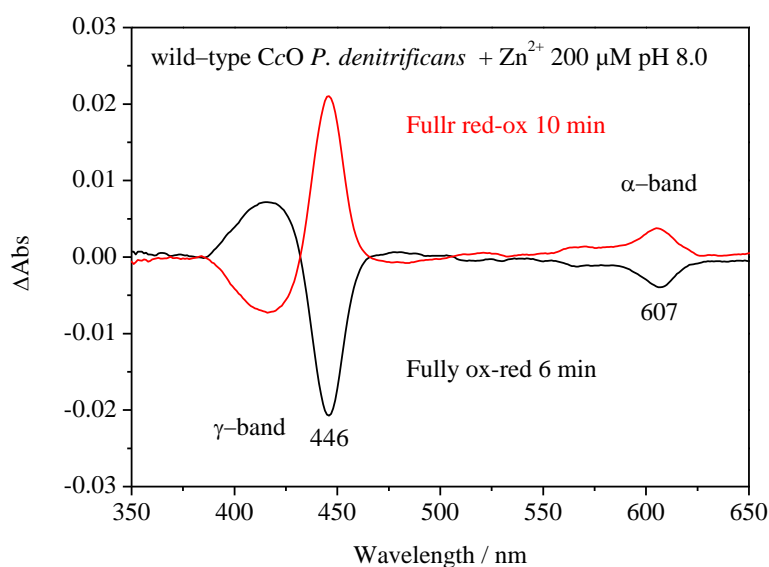


Figure 3.3.3. UV-Vis difference spectra of the CcO at pH 8.0

Figure 3.3.4. UV-Vis difference spectra of the CcO in presence of 200 μM of Zn^{2+} at pH 8.0.

3.3.2.2. FTIR difference spectroscopy

The oxidized minus reduced FTIR difference spectra of the CcO from *P. denitrificans* in the native and in the Zn-inhibited form are shown in the **Figure 3.3.5**. The difference spectra of the wild-type are identical to the ones previously reported.^{116,119,120,145,147,223} The spectra show the typical signature of protonated acidic residues in the region above 1700 cm^{-1} where a positive signal is seen at 1747 cm^{-1} and a negative one at 1735 cm^{-1} . Both signals were previously assigned to the highly conserved Glu278 residue.¹⁴⁷ These signals are

typical of conformational changes in the environment of this amino acid during the course of the redox reaction.

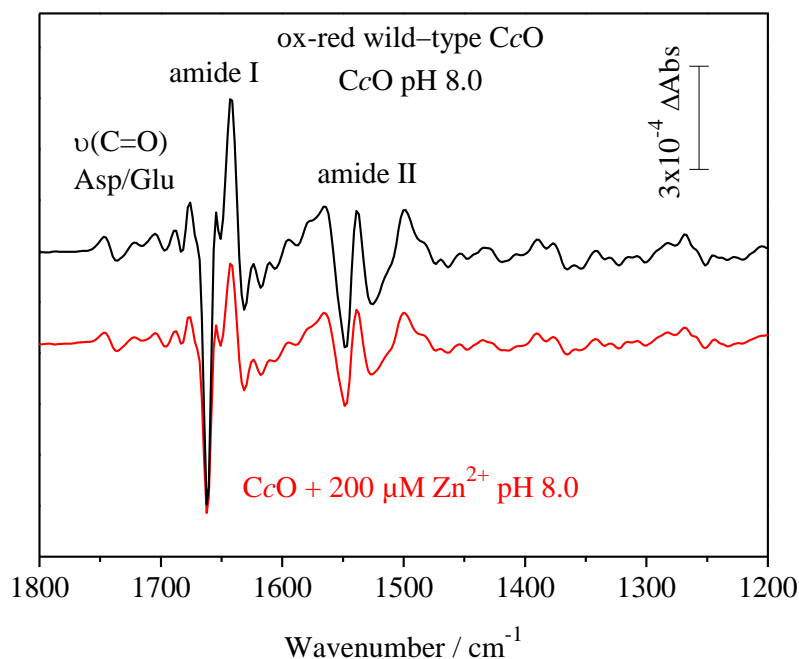


Figure 3.3.5. Ox-red FTIR difference spectra in the region 1800–1000 cm^{-1} of the CcO before (black) and after the inhibition (red).

Other redox active protonated acidic residues contribute at 1723 and 1705 cm^{-1} . Their environment is affected by the redox reaction of the heme a_3 . The negative signal appearing at 1696 cm^{-1} can be assigned to the $\nu(\text{C}=\text{O})$ vibration of protonated heme propionates or acidic residues.¹²⁰ Upon oxidation, the heme propionates are deprotonated and give rise to positive signals in the amide II region (See below).

The signals appearing at 1688 and 1662 cm^{-1} may originate from the backbone reorganization. These signals might arise from the β -sheets of the subunit II. Detailed band assignments are presented in the **Appendix 5**.

The positive signal observed at 1676 cm^{-1} can be tentatively assigned to the $\nu(\text{C}=\text{O})$ vibration of the CHO moiety of the heme a_3 . The amide I region contains sharp signals at 1662 and 1642 cm^{-1} . The former one contains overlapping signals from the α -helical backbone reorganization as well as from the $\nu(\text{C}=\text{O})$ vibration of the CHO moiety of the heme a_3 . The Arg side chain absorption might contribute to this signal. In addition, the $\nu(\text{C}=\text{O})$ vibration of the CHO moiety of the oxidized heme a which can be found at 1642 cm^{-1} , overlaps with the amide I absorption.

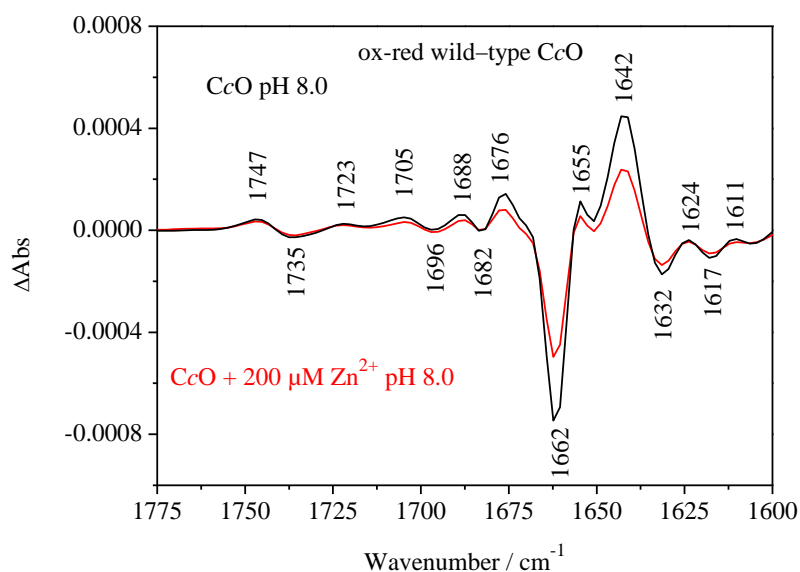


Figure 3.3.6. Enlarged view of the ox-red FTIR difference spectra in the region 1775–1600 cm^{-1} of the CcO before (black) and after the inhibition (red).

The amide II region is dominated by the $\nu(\text{COO}^-)^{\text{as}}$ vibrations of heme propionates as well as of Asp and Glu. Furthermore, the ν_{37} and ν_{38} vibrations of the hemes are expected in this spectral region (**Figure 3.3.7**). The detailed band assignments of the whole 1800–1200 cm^{-1} spectral range are presented in the **Appendix 5**.

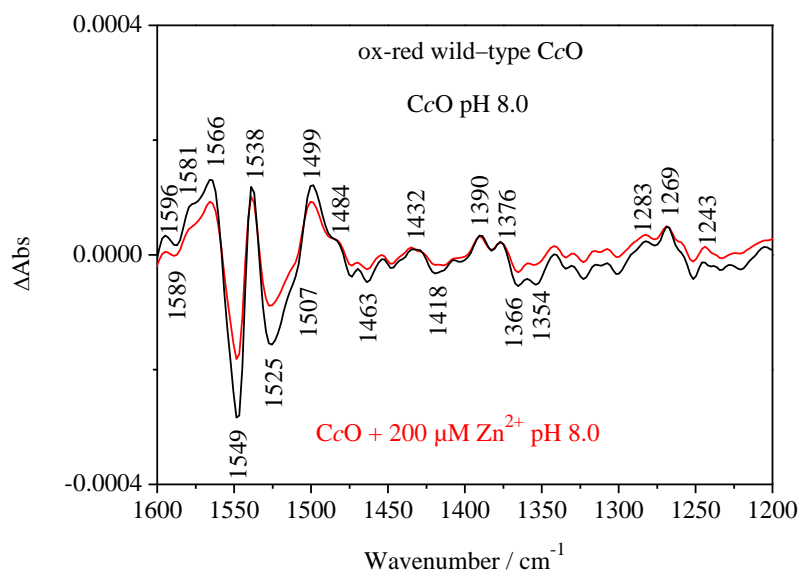


Figure 3.3.7. Enlarged view of the ox-red FTIR difference spectra in the region 1600–1200 cm^{-1} of the CcO before (black) and after the inhibition (red).

The inhibition did not cause major spectral modification in the difference spectrum (**Figure 3.3.5** and **Figure 3.3.7**). It should be noted that the whole difference spectrum recorded in presence of Zn cations has a lower intensity. Besides, the binding of Zn might cause subtle changes, difficult to observe by simple comparison of the difference spectra. Thus, the double

difference spectrum can provide information about the modifications occurring upon inhibition.

The double difference spectrum of the Zn-inhibited CcO minus the native CcO is calculated by subtracting interactively the oxidized minus reduced difference spectrum of the native CcO from that of the inhibited CcO. Indeed, the positive signal arises from the inhibited enzyme, and the negative ones from the native form of the enzyme. In order to obtain the double difference, the difference spectra were interactively subtracted by normalizing the spectra to the Glu278 signature, to the amide I, to the amide II or to the δ_{42} vibration of the hemes (1269 cm^{-1}). The double difference spectrum shown in the **Figure 3.3.8** was obtained when the normalization of the amide II or the δ_{42} vibration of the hemes is adopted (See **Appendix 6**).

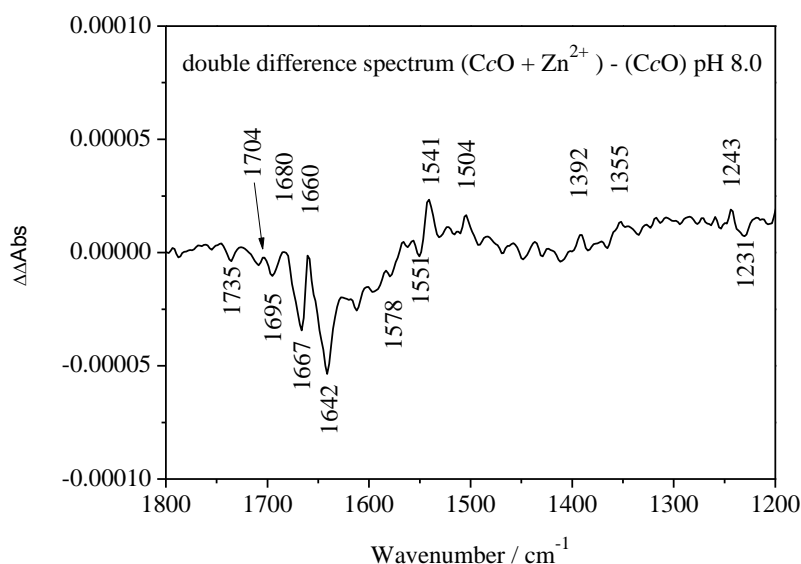


Figure 3.3.8. Double difference spectrum in the 1800–1000 cm^{-1} range of the inhibited CcO minus the native CcO at pH 8.0.

The double difference spectrum shows that the signature of the protonated acidic residues is not affected by the inhibition. In other words, the inhibition had no effect on the Glu278 residue. The binding of Zn cations seems then to perturb only the delivery of protons to the active site of the enzyme.

In the amide I region, a negative signal is seen at 1695 cm^{-1} . This signal can be assigned to the $\nu(\text{C}=\text{O})$ vibration of Asn or the heme propionates.¹²⁰ This signal is positive in the difference spectrum of the enzyme. This signal appears as a negative signal in the double difference spectrum, which means that it loses intensity upon inhibition. This observation allows us to conclude that the binding of Zn cations affect the environment of this residue. The positive signal appearing at 1680 cm^{-1} can be assigned to the $\nu(\text{CN}_3\text{H}_5)$ vibration of the Arg side chain

(**Figure 3.3.8**). This signal may overlap with the amide I vibration (β -sheet). The reduced heme a_3 gives rise to a signal at 1660 cm^{-1} . The oxidized heme a_3 absorbs at 1642 cm^{-1} . These signals can be assigned to the amide I signals of β -sheet and α -helices, respectively.²²³ Thus, the double difference spectrum shows a typical signature of the heme a_3 during the course of the electrochemical reaction. The signs of these signals are reversed in the double difference spectrum. Accordingly, the inhibition of the CcO by Zn cations slows down the redox reaction of the heme a_3 . The amide II region contains several weak signals; only the most intense ones will be discussed. Most of these signals arise from the $\nu(\text{COO}^-)^{\text{as}}$ vibration of the heme propionates as well as of the side chain of protonated acidic residues (**Figure 3.3.8**). Among these signals, a negative feature at 1551 cm^{-1} is tentatively assigned to the Glu78 residue of subunit II and a positive feature at 1541 cm^{-1} . A positive signal appears at 1504 cm^{-1} upon inhibition (**Figure 3.3.8**). The frequency of this signal is too low to be assigned to either the $\nu(\text{COO}^-)^{\text{as}}$ vibration or to amide II modes. The $\nu(\text{COO}^-)^{\text{s}}$ vibrations are expected around 1400 cm^{-1} . The double difference spectrum shows a positive signal at 1392 cm^{-1} . This signal can be assigned to the $\nu(\text{COO}^-)^{\text{s}}$ vibration of deprotonated acidic residue. The region below 1270 cm^{-1} is typical for the δ_{42} vibrations of the hemes. The double difference spectrum shows two signals, one positive at 1243 , and one negative at 1231 cm^{-1} . These signals can be assigned to the δ_{42} vibrations of either heme a or heme a_3 . The upshift of the δ_{42} vibration upon inhibition is in line with the direct effect of the Zn binding on the redox reaction (**Figure 3.3.8**).

3.3.2.3. FTIR difference spectroscopy after H–D exchange

The H–D exchange was performed in order to better visualize the signals in the amide II region. Compared to the difference spectrum of CcO recorded at pH 8.0, the one recorded at pD 8.0 exhibits an additional negative signal at 1404 cm^{-1} (**Figure 3.3.9**). The signal can be assigned to the amide II' vibration. Furthermore, the negative signal observed at 1525 cm^{-1} in the difference spectrum recorded at pH 8.0 loses intensity upon H–D exchange, confirming thus the contribution of the amide II band to this signal. It should be noted that the difference spectrum recorded at pD 8.0 is similar to the previously reported spectrum.¹⁴⁷ The exchange is judged to exceed 80 % from the decrease of the amide II band (See **Appendix 7**).

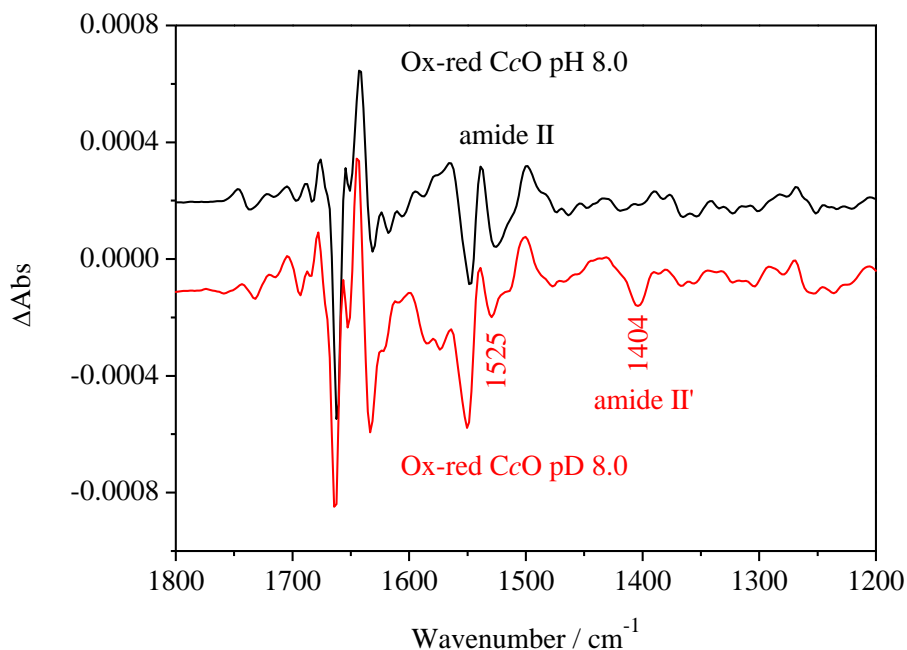


Figure 3.3.9. Comparison between the oxidized minus reduced difference spectra of the wild-type CcO recorded at pH 8.0 (black) and at pD 8.0 (red).

The difference spectra of the native form and the inhibited form of CcO recorded at pD 8.0 are shown in the **Figure 3.3.10**. The signature of the protonated acidic residues is not affected by the inhibition, as expected from the spectra obtained at pH 8.0.

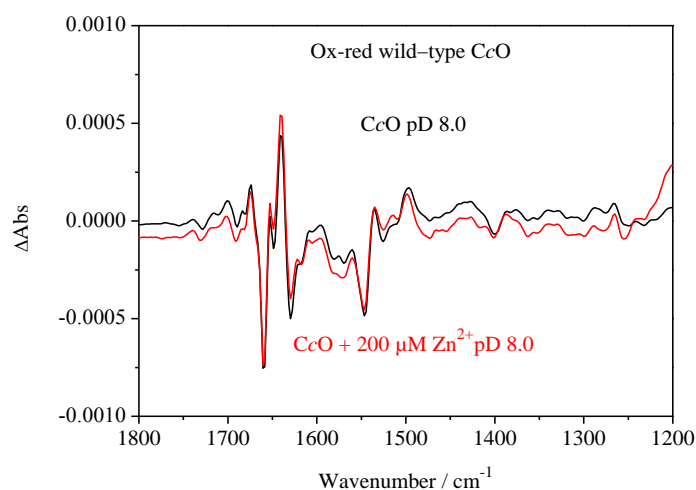


Figure 3.3.10. Ox-red FTIR difference spectra in the region 1800–1200 cm^{-1} of the CcO recorded at pD 8.0 before (black) and after the inhibition (red).

In the amide II region (**Figure 3.3.11**), the positive signal observed at 1576 cm^{-1} in absence of Zn cations almost disappears upon inhibition. This signal can be assigned to the $\nu(\text{COO}^-)^{\text{as}}$ vibration of the heme propionates as well as of the side chain of deprotonated acidic residues, most likely the Glu78 of subunit II. It should be noted that a similar signal can be observed in the double difference spectrum calculated for the data obtained at pH 8.0. However the

intensity is low. This behavior could result from the binding of Zn cations to a deprotonated acidic residue which shifts the signal from its original position. On the other hand, the signal can be arising from the heme propionates as well.

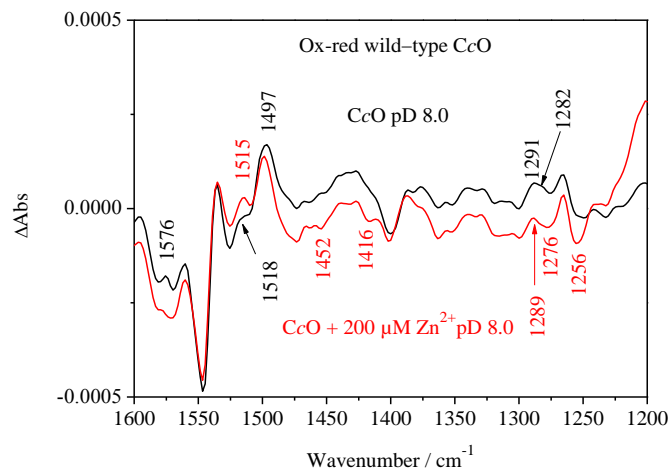


Figure 3.3.11. Enlarged view of the ox-red FTIR difference spectra in the region 1800–1200 cm^{-1} of the CcO recorded at pD 8.0 before (black) and after the inhibition (red).

The shoulder appearing at 1515 cm^{-1} in the difference spectrum of the native form becomes a well-defined signal upon inhibition (**Figure 3.3.11**). The signal is characteristic of ring motions of neutral Tyr. Previous mutational analysis combined with isotopic labeling of the Tyr residues of CcO from *P. denitrificans* showed that no Tyr residue has a significant absorption at 1515 cm^{-1} at pH 7.0.¹⁴⁶ Furthermore, the K-pathway does not contain any Tyr residue with this spectral feature. On the other hand, the Tyr35 located near to the D-pathway, may be at the origin of this signal. Besides, the Tyr35 remains in the neutral form during the redox reaction. It should be noted that the Tyr35Phe mutated CcO retains 60 % of the electron transfer activity, and full proton pumping activity.¹⁴⁶ Indeed, beside of the high affinity binding site of Zn cations, another binding site probably exists. This latter one is probably interacting with the Tyr35 residue.

In the amide II' region (**Figure 3.3.11**), a negative signal appears at 1416 cm^{-1} which can be assigned to the $\nu(\text{COO}^-)^s$ vibration of the heme propionates as well as of the side chain of deprotonated acidic residues. The appearance of this signal in the difference spectrum of the inhibited enzyme reflects the perturbation of either the propionates or a deprotonated acidic residue.

3.3.2.4. UV-Vis titration

In order to better understand the Zn binding to the CcO on the hemes, the UV-Vis titrations were performed to determine the midpoint potentials of the hemes before and after the inhibition. The Soret band observed at 445 nm was used to determine the midpoint potentials of the hemes. The spectra recorded during the oxidative titration of the inhibited CcO are shown in the **Appendix 8**.

The investigation of the CcO by means of UV-Vis difference spectroscopy led to establish an anti-cooperativity model between the two heme centers, so-called “*neo-classical model*” (**Figure 3.3.12**).²²⁴ According to this model, the first electron has an equal affinity to either heme *a* or *a*₃. If the electron is bound to the heme *a* ($E_m a (R)$), the binding of the second electron to the heme *a*₃ is inhibited ($E_m a_3 (O)$), and vice versa. The redox potentials of both are strictly coupled their contributions overlap in the UV-Vis.

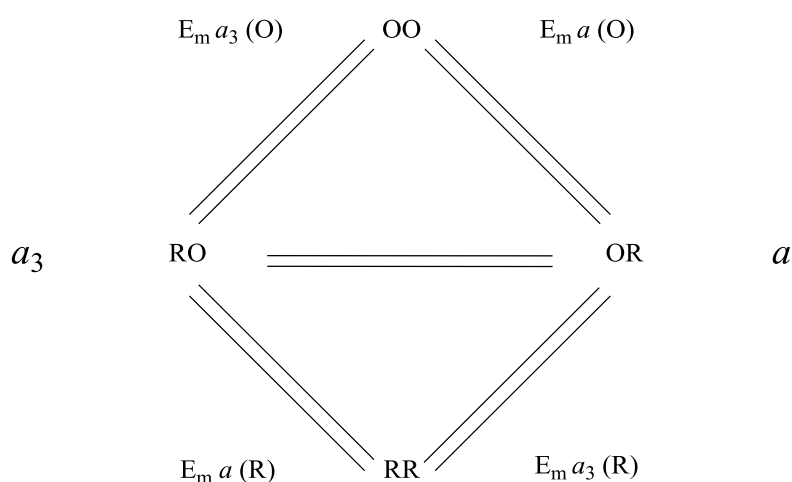


Figure 3.3.12. The neo-classical model of the anti-cooperativity of the heme centers of CcO. The left site is the *a*₃ site and the right site is the *a* site. E_m stands for the midpoint potential, R for the reduced state and O for the oxidized state. The letter in parenthesis shown for each E_m indicate the redox state of each center not undergoing a redox reaction.

The fitting of the absorbance change of the Soret band to the Nernst equation for our data are shown in the **Figure 3.3.13**. Two midpoint potentials can be observed, the low midpoint potential includes the heme *a*₃ and the high one includes the heme *a* redox transitions. The addition of Zn cations to the enzyme induced an upshift of both redox transitions. The most affected one is the higher one where it shifts from +97 mV to +161 mV.

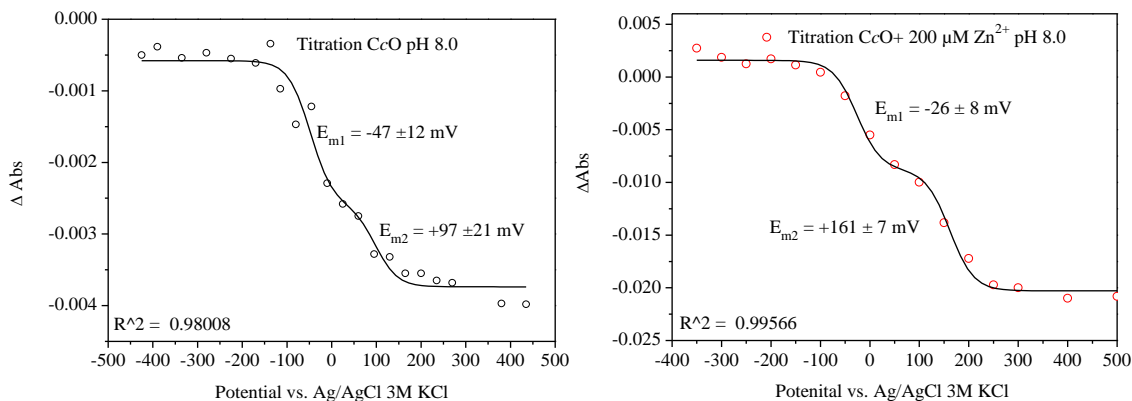


Figure 3.3.13. Titration curves of the wild-type CcO in the native form (left panel) and in presence of Zn cations (right panel).

The gap between the low and high potentials becomes larger in presence of Zn cations, however, the reversibility of the heme *a* is not ideal. The observed shift of the midpoint potentials affects probably the efficiency of the electron transfer from the Cu_A to the heme *a*. The observed shifts are in line with the data obtained by FTIR difference spectroscopy. Zn binding blocks the proton transfer. Two interaction sites are discussed: first, in the vicinity of the of the proton exit-pathway. Second, the site involving Glu78 of the subunit II, close to the K-pathway entrance. The Glu78 of the subunit II of CcO from *Rhodobacter sphaeroides* was shown by X-ray crystallography to bind Zn.¹⁰⁸ The crystal structure of the Zn bound CcO from *P. denitrificans* is not available yet. In order to check whether or not if the Glu78 is involved in the binding of Zn cations, the Glu78Ala mutation of CcO from *P. denitrificans* was investigated.

3.3.3. Difference spectroscopy of the Glu78Ala CcO

3.3.3.1. UV-Vis difference spectroscopy

The UV-Vis difference spectra of the Glu78Ala samples are similar to those obtained for the wild-type enzyme. The reaction rates are slower than the ones observed for the wild-type. The fully oxidized mutant is reached eight minutes after the application of the oxidizing potential, and the fully reduced one after ten minutes (**Figure 3.3.14**).

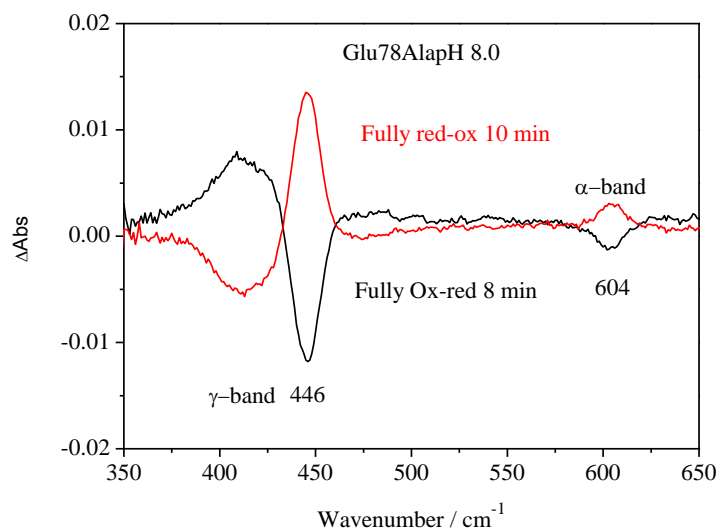


Figure 3.3.14. UV-Vis difference spectra of the Glu78Ala CcO at pH 8.0.

Upon inhibition, the redox reaction becomes even slower (**Figure 3.3.15**). The oxidation of the enzyme takes ten minutes to be achieved, the reduction takes fourteen minutes. The slower reaction times give direct evidence on the binding of Zn cations to the mutant. Thus, the Glu78 of the subunit II is not an exclusive binding site.

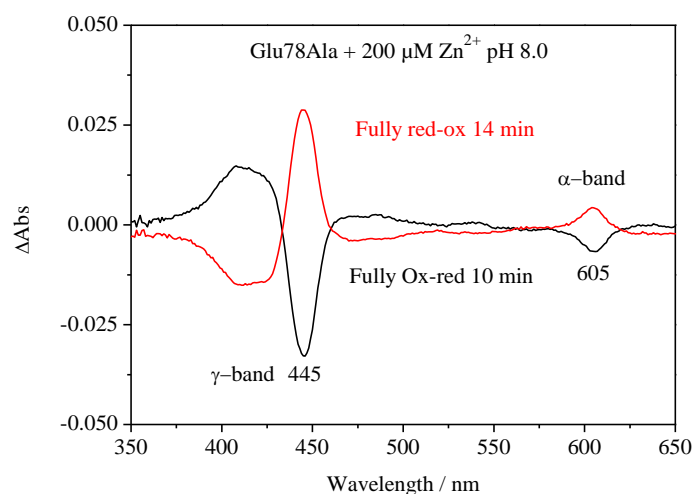


Figure 3.3.15. UV-Vis difference spectra of the Glu78Ala CcO in presence of Zn cations at pH 8.0.

3.3.3.2. FTIR difference spectroscopy

The oxidized minus reduced FTIR difference spectra of the Glu78Ala samples in presence and absence of Zn cations are shown in the **Figure 3.3.16**.

The spectra of the mutant are similar to those obtained for the wild-type enzyme. However, subtle changes might occur due to the point mutation of the Glu78.²¹³

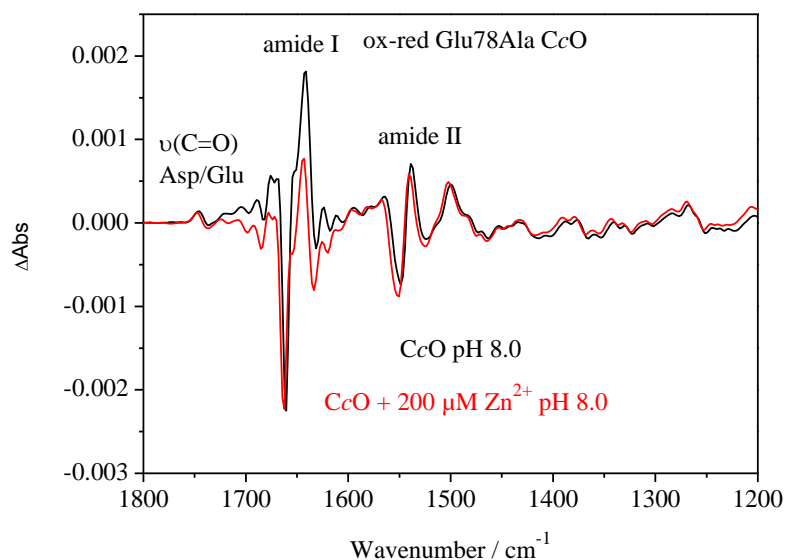


Figure 3.3.16. Ox-red FTIR difference spectra in the region 1800–1200 cm^{-1} of the Glu78Ala CcO recorded at pH 8.0 before (black) and after the inhibition (red).

Before discussing the effect of Zn binding to the mutant, the effect of the mutation on the difference spectrum needs to be visualized. In order to do so, the double difference spectrum obtained from the subtraction of the difference spectrum of the mutant from that of the wild-type is calculated (**Figure 3.3.17**). The double difference spectrum shows several signals in the amide I region that may arise from the hemes as well as from the backbone reorganization. It is thus clear that the mutation affects the redox reactions of the hemes. In the amide II region, a broad positive signal is seen with two maxima at 1576 and 1554 cm^{-1} . The fact that these signals are of positive signs means that the residue responsible of these signals is present in the wild-type and not in the mutation, for instance, the Glu78Ala mutation. The assignment of these signals to the $\nu(\text{COO}^-)^{\text{as}}$ vibration of the side chain of Glu78 is likely. Previous FTIR investigation of both, the wild-type and the Glu78Ala mutation at pH 7.0 allowed the assignment of a signal at 1547 cm^{-1} to the side chain of absorption of Glu78.²¹³ Accordingly, the signal observed, in the double difference spectrum calculated at pH 8.0, at 1554 cm^{-1} is tentatively assigned to the Glu78 residue. Furthermore, the double difference spectrum exhibits a positive signal at 1405 cm^{-1} . This signal can be arising from the $\nu(\text{COO}^-)^{\text{s}}$ vibration of either the Glu78 or the propionates.

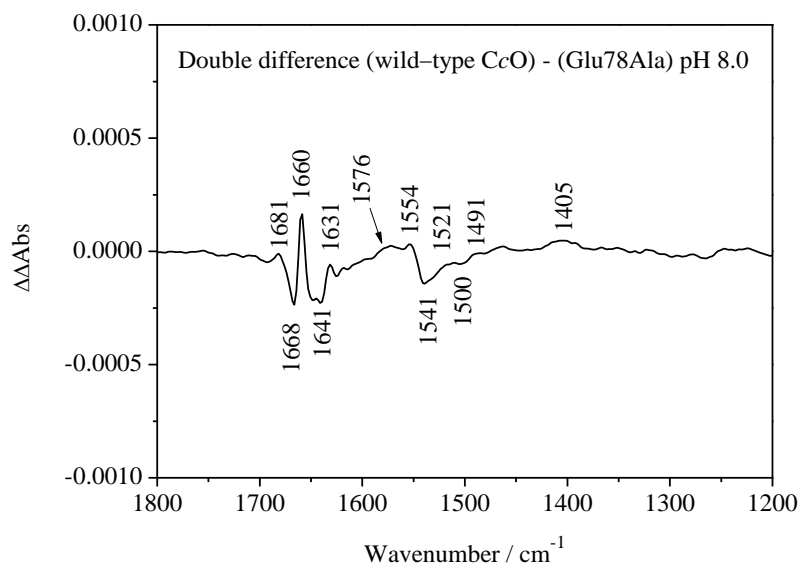


Figure 3.3.17. Double difference spectrum of the wild-type CcO minus Glu78Ala CcO recorded at pH 8.0. The difference spectra were normalized to the δ_{42} vibration of the hemes.

The spectral modifications caused by the binding of Zn cations to the inhibited Glu78Ala mutation can be seen in the double difference spectrum calculated by subtracting the difference spectrum of the inhibited enzyme from the difference spectrum of the mutant alone (**Figure 3.3.18**). It should be noted that the same approach was used to obtain the double difference spectrum where the normalization of several signals was performed (See **Appendix 9**).

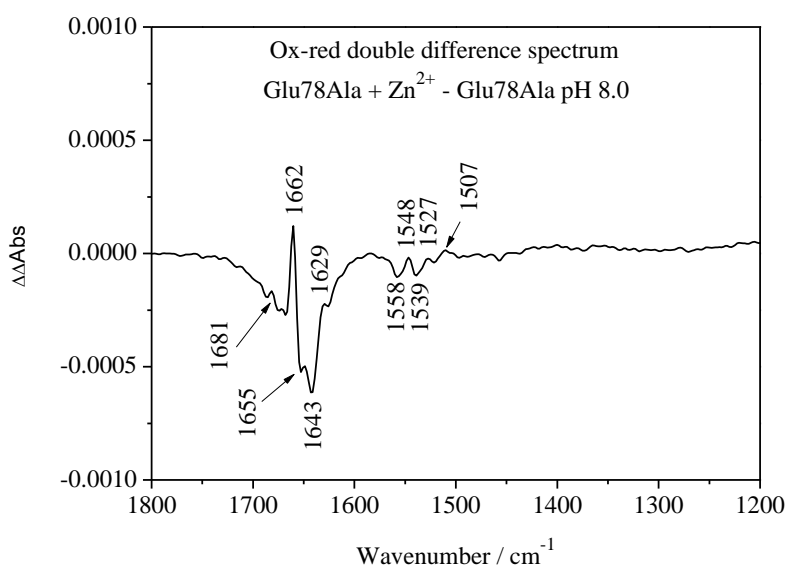


Figure 3.3.18. Double difference spectrum of the inhibited Glu78Ala CcO plus Zn^{2+} minus the native Glu78Ala at pH 8.0. The difference spectrum was normalized to the δ_{42} vibration of the hemes.

The double difference spectrum shows no modifications in the signature of the protonated Glu278. It is thus clear that the binding of Zn cations to this residue in the D-pathway is unlikely. On the other hand, the region where the $\nu(\text{C}=\text{O})$ vibrations of other protonated acidic residues and the protonated heme propionates is affected by the inhibition can be seen (**Figure 3.3.18**); however, the baseline drifts slightly due to the water absorption in the amide I region. This negative signal results from the deprotonation of acidic residues and/or the heme propionates.

In the amide I region, sharp positive and negative signals can be seen. Those signals were previously assigned mainly to the heme a_3 and to backbone contribution.²²³ The oxidized minus reduced difference spectra of both, the heme a and a_3 were reported elsewhere.²²³ The reported oxidized minus reduced difference spectrum of the heme a_3 showed positive signals at 1656 and 1642 cm^{-1} and negative signals at 1662 and 1632 cm^{-1} . The double difference spectrum presented here shows similar signals, but with reversed signs. Thus, we assign these signals to the heme a_3 vibrations. The fact that these signals are reversed in the double difference spectrum indicates that the binding of Zn cations to the mutant inhibits the redox reaction of the heme a_3 .

The amide II region shows two negative and two positive signals. The negative ones at 1558 and 1539 cm^{-1} , the positive ones at 1548 and 1527 cm^{-1} . These signals fit well with the side chain absorptions of deprotonated acidic residue or the heme propionates. Based on the ^{13}C -isotopic labeling of the heme propionates, these moieties are expected to contribute at approximately 1570 and 1538 cm^{-1} .¹²⁰ Indeed, the deprotonation of acidic residue observed in the region above 1700 cm^{-1} , would give rise to the positive signal at 1548 cm^{-1} . The other positive signal arising at 1527 cm^{-1} can be assigned to the amide II modes.

The negative signals arising at 1558 and 1539 cm^{-1} can be arising from the side chain absorptions of deprotonated acidic residues addressed by the electrochemical reaction. It can be expected that the Zn binding site is located within the exit-pathways. A possible candidate is the Asp399 residue which has a pK_a close to 4.8, and gives rise to a signal at 1556 cm^{-1} at pH higher than 4.8.²²⁵ The implication of this residue in the binding of Zn cations would support the decreased redox activity. Studies on the Asp399 mutant enzyme would help determining whether or not this residue bind Zn cations.

3.3.3.3. UV-Vis titration

The binding of Zn cations to the mutant enzyme showed a decrease in the redox activity of the heme a_3 . The spectra recorded during the oxidative titration of the Glu78Ala CcO are shown in the **Appendix 10**.

The UV-Vis titration was performed on both, the mutant and its inhibited form. The obtained results are shown in the **Figure 3.3.19**. The midpoint potentials of both hemes are upshifted due to the mutation of the Glu78 residue in contrast to the wild-type. The upshift of the high midpoint potential is more pronounced than the low one. Indeed, the Glu78 mutation has a considerable indirect effect on the electron transfer of the hemes. Upon inhibition, the midpoint potentials of both hemes are not significantly affected. Therefore, the modifications observed by FTIR difference spectroscopy upon inhibition of the Glu78Ala mutant might be indirect effects of the binding of Zn cations to the exit-pathways.

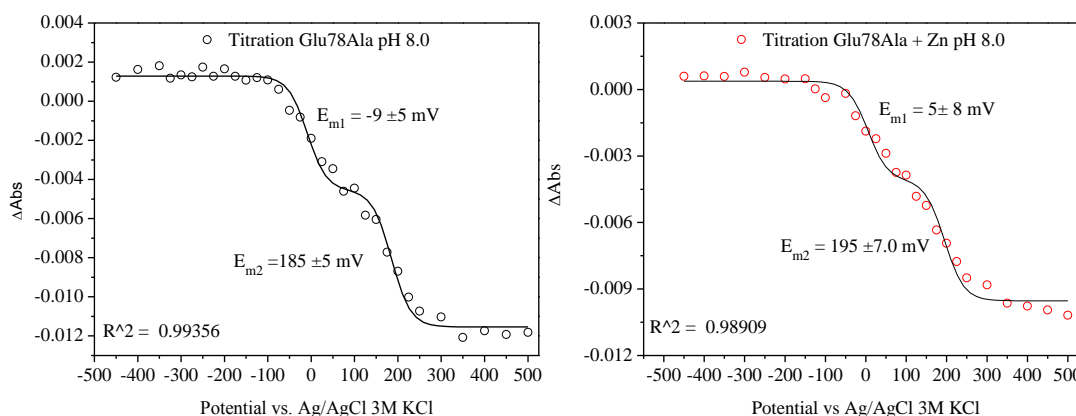


Figure 3.3.19. Titration curves of the Glu78Ala CcO in the native form (left panel) and in presence of Zn cations (right panel).

3.3.4. Conclusion

The binding of Zn cations to the CcO from *P. denitrificans* is shown to affect the proton transfer by the K-pathway. The results obtained by FTIR and UV-Vis difference spectroscopies point towards the decrease of the electron transfer reaction. Furthermore, the midpoint potential of the hemes are more positive in presence of Zn cations, thus the reduction of molecular oxygen at the active site could be affected. The redox signature of the Glu278 is not affected by the inhibition.

The data obtained by the FTIR difference spectroscopy show that Zn cations are probably bound to deprotonated acidic residues, including the Glu78 residue of subunit II.

The addition of Zn cations to the mutant Glu78Ala sample still induces a decrease of the reaction rates. Thus, the Zn cations still bind to the CcO lacking the Glu78 residue. These observations allowed suggesting another binding site of Zn cations than the K-pathway. Furthermore, the FTIR difference spectroscopy showed that the electron transfer by the heme a_3 is affected by the binding of Zn cations to the mutant. Therefore, the binding site of Zn cations is suggested to be close to the heme a_3 . The Asp399 residue is suggested to be a possible ligand of Zn cations since it was also shown to be involved in hydrogen bonding with the propionates of the heme a_3 . The mutation of this residue against Lys showed a considerable loss of proton pumping activity. Additionally, other acidic residues such as the Asp193 or Glu218 from the exit-pathways are also possible candidates to bind Zn cations. Yet, these suggestions still need to be supported by site-directed mutagenesis to confirm whether or not the Asp399 or other potential candidates bind Zn cations.

3.4. Far infrared spectroscopy

3.4.1. Introduction and development of the method

The FIR spectral domain is of great importance due to the rich chemical and physical processes observable. The lower frequency region is little studied for proteins. Besides the backbone vibrations observed in the MIR domain, other backbone vibrations can be found in the low frequency range, namely the amide IV, V, VI (800–500 cm^{-1}) and VII (below 250 cm^{-1}). The amide VI band was first described for N-Methylacetamide.²²⁶ In polyamide-containing polymers¹⁸⁰ (and references therein) the amide VI band appears at 580–590 cm^{-1} for polyesters and that the band position depends on the crystalline form.¹⁸⁰

The FIR domain contains also the metal–ligand vibrations in the 500–250 cm^{-1} region. The metal–ligand vibrations are of great importance to investigate proteins. The observation of the metal–ligand vibrations was done almost all the time by means of Raman and resonance Raman spectroscopies. In the mean time, these signals are accessible thanks to the technical development of the optical elements of FTIR spectrometers. It should be noted that the absorption coefficient of the metal–ligand vibrations is low, and only little sample is available for proteins that are then diluted in aqueous solutions. Indeed, the study of metal–ligand vibrations requires powerful FIR sources, such as the Hg–vapor source or even better, synchrotron light source. In addition, the development of diamond crystal ATR allows recording the spectra in the whole MIR and FIR domains (4000–50 cm^{-1}). The investigation of proteins by means of FIR spectroscopy is gives also access to the contribution of hydrogen bonding collective motions observed below 300 cm^{-1} . These collective motions involve large number of atoms and give rise to a broad band below 300 cm^{-1} . Such a band was previously observed for water,¹⁷⁸ and hydrogen bonded systems with large proton polarizabilities.²²⁷ Similar collective motions in biological macromolecules such as proteins give also rise to a large band in the FIR range.²²⁸ Besides of the contribution of intra– and intermolecular hydrogen bonding of proteins, the collective motions include also contributions from water chains within proteins and the hydration shells.^{229–231}

In recent years, the FIR or terahertz (THz = 30 cm^{-1}) spectral region has seen a flurry of research activity. Research activities in this spectral domain started with the prediction of the collective structural vibrational modes first presented almost 40 years ago for DNA.²³² The FIR contribution of a wide range of molecules is dominated by vibrations involving a substantial fraction of the atoms forming the molecule and motion associated with

intermolecular hydrogen bond vibrations. The study of their temperature–dependence makes it possible to clarify the role of intermolecular forces, since temperature has a large effect on Hydrogen–bonding. Further activities in the field include investigations of the time resolved reorganization of water within a protein refolding process in the picoseconds time scale.^{178,233}

Typical ATR spectrum of a metalloprotein, i.e. the Rieske protein in pure water is shown in **Figure 3.4.1** where the backbone vibrations, the metal–ligand vibrations as well as the hydrogen bonding collective motions can be observed.

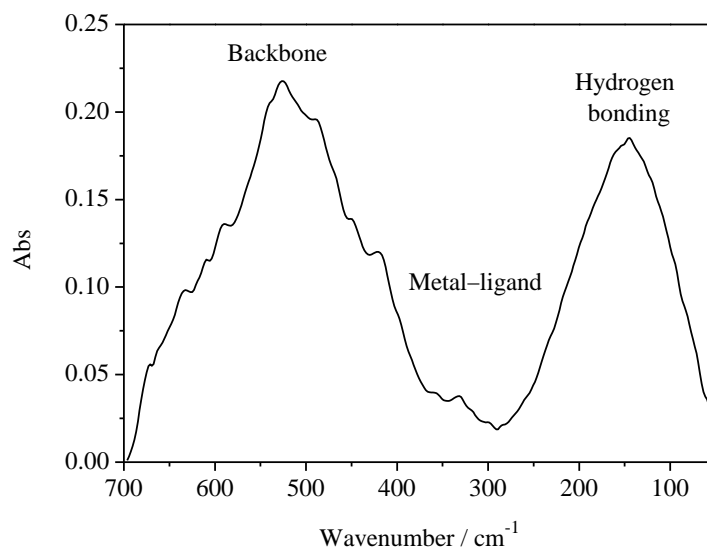


Figure 3.4.1. Typical contribution found in the FIR spectrum of a metalloprotein (Rieske).

However, protein samples are investigated in buffered solution, most of the time containing salt. It is thus crucial to determine the buffer and the salt contributions to the FIR spectral range which may overlap with the protein contributions. **Figure 3.4.2** shows the spectra of the NDF of *E. coli* in 50 mM MES buffer at pH 6.0 containing 50 mM KCl and the buffer alone. The MES buffer has a high intensity at the given conditions. In addition, the protein concentration is not very high (Typically ~ 1 mM). Thus, the contributions of the protein are masked by the contribution of the buffer.

In the region below 300 cm⁻¹, the hydrogen bonding collective motions are involved. Both spectra show a sharp band at 162 cm⁻¹. This signal is arising from the hydrogen bonds polarized by the salt.²³⁴ These observations lead us to conclude that the buffer and the salt concentration need to be the low in order to observe the contribution of the protein.

When the concentration of the buffer and salt is decreased to 20 mM (**Figure 3.4.3**), the contributions of the NDF protein can be probed without overlapping with the buffer or the salt.

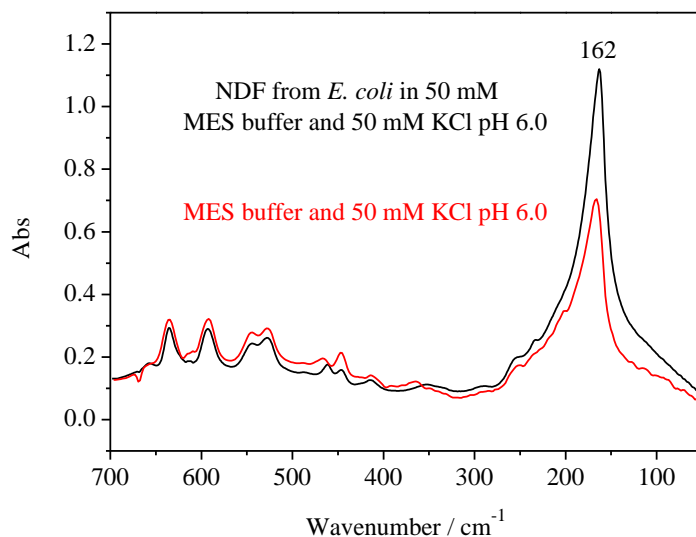


Figure 3.4.2. FIR-ATR absorbance spectra of the NDF (black) and the MES buffer (red).

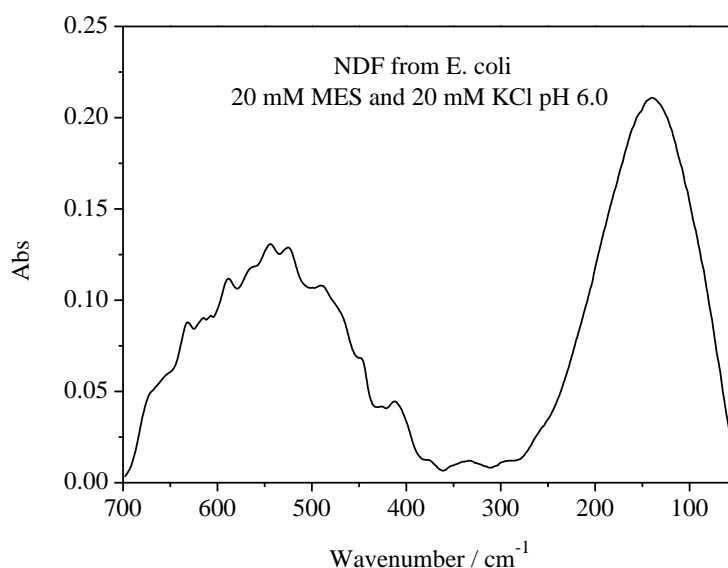


Figure 3.4.3. FIR ATR absorbance spectrum of the NDF in 20 mM MES buffer at pH 6.0 containing 20 mM KCl.

3.4.2. Amide VI

3.4.2.1. Introduction

In the FIR domain, the amide IV, V, VI ($800\text{--}500\text{ cm}^{-1}$) and VII (below 250 cm^{-1}) are found. Beside the amide I band, the amide II, III and V bands were previously reported to be sensitive to the secondary structure modifications of proteins and peptides.²³⁵⁻²³⁷ The amide I band, typically observed between 1700 and 1600 cm^{-1} includes the $\nu(\text{C}=\text{O})$ vibration of the amide group in a hydrogen bonding dependent manner.^{235,237-240}

Oberg *et al.*²⁴¹ used the comparison between the circular dichroism and infrared spectroscopy to obtain an accurate secondary structure analysis of a set of 50 proteins. It was described that circular dichroism is more accurate in the determination of the α -helical conformation than infrared spectroscopy. On the other hand, the β -sheet conformation is clearly identified using the amide I and amide II bands positions in an infrared spectroscopic approach, as compared to the circular dichroism.¹³⁹ Generally the use of the amide I band for the analysis of the secondary structures of proteins is well established.

The lower frequency region is little studied for proteins and as consequence the specificity of the amide VI band towards secondary structure of proteins was not analyzed yet; to our knowledge. The amide VI band was first described for N-Methylacetamide.²²⁶ In polyamide-containing polymers¹⁸⁰ (and references therein) the amide VI band appears at 580-590 cm^{-1} for polyesters and that the band position depends on the crystalline form.¹⁸⁰

Both, the amide IV and amide VI bands arise from in-plane and out-of-plane motions of the CONH group in the peptide backbone and are expected in the region 700-500 cm^{-1} , leading to controversial descriptions concerning the vibrational modes of the amide IV and VI bands. Studies attributed the vibrational mode to the $\delta(\text{C}=\text{O}/\text{C}-\text{C}-\text{N})$ of the amide function.^{140,180,226}

According to the literature, these modes are generally not observed in Raman spectra.²⁴²

Here we examine the amide VI band of a set of poly amino acids that show a well-known structural arrangement. Poly-L-lysine (PLL) is one of the most used model compounds in the field of protein aggregation since the transition that can be induced from the α -helical and the β -sheet form is the same that is discussed to take place during the protein aggregation process.^{243,244}

This transition is pH- and temperature-dependent. Venyaminov and Kalnin¹³⁹ showed that PLL has a random coil conformation at neutral pH. The changes to α -helix are observed around pH 11.2. Moreover, at this pH value, heating to 30-40 $^{\circ}\text{C}$ leads to the formation of the β -sheet conformation. The chain length is a major factor for the exact transition temperature; for chains shorter than 10 kDa, the transition does not take place.²⁴³

As a reference for the pure α -helical form, poly-L-alanine (PLA) is available. The previous vibrational analysis of the α -helical form was supported by the ab initio theoretical calculation, and the signals observed in the region 517-530 cm^{-1} were assigned to the amide IV band and not the amide VI band.²⁴⁵ The study reveals the complexity of this amide band. The band arises from the mixture of multiple, coupled vibrational modes: the $\delta_{\text{ip}}(\text{C}=\text{O})$ vibration, the $\delta_{\text{def}}(\text{C}-\text{C}-\text{N})$ vibration and $\delta_{\text{def}}(\text{C}-\text{C})$ vibration. To avoid ambiguities the

expression “amide VI” will be used to designate the band appearing in the region 590–490 cm^{-1} .

In order to better understand the relation between the secondary structure and the amide VI position, data obtained for the poly amino acids with a well defined structure are compared to data for proteins from the respiratory chain where the secondary structure is mostly of a mixed character. The studied proteins are the bc_1 , CcO and the Rieske protein. The structure of these proteins is known.^{85,104,105,246}

3.4.2.2. Model compounds

3.4.2.2.1. PLL

Figure 3.4.4 shows the amide I (amide I' for the deuterated samples) and amide VI band (amide VI' for the deuterated samples) of the PLL films in H_2O (Black), in D_2O (Red), at pH 11.20 (Blue) and at pD 11.20 (Magenta). The signals of the amide I/amide I' band are observed at 1652 cm^{-1} in D_2O and at 1656 cm^{-1} in water. The signal position is typical for α -helical contributions.²³⁵

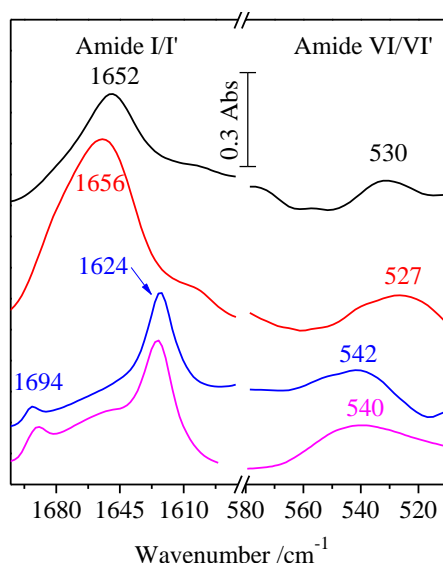


Figure 3.4.4. Amide I/amide I' and amide VI/amide VI' band of PLL in H_2O (Black), in D_2O (Red), at pH 11.20 (Blue) and at pD 11.20 (Magenta).

Once the pH (D) is raised to 11.20, the signal splits into two peaks at 1626 and 1694 cm^{-1} indicating that β -sheets are formed. In the FIR, the amide VI signal appears at 530 cm^{-1} for the PLL dissolved in water and at 542 cm^{-1} for the sample at a pH value of 11.20. The amide VI' is observed at 527 cm^{-1} at neutral pD and shifts to 540 cm^{-1} at pD 11.20. It is known that a higher temperature is necessary for the transition from α -helical to the β -sheets form,^{139,244}

here it occurs at room temperature. This difference may be explained by the strong interaction of the film with the surface that is absent in the diluted solutions often used.

Based on the secondary structure analysis of the data presented in Figure 3.4.4, it can be concluded that in pure water the α -helices predominate the amide I band with a relative contribution of 86 % (Table 3.4-1). In the case of the sample dissolved in D₂O, the relative contribution for α -helices seems to be reduced to 69 % (Table 3.4-1).

This discrepancy may be explained by the fact that in PLL a full H-D exchange was not possible due to internal water molecules. The incomplete shift of the amide II to amide II' position confirms this interpretation; the analysis of the low frequency region is thus only possible in a quantitative way in order to allow the attribution of the bands position. No random coils and only a small percentage of β -sheet elements (4-9 %) have been calculated for the amide I band. At pH 11.20 (pD 11.20) the relative contribution of the α -helices is decreased to ~ 10 % while the contribution of β -sheet is increased to ~ 75 % (Table 3.4-1). This behavior is attributed to the aggregation of PLL at pH 11.20 (pD 11.20). The double signals appearing in the spectrum at 1694 and 1626 cm⁻¹ are typical for the intermolecular β -sheet formation.^{85,247,248} They are also marker bands of the aggregation.²⁴⁹

We note that a clear difference between the random coil signal and the other secondary structure elements is not always evident from the fits of the amide I range. Whenever fitted we note it in the text, however, present it together with β -sheet structures in the table, in order to be able to show a clear number.

In the region of the amide VI/amide VI' band a large signal can be observed (Figure 3.4.4). An upshift of the maxima from ~ 527 cm⁻¹ to ~ 542 cm⁻¹ is observed when the pH/pD is raised from neutral to basic. We attribute this upshift of 15 cm⁻¹ to the secondary structure transition. The signal appearing around 527 cm⁻¹ is thus attributed to a predominately α -helical contribution and the one at 542 cm⁻¹ to β -sheet contributions (Table 3.4-1, note: maxima given here arise from the fit). The fitting of the amide bands was based on the second derivatives of the spectra (See Appendix 11). This assignment is confirmed by the good correlation between the relative contributions of α -helix to the amide I (I') and at the same time to the VI (VI') bands. In contrast to the signal for the α -helical compound, the β -sheet and β -turns contributions seem to be well defined at this pH (pD) value, perhaps due to a side chain contribution in the low frequency spectral range.¹⁷⁷ The H-D exchange slightly affects the amide VI' position: The β -sheet contribution is observed at 545 cm⁻¹ at pD 11.20, and at 539 cm⁻¹ at pH 11.20. At pH 11.20, the contribution from β -sheet and random coils is estimated to be 79 % from the MIR data and 69 % from the FIR data (Table 3.4-1).

Sample	PLL H ₂ O	PLL D ₂ O	PLL pH 11.20	PLL pD 11.20	
Amide I	% α -helix	86 (1658)	69 (1656)	10 (1652)	11 (1658)
	% β -sheet and random coils	4 (1695/1626)	9 (1620)	59 (1626) 20 (1694/1645/1638)	70(1628) 4(1648) 7(1674)
	% β -turns	10 (1685)	19 (1672/1684)	11 (1688/1668)	8 (1694)
	% other contributions		3 (1600)		
Amide VI	% α -helix	81 (524/530)	69 (526)	8 (529)	12 (518)
	% β -sheet and random coils	10 (539)	21 (541)	69 (539/533)	79 (545)
	% β -turns		1 (554)	19 (552)	8 (557)
	% other contributions	9 (508)	9 (507)	4 (508)	1 (508)

Table 3.4-1. Percentage of the secondary structure elements of all the PLL samples calculated from the fitting of Gaussians in the MIR and FIR. (The corresponding positions in cm⁻¹ are indicated in parentheses). We note that the “other contributions” involve signals from amino acid side chains.

The α -helical contribution arising at 529 cm⁻¹ also correlates with the one observed in the amide I spectral range. The signal at 552 cm⁻¹ can be assigned to β -turns. The signal at 533 cm⁻¹ is assigned to random coils; however it is difficult to be distinguished from the β -sheet signal.

3.4.2.2.2. PLA and PLH samples

The PLA is a model compound that was extensively studied by several techniques.^{139,245,250} The exact conformation of the peptide is highly dependent on the sample preparation, pH and temperature.²⁴⁵ The FTIR spectroscopic study of the PLA at pD 9.0 in the MIR domain shows an amide I' band (Figure 3.4.5) typical for a secondary structure organized in a α -helical conformation (Table 3.4-2). The β -sheet contribution is very small at pD 9.0. In the FIR domain, the amide VI' is also found at 524 cm⁻¹, the respective low frequency position for the α -helical contributions (Figure 3.4.5).

The analysis of the amide VI' band shows that 73 % of the secondary structure is organized in. The relative β -sheet contribution is calculated to be 20 % and 7 % of the total conformation of PLA is assigned to β -turns. From the amide I' band, the α -helical form it can be estimated to be 49 % (Table 3.4-2). The fitting of the amide bands was based on the second derivatives of the spectra (See Appendix 12).

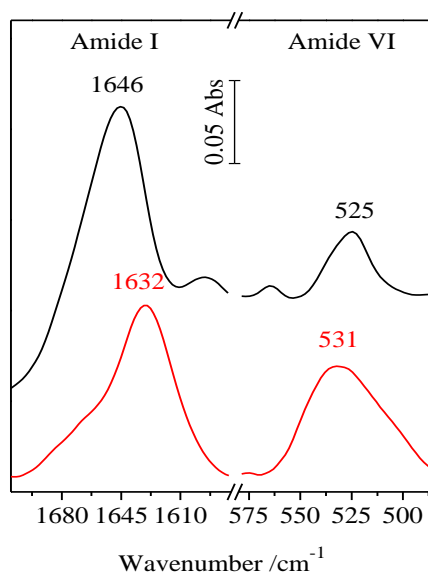


Figure 3.4.5. Amide I and amide VI band of: PLA at pD 9.0 (Black) and PLH at pD 7.0 (Red).

The spectra of PLH are also recorded in the MIR and FIR domains at pD 7.0 (Figure 3.4.5) and the signals show a structure where more than 60 % of the peptide are organized in the β -sheet conformation (Table 3.4-2). Based on the analysis of amide VI' signal and of the amide I' signal, the relative contribution of the β -sheet structural elements can be estimated to be 60 %. The contributions of the α -helical and the β -turn secondary structure elements, depicted in the amide I' and VI' region, correlate well (Table 3.4-2).

Sample		PLA pD 9.0	PLH pD 7.0
Amide I	% α -helix	49 (1661/1649)	28 (1654)
	% β -sheet and random coils	43 (1684/1639/1633)	61 (1630)
	% β -turns		11 (1684/1670)
Amide VI	% α -helix	73 (524)	25 (517)
	% β -sheet and random coils	20 (538)	59 (540)
	% β -turns	7 (565)	11 (552)
	% other contributions		5 (500)

Table 3.4-2. Percentage of the secondary structure elements of the PLA pD 9.0 and PLH pD 7.0 calculated from the fitting of Gaussians in the MIR and FIR. (The corresponding positions in cm^{-1} are indicated in parentheses). We note that the "other contributions" involve signals from amino acid side chains.

3.4.2.2.3. Protein samples

Figure 3.4.6 gives a general view of the amide I band from 1700 to 1600 cm^{-1} and the amide VI band in the far IR range from 590 to 490 cm^{-1} of different proteins from the respiratory chain. The amide I bands of the CcO and the bc_1 appear at 1655 and 1650 cm^{-1} (Figure 3.4.6), respectively; both maxima indicate a high α -helical contribution. This is in line with the X-ray structure.^{104,105}

The analysis of the amide I band shows that 55 % of the secondary structure of the bc_1 is organized as α -helices (Table 3.4-3), whereas the β -sheet contribution is 32 %. The CcO signal shows, besides a high ratio of the α -helix contribution, considerable amounts of β -sheet (32 %). The fitting of the amide bands was based on the second derivatives of the spectra (See Appendix 13). The results obtained for the amide VI band of the CcO show a maximum at 527 cm^{-1} . The detailed analysis of this band (Table 3.4-3) shows that the amide I and amide VI band are well correlated and both of them indicate, as expected, a high α -helical contribution. It seems, however, that the amide VI analysis led to the overestimation of the α -helical and to the underestimation of the β -sheet contribution when compared to the crystal structure. No signal was assigned to β -turns in the amide VI signal, while 9 % of the signal is supposed to involve contributions from amino acid side chains. The same observation can be made for the bc_1 , where the crystal structure shows a predominately α -helical structure.^{85,104,105} The amide I band indicated 55 % and again the amide VI band led to an overestimation of the α -helical contribution (66 %). The β -sheet and β -turns contributions, as depicted from the amide VI, are underestimated most likely because of the important side chain contribution appearing at 505 cm^{-1} (Table 3.4-3).

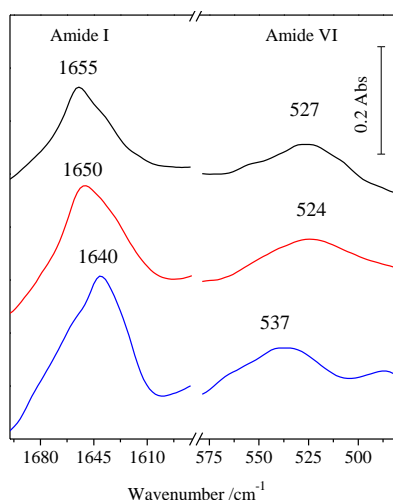


Figure 3.4.6. Amide I and amide VI bands of: the CcO (Black), the bc_1 (Red) and the Rieske protein (Blue).

Sample (PDB code)	CcO (3HB3)	bc_1 (1ZRT)	Rieske (RIE)	
X-ray data	% α -helix	46	52	3
	% β -sheet	18	4	29
	Unassigned	36	44	58
Amide I	% α -helix	51 (1653)	55 (1652)	15 (1661)
	% β -sheet and random coils	32 (1621/1633)	32 (1636)	72 (1626/1641)
	% β -turns	17 (1673/1681)	10 (1676)	13 (1680)
	% other contributions		3 (1612)	
	% α -helix	53 (522)	66 (526)	21(524)
Amide VI	% β -sheet and random coils	31 (540)	10 (542)	60 (539)
	% β -turns	7 (556)	14 (552)	18 (552)
	% other contributions	9 (508)	10 (505)	

Table 3.4-3. Percentage of the secondary structure elements of all investigated proteins calculated, fitting of Gaussians in the MIR and FIR. (The corresponding positions in cm^{-1} are indicated in parentheses). The PDB code of each structure is indicated in bold. We note that the “other contributions” involve signals from amino acid side chains.

The water-soluble fragment of the Rieske protein from *T. thermophilus* has an overall β -sheet fold.²⁴⁶ Again, comparing amide I and VI, the β -sheet contribution is underestimated by the amide VI analysis (Table 3.4-3). Another major difference is the clear discrepancies to the data from the X-ray analysis. Since Fe-S vibrations (i. e. out-of-phase breathing motions of the linked FeS_4 tetrahedra) are expected in this spectral range,²⁵¹ some overlapping may be expected. In this case the amide IV signal cannot be used to analyze the secondary structure in Fe-S proteins.

3.4.2.3. Conclusion

The amide VI band in the far infrared was probed on the basis of a set of three different polyamino acids, with well-defined secondary structures each and three different proteins, with known crystal structures, respectively. This signal includes the $\delta(\text{C}=\text{O}/\text{C}-\text{C})$ vibration. The position of the amide VI band for each secondary structure element was determined on the basis of the comparison with the amide I data simultaneously obtained on the same samples. We note that the amide I signal is about three times more intense than the amide VI band. Furthermore, the penetration depth is $\sim 5 \mu\text{m}$ at 500 cm^{-1} and $\sim 1 \mu\text{m}$ at 1650

cm^{-1} . Thus, the intensity of the amide VI band is five times artificially enhanced in contrast to the amide I band. Signals observed in the spectral region around $517\text{--}530\text{ cm}^{-1}$ could be correlated with α -helical structures and the region $540\text{--}545\text{ cm}^{-1}$ with β -sheet conformations. The signals appearing at $\sim 565\text{ cm}^{-1}$ could be discussed to arise from β -turns and the random coils to be contributing at $\sim 535\text{ cm}^{-1}$, however are not really found to be distinguishable from the β -sheet signals. For α -helices and β -sheet, a good agreement between the expected structure and the respective analysis of the relative contribution within the amide I and the amide VI band was found. The amide VI band of other peptides and proteins was investigated in the laboratory and the analysis corroborate with the data presented here. We note, however, that the amide VI band seems to be less accurate when it comes to determine the amount of β -turns and random coils present in the studied sample. In some cases contributions from the amino acid side chains lead to over or under estimation of a relative contribution. Fe-S center seem to show overlapping signals in the same spectral region.

This study was the first analysis on the specificity of the amide VI band for the contributions of secondary structural elements. The data obtained is important in light of the increasing number of studies in the field of far infrared spectroscopy on proteins, with conventional and synchrotron light sources. Reaction induced FTIR difference spectra are now being obtained below 1000 cm^{-1} ^{164,165} and the study presented here will allow interpreting difference signals in the spectral range of the amide VI band as conformational changes of the protein backbone.

3.4.3. Far infrared electrochemically induced FITR difference spectroscopy

3.4.3.1. Horse heart cytochrome *c*

The electrochemically induced FIR difference spectroscopy can provide valuable information about both, the oxidized and reduced forms of proteins. The first electrochemically induced FIR spectra of proteins were reported for the horse heart cytochrome *c* (**Figure 3.4.7**) and its model compounds and the data were obtained using wedged diamond windows (to suppress interference oscillations) for the sample compartment and a He-cooled bolometer as detector. ^{164,165}

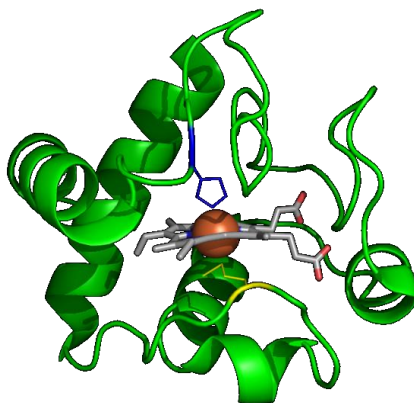


Figure 3.4.7. Structure of the horse heart cytochrome *c* (PDB code 1HRC). The heme is colored in white, the coordinating His in blue and the coordinating Met in yellow.

At the same time, the development of the FIR electrochemically induced difference spectroscopy has begun in our laboratory. The first successful experiments were done at the ANKA facility, where the Hg-vapor lamp was used as source of FIR light. The emission spectra of globalar, Hg-vapor and synchrotron FIR sources are shown in Appendix 14. The electrochemical cell developed by Moss and co-workers,¹⁴⁴ was modified where 2 mm thickness silicon windows replace the calcium fluoride windows to reach the FIR domain. The horse heart cytochrome *c* was studied and the difference spectrum obtained after five redox cycles is similar to the one reported by Berthomieu *et al.*¹⁶⁵ (**Figure 3.4.8A**). We can show that the FIR redox signature of the metal-ligand vibrations of the cytochrome *c* is accessible without using wedged diamond windows. The difference spectrum was reproduced in the laboratory in Strasbourg where the spectral region between 900 and 800 cm^{-1} is accessible using the silicon windows (**Figure 3.4.8B**).

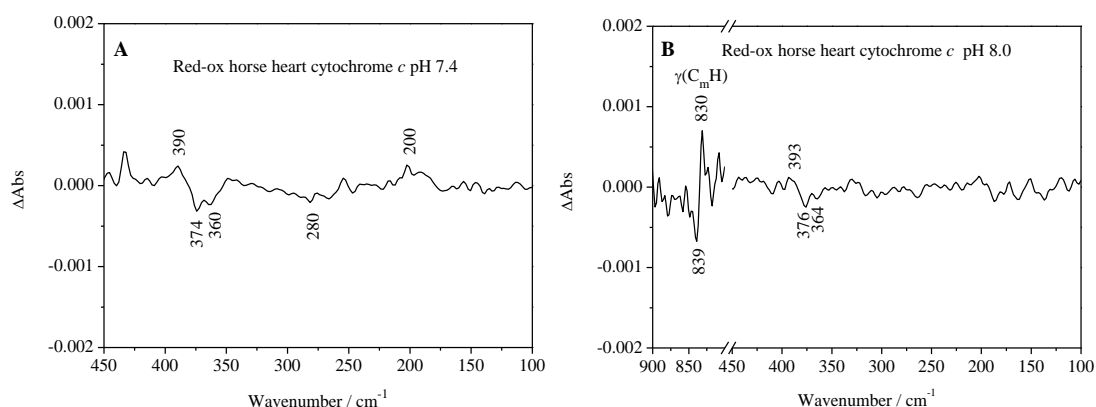


Figure 3.4.8. (A) Reduced minus oxidized difference spectrum of the horse heart cytochrome *c* obtained in the ANKA synchrotron facility and (B) obtained in the laboratory in Strasbourg.

This spectral region contains the $\gamma(\text{C}_m\text{H})$ vibration, typical for heme cofactors. On the other hand, the spectra recorded using the 2 mm thickness silicon windows can be improved using 1

mm thickness silicon windows. It should be noted that the parallel positioning of silicon windows must be avoided in order to prevent multiple reflection phenomenon, causing the loss of the infrared signal. In addition, the pathlength is reduced below $6\ \mu\text{m}$ to overcome the high absorption of the solvent (**Figure 3.4.9**).

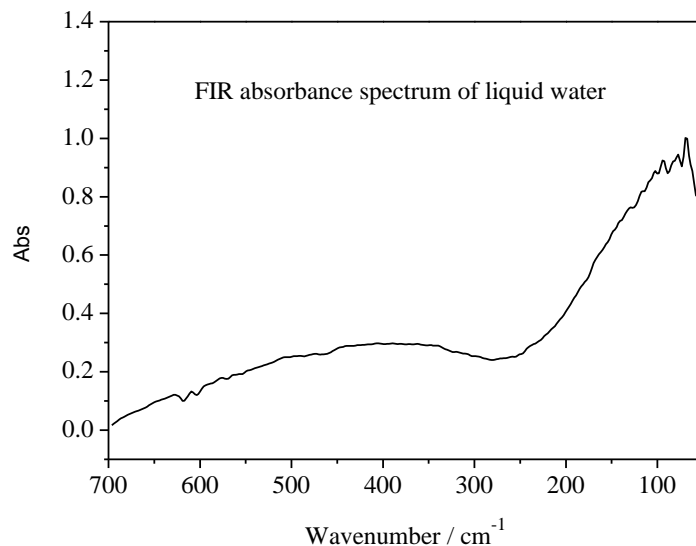


Figure 3.4.9. FIR ATR absorbance spectrum of liquid water.

The different FIR setups used for to perform the electrochemically induced difference spectroscopy are presented in the **Figure 3.4.10**.

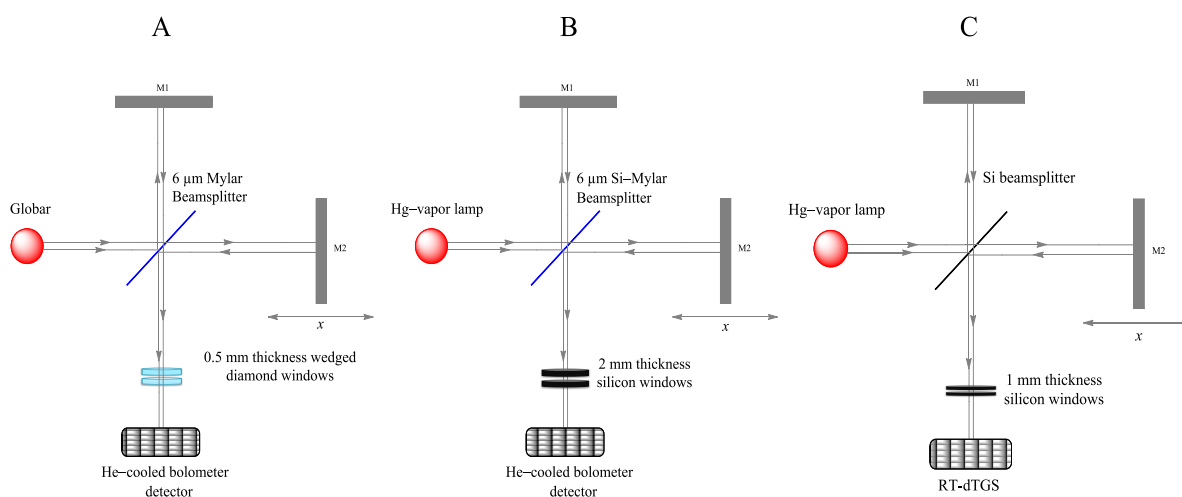


Figure 3.4.10. Optical setups for the electrochemically induced FIR difference spectroscopy. (A) The setup developed by Berthomieu *et al.*, (B) the setup used at ANKA and (C) the setup developed in our laboratory.

The cell developed by Berthomieu *et al.* allows recording difference spectra in the spectral region of $650\text{--}50\ \text{cm}^{-1}$. However, the Mylar beamsplitter has a high absorption at $375\ \text{cm}^{-1}$. The setup accessible at the ANKA facility is also equipped with Mylar beamsplitter while the one used in our laboratory is equipped with a silicon beamsplitter which has a sharp

absorption at 620 cm^{-1} . The region below 620 cm^{-1} is completely accessible without observing signals from the optics. On the other hand, the spectrometer in our laboratory is equipped with a RT-dTGS detector instead of the He-cooled bolometer used at the ANKA facility, leading to a lower signal-to-noise ratio.

3.4.3.2. Rubredoxin

The optimization of the electrochemical cell to the lower frequency region allowed recording the electrochemically induced FIR difference spectra of several ISP. Hence we report the absorbance and the electrochemically induced FIR difference spectra of various ISP containing one, two, or four iron atoms (**Figure 3.4.11**).

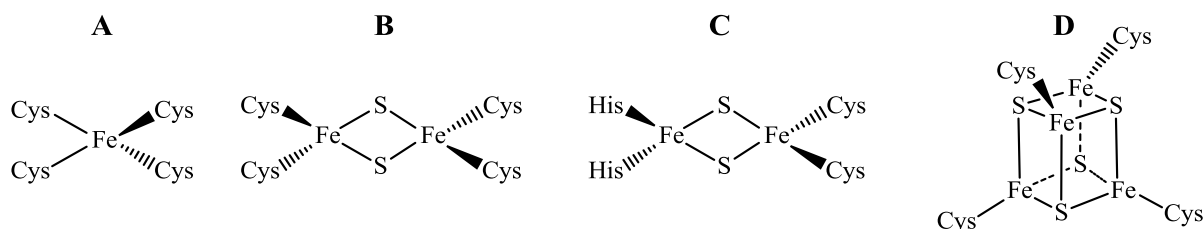


Figure 3.4.11. Iron-sulfur clusters of (A) Rb from *C. pasteurianum*, (B) Fd from spinach, (C) Rieske from *T. thermophilus* and (D) Fd from *C. pasteurianum*.

Rbs are small electron carriers in various redox chains. The prosthetic group of Rb consists of one iron atom coordinated by four Cys (**Figure 3.4.11A**). The crystal structure of Rb from *C. pasteurianum* was determined (**Figure 3.4.12**).²⁵²

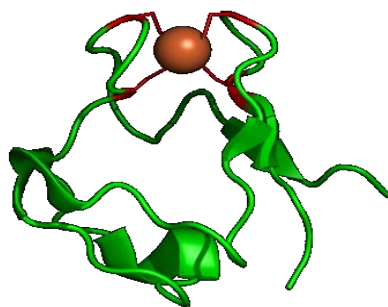


Figure 3.4.12. Crystal structure of Rb from *C. pasteurianum* (PDB code 1FHH). The iron is presented as a sphere and the coordinating Cys are in red.

The redox potential of the Rb from *C. pasteurianum* (-77 mV vs. SHE' in the wild-type) is sensitive to the hydrogen bonding network around the cluster.^{253,254}

The FIR absorbance spectrum of the oxidized Rb from *C. pasteurianum* (**Figure 3.4.13**) shows several signals which mainly arise from the metal-ligand vibrations. The high frequency range ($700\text{--}400\text{ cm}^{-1}$) is dominated by the overtone of the breathing mode of the

Fe-4S tetrahedron. The frequency range between 400 and 200 cm^{-1} is dominated by the $\nu(\text{Fe-S})$ vibrations. The lower frequency range is dominated by the $\delta(\text{Fe-S})$ vibrations. The tentative assignments of the observed signals are given in the **Table 3.4-4**. It should be noted that the coupling of the metal–ligand vibrational modes to those of the protein is not excluded.

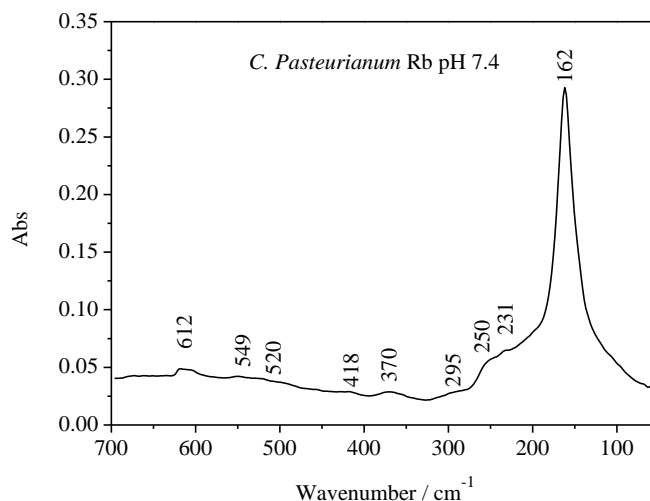


Figure 3.4.13. FIR absorbance spectrum of the Rb from *C. pasteurianum* at pH 7.4.

Wavenumber (cm^{-1})	Tentative assignment ^{234,255-258}
612	Overtone of the Fe–4S breathing mode
549	Amide VI / $\delta(\text{S-C-C})$ Cys ligands
520	Overtone of the $\nu(\text{Fe-S})$ vibration
418	$\nu(\text{Fe-S})^{\text{as}}$ vibration
370	$\nu(\text{Fe-S})^{\text{as}}$ vibration
295	Fe–4S breathing mode / $\nu(\text{Fe-S})^{\text{s}}$ vibration
250	$\delta(\text{Fe-S-C})$ vibration
162	hydrogen bonds in presence of salt

Table 3.4-4. Assignments of the infrared signal observed in the FIR spectrum of the oxidized Rb from *C. pasteurianum*.

Even though the resonance Raman signals arising from the oxidized Fe–S cluster of Rb are well described, less information is available on the vibrational signals in the reduced form due to the loss of the color of the S→F charge transfer band.

With the use of the nuclear vibrational spectroscopy Xiao *et al.*²⁵⁹ obtained the spectrum of the reduced Rb and they showed that the $\nu(\text{Fe-S})$ vibrations shift to lower frequencies reflecting an elongation of the Fe–S bonds.

Here we report for the first time the electrochemically induced FIR spectrum of the Rb from *C. pasteurianum*. This method allows the observation of the redox signature of the Fe–S cluster in the FIR range (**Figure 3.4.14**).

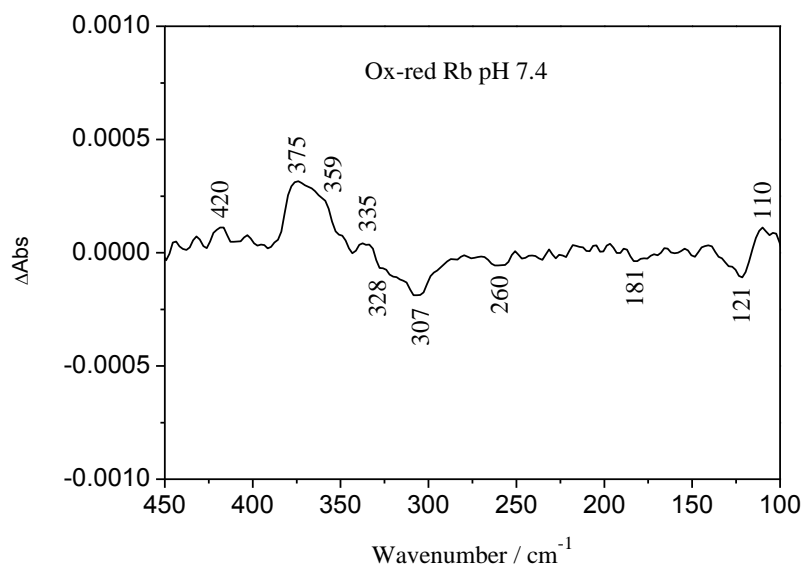


Figure 3.4.14. Electrochemically induced difference spectrum of the Rb from *C. pasteurianum* at pH 7.4 in the 450–100 cm^{-1} spectral range.

The main feature observed in the difference spectrum is the broad positive signal with two maxima at 375 and 359 cm^{-1} which were previously assigned to the $\nu(\text{Fe-S})^{\text{as}}$ vibration.²⁵⁵ The reduced form exhibits a broad signal with two minima at 328 and 307 cm^{-1} . In line with previously reported data, the lengthening of the Fe–S bond occurs upon reduction (ref.²⁵⁹ and references therein). Furthermore, the negative broad signal is of slightly lower intensity than the positive one. Indeed, the absorption coefficients of the $\nu(\text{Fe-S})^{\text{as}}$ modes are weaker in the reduced form. This behavior could result from the change in symmetry upon reduction. Beside the large feature that dominates the difference spectrum, several signals can be observed in the higher and lower frequency ranges. The positive signal at 420 cm^{-1} can be assigned to the $\nu(\text{Fe-S})^{\text{as}}$ vibration of the oxidized protein. This signal is downshifted in the reduced form towards 410 cm^{-1} . However, the negative signal observed at 410 cm^{-1} is weak and might be associated with noise from the instrument. Alternatively, the positive signal at 420 cm^{-1} does not shift, however shows a weaker absorption coefficient in the reduced form. The spectral region below 300 cm^{-1} contains three negative signals appearing at 260, 181 and 121 cm^{-1} . These signals arise from the bending motions of the Fe–S cluster.

The low frequency region contains the vibrational modes arising from the cluster itself, the large scale motions of the protein, as well as the internal hydrogen bonding signature.²⁶⁰ The low frequency signals cannot be accurately assigned.

3.4.3.3. Ferredoxin

3.4.3.3.1. [2Fe–2S] Ferredoxin

Plant chloroplast Fd are small electron carriers. Their prosthetic group consists of a dinuclear iron center in which the iron atoms are bridged by two inorganic sulfides. The cluster is held within the protein by the ligation of each iron atom to two Cys residues (**Figure 3.4.11B**). The crystal structure of the [2Fe–2S] Fd from Spinach was determined (Figure 3.4.15).¹³⁰ The protein has a redox potential of about -400 mV vs. SHE'.¹³³ Raman and resonance Raman spectroscopies have been extensively used to investigate the [2Fe–2S] Fd in the oxidized^{251,261-265} as well as in the reduced state.²⁶⁶⁻²⁶⁸

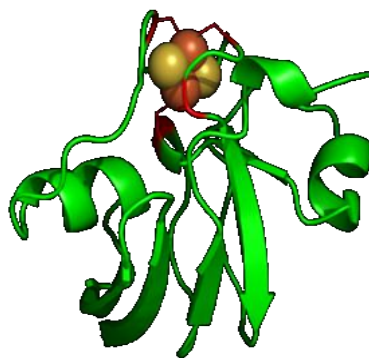


Figure 3.4.15. Crystal structure of Fd from spinach (PDB code 1A70). The iron atoms are in orange, the sulfur in yellow and the coordinating Cys in red.

The FIR absorbance spectrum of Fd from spinach was recorded at pH 7.5 (**Figure 3.4.16**). The spectrum exhibits an intense signal at 362 cm^{-1} and several signals with much lower intensities. It should be noted that the Fe–S vibrations of the [2Fe–2S] cluster can arise from the Fe–S bonds of the [2Fe–2S] itself as well as from the Fe–S of the coordinating Cys. Hereafter the former will be called the *bridging* Fe–S vibrations, denoted with the subscript “b” and the latter will be called *terminal* Fe–S vibrations, denoted with the subscript “t”. The spectral region below 550 cm^{-1} shows nine well-resolved signals among which eight can be assigned to the Fe–S vibrations. The broad signal centered at 102 cm^{-1} arises from the hydrogen bonding signature. The detailed bands assignment is done according to ref.^{251,265-268} and listed in the **Table 3.4-5**.

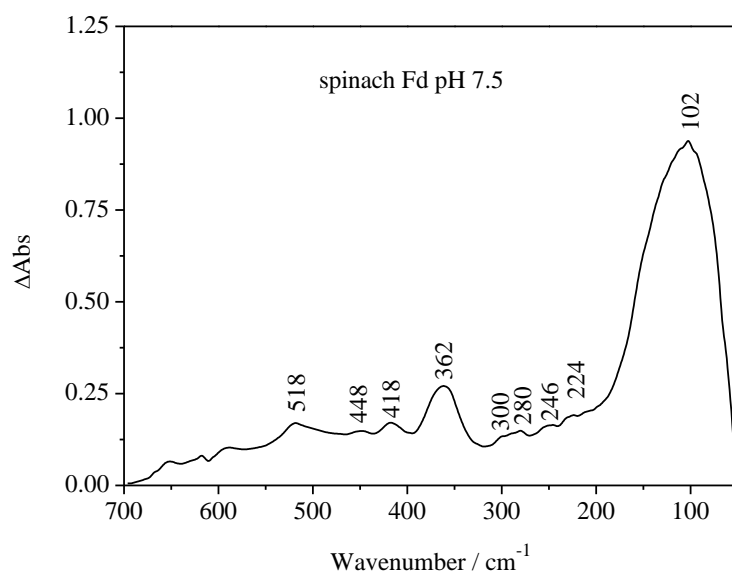


Figure 3.4.16. FIR absorbance spectrum of the Fd from Spinach at pH 7.5.

Wavenumber (cm ⁻¹)	Tentative assignment ^{251,265-268}
518	Amide VI / $\delta(\text{S-C-C})$ Cys ligands
448	$\nu(\text{Fe-S}^{\text{b}})$ vibration
418	$\nu(\text{Fe-S}^{\text{b}})$ vibration
362	$\nu(\text{Fe-S}^{\text{b}}) + \nu(\text{Fe-S}^{\text{l}})$ vibration
300	$\nu(\text{Fe-S}^{\text{l}})$ vibration
280	$\nu(\text{Fe-S}^{\text{l}})$ vibration
246	$\delta(\text{Fe-S-C}) + \delta(\text{Fe-S-Fe})$ vibration
224	$\delta(\text{Fe-S-C}) + \delta(\text{Fe-S-Fe})$ vibration
102	Hydrogen bonding

Table 3.4-5. Assignments of the infrared signal observed in the FIR spectrum of the oxidized Fd from Spinach.

The signals observed at 448 and 418 cm⁻¹ involve pure $\nu(\text{Fe-S}^{\text{b}})$ vibrations. The most intense signal is observed at 362 cm⁻¹ and can be assigned to the coupled $\nu(\text{Fe-S}^{\text{b}})$ and $\nu(\text{Fe-S}^{\text{l}})$ vibrations. Below this intense signal, the weak signals observed at 300 and 280 cm⁻¹ are mainly arising from the $\nu(\text{Fe-S}^{\text{l}})$. At lower frequencies, the Fe-S vibrations are more tightly coupled, mainly to the Cys ligand vibrations.

The redox signature of the Fe-S vibration of Fd from spinach is presented in the **Figure 3.4.17**. The negative signals appearing at 400 and 380 cm⁻¹ can be assigned to the $\nu(\text{Fe-S}^{\text{b}})$ vibration of the reduced cluster. Despite the fact that the absorbance spectrum was recorded in the oxidized state, that shows two signals at 448 and 418 cm⁻¹, the signals corresponding to the oxidized form of the electrochemically induced spectrum do not contain such signals. This might result from the low intensities of these signals. The positive peak appearing at 390 cm⁻¹

may arise from the $\nu(\text{Fe-S}^{\text{b}})$ vibration of the oxidized cluster. This signal is not well-resolved in the absorbance spectrum. The intense signal observed in the absorbance spectrum at 362 cm^{-1} is splitted into two signals, at 360 and 340 cm^{-1} and both signals can be assigned to the coupled $\nu(\text{Fe-S}^{\text{b}})$ and $\nu(\text{Fe-S}^{\text{t}})$ vibrations.^{266,267} Below these signals, several negative signals arise and can be assigned to the $\nu(\text{Fe-S}^{\text{t}})$ vibrations of the reduced cluster.

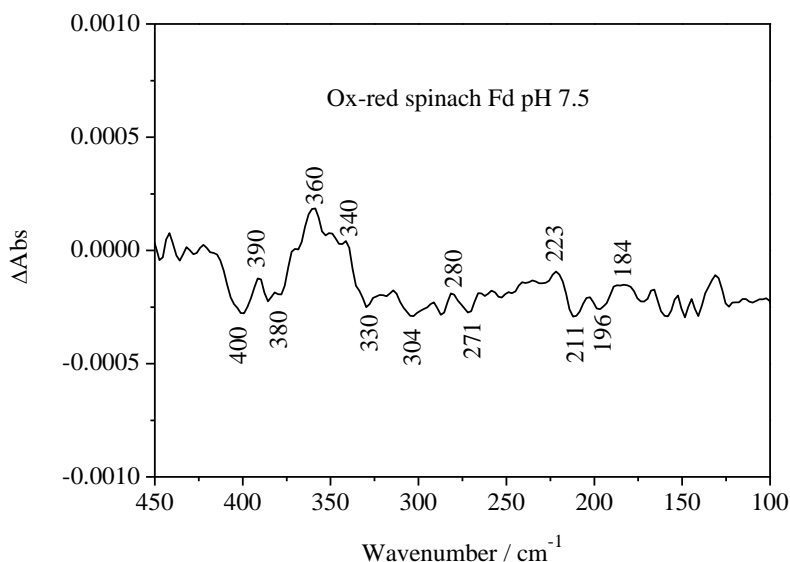


Figure 3.4.17. Electrochemically induced FTIR difference spectrum of the Fd from Spinach at pH 7.5 in the $450\text{--}100\text{ cm}^{-1}$ spectral range.

Below 250 cm^{-1} , the coupled $\delta(\text{Fe-S-C})$ and $\delta(\text{Fe-S-Fe})$ vibration is observed at 223 cm^{-1} in the oxidized form and it shifts towards 211 and 196 cm^{-1} upon reduction. The downshift trend indicates a geometrical change of the cluster itself and of the Cys ligand. Although the Fe-S elongation favors the coupling upon reduction, a decoupling phenomenon could be the origin of the splitting of low frequency signals observed in the reduced form.

The hydrogen bonding modifications occurring upon the backbone reorganization are expected to occur below 200 cm^{-1} , however, the signal-to-noise ratio is low because of the high absorption of the solvent.

3.4.3.3.2. [4Fe-4S] Ferredoxin

The cuban [4Fe-4S] cluster can be found in the bacterial Fd (type-II) (Figure 3.4.11D). The *C. pasteurianum* Fd contains two copies of [4Fe-4S] cluster (Figure 3.4.18)²⁶⁹ with indistinguishable pH-independent midpoint potentials.²⁷⁰

The FIR absorbance spectrum of the oxidized $2[4\text{Fe-4S}]$ Fd from *C. pasteurianum* recorded at pH 7.5 is shown in Figure 3.4.19. The spectrum shows similar features as compared to the

spectrum of the [2Fe–2S] cluster of the Fd from spinach, namely, an intense signal between 354 cm^{-1} and a few weaker signals on both sides. It should be noted that the signals positions are almost the same compared to those arising from the Fd from Spinach.

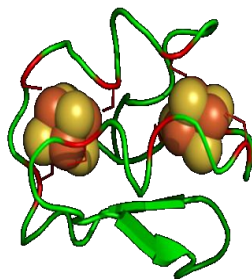


Figure 3.4.18. Solution structure of the Fd from *C. pasteurianum* (PDB code 1CLF). The iron atoms are in orange, the sulfur in yellow and the coordinating Cys in red.

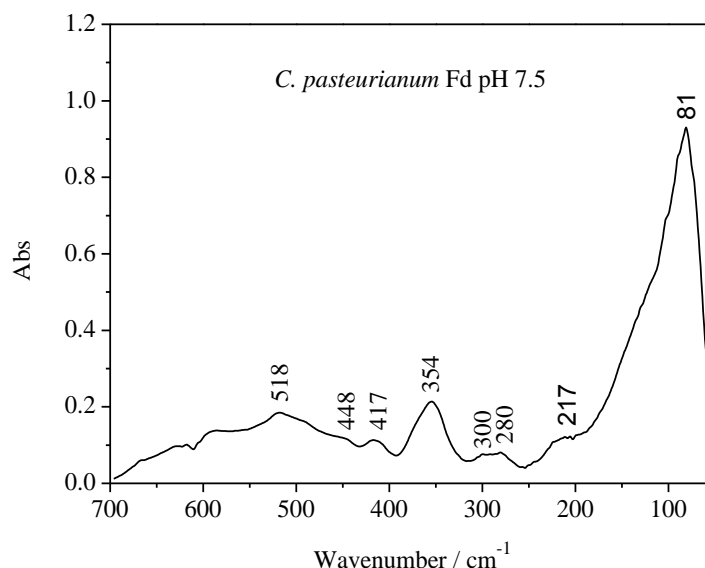


Figure 3.4.19. FIR absorbance spectrum of the Fd from *C. pasteurianum* at pH 7.5.

According to the previously reported vibrational data, the broad intense signal appearing at 354 cm^{-1} can be assigned to the $\nu(\text{Fe}-\text{S}^{\text{I}})$ vibration.²⁷¹ The vibrations of higher energy are mainly arising from the $\nu(\text{Fe}-\text{S}^{\text{I}})$ vibrations whereas the lower energy vibrations are mainly arising from $\nu(\text{Fe}-\text{S}^{\text{b}})$ vibrations. The information is also represented in **Table 3.4-6**.²⁷¹⁻²⁷³

Despite the striking similarities between the FIR absorbance spectra of [2Fe–2S] and [4Fe–4S] proteins, the electrochemically induced difference spectra are quite different. The FIR electrochemically induced difference spectrum of the 2[4Fe–4S] Fd from *C. pasteurianum* is shown in **Figure 3.4.20**.

Wavenumber (cm ⁻¹)	Tentative assignment ²⁷¹⁻²⁷³
518	Amide VI / $\delta(\text{S-C-C})$ Cys ligands
448	$\nu(\text{Fe-S})$ vibration
417	$\nu(\text{Fe-S}^t)$ vibration
354	$\nu(\text{Fe-S}^t)$ vibration
300	$\nu(\text{Fe-S}^b)$ vibration
280	$\nu(\text{Fe-S}^b)$ vibration
217	$\delta(\text{Fe-S-C}) + \delta(\text{Fe-S-Fe})$ vibration
81	Hydrogen bonding

Table 3.4-6. Assignments of the infrared signal observed in the FIR spectrum of the oxidized Fd from *C. pasteurianum*.

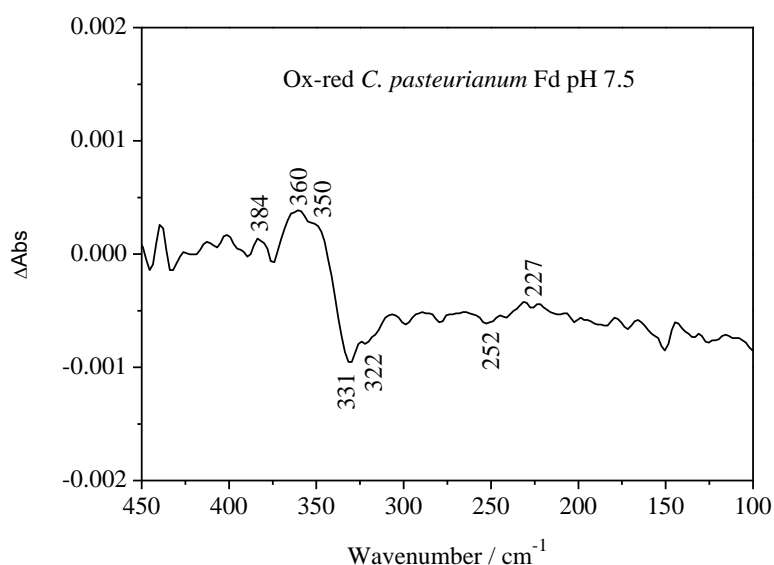


Figure 3.4.20. Electrochemically induced FTIR difference spectrum of the Fd from *C. pasteurianum* at pH 7.5 in the 450–100 cm⁻¹ spectral range.

The difference spectrum shows a large positive signal with two maxima at 360 and 350 cm⁻¹. These signals were previously assigned to the $\nu(\text{Fe-S}^t)$ vibrations. Upon reduction, these signals are downshifted towards 331 and 322 cm⁻¹, respectively. Thus, the reduction of the cluster is accompanied by the Fe-S^t bond lengthening and a reorganization of the coordinating Cys. On the other, hand, the Fe-S^b modes observed in the absorbance spectrum of the oxidized form do not exhibit significant downshifts upon reduction. This behavior indicates the rigidity of the cluster itself resulting from the immobility of the atoms during the course of the redox reaction.

While the high frequency range reflects the motion of the Fe-S^t bonds, the lower frequency region shows the deformation of the cluster coupled to the motions of the ligands.

3.4.3.4. [2Fe–2S] Rieske protein

Rieske-type [2Fe–2S] clusters are important in central biological electron transfer reactions such as respiration and photosynthesis.^{274,275} In the cytochrome *bc*₁/*b*₆*f* family, the Rieske protein contributes to the high potential electron transfer chain that involves a complex bifurcated mechanism.⁸⁸ All Rieske-type proteins consist of an [2Fe–2S] core with two cysteine and two histidine side chains as ligands (**Figure 3.4.21**).^{137,153,246,276,277} These two histidines seem to be responsible for the pH dependence of the redox potential in the Rieske [2Fe–2S] center.^{98,137} Both histidines accept protons in a close pH range and apparent pK_a values for the oxidized *T. thermophilus* Rieske center, were reported at values of 7.8 and 9.6.⁹⁸ The first accepted proton is stabilized by both histidines. A recent study showed that the overall structure of the protein remains the same at a low pH value, where both histidines are protonated. However, some local modifications were observed around the cluster.²⁷⁸

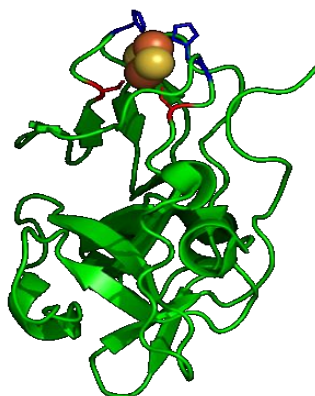


Figure 3.4.21. Crystal structure of the Rieske protein from *T. thermophilus* (PDB code 1NYK). The iron atoms are in orange, the sulfur in yellow, the coordinating Cys in red and the coordinating His in blue.

The crucial role of the hydrogen bonds in the immediate cluster environment on the redox potential and on the proton affinity of the two histidines was discussed on the basis of the first X-ray structures^{276,279} and it was shown that all sulfur atoms of the cluster participate to the formation of complex hydrogen bonded network. The interplay of this network was explored on the basis of site directed mutagenesis studies; a study that revealed a lower redox potential for mutants with a lower number of hydrogen bonds and indicated a clear influence of the hydrogen bonds on the Fe–S electronic paramagnetic resonance spectroscopic properties.^{138,251,280,281} In addition, resonance Raman studies demonstrated a direct influence of the hydrogen bonds on the Fe–S vibrations, both, terminal and bridging modes.²⁸² Moreover, studies performed with the help of Poisson–Boltzmann calculations indicated that the lower pK_a value of the histidine coordinating the iron in the so called *bc*-type Rieske proteins is

found due to the presence of hydrogen bonds towards the cluster and the absence of negatively charged side chains in the vicinity of the cluster.^{283,284} In conclusion, both geometric and electronic properties of the cluster are influenced by the hydrogen bonding environment and we thus chose to probe this protein with the FIR spectroscopic approach. Hydrated films of the Rieske protein have been studied for the pH values 6.0, 8.0, 10.2 and in pure water from 600 to 50 cm^{-1} (**Figure 3.4.22**).

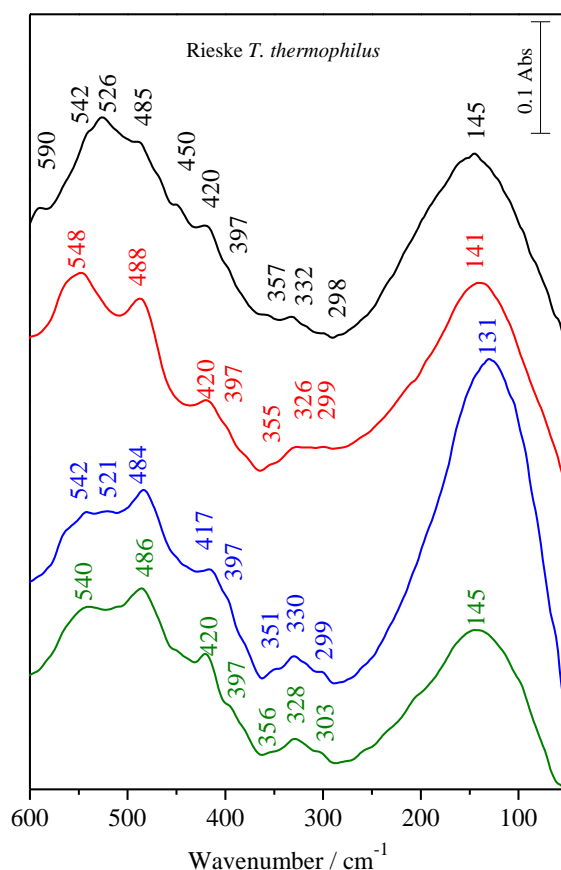


Figure 3.4.22. Absorbance spectra of the Rieske protein in the 600–50 cm^{-1} spectral range for pH 6.0 (black), 8.0 (red), 10.2 (blue) and in pure water (green).

The spectrum of the Rieske protein in pure water (pH ~ 6.5) exhibits similar features as in the buffered samples (**Figure 3.4.22**) and only small shifts can be detected. This behavior indicates that the buffer has no significant effect on the hydrogen bonding signature.

Three main regions can be distinguished in the low frequency area. The predominant features of the vibrational spectra of the proteins between 600 and 500 cm^{-1} are in general attributed to motions of the amide linkage. In the data presented here. The backbone signals are found as a broad signal covering the 590–500 cm^{-1} region, involving the so called amide VI mode. This can be assigned to the coupled $\delta(\text{C}=\text{O}/\text{C}-\text{C}-\text{N})$.²⁴⁵

The assignments described below for the Fe–S vibrations are based on theoretical calculations and on a comparison to Raman data (**Table 3.4-7**).^{282,285-287} To our knowledge, no infrared data for the Fe–S vibrations in Rieske proteins and other Fe–S proteins is available yet. However, several theoretical calculations can be found for the Fd-type [2Fe–2S] core²⁸⁸ and the Rieske-type [2Fe–2S] core.²⁸⁹ On this basis, the signals are tentatively assigned to the bridging, terminal Fe–S, or Fe–N vibrations. Since vibrational modes are often coupled in this frequency range and may involve anharmonicity effects, it can be expected that the signals represent complex motions.

Between 500 and 400 cm^{-1} a shoulder is observed at 485 cm^{-1} at pH 6.0. The signal becomes a well-defined peak upon the increase of pH. Since the feature shifts to higher frequencies upon cooling the signal may be arising from a bending motion of the cluster.²⁹⁰ A definite assignment of the signals at 485 and 450 cm^{-1} , will, however need support by an isotopic labeling approach of the metal centre.

The signal observed at 450 cm^{-1} is only evident for pH 6.0 indicating an effect on the protonation state of the histidines on this motion. However, the frequency of this signal is too high to be originating from a Fe–N mode alone. It is thus most likely coupled to an $\nu(\text{Fe–S}^{\text{b}})$ vibration where the involved Fe atom is the one coordinated by the histidines residues. The signal observed at 420 cm^{-1} at pH 6.0 and 8.0 shifts to 417 cm^{-1} when the pH reaches 10.2. This shift is accompanied by a slight broadening of the signal. This signal can be assigned to the $\nu(\text{Fe–S}^{\text{b}})$ vibration. Also, the coupling with other modes involving the coordinating histidines is probable. An alternative explanation would involve the modification of the hydrogen bonding network around the cluster upon change of pH. As mentioned in the introduction, it is known from the crystal structures of the Rieske protein from *T. thermophilus* that the hydrogen bonding network plays a crucial role in tuning the midpoint potential of the protein.^{153,246,291} Furthermore, the alteration of the hydrogen bonding network is known to have an important impact on the geometry of the Fe–S cluster.²⁴⁶ The loss of a hydrogen bond may have an impact on the vibrational motions and thus on the position of the peak. The concerned hydrogen bond could be the one located between Leu135 residue and the S2 atom of the cluster or the one between the Ser157 residue and the S1 atom of the cluster (*T. thermophilus* numbering).²⁴⁶

In the spectral range between 400 and 200 cm^{-1} further metal–ligand vibrations can be interpreted. The signal seen at 357 cm^{-1} for a pH value of 6.0, shifts to lower frequencies at higher pH values reflecting the effect of the protonation state of the histidine on the cluster vibrations.

This signal can be attributed to the Fe–S^t stretching vibration.^{286,289} The downshift of this signal reflects once more the influence of the histidine protonation state on the rigidity of the [2Fe–2S] cluster since the downshift can be correlated to the strengthening of the Fe–S^t bonds at high pH values.

	pH 6.0	pH 8.0	pH 10.15	Pure Water pH ~6.5	Assignments
Wavenumber (cm ⁻¹)	542	548	542	540	Amide VI $\delta(\text{C}=\text{O}/\text{C}-\text{C}-\text{N})$
	526	-	521	-	Amide VI $\delta(\text{C}=\text{O}/\text{C}-\text{C}-\text{N})$
	485	488	484	486	$\delta(\text{Fe}-\text{S}^{\text{b}}-\text{Fe})$
	450	-	-	-	$\nu(\text{Fe}-\text{S}^{\text{b}})$ ²⁸⁹
	420	420	417	420	$\nu(\text{Fe}-\text{S}^{\text{b}})$ ^{286,289} $\nu(\text{Fe}-\text{S}^{\text{b}})$ ^{286,289}
	397	397	397	397	$\text{C}_\beta-\text{C}_\gamma-\text{C}_\delta$ bending mode of coordinating imidazole ²⁸⁹
	357	355	351	353	$\nu(\text{Fe}-\text{S}^{\text{t}})$ ²⁸⁶
	332	326	330	328	$\nu(\text{Fe}-\text{S}^{\text{b}})$ ^{286,289} $\nu(\text{Fe}-\text{N})$ ²⁸⁶
	298	299	299	303	bending mode at C _γ of coordinating Imidazole planes ²⁸⁹
	145	141	131	143	Hydrogen bonding signature ²⁶⁰

Table 3.4-7. Overview on the assignments of the Rieske protein vibrations in the FIR range at pH 6.0, 8.0, 10.2 and in pure water.

Below 350 cm⁻¹, a weak signal arises at 332 cm⁻¹ for the fully protonated sample. The signal gains intensity at pH 10.2 and in contrast to the signal at 357 cm⁻¹, it shifts to lower frequencies. The Fe–S^b bond at pH 10.2 seems to be shorter than at pH 6.0. Therefore, the cluster itself is becoming more compact than the one at pH 6.0. It should be noted that the most important downshift is observed at pH 8.0. The Fe–N vibrations are expected to occur below 300 cm⁻¹ but will also be coupled to the Fe–S vibrations. One weak signal appears at 298 cm⁻¹ at pH 6.0. In addition to the slight upshift, the intensity of the signal becomes more important upon increase of pH. We tentatively assign this signal to the Fe–N stretching vibration that may be overlapping with the bending mode at C_γ of the coordinating imidazole planes.²⁸⁹

The electrochemically induced difference spectra of the Rieske protein at three different pH values are presented in **Figure 3.4.23**. The Fe–S^b modes observed at 420 cm⁻¹ in the

absorbance spectra of the oxidized form are presented as positive signals in the redox induced spectra at all pH values. The corresponding modes in the reduced form appear at 403 and 392 cm^{-1} . The fact that these signals are not sensitive to the pH variation indicates that the motion of the core of the cluster is not affected by the protonation state of the coordinating His. A broad signal in the absorbance spectra appears at 380 cm^{-1} as a positive signal in the difference spectra. This signal can be assigned to the $\nu(\text{Fe-S}^{\text{I}})$ vibration. The signal shifts to lower frequencies upon reduction. The sensitivity of the $\nu(\text{Fe-S}^{\text{I}})$ vibrations are represented by the signals at 336/325 and 335/325 cm^{-1} at pH 10.2 and 8.0, respectively. These signals are not redox sensitive at pH 6.0. The protonation state of the coordinating His affects the motion of the coordinating Cys at pH values higher than 6.0. Furthermore, the positive signal appearing at 280 cm^{-1} in the difference spectrum recorded at pH 10.2 is not observed at lower pH values. It is thus likely to assign this signal to the $\nu(\text{Fe}^{\text{III}}\text{-N})$ of the negatively charged His ligand. The corresponding negative signal appears as a broad signal centered at 267 cm^{-1} . This signal was previously observed in the resonance Raman spectrum of the Rieske protein recorded at pH 10.1 and it was assigned to the $\nu(\text{Fe}^{\text{III}}\text{-N})$. In addition, these signals overlap with the bending mode at C γ of coordinating imidazole planes. It should be noted that the hydrogen bonding network around the cluster may affect the frequencies of these signals during the course of the redox reaction. At pH 8.0, a couple of signals are observed at 253–247 cm^{-1} which might arise from the $\nu(\text{Fe-S}^{\text{I}})$ and $\nu(\text{Fe-N})$ vibrations.

At pH 6.0, a positive signal appearing at 311 cm^{-1} can be assigned to the $\nu(\text{Fe-S}^{\text{I}})$ vibrations along the Fe–Fe direction. Upon reduction the signal is downshifted towards 303 cm^{-1} .

In lower frequency region, vibrations arising from the collective motions of the protein as well as from the internal hydrogen bonding network are expected. However, the high absorption of the solvent in the low frequency region leads to a decrease of the signal-to-noise ratio.

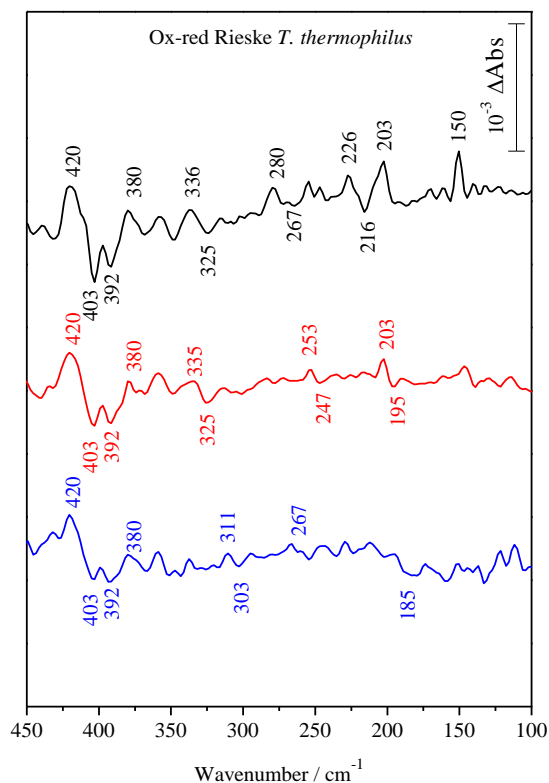


Figure 3.4.23. Electrochemically induced difference spectra of the Rieske from *T. thermophilus* at pH: 10.2 (black), 8.0 (red) and 6.0 (blue) in the 450–100 cm^{-1} spectral range.

3.4.3.5. NADH deshydrogenase fragment of the complex I

The NDF is the soluble part of the complex I, it contains nine Fe–S clusters (**Figure 3.4.24**).⁵⁵ It catalyzes the oxidation of NADH and transfers electrons to the quinone binding site via the Fe–S clusters. The mechanism of the NDF is not fully understood, the electrochemically induced FIR spectroscopy could help for better understanding it.

The complexity of the enzyme makes the vibrational assignments quite complicated. In order to accurately assign the FIR signals, two samples were prepared, one with unlabelled iron (^{56}Fe) and another one with isotopically labelled iron (^{54}Fe) (See **2. Materials and methods**). The replacement of the native Fe by a lighter isotope would shift the metal–ligand vibrations to higher frequencies.

The FIR absorbance spectra of both, unlabelled and labelled samples were recorded with a 2 cm^{-1} resolution (**Figure 3.4.25**). The spectra are quite similar in the spectral region below 500 cm^{-1} whereas in the region above, the signals are not conserved in both spectra. The spectrum of the MES buffer is shown in **Figure 3.4.2**.

The signals that might have emerged from the metal–ligand vibrations do not show significant shifts upon labeling because the signals are large (assignments are similar to those done for the Rb and Fd samples). On the other hand, a slight upshift of the signal at 488 cm^{-1}

in the unlabelled sample takes place in the labelled one. An additional signal is observed at 447 cm^{-1} in spectrum of the ^{54}Fe -labelled sample. This signal may result from the decoupling of an Fe–S vibration, coupled to another one in the spectrum of the unlabelled sample. The spectrum of the unlabelled sample shows a broad signal at 261 cm^{-1} , barely visible in the spectrum of the labelled one due to the overlapping with the hydrogen bonding signal.

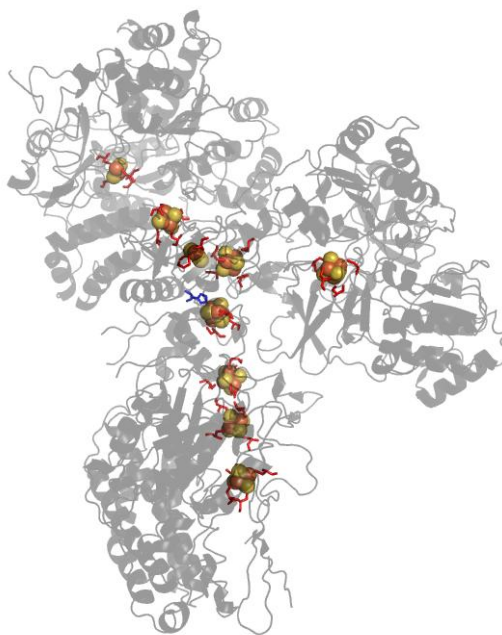


Figure 3.4.24. The Fe–S clusters of the NDF. The backbone is in light grey, the Fe–S clusters are in balls, the coordinating His residue is in bleu and the Cys residues in red.

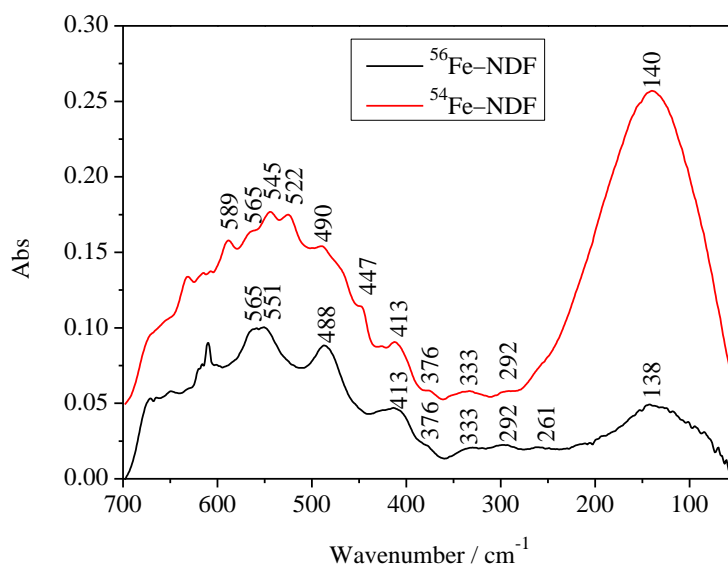


Figure 3.4.25. FIR absorbance spectra of the ^{56}Fe -NDF (black) and of the ^{54}Fe -labelled NDF (red).

The electrochemically induced difference spectra of both samples were recorded in the MIR (**Figure 3.4.26**) and FIR range (**Figure 3.4.27**). The spectra obtained in the MIR range are

similar to the previously reported difference spectra of NDF.⁶⁹ In addition no significant shift was observed in this spectral range upon labeling.

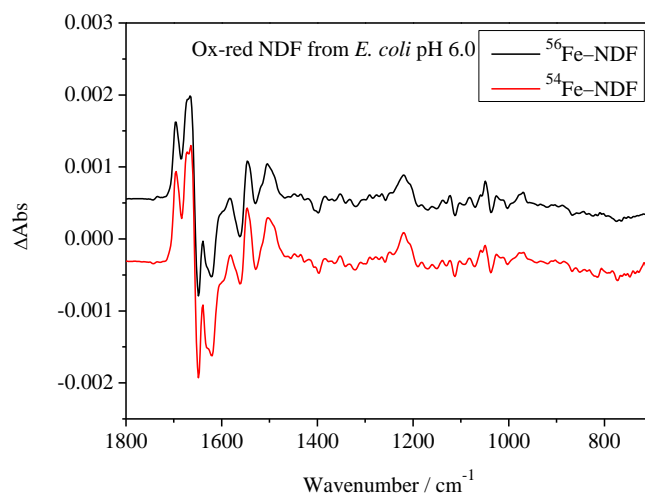


Figure 3.4.26. MIR electrochemically induced difference spectra of the ^{56}Fe -NDF (black) and of the ^{54}Fe -labelled NDF (red).

The FIR difference spectra show unexpected low similarities to each other, or to the ones obtained for the lighter ISP shown above. However, intense signals are observed in the region between 400 and 300 cm^{-1} , typical for the $\nu(\text{Fe-S})$ vibrations. The signal observed at 347 cm^{-1} in the spectrum of the unlabelled sample shifts to 350 cm^{-1} in the spectrum of the ^{54}Fe -labelled sample. This signal was previously assigned to the $\nu(\text{Fe-S}^{\text{I}})$ vibration (**Figure 3.4.27**). This negative signal observed at 341 cm^{-1} might be arising from the $\nu(\text{Fe-S}^{\text{I}})$ vibration of reduced clusters. The low similarity of the NDF FIR difference spectra shows the limit of the method, which is likely not successful when studying large proteins such as NDF.

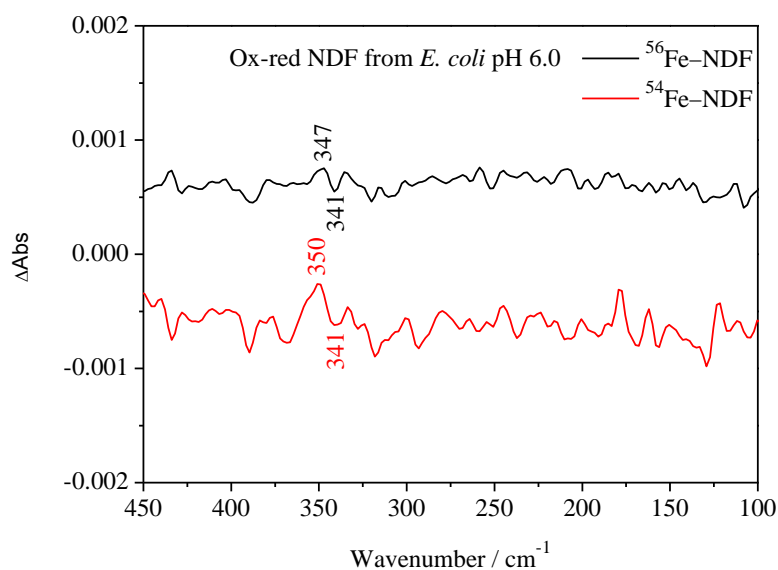


Figure 3.4.27. FIR electrochemically induced difference spectra of the ^{56}Fe -NDF (black) and of the ^{54}Fe -labelled NDF (red).

3.4.3.6. Conclusion

The FIR spectra presented in this study offer an overview on the vibrational modes of several Fe–S clusters as well as of their redox signature.

The electrochemically induced difference spectroscopy applied in the FIR range offers a unique tool to observe “in action” the prosthetic groups of the ISP. The method shows that each cluster type has its own redox signature despite the similarities observed in the absorbance spectra. Furthermore, the difference spectra of the Rieske protein recorded at different pH values shows that the core of the cluster is not sensitive to the protonation state of the coordinating His. On the other hand, the effect of the protonation states of the coordinating His is extended beyond the cluster to reach the coordinating Cys.

Together, the data presented here and the previously reported vibrational data on the Fe-S cluster offer a solid basis to the investigation of larger ISP like the respiratory complex I and II. The assignment of the Rieske protein redox signals can be helpful in the future to the understanding of the difference spectra of the respiratory complex III.

Finally, the FIR difference spectroscopy is a promising tool to investigate the metal–ligand vibrations of proteins containing other chromospheres. Despite the good performance of this method regarding the metal–ligand vibration, it still needs optimization to increase the signal–to–noise ratio, especially in the lower frequency region where the water absorption is too high.

3.4.4. Far infrared hydrogen bonding signature

3.4.4.1. Introduction

The use of the FIR spectral range allows obtaining simultaneously information on local environment of cofactors and the overall hydrogen bonding structure of proteins. A temperature dependent approach is introduced for the Rieske-type [2Fe–2S] protein from *T. thermophilus* and for the LFA-I domain of integrin.

3.4.4.2. [2Fe–2S] Rieske protein from *T. thermophilus*

The temperature dependence (294–30 K) of the Rieske protein at pH 6.0, 8.0, and 10.2 in the spectral range from 600–75 cm^{-1} is shown in the left panel of the **Figure 3.4.4**. We note that the vibrations themselves are not temperature dependent; however, shifts can be expected on the basis of the perturbation of the hydrogen bonding, tertiary structure changes, and other structural variations. IR stretching modes are generally suggested to move to lower frequencies and bending modes to adopt higher frequencies with lower temperatures.^{290,292} Furthermore, strength and number of the hydrogen bonds is expected to increase.²⁹³ In the amide VI domain, between 570 and 540 cm^{-1} (Analyzed above), the only effect observed for each pH value is a weak increase of the absorbance upon cooling, thus excluding a noticeable change in secondary structure at low temperatures. Bands at 450, 420 and 398 cm^{-1} , assigned to Fe–S^b stretching vibrational mode are slightly affected by the temperature decrease. In contrast hitherto, the band tentatively assigned to Fe–S^b–Fe vibration and centered at 478 cm^{-1} , is shifted towards higher wavenumbers ($\Delta\nu = 4 \text{ cm}^{-1}$) when temperature is decreasing. This effect confirms the attribution to a deformation vibrational mode. These shifts are independent of the pH and thus of the histidine protonation state and the local environment of the cluster. We note that the signal includes contributions of other motions that might overlap the pH dependency.

Below 350 cm^{-1} , the hydrogen bonding signature is observed (intra- and intermolecular modes).^{230,233,260} The intensity of this broad and strong band increases when temperature is decreasing for each pH value studied. This result indicates the presence of a higher number of hydrogen bonds within the protein upon cooling, but no phase transition. The upshift of the band maximum reveals a strengthening of the interaction. Proteins have been reported to

show a linear increase of the signal intensity upon cooling at temperatures around 200 K, also called glass-like transition.²⁹⁴⁻²⁹⁷

The right panel of the **Figure 3.4.4.** highlights the temperature dependence of the hydrogen bonding mode at pH 6.0, 8.0, and 10.2. For the transition of the hydrogen bonding features several positions between 187 and 195 cm^{-1} have been analyzed. The temperature dependence of the signal is not changing between pH 6.0, 8.0, and 10.2 until 150 K. importantly; below 150 K different evolutions are seen in function of the pH (*i.e.* correlating with the protonation state of the coordinating histidines). At pH 6.0, where both histidines at the Fe–S cluster are protonated, a plateau is observed between 150 and 100 K, whereas the absorption continues to increase at pH 10.2 where the two histidines are deprotonated.

The measurement of the sample at the intermediate pH value of 8.0 shows a behavior close to the experiment at a pH value of 6.0. These observations can be interpreted in terms of the strengthening of the hydrogen bonds which is greater at pH 10.2 than at lower pH. We conclude from these latter results a more rigid structure at pH 10.2. This is in line with the temperature dependence of the signal between 301 and 333 cm^{-1} , that includes coordinates from the Fe–S vibrations.

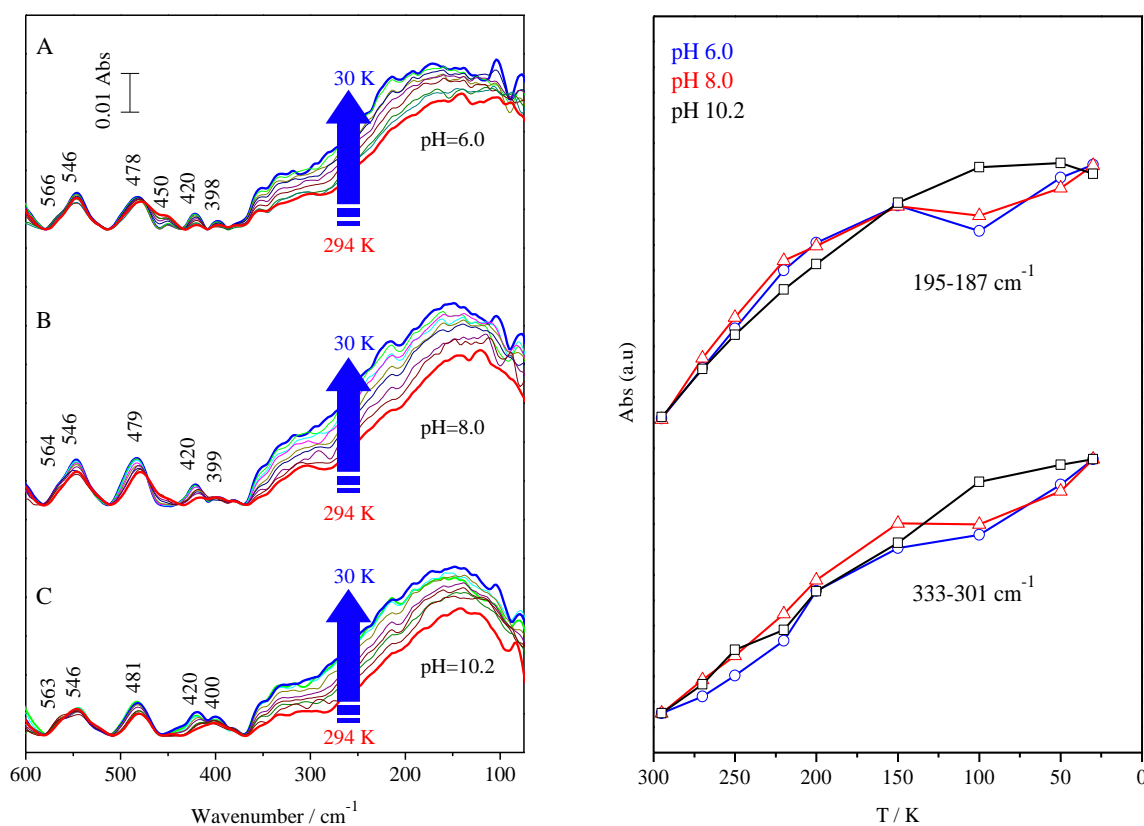


Figure 3.4.4. (Left panel) Temperature dependence of the absorbance spectra of the Rieske protein for pH (a) 6.0, (b) 8.0, and (c) 10.2 in the 600–75 cm^{-1} spectral range. (Right panel) Temperature dependence of the hydrogen bonding mode of the Rieske protein at pH 6.0 (blue line), 8.0 (red line), and 10.2 (black line) in the 195–187 cm^{-1} and 333–301 cm^{-1} ranges.

We note that the protein studied here, originates from a thermophilic system, and it will certainly present a different behavior than an analogous system from a mesophilic organism. Transition temperatures and pK_a values observed are certainly shifted. The thermophilic protein is extremely stable towards temperature variation and did not show, at any point of the experiments, a loss of the overall structural integrity.

3.4.4.3. LFA-I domain of integrin

3.4.4.3.1. Introduction

Integrins are transmembrane proteins residing in the plasma membrane of multicellular organisms. They are involved mainly in cell–adhesion and cellular signaling and they undergo a conformational changing upon activation.^{298,299} The activation process of integrins depends on the nature of the bound metal. Thus, by varying the metal, we can access to both, active and inactive forms of integrins. This feature makes integrins good candidates to investigate the effect of metal binding on the hydrogen bonding signature.

Integrins are implicated in a multitude of biological functions such as embryogenesis, immune response, haemostasis, inflammation and maintenance of tissue integrity. They constitute a large family of $\alpha\beta$ heterodimeric transmembrane proteins. Each monomer has a large extracellular domain. The most unusual feature of integrins compared to other adhesion molecules is that the ability of their extracellular domains to bind ligands can be activated on a timescale of ≤ 1 s by signals within the cell. Some of these integrins has an “inserted” domain (the I–domain) of the Leukocyte Function Associated antigen–I (LFA–I) integrin in its α –chain. The I–domain (**Figure 3.4.28**) includes about 200 amino acids in length and contains the site for binding to soluble or membrane anchored ligands. It adopts a Rossman–type fold with a central hydrophobic β –sheet surrounded by α –helices.

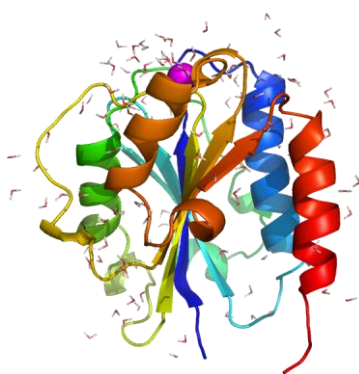


Figure 3.4.28. Cartoon view of the closed I-domain taken from the low affinity structure (PDB code 1LFA). The MIDAS magnesium ion is shown as a magenta sphere. The $\alpha 7$ helice is colored in red.

Integrins can be found in two conformations, open and closed conformation. These conformations stand for, activate and inactive forms, respectively. In the inactive form, the transmembrane “legs” of the heterodimers are stuck together, they separate upon activation.

Depending on the position of the $\alpha 7$ helix, the I-domain has a ligand binding competent structure in the active form and a low affinity conformation in the inactive form. The conformational dynamics of the I-domain has been found to have a strong impact on its recognition properties. Theoretical calculations have shown that correlated motions couple the C-terminal $\alpha 7$ helix to the MIDAS.

Ligand binding to its Metal Ion Dependent Adhesion Site (MIDAS) requires a divalent metal ion with octahedral coordination provided by conserved residues in loops of the I-domain structure and the side chain of a glutamate residue of the physiological ligand. Besides the most abundant Mg^{2+} dication, other metal ions have been found to bind to the I-domain. In fact, the closed conformation can be seen with Ca^{2+} , Mg^{2+} , Mn^{2+} , Cd^{2+} , or no metal in the MIDAS, and the open conformation can be seen with Mg^{2+} , Co^{2+} , Zn^{2+} , Mn^{2+} , Cd^{2+} , and Ni^{2+} in the MIDAS. Biological analysis suggest that the affinity of this domain towards its natural ligand is modulated by the disposition of the C-terminal $\alpha 7$ helix, which serves as a critical transmitter of conformational and ligand binding signal to the rest of the integrin.

The FIR hydrogen bonding collective motions have been probed for the LFA-I domain with different metal cations bound; i.e. Mg^{2+} , Mn^{2+} and Ca^{2+} where the LFA-I domain adopts an open conformation and Fe^{2+} , where it adopts a closed conformation.

3.4.4.3.2. Far infrared hydrogen bonding signature

The temperature dependent spectra of the LFA-I domain with the different cations are shown in the **Figure 3.4.29**. Upon cooling, the spectra gain intensity until reaching a plateau below 250 K.

This behavior is independent of the nature of the metal cation. The increase of the intensity upon cooling was also observed for the Rieske protein. The strengthening of the hydrogen bonding upon cooling is responsible of the increasing. The increasing of the absorption at temperatures below 250 K becomes less pronounced. This behavior is in line with a glass-like transition occurring at around 250 K.²⁹⁴⁻²⁹⁷ Besides, the spectra show a strong band at around 168 cm^{-1} . This signal shifts to higher frequencies upon cooling by approximately 10 cm^{-1} . In control experiments on the buffer alone, this signal was also observed at the same

frequency at room temperature, and shifts to higher frequencies upon cooling (See **Appendix 15**).

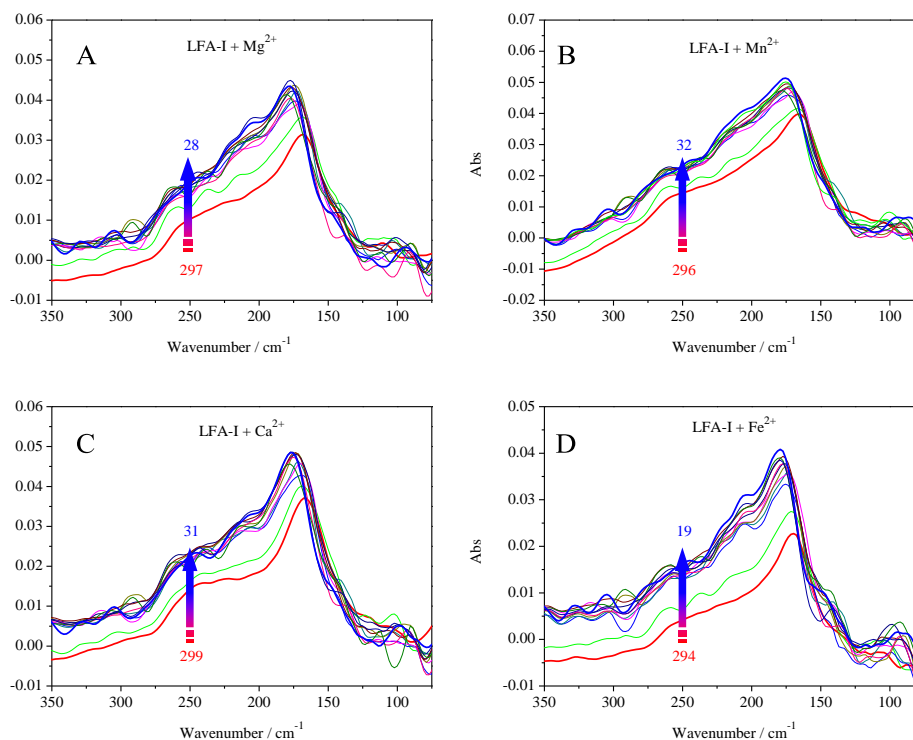


Figure 3.4.29. FIR temperature dependent spectra of the LFA-I domain at pH 7.4 in presence of (A) Mg, (B) Mn, (C) Ca and (D) Fe cations.

This observation indicates that the intense signal can be assigned to the buffer contribution. Despite the fact the binding of Fe cations leads to the inactive form of the LFA-I domain, the far infrared spectra of all the samples are quite similar. Thus, the hydrogen bonding network shows a similar behavior in all the samples. In other words, the tertiary structure of the LFA-I domain is conserved no matter what the cation is. The local reorganization of the protein around the MIDAS does not affect the whole protein.

3.4.4.3.1. Conclusion

The use of the FIR or terahertz spectral region has strongly expanded in the last years due to the unique sensitivity of this spectral region to collective molecular motions that are crucial to biological processes. These global motions are influenced by the conformational state as well as the specific arrangement of intra- and intermolecular hydrogen bonds. In this work we analyzed the temperature dependence of a spectral feature, which includes the contributions of the internal hydrogen bonds of the studied Rieske protein and structural water. The temperature dependent transitions between 294 and 30 K are found to strongly

depend on the protonation state of the residues that coordinate the Fe–S cluster and the results suggest a more rigid structure at a pH >10, including the overall H-bonding features. The electrochemically induced FTIR difference spectra at the respective pH values demonstrate a clear dependence for the redox induced reorganization of the cluster and importantly the Fe–S cluster vibrations themselves are found to be shifted.

The strengthening of the hydrogen bonding environment induced by the structural characteristics of the deprotonated coordinating histidine residues in the direct environment of the cluster is well known, and was previously presented on the basis of side directed mutagenesis, electrostatic calculations and structural analysis.^{138,280,281} Here we studied the motion associated with intermolecular hydrogen bond vibrations of the overall protein in the FIR. On the basis of the global change of the temperature dependence of the hydrogen bonding in function of pH we conclude that the environment of cluster is mediated by a variation of the overall tertiary structure.

The far infrared spectra of the LFA–I domain recorded as a function of temperature showed a glass–like transition around 250 K. The variation of the metal cation within the MIDAS did not affect the tertiary structure of the LFA–I domain.

4. Summary

The metal-containing cofactors play pivotal roles in biology. The understanding of the interaction between metal cations and proteins is a key step toward the elucidation of the biological functions of proteins. FTIR spectroscopy offers a valuable analytical tool to investigate proteins and to learn more about the relationship between the different cofactors and their biological function. In this thesis, different aspects of the role of metals in proteins were elucidated on the basis of this technique.

Since proteins are complex entities, the use of model compounds as metal-binding sites is helpful regarding the investigation of metal-binding modes in macromolecular, such as metalloproteins. The coordination of Cu cations within Poly-L-histidine offers a reliable model to mimic the binding of Cu cations in metalloproteins. The MIR and FIR spectral ranges present a global view about the effect of the Cu binding on the backbone reorganization of PLH. The binding process itself was also probed thanks to the metal-ligand vibrations occurring in the low frequency range. The study carried out at pD 7.0 suggested the binding of Cu cations by the N^ε atom of the Im ring. At pD 9.5, the binding of Cu induced the deprotonation of backbone nitrogen as well as the Im ring. Indeed, both nitrogen atoms of the Im ring became available for Cu. The FIR spectra exhibited Cu-Im signals below 350 cm⁻¹ which can be assigned to the $\nu(\text{Cu-Im})$, $\gamma(\text{Cu-Im})$ and $\delta_{\text{def}}(\text{Cu-Im})$ vibrations. These FIR signals can be used as marker bands of the Cu coordination. The study performed on an amyloid model peptide, called Cu-amyloid-beta 16 in the MIR range gave new insights about the exact binding modes of His. On the other hand, the binding of Cu cations by the backbone carbonyls as well as by the NH₂ terminus of the Asp1 are difficult to probe in the MIR range due to the complexity of the spectra.

In the second part of the thesis, the proton pumping respiratory enzymes were studied, they are crucial to biological energy conversion. They couple redox reactions to proton pumping across the membrane. The capture and release of protons take place via proton pathways conceived for this purpose. The elucidation of the pumping mechanism at the molecular level helps better understanding the function of the respiratory enzymes. FTIR difference spectroscopy applied on respiratory chain enzymes inhibited by Zn cations afforded valuable

information about the Zn binding effects on the studied enzymes. FTIR data obtained for the *R. capsulatus bc₁* samples showed that the Glu295 is protonated in both, the oxidized and the reduced forms of the enzyme. The acidic residue signature gives rise to a positive signal at 1740 cm⁻¹ which shifts towards 1720 cm⁻¹ upon reduction. The 20 cm⁻¹ downshift is an indicator of conformational changing of the residue during the redox reaction. The FTIR data points towards the deprotonation of the crucial residue upon Zn binding. The Zn binding prevents the conformational changing of the Glu295 residue, and thus blocks the proton exit pathway. This observation was confirmed by the mutation of the Glu295 residue, where Zn cations seem to bind to another acidic residue, most likely, to the Asp278 residue. The depletion of the Rieske protein gave new insight into the importance of the conformation of the Zn binding site in the *bc₁* complex. The CcO from *P. denitrificans* has two proton-input pathways, namely the D- and the K-pathways. The exact exit pathways are still unknown. The binding of Zn cations was shown to take place via a deprotonated acidic residue, probably the Glu78 residue of the subunit II. The mutation of this residue against Ala does not prevent the binding of Zn cations. The data obtained for the mutant points toward the binding of Zn cations to a deprotonated acidic residue, most likely at the exit pathway. Furthermore, the binding of Zn cations to the CcO upshifts the midpoint potential of the hemes. The alteration of the redox reaction at the active site might result from the decoupling of the electron transfer reaction and the proton pumping.

The development of the FTIR difference spectroscopy in the low frequency region was one of the main goals of this thesis. The backbone contribution to the FIR spectra of proteins gives rise to a signal in the region around 580–490 cm⁻¹. This signal was assigned to the amide VI vibration. Using model compounds and respiratory chain proteins with known structures, we established a correlation between the amide VI frequency and the secondary structure elements. The contributions appearing in the 517–530 cm⁻¹ spectral range were assigned to the α -helical secondary structures; the signals appearing in the 540–545 cm⁻¹ spectral range were assigned to β -sheet. It was possible to record the electrochemically induced FTIR difference spectra in the FIR domain showing that this spectral range is now accessible for the investigation of metalloproteins in solution. Due to the high absorption of the solvent, and the low absorption coefficient of the metal-ligand vibrations, the electrochemical cell was optimized. The procedure started by testing the feasibility of the experiment on the horse heart cytochrome *c* samples. The optimization of the method allowed reproducing the difference

spectra obtained by Berthomieu, *et al.*¹⁶⁵. In the region below 200 cm^{-1} , where the connectivity band of water occurs, the use of synchrotron light as FIR source is necessary. After performing the primary experiments with the cytochrome *c*, we focused on iron–sulfur proteins and different redox signature of the Fe–S centers were obtained in the region $450\text{--}200\text{ cm}^{-1}$. Briefly, the data points towards the shortening of the Fe–S bonds upon reduction. The effect of pH on the redox–active vibrational modes of the Rieske protein from *T. thermophilus* was also probed by means of FTIR difference spectroscopy in the low frequency range. The Fe–N vibrations arising from the Fe–His bonds were observed below 300 cm^{-1} . The Fe–N vibration arising from a deprotonated His exhibits a signal at 280 cm^{-1} . This signal can be used as a marker band for such coordination. The investigation of iron–sulfur proteins in the FIR range allows understanding the redox behavior of larger complex proteins, such as the NDF, which contains nine Fe–S clusters. In order to accurately assign the difference signals in NDF, ^{54}Fe –labelled samples were also investigated. However, the difference spectra of the labelled and unlabelled samples are not similar to each other. The signal–to–noise ratio is low, due to the large size of the protein. Thus, under these experimental conditions it is difficult to obtain a reproducible difference spectrum of large proteins; otherwise, very concentrated samples are required.

Finally, the hydrogen bonding within proteins, that gives rise to a broad band below 300 cm^{-1} , was investigated in a temperature dependent manner. Upon cooling, the hydrogen bonding signatures of the Rieske protein gained intensity, which indicates the formation of stronger hydrogen bonds at low temperatures. The different samples show glass–like transition cooling until 150 K.

In conclusion, the far infrared difference spectroscopy is a promising tool for the study of proteins. This technique will be used to obtain the far infrared difference spectra of respiratory enzymes such as the cytochrome *bc*₁ complex and the cytochrome *c* oxidase.

5. References

- (1) Waldron, K. J.; Rutherford, J. C.; Ford, D.; Robinson, N. J. Metalloproteins and metal sensing. *Nature* **2009**, *460*, 823-830.
- (2) Valko, M.; Morris, H.; Cronin, M. T. Metals, toxicity and oxidative stress. *Curr Med Chem* **2005**, *12*, 1161-1208.
- (3) Dudev, T.; Lim, C. Metal binding affinity and selectivity in metalloproteins: insights from computational studies. *Annu Rev Biophys* **2008**, *37*, 97-116.
- (4) Rulisek, L.; Vondrasek, J. Coordination geometries of selected transition metal ions (Co²⁺, Ni²⁺, Cu²⁺, Zn²⁺, Cd²⁺, and Hg²⁺) in metalloproteins. *J Inorg Biochem* **1998**, *71*, 115-127.
- (5) Hodgkin, A. L.; Huxley, A. F. A quantitative description of membrane current and its application to conduction and excitation in nerve. *J Physiol* **1952**, *117*, 500-544.
- (6) Catterall, W. A. A 3D view of sodium channels. *Nature* **2001**, *409*, 988-989, 991.
- (7) Doyle, D. A.; Morais Cabral, J.; Pfuetzner, R. A.; Kuo, A.; Gulbis, J. M.; Cohen, S. L.; Chait, B. T.; MacKinnon, R. The structure of the potassium channel: molecular basis of K⁺ conduction and selectivity. *Science* **1998**, *280*, 69-77.
- (8) Tsien, R. W.; Tsien, R. Y. Calcium channels, stores, and oscillations. *Annu Rev Cell Biol* **1990**, *6*, 715-760.
- (9) Clapham, D. E. Calcium signaling. *Cell* **2007**, *131*, 1047-1058.
- (10) Saris, N. E.; Mervaala, E.; Karppanen, H.; Khawaja, J. A.; Lewenstam, A. Magnesium. An update on physiological, clinical and analytical aspects. *Clin Chim Acta* **2000**, *294*, 1-26.
- (11) Ferreira, K. N.; Iverson, T. M.; Maghlaoui, K.; Barber, J.; Iwata, S. Architecture of the photosynthetic oxygen-evolving center. *Science* **2004**, *303*, 1831-1838.
- (12) Law, N. A.; Caudle, M. T.; Pecoraro, V. L. *Manganese Redox Enzymes and Model Systems: Properties, Structures, and Reactivity*, 1998; Vol. 46.
- (13) Cousins, R. J.; Liuzzi, J. P.; Lichten, L. A. Mammalian zinc transport, trafficking, and signals. *J Biol Chem* **2006**, *281*, 24085-24089.
- (14) Maret, W.; Vallee, B. L. Thiolate ligands in metallothionein confer redox activity on zinc clusters. *Proc Natl Acad Sci U S A* **1998**, *95*, 3478-3482.
- (15) Krezel, A.; Hao, Q.; Maret, W. The zinc/thiolate redox biochemistry of metallothionein and the control of zinc ion fluctuations in cell signaling. *Arch Biochem Biophys* **2007**, *463*, 188-200.
- (16) Auld, D. S. Zinc coordination sphere in biochemical zinc sites. *Biometals* **2001**, *14*, 271-313.
- (17) Pavletich, N. P.; Pabo, C. O. Zinc finger-DNA recognition: crystal structure of a Zif268-DNA complex at 2.1 Å. *Science* **1991**, *252*, 809-817.
- (18) Berg, J. M.; Shi, Y. The galvanization of biology: a growing appreciation for the roles of zinc. *Science* **1996**, *271*, 1081-1085.
- (19) Ragsdale, S. W. Nickel-based Enzyme Systems. *J Biol Chem* **2009**, *284*, 18571-18575.
- (20) Quiroz, S.; Kim, J. K.; Mulrooney, S. B.; Hausinger, R. P. Chaperones of Nickel Metabolism. *in Met ions life sci* **2007**, *2*, 519-544.
- (21) Kasprzak, K. S.; Salnikow, K. Nickel Toxicity and Carcinogenesis. *in Met ions life sci* **2007**, *2*, 621-662.
- (22) Neilands, J. B. Microbial iron compounds. *Annu Rev Biochem* **1981**, *50*, 715-731.

- (23) Theil, E. C. Ferritin: structure, gene regulation, and cellular function in animals, plants, and microorganisms. *Annu Rev Biochem* **1987**, *56*, 289-315.
- (24) Aisen, P.; Listowsky, I. Iron transport and storage proteins. *Annu Rev Biochem* **1980**, *49*, 357-393.
- (25) Halliwell, B.; Gutteridge, J. M. Oxygen toxicity, oxygen radicals, transition metals and disease. *Biochem J* **1984**, *219*, 1-14.
- (26) Caughey, W. S. Porphyrin proteins and enzymes. *Annu Rev Biochem* **1967**, *36*, 611-644.
- (27) Thony-Meyer, L. Biogenesis of respiratory cytochromes in bacteria. *Microbiol Mol Biol Rev* **1997**, *61*, 337-376.
- (28) Malmstrom, B. G.; Neilands, J. B. Metalloproteins. *Annu Rev Biochem* **1964**, *33*, 331-354.
- (29) Lill, R.; Muhlenhoff, U. Maturation of iron-sulfur proteins in eukaryotes: mechanisms, connected processes, and diseases. *Annu Rev Biochem* **2008**, *77*, 669-700.
- (30) Beinert, H.; Holm, R. H.; Munck, E. Iron-sulfur clusters: nature's modular, multipurpose structures. *Science* **1997**, *277*, 653-659.
- (31) Venkateswara Rao, P.; Holm, R. H. Synthetic analogues of the active sites of iron-sulfur proteins. *Chem Rev* **2004**, *104*, 527-559.
- (32) Rees, D. C. Great metalloclusters in enzymology. *Annu Rev Biochem* **2002**, *71*, 221-246.
- (33) Battersby, A. R. Biosynthesis of vitamin B12. *Acc Chem Res* **1993**, *26*, 15-21.
- (34) Seetharam, B. Receptor-mediated endocytosis of cobalamin (vitamin B12). *Annu Rev Nutr* **1999**, *19*, 173-195.
- (35) Sennett, C.; Rosenberg, L. E.; Mellman, I. S. Transmembrane transport of cobalamin in prokaryotic and eukaryotic cells. *Annu Rev Biochem* **1981**, *50*, 1053-1086.
- (36) Vogel, T.; Dali-Youcef, N.; Kaltenbach, G.; Andres, E. Homocysteine, vitamin B12, folate and cognitive functions: a systematic and critical review of the literature. *Int J Clin Pract* **2009**, *63*, 1061-1067.
- (37) Fenech, M. The role of folic acid and Vitamin B12 in genomic stability of human cells. *Mutat Res* **2001**, *475*, 57-67.
- (38) Kobayashi, M.; Shimizu, S. Cobalt proteins. *Eur J Biochem* **1999**, *261*, 1-9.
- (39) Huffman, D. L.; O'Halloran, T. V. Function, structure, and mechanism of intracellular copper trafficking proteins. *Annu Rev Biochem* **2001**, *70*, 677-701.
- (40) Sykes, A. In *Long-Range Electron Transfer in Biology* 1991, p 175-224.
- (41) MacPherson, I. S.; Murphy, M. E. Type-2 copper-containing enzymes. *Cell Mol Life Sci* **2007**, *64*, 2887-2899.
- (42) Jaenicke, E.; Decker, H. Functional changes in the family of type 3 copper proteins during evolution. *Chembiochem* **2004**, *5*, 163-169.
- (43) Matoba, Y.; Kumagai, T.; Yamamoto, A.; Yoshitsu, H.; Sugiyama, M. Crystallographic evidence that the dinuclear copper center of tyrosinase is flexible during catalysis. *J Biol Chem* **2006**, *281*, 8981-8990.
- (44) Solomon, E. I.; Baldwin, M. J.; Lowery, M. D. Electronic structures of active sites in copper proteins: contributions to reactivity. *Chem Rev* **1992**, *92*, 521-542.
- (45) Lancaster, K. M.; George, S. D.; Yokoyama, K.; Richards, J. H.; Gray, H. B. Type-zero copper proteins. *Nat Chem* **2009**, *1*, 711-715.
- (46) Waldron, K. J.; Robinson, N. J. How do bacterial cells ensure that metalloproteins get the correct metal? *Nat Rev Microbiol* **2009**, *7*, 25-35.
- (47) Ranquet, C.; Ollagnier-de-Choudens, S.; Loiseau, L.; Barras, F.; Fontecave, M. Cobalt stress in *Escherichia coli*. The effect on the iron-sulfur proteins. *J Biol Chem* **2007**, *282*, 30442-30451.

- (48) Ross, C. A.; Poirier, M. A. Protein aggregation and neurodegenerative disease. *Nat Med* **2004**, *10 Suppl*, S10-17.
- (49) Reinhard, C.; Hebert, S. S.; De Strooper, B. The amyloid-beta precursor protein: integrating structure with biological function. *EMBO J* **2005**, *24*, 3996-4006.
- (50) Smith, D. G.; Cappai, R.; Barnham, K. J. The redox chemistry of the Alzheimer's disease amyloid beta peptide. *Biochim Biophys Acta* **2007**, *1768*, 1976-1990.
- (51) Dudkina, N. V.; Kouril, R.; Peters, K.; Braun, H. P.; Boekema, E. J. Structure and function of mitochondrial supercomplexes. *Biochim Biophys Acta* **2009**.
- (52) Schagger, H. Respiratory chain supercomplexes of mitochondria and bacteria. *Biochim Biophys Acta* **2002**, *1555*, 154-159.
- (53) Lehninger, A. L. *Biochemistry, 2nd edition*, pp. 443-542. Worth Publishers, New York., 1975.
- (54) Carroll, J.; Fearnley, I. M.; Shannon, R. J.; Hirst, J.; Walker, J. E. Analysis of the subunit composition of complex I from bovine heart mitochondria. *Mol Cell Proteomics* **2003**, *2*, 117-126.
- (55) Sazanov, L. A.; Hinchliffe, P. Structure of the hydrophilic domain of respiratory complex I from *Thermus thermophilus*. *Science* **2006**, *311*, 1430-1436.
- (56) Guenebaut, V.; Vincentelli, R.; Mills, D.; Weiss, H.; Leonard, K. R. Three-dimensional structure of NADH-dehydrogenase from *Neurospora crassa* by electron microscopy and conical tilt reconstruction. *J Mol Biol* **1997**, *265*, 409-418.
- (57) Degli Esposti, M. Inhibitors of NADH-ubiquinone reductase: an overview. *Biochim Biophys Acta* **1998**, *1364*, 222-235.
- (58) Friedrich, T.; van Heek, P.; Leif, H.; Ohnishi, T.; Forche, E.; Kunze, B.; Jansen, R.; Trowitzsch-Kienast, W.; Hofle, G.; Reichenbach, H.; et al. Two binding sites of inhibitors in NADH: ubiquinone oxidoreductase (complex I). Relationship of one site with the ubiquinone-binding site of bacterial glucose:ubiquinone oxidoreductase. *Eur J Biochem* **1994**, *219*, 691-698.
- (59) Efremov, R. G.; Baradaran, R.; Sazanov, L. A. The architecture of respiratory complex I. *Nature* **2010**, *465*, 441-445.
- (60) Sled, V. D.; Rudnitsky, N. I.; Hatefi, Y.; Ohnishi, T. Thermodynamic analysis of flavin in mitochondrial NADH:ubiquinone oxidoreductase (complex I). *Biochemistry* **1994**, *33*, 10069-10075.
- (61) Mamedova, A. A.; Holt, P. J.; Carroll, J.; Sazanov, L. A. Substrate-induced conformational change in bacterial complex I. *J Biol Chem* **2004**, *279*, 23830-23836.
- (62) Verkhovskaya, M. L.; Belevich, N.; Euro, L.; Wikstrom, M.; Verkhovsky, M. I. Real-time electron transfer in respiratory complex I. *Proc Natl Acad Sci U S A* **2008**, *105*, 3763-3767.
- (63) Kussmaul, L.; Hirst, J. The mechanism of superoxide production by NADH:ubiquinone oxidoreductase (complex I) from bovine heart mitochondria. *Proc Natl Acad Sci U S A* **2006**, *103*, 7607-7612.
- (64) Kudin, A. P.; Bimpong-Buta, N. Y.; Vielhaber, S.; Elger, C. E.; Kunz, W. S. Characterization of superoxide-producing sites in isolated brain mitochondria. *J Biol Chem* **2004**, *279*, 4127-4135.
- (65) Yagi, T.; Matsuno-Yagi, A. The proton-translocating NADH-quinone oxidoreductase in the respiratory chain: the secret unlocked. *Biochemistry* **2003**, *42*, 2266-2274.
- (66) Flemming, D.; Stolpe, S.; Schneider, D.; Hellwig, P.; Friedrich, T. A possible role for iron-sulfur cluster N2 in proton translocation by the NADH: ubiquinone oxidoreductase (complex I). *J Mol Microbiol Biotechnol* **2005**, *10*, 208-222.
- (67) Euro, L.; Belevich, G.; Verkhovsky, M. I.; Wikstrom, M.; Verkhovskaya, M. Conserved lysine residues of the membrane subunit NuoM are involved in energy conversion

- by the proton-pumping NADH:ubiquinone oxidoreductase (Complex I). *Biochim Biophys Acta* **2008**, 1777, 1166-1172.
- (68) Flemming, D.; Hellwig, P.; Lepper, S.; Kloer, D. P.; Friedrich, T. Catalytic importance of acidic amino acids on subunit NuoB of the Escherichia coli NADH:ubiquinone oxidoreductase (complex I). *J Biol Chem* **2006**, 281, 24781-24789.
- (69) Flemming, D.; Hellwig, P.; Friedrich, T. Involvement of tyrosines 114 and 139 of subunit NuoB in the proton pathway around cluster N2 in Escherichia coli NADH:ubiquinone oxidoreductase. *J Biol Chem* **2003**, 278, 3055-3062.
- (70) Kotlyar, A. B.; Sled, V. D.; Burbaev, D. S.; Moroz, I. A.; Vinogradov, A. D. Coupling site I and the rotenone-sensitive ubisemiquinone in tightly coupled submitochondrial particles. *FEBS Lett* **1990**, 264, 17-20.
- (71) Vinogradov, A. D.; Sled, V. D.; Burbaev, D. S.; Grivennikova, V. G.; Moroz, I. A.; Ohnishi, T. Energy-dependent Complex I-associated ubisemiquinones in submitochondrial particles. *FEBS Lett* **1995**, 370, 83-87.
- (72) Vinogradov, A. D. Respiratory complex I: structure, redox components, and possible mechanisms of energy transduction. *Biochemistry (Mosc)* **2001**, 66, 1086-1097.
- (73) Friedrich, T.; Hellwig, P. Redox-induced conformational changes within the Escherichia coli NADH ubiquinone oxidoreductase (complex I): An analysis by mutagenesis and FT-IR spectroscopy. *Biochim Biophys Acta* **2010**.
- (74) Sharpley, M. S.; Hirst, J. The inhibition of mitochondrial complex I (NADH:ubiquinone oxidoreductase) by Zn²⁺. *J Biol Chem* **2006**, 281, 34803-34809.
- (75) Giachini, L.; Francia, F.; Veronesi, G.; Lee, D. W.; Daldal, F.; Huang, L. S.; Berry, E. A.; Cocco, T.; Papa, S.; Boscherini, F.; Venturaoli, G. X-Ray absorption studies of Zn²⁺ binding sites in bacterial, avian, and bovine cytochrome bc₁ complexes. *Biophys J* **2007**, 93, 2934-2951.
- (76) Ruprecht, J.; Yankovskaya, V.; Maklashina, E.; Iwata, S.; Cecchini, G. Structure of Escherichia coli succinate:quinone oxidoreductase with an occupied and empty quinone-binding site. *J Biol Chem* **2009**, 284, 29836-29846.
- (77) Lancaster, C. R.; Kroger, A.; Auer, M.; Michel, H. Structure of fumarate reductase from Wolinella succinogenes at 2.2 Å resolution. *Nature* **1999**, 402, 377-385.
- (78) Haas, A. H.; Lancaster, C. R. Calculated coupling of transmembrane electron and proton transfer in dihemic quinol:fumarate reductase. *Biophys J* **2004**, 87, 4298-4315.
- (79) Lancaster, C. R. Wolinella succinogenes quinol:fumarate reductase-2.2-Å resolution crystal structure and the E-pathway hypothesis of coupled transmembrane proton and electron transfer. *Biochim Biophys Acta* **2002**, 1565, 215-231.
- (80) Xia, D.; Yu, C. A.; Kim, H.; Xia, J. Z.; Kachurin, A. M.; Zhang, L.; Yu, L.; Deisenhofer, J. Crystal structure of the cytochrome bc₁ complex from bovine heart mitochondria. *Science* **1997**, 277, 60-66.
- (81) Iwata, S.; Lee, J. W.; Okada, K.; Lee, J. K.; Iwata, M.; Rasmussen, B.; Link, T. A.; Ramaswamy, S.; Jap, B. K. Complete structure of the 11-subunit bovine mitochondrial cytochrome bc₁ complex. *Science* **1998**, 281, 64-71.
- (82) Mulkidjanian, A. Y. Ubiquinol oxidation in the cytochrome bc₁ complex: reaction mechanism and prevention of short-circuiting. *Biochim Biophys Acta* **2005**, 1709, 5-34.
- (83) Zhang, Z.; Huang, L.; Shulmeister, V. M.; Chi, Y. I.; Kim, K. K.; Hung, L. W.; Crofts, A. R.; Berry, E. A.; Kim, S. H. Electron transfer by domain movement in cytochrome bc₁. *Nature* **1998**, 392, 677-684.
- (84) Lange, C.; Hunte, C. Crystal structure of the yeast cytochrome bc₁ complex with its bound substrate cytochrome c. *Proc Natl Acad Sci U S A* **2002**, 99, 2800-2805.

- (85) Berry, E. A.; Huang, L. S.; Saechao, L. K.; Pon, N. G.; Valkova-Valchanova, M.; Daldal, F. X-Ray Structure of Rhodobacter Capsulatus Cytochrome bc (1): Comparison with its Mitochondrial and Chloroplast Counterparts. *Photosynth Res* **2004**, *81*, 251-275.
- (86) Esser, L.; Elberry, M.; Zhou, F.; Yu, C. A.; Yu, L.; Xia, D. Inhibitor-complexed structures of the cytochrome bc1 from the photosynthetic bacterium Rhodobacter sphaeroides. *J Biol Chem* **2008**, *283*, 2846-2857.
- (87) Kurisu, G.; Zhang, H.; Smith, J. L.; Cramer, W. A. Structure of the Cytochrome b6f Complex of Oxygenic Photosynthesis: Tuning the Cavity. *Science* **2003**, *302*, 1009-1014.
- (88) Mitchell, P. The protonmotive Q cycle: a general formulation. *FEBS lett* **1975**, *59*, 137-139.
- (89) Mitchell, P. Protonmotive redox mechanism of the cytochrome b-c1 complex in the respiratory chain: protonmotive ubiquinone cycle. *FEBS lett* **1975**, *56*, 1-6.
- (90) Crofts, A. R. The Q-cycle - A Personal Perspective. *Photosynth Res* **2004**, *80*, 223-243.
- (91) Crofts, A. R.; Meinhardt, S. W.; Jones, K. R.; Snozzi, M. The role of the quinone pool in the cyclic electron-transfer chain of Rhodospseudomonas sphaeroides A modified Q-cycle mechanism. *Biochim Biophys Acta* **1983**, *723*, 202-218.
- (92) Crofts, A. R.; Holland, J. T.; Victoria, D.; Kolling, D. R.; Dikanov, S. A.; Gilbreth, R.; Lhee, S.; Kuras, R.; Kuras, M. G. The Q-cycle reviewed: How well does a monomeric mechanism of the bc(1) complex account for the function of a dimeric complex? *Biochim Biophys Acta* **2008**, *1777*, 1001-1019.
- (93) Covian, R.; Gutierrez-Cirlos, E. B.; Trumpower, B. L. Anti-cooperative oxidation of ubiquinol by the yeast cytochrome bc1 complex. *J Biol Chem* **2004**, *279*, 15040-15049.
- (94) Cooley, J. W.; Lee, D. W.; Daldal, F. Across membrane communication between the Q(o) and Q(i) active sites of cytochrome bc(1). *Biochemistry* **2009**, *48*, 1888-1899.
- (95) Castellani, M.; Covian, R.; Kleinschroth, T.; Anderka, O.; Ludwig, B.; Trumpower, B. L. Direct demonstration of half-of-the-sites reactivity in the dimeric cytochrome bc1 complex: enzyme with one inactive monomer is fully active but unable to activate the second ubiquinol oxidation site in response to ligand binding at the ubiquinone reduction site. *J Biol Chem* **2010**, *285*, 502-510.
- (96) Hunte, C.; Koepke, J.; Lange, C.; Rossmann, T.; Michel, H. Structure at 2.3 Å resolution of the cytochrome bc(1) complex from the yeast *Saccharomyces cerevisiae* co-crystallized with an antibody Fv fragment. *Structure* **2000**, *8*, 669-684.
- (97) Iwaki, M.; Yakovlev, G.; Hirst, J.; Osyczka, A.; Dutton, P. L.; Marshall, D.; Rich, P. R. Direct observation of redox-linked histidine protonation changes in the iron-sulfur protein of the cytochrome bc1 complex by ATR-FTIR spectroscopy. *Biochemistry* **2005**, *44*, 4230-4237.
- (98) Zu, Y.; Fee, J. A.; Hirst, J. Complete thermodynamic characterization of reduction and protonation of the bc(1)-type Rieske [2Fe-2S] center of *Thermus thermophilus*. *J Am Chem Soc* **2001**, *123*, 9906-9907.
- (99) Hunte, C.; Palsdottir, H.; Trumpower, B. L. Protonmotive pathways and mechanisms in the cytochrome bc1 complex. *FEBS lett* **2003**, *545*, 39-46.
- (100) Crofts, A. R.; Hong, S.; Ugulava, N.; Barquera, B.; Gennis, R.; Guergova-Kuras, M.; Berry, E. A. Pathways for proton release during ubihydroquinone oxidation by the bc(1) complex. *Proc Natl Acad Sci U S A* **1999**, *96*, 10021-10026.
- (101) Berry, E. A.; Zhang, Z.; Bellamy, H. D.; Huang, L. Crystallographic location of two Zn(2+)-binding sites in the avian cytochrome bc(1) complex. *Biochim Biophys Acta* **2000**, *1459*, 440-448.
- (102) Giachini, L.; Francia, F.; Veronesi, G.; Lee, D. W.; Daldal, F.; Huang, L. S.; Berry, E. A.; Cocco, T.; Papa, S.; Boscherini, F.; Venturoli, G. X-Ray absorption studies of Zn²⁺

- binding sites in bacterial, avian, and bovine cytochrome bc₁ complexes. *Biophys J* **2007**, *93*, 2934-2951.
- (103) Tsukihara, T.; Aoyama, H.; Yamashita, E.; Tomizaki, T.; Yamaguchi, H.; Shinzawa-Itoh, K.; Nakashima, R.; Yaono, R.; Yoshikawa, S. The whole structure of the 13-subunit oxidized cytochrome c oxidase at 2.8 Å. *Science* **1996**, *272*, 1136-1144.
- (104) Koepke, J.; Olkhova, E.; Angerer, H.; Muller, H.; Peng, G.; Michel, H. High resolution crystal structure of *Paracoccus denitrificans* cytochrome c oxidase: new insights into the active site and the proton transfer pathways. *Biochim Biophys Acta* **2009**, *1787*, 635-645.
- (105) Iwata, S.; Ostermeier, C.; Ludwig, B.; Michel, H. Structure at 2.8 Å resolution of cytochrome c oxidase from *Paracoccus denitrificans*. *Nature* **1995**, *376*, 660-669.
- (106) Richter, O. M.; Ludwig, B. Electron transfer and energy transduction in the terminal part of the respiratory chain - lessons from bacterial model systems. *Biochim Biophys Acta* **2009**, *1787*, 626-634.
- (107) Branden, G.; Gennis, R. B.; Brzezinski, P. Transmembrane proton translocation by cytochrome c oxidase. *Biochim Biophys Acta* **2006**, *1757*, 1052-1063.
- (108) Qin, L.; Mills, D. A.; Hiser, C.; Murphree, A.; Garavito, R. M.; Ferguson-Miller, S.; Hosler, J. Crystallographic location and mutational analysis of Zn and Cd inhibitory sites and role of lipidic carboxylates in rescuing proton path mutants in cytochrome c oxidase. *Biochemistry* **2007**, *46*, 6239-6248.
- (109) Salje, J.; Ludwig, B.; Richter, O. M. Is a third proton-conducting pathway operative in bacterial cytochrome c oxidase? *Biochem Soc Trans* **2005**, *33*, 829-831.
- (110) Alben, J. O.; Moh, P. P.; Fiamingo, F. G.; Altschuld, R. A. Cytochrome oxidase (a₃) heme and copper observed by low-temperature Fourier transform infrared spectroscopy of the CO complex. *Proc Natl Acad Sci U S A* **1981**, *78*, 234-237.
- (111) Hayashi, T.; Lin, M. T.; Ganesan, K.; Chen, Y.; Fee, J. A.; Gennis, R. B.; Moenne-Loccoz, P. Accommodation of two diatomic molecules in cytochrome bo: insights into NO reductase activity in terminal oxidases. *Biochemistry* **2009**, *48*, 883-890.
- (112) Pinakoulaki, E.; Ohta, T.; Soulimane, T.; Kitagawa, T.; Varotsis, C. Detection of the His-heme Fe²⁺-NO species in the reduction of NO to N₂O by ba₃-oxidase from *thermus thermophilus*. *J Am Chem Soc* **2005**, *127*, 15161-15167.
- (113) Adelroth, P.; Ek, M. S.; Mitchell, D. M.; Gennis, R. B.; Brzezinski, P. Glutamate 286 in cytochrome aa₃ from *Rhodobacter sphaeroides* is involved in proton uptake during the reaction of the fully-reduced enzyme with dioxygen. *Biochemistry* **1997**, *36*, 13824-13829.
- (114) Junemann, S.; Meunier, B.; Gennis, R. B.; Rich, P. R. Effects of mutation of the conserved lysine-362 in cytochrome c oxidase from *Rhodobacter sphaeroides*. *Biochemistry* **1997**, *36*, 14456-14464.
- (115) Branden, M.; Sigurdson, H.; Namslauer, A.; Gennis, R. B.; Adelroth, P.; Brzezinski, P. On the role of the K-proton transfer pathway in cytochrome c oxidase. *Proc Natl Acad Sci U S A* **2001**, *98*, 5013-5018.
- (116) Durr, K. L.; Koepke, J.; Hellwig, P.; Muller, H.; Angerer, H.; Peng, G.; Olkhova, E.; Richter, O. M.; Ludwig, B.; Michel, H. A D-pathway mutation decouples the *Paracoccus denitrificans* cytochrome c oxidase by altering the side-chain orientation of a distant conserved glutamate. *J Mol Biol* **2008**, *384*, 865-877.
- (117) Pfitzner, U.; Hoffmeier, K.; Harrenga, A.; Kannt, A.; Michel, H.; Bamberg, E.; Richter, O. M.; Ludwig, B. Tracing the D-pathway in reconstituted site-directed mutants of cytochrome c oxidase from *Paracoccus denitrificans*. *Biochemistry* **2000**, *39*, 6756-6762.
- (118) Branden, M.; Tomson, F.; Gennis, R. B.; Brzezinski, P. The entry point of the K-proton-transfer pathway in cytochrome c oxidase. *Biochemistry* **2002**, *41*, 10794-10798.

- (119) Behr, J.; Michel, H.; Mantele, W.; Hellwig, P. Functional properties of the heme propionates in cytochrome c oxidase from *Paracoccus denitrificans*. Evidence from FTIR difference spectroscopy and site-directed mutagenesis. *Biochemistry* **2000**, *39*, 1356-1363.
- (120) Behr, J.; Hellwig, P.; Mantele, W.; Michel, H. Redox dependent changes at the heme propionates in cytochrome c oxidase from *Paracoccus denitrificans*: direct evidence from FTIR difference spectroscopy in combination with heme propionate ¹³C labeling. *Biochemistry* **1998**, *37*, 7400-7406.
- (121) Wikstrom, M.; Verkhovsky, M. I. Mechanism and energetics of proton translocation by the respiratory heme-copper oxidases. *Biochim Biophys Acta* **2007**, *1767*, 1200-1214.
- (122) Brzezinski, P.; Gennis, R. B. Cytochrome c oxidase: exciting progress and remaining mysteries. *J Bioenerg Biomembr* **2008**, *40*, 521-531.
- (123) Papa, S.; Capitanio, N.; Capitanio, G.; Palese, L. L. Protonmotive cooperativity in cytochrome c oxidase. *Biochim Biophys Acta* **2004**, *1658*, 95-105.
- (124) Nakamoto, R. K.; Ketchum, C. J.; al-Shawi, M. K. Rotational coupling in the F₀F₁ ATP synthase. *Annu Rev Biophys Biomol Struct* **1999**, *28*, 205-234.
- (125) Johnson, D. C.; Dean, D. R.; Smith, A. D.; Johnson, M. K. Structure, function, and formation of biological iron-sulfur clusters. *Annu Rev Biochem* **2005**, *74*, 247-281.
- (126) Bau, R.; Rees, D. C.; Kurtz Jr, D. M.; Scott, R. A.; Huang, H.; Adams, M. W. W.; Eidsness, M. K. Crystal structure of rubredoxin from *Pyrococcus furiosus* at 0.95 Å resolution, and the structures of N-terminal methionine and formylmethionine variants of Pf Rd. Contributions of N-terminal interactions to thermostability. *J Biol Inorg Chem* **1998**, *3*, 484-493.
- (127) Dauter, Z.; Wilson, K. S.; Sieker, L. C.; Moulis, J. M.; Meyer, J. Zinc- and iron-rubredoxins from *Clostridium pasteurianum* at atomic resolution: a high-precision model of a ZnS₄ coordination unit in a protein. *Proc Natl Acad Sci U S A* **1996**, *93*, 8836-8840.
- (128) Frey, M.; Sieker, L.; Payan, F.; Haser, R.; Bruschi, M.; Pepe, G.; LeGall, J. Rubredoxin from *Desulfovibrio gigas*. A molecular model of the oxidized form at 1.4 Å resolution. *J Mol Biol* **1987**, *197*, 525-541.
- (129) Stenkamp, R. E.; Sieker, L. C.; Jensen, L. H. The structure of rubredoxin from *Desulfovibrio desulfuricans* strain 27774 at 1.5 Å resolution. *Proteins* **1990**, *8*, 352-364.
- (130) Binda, C.; Coda, A.; Aliverti, A.; Zanetti, G.; Mattevi, A. Structure of the mutant E92K of [2Fe-2S] ferredoxin I from *Spinacia oleracea* at 1.7 Å resolution. *Acta Crystallogr D Biol Crystallogr* **1998**, *54*, 1353-1358.
- (131) Bertini, I.; Donaire, A.; Feinberg, B. A.; Luchinat, C.; Piccioli, M.; Yuan, H. Solution structure of the oxidized 2[4Fe-4S] ferredoxin from *Clostridium pasteurianum*. *Eur J Biochem* **1995**, *232*, 192-205.
- (132) Kissinger, C. R.; Sieker, L. C.; Adman, E. T.; Jensen, L. H. Refined crystal structure of ferredoxin II from *Desulfovibrio gigas* at 1.7 Å. *J Mol Biol* **1991**, *219*, 693-715.
- (133) Beinert, H. Iron-sulfur proteins: ancient structures, still full of surprises. *J Biol Inorg Chem* **2000**, *5*, 2-15.
- (134) Menin, L.; Gaillard, J.; Parot, P.; Schoepp, B.; Nitschke, W.; Vermeglio, A. Role of HiPIP as electron donor to the RC-bound cytochrome in photosynthetic purple bacteria. *Photosyn Res* **1998**, *55*, 343-348.
- (135) Duff, J. L. C.; Breton, J. L. J.; Butt, J. N.; Armstrong, F. A.; Thomson, A. J. Novel redox chemistry of [3Fe-4S] clusters: Electrochemical characterization of the all-Fe(II) form of the [3Fe-4S] cluster generated reversibly in various proteins and its spectroscopic investigation in *Sulfolobus acidocaldarius* ferredoxin. *J Am Chem Soc* **1996**, *118*, 8593-8603.
- (136) Leggate, E. J.; Bill, E.; Essigke, T.; Ullmann, G. M.; Hirst, J. Formation and characterization of an all-ferrous Rieske cluster and stabilization of the [2Fe-2S](0) core by protonation. *Proc Natl Acad Sci USA* **2004**, *101*, 10913-10918.

- (137) Kolling, D. J.; Brunzelle, J. S.; Lhee, S.; Crofts, A. R.; Nair, S. K. Atomic resolution structures of Rieske iron-sulfur protein: Role of hydrogen bonds in tuning the redox potential of iron-sulfur clusters. *Structure* **2007**, *15*, 29-38.
- (138) Schroter, T.; Hatzfeld, O. M.; Gemeinhardt, S.; Korn, M.; Friedrich, T.; Ludwig, B.; Link, T. A. Mutational analysis of residues forming hydrogen bonds in the Rieske [2Fe-2S] cluster of the cytochrome bc(1) complex in *Paracoccus denitrificans*. *Eur J Biochem* **1998**, *255*, 100-106.
- (139) Venyaminov, S.; Kalnin, N. N. Quantitative IR spectrophotometry of peptide compounds in water (H₂O) solutions. II. Amide absorption bands of polypeptides and fibrous proteins in alpha-, beta-, and random coil conformations. *Biopolymers* **1990**, *30*, 1259-1271.
- (140) Goormaghtigh, E.; Cabiaux, V.; Ruyschaert, J. M. Determination of soluble and membrane protein structure by Fourier transform infrared spectroscopy. III. Secondary structures. *Subcell Biochem* **1994**, *23*, 405-450.
- (141) Jung, C. Insight into protein structure and protein-ligand recognition by Fourier transform infrared spectroscopy. *J Mol Recognit* **2000**, *13*, 325-351.
- (142) Bandekar, J. Amide modes and protein conformation. *Biochim Biophys Acta* **1992**, *1120*, 123-143.
- (143) Kong, J.; Yu, S. Fourier transform infrared spectroscopic analysis of protein secondary structures. *Acta Biochim Biophys Sin (Shanghai)* **2007**, *39*, 549-559.
- (144) Moss, D.; Navedryk, E.; Breton, J.; Mantele, W. Redox-linked conformational changes in proteins detected by a combination of infrared spectroscopy and protein electrochemistry. Evaluation of the technique with cytochrome c. *Eur J Biochem* **1990**, *187*, 565-572.
- (145) Hellwig, P.; Rost, B.; Kaiser, U.; Ostermeier, C.; Michel, H.; Mantele, W. Carboxyl group protonation upon reduction of the *Paracoccus denitrificans* cytochrome c oxidase: direct evidence by FTIR spectroscopy. *FEBS Lett* **1996**, *385*, 53-57.
- (146) Hellwig, P.; Pfitzner, U.; Behr, J.; Rost, B.; Pesavento, R. P.; Donk, W. V.; Gennis, R. B.; Michel, H.; Ludwig, B.; Mantele, W. Vibrational modes of tyrosines in cytochrome c oxidase from *Paracoccus denitrificans*: FTIR and electrochemical studies on Tyr-D4-labeled and on Tyr280His and Tyr35Phe mutant enzymes. *Biochemistry* **2002**, *41*, 9116-9125.
- (147) Hellwig, P.; Behr, J.; Ostermeier, C.; Richter, O. M.; Pfitzner, U.; Odenwald, A.; Ludwig, B.; Michel, H.; Mantele, W. Involvement of glutamic acid 278 in the redox reaction of the cytochrome c oxidase from *Paracoccus denitrificans* investigated by FTIR spectroscopy. *Biochemistry* **1998**, *37*, 7390-7399.
- (148) Goormaghtigh, E.; Raussens, V.; Ruyschaert, J. M. Attenuated total reflection infrared spectroscopy of proteins and lipids in biological membranes. *Biochim Biophys Acta* **1999**, *1422*, 105-185.
- (149) Zscherp, C.; Barth, A. Reaction-induced infrared difference spectroscopy for the study of protein reaction mechanisms. *Biochemistry* **2001**, *40*, 1875-1883.
- (150) Sevenou, O.; Hill, S. E.; Farhat, I. A.; Mitchell, J. R. Organisation of the external region of the starch granule as determined by infrared spectroscopy. *Int J Biol Macromol* **2002**, *31*, 79-85.
- (151) Rich, P. R.; Iwaki, M. Methods to probe protein transitions with ATR infrared spectroscopy. *Mol Biosyst* **2007**, *3*, 398-407.
- (152) Hielscher, R. The role of lipids and nucleotides in the catalytic mechanism of proteins from the respiratory chain: an electrochemical and infrared spectroscopic approach. University of Strasbourg, **2009**.
- (153) Fee, J. A.; Findling, K. L.; Yoshida, T.; Hille, R.; Tarr, G. E.; Hearshen, D. O.; Dunham, W. R.; Day, E. P.; Kent, T. A.; Munck, E. Purification and characterization of the

- Rieske iron-sulfur protein from *Thermus thermophilus*. Evidence for a [2Fe-2S] cluster having non-cysteine ligands. *J Biol Chem* **1984**, *259*, 124-133.
- (154) Bungert, S.; Krafft, B.; Schlesinger, R.; Friedrich, T. One-step purification of the NADH dehydrogenase fragment of the *Escherichia coli* complex I by means of Strep-tag affinity chromatography. *FEBS Lett* **1999**, *460*, 207-211.
- (155) Grull, J. M.; Hennecke, H.; Frohler, J.; Thomale, J.; Nass, G.; Bock, A. *Escherichia coli* mutants overproducing phenylalanyl- and threonyl-tRNA synthetase. *J Bacteriol* **1979**, *137*, 480-489.
- (156) Braun, M.; Bungert, S.; Friedrich, T. Characterization of the overproduced NADH dehydrogenase fragment of the NADH:ubiquinone oxidoreductase (complex I) from *Escherichia coli*. *Biochemistry* **1998**, *37*, 1861-1867.
- (157) Davidson, E.; Ohnishi, T.; Tokito, M.; Daldal, F. *Rhodobacter capsulatus* mutants lacking the Rieske FeS protein form a stable cytochrome bc₁ subcomplex with an intact quinone reduction site. *Biochemistry* **1992**, *31*, 3351-3358.
- (158) Osyczka, A.; Zhang, H.; Mathe, C.; Rich, P. R.; Moser, C. C.; Dutton, P. L. Role of the PEWY glutamate in hydroquinone-quinone oxidation-reduction catalysis in the Qo Site of cytochrome bc₁. *Biochemistry* **2006**, *45*, 10492-10503.
- (159) Zimmerman, T.; Oyarzabal, J.; Sebastian, E. S.; Majumdar, S.; Tejo, B. A.; Siahaan, T. J.; Blanco, F. J. ICAM-1 peptide inhibitors of T-cell adhesion bind to the allosteric site of LFA-1. An NMR characterization. *Chem Biol Drug Des* **2007**, *70*, 347-353.
- (160) Torreggiani, A.; Tamba, M.; Bonora, S.; Fini, G. Raman and IR study on copper binding of histamine. *Biopolymers* **2003**, *72*, 290-298.
- (161) Mesu, J. G.; Visser, T.; Beale, A. M.; Soulimani, F.; Weckhuysen, B. M. Host-guest chemistry of copper(II)-histidine complexes encaged in zeolite Y. *Chemistry* **2006**, *12*, 7167-7177.
- (162) Mesu, J. G.; Visser, T.; Soulimani, F.; van Faassen, E. E.; de Peinder, P.; Beale, A. M.; Weckhuysen, B. M. New insights into the coordination chemistry and molecular structure of copper(II) histidine complexes in aqueous solutions. *Inorg Chem* **2006**, *45*, 1960-1971.
- (163) Miura, T.; Satoh, T.; Takeuchi, H. Role of metal-ligand coordination in the folding pathway of zinc finger peptides. *Biochim Biophys Acta* **1998**, *1384*, 171-179.
- (164) Marboutin, L.; Desbois, A.; Berthomieu, C. Low-frequency heme, iron-ligand, and ligand modes of imidazole and imidazolate complexes of iron protoporphyrin and microperoxidase in aqueous solution. An analysis by far-infrared difference spectroscopy. *J Phys Chem B* **2009**, *113*, 4492-4499.
- (165) Berthomieu, C.; Marboutin, L.; Dupeyrat, F.; Bouyer, P. Electrochemically induced FTIR difference spectroscopy in the mid- to far infrared (200 microm) domain: a new setup for the analysis of metal-ligand interactions in redox proteins. *Biopolymers* **2006**, *82*, 363-367.
- (166) Dorr, S.; Schade, U.; Hellwig, P.; Ortolani, M. Characterization of temperature-dependent iron-imidazole vibrational modes in far infrared. *J Phys Chem B* **2007**, *111*, 14418-14422.
- (167) Levitzki, A.; Pecht, I.; Berger, A. The copper-poly-L-histidine complexes. II. Physicochemical properties. *J Am Chem Soc* **1972**, *94*, 6844-6848.
- (168) Kowalik-Jankowska, T.; Ruta, M.; Wisniewska, K.; Lankiewicz, L. Coordination abilities of the 1-16 and 1-28 fragments of beta-amyloid peptide towards copper(II) ions: a combined potentiometric and spectroscopic study. *J Inorg Biochem* **2003**, *95*, 270-282.
- (169) Kallay, C.; Varnagy, K.; Malandrinos, G.; Hadjiliadis, N.; Sanna, D.; Sovago, I. Copper(II) complexes of terminally protected pentapeptides containing three histidyl residues in alternating positions, Ac-His-Xaa-His-Yaa-His-NH₂. *Dalton Trans* **2006**, 4545-4552.

- (170) Mesu, J. G.; Visser, T.; Soulimani, F.; Weckhuysen, B. M. Infrared and Raman spectroscopic study of pH-induced structural changes of L-histidine in aqueous environment. *Vib Spectrosc* **2005**, *39*, 114-125.
- (171) Muehlinghaus, J.; Zundel, G. Infrared investigation of poly-L-histidine structure dependent on protonation. *Biopolymers* **1971**, *10*, 711-719.
- (172) Hasegawa, K.; Ono, T.; Noguchi, T. Vibrational spectra and ab initio DFT calculations of 4-methylimidazole and its different protonation forms: Infrared and raman markers of the protonation state of a histidine side chain. *J Phys Chem B* **2000**, *104*, 4253-4265.
- (173) Loeffen, P. W.; Pettifer, R. F.; Fillaux, F.; Kearley, G. J. Vibrational Force-Field of Solid Imidazole from Inelastic Neutron-Scattering. *J Chem Phys* **1995**, *103*, 8444-8455.
- (174) Miura, T.; Satoh, T.; Hori-i, A.; Takeuchi, H. Raman marker bands of metal coordination sites of histidine side chains in peptides and proteins. *J Raman Spectrosc* **1998**, *29*, 41-47.
- (175) Hasegawa, K.; Ono, T.; Noguchi, T. Ab initio density functional theory calculations and vibrational analysis of zinc-bound 4-methylimidazole as a model of a histidine ligand in metalloenzymes. *J Phys Chem A* **2002**, *106*, 3377-3390.
- (176) Drozdowski, P.; Kordon, E. Isotopic studies of the metal-ligand vibrations in histamine complexes with copper(II). *Spectrochim Acta A Mol Biomol Spectrosc* **2000**, *56A*, 1299-1304.
- (177) Wolpert, M.; Hellwig, P. Infrared spectra and molar absorption coefficients of the 20 alpha amino acids in aqueous solutions in the spectral range from 1800 to 500 cm(-1). *Spectrochim Acta A Mol Biomol Spectrosc* **2006**, *64*, 987-1001.
- (178) Brubach, J. B.; Mermet, A.; Filabozzi, A.; Gerschel, A.; Roy, P. Signatures of the hydrogen bonding in the infrared bands of water. *J Chem Phys* **2005**, *122*, 184509.
- (179) Zelsmann, H. R. Temperature-Dependence of the Optical-Constants for Liquid H₂O and D₂O in the Far Ir Region. *Journal of Molecular Structure* **1995**, *350*, 95-114.
- (180) Maklakov, L. I. Low-frequency vibrational spectroscopy of amides and urethanes. *Russ Chem Rev* **1997**, *66*, 375-388.
- (181) Faller, P. Copper and zinc binding to amyloid-beta: coordination, dynamics, aggregation, reactivity and metal-ion transfer. *Chembiochem* **2009**, *10*, 2837-2845.
- (182) Murakami, K.; Irie, K.; Ohigashi, H.; Hara, H.; Nagao, M.; Shimizu, T.; Shirasawa, T. Formation and stabilization model of the 42-mer Aβ radical: implications for the long-lasting oxidative stress in Alzheimer's disease. *J Am Chem Soc* **2005**, *127*, 15168-15174.
- (183) Smith, D. P.; Smith, D. G.; Curtain, C. C.; Boas, J. F.; Pilbrow, J. R.; Ciccotosto, G. D.; Lau, T. L.; Tew, D. J.; Perez, K.; Wade, J. D.; Bush, A. I.; Drew, S. C.; Separovic, F.; Masters, C. L.; Cappai, R.; Barnham, K. J. Copper-mediated amyloid-beta toxicity is associated with an intermolecular histidine bridge. *J Biol Chem* **2006**, *281*, 15145-15154.
- (184) Miura, T.; Suzuki, K.; Kohata, N.; Takeuchi, H. Metal binding modes of Alzheimer's amyloid beta-peptide in insoluble aggregates and soluble complexes. *Biochemistry* **2000**, *39*, 7024-7031.
- (185) Dorlet, P.; Gambarelli, S.; Faller, P.; Hureau, C. Pulse EPR spectroscopy reveals the coordination sphere of copper(II) ions in the 1-16 amyloid-beta peptide: a key role of the first two N-terminus residues. *Angew Chem Int Ed Engl* **2009**, *48*, 9273-9276.
- (186) Shin, B. K.; Saxena, S. Direct evidence that all three histidine residues coordinate to Cu(II) in amyloid-beta1-16. *Biochemistry* **2008**, *47*, 9117-9123.
- (187) Jiang, D.; Men, L.; Wang, J.; Zhang, Y.; Chickenyen, S.; Wang, Y.; Zhou, F. Redox reactions of copper complexes formed with different β-amyloid peptides and their neuropathological relevance. *Biochemistry* **2007**, *46*, 9270-9282.
- (188) Damante, C. A.; Osz, K.; Nagy, Z.; Pappalardo, G.; Grasso, G.; Impellizzeri, G.; Rizzarelli, E.; Sovago, I. The metal loading ability of beta-amyloid N-terminus: a combined

- potentiometric and spectroscopic study of copper(II) complexes with beta-amyloid(1-16), its short or mutated peptide fragments, and its polyethylene glycol (PEG)-ylated analogue. *Inorg Chem* **2008**, *47*, 9669-9683.
- (189) Shearer, J.; Szalai, V. A. The amyloid-beta peptide of Alzheimer's disease binds Cu(I) in a linear bis-his coordination environment: insight into a possible neuroprotective mechanism for the amyloid-beta peptide. *J Am Chem Soc* **2008**, *130*, 17826-17835.
- (190) Hureau, C.; Coppel, Y.; Dorlet, P.; Solari, P. L.; Sayen, S.; Guillon, E.; Sabater, L.; Faller, P. Deprotonation of the Asp1-Ala2 peptide bond induces modification of the dynamic copper(II) environment in the amyloid-beta peptide near physiological pH. *Angew Chem Int Ed Engl* **2009**, *48*, 9522-9525.
- (191) Drew, S. C.; Noble, C. J.; Masters, C. L.; Hanson, G. R.; Barnham, K. J. Pleomorphic copper coordination by Alzheimer's disease amyloid-beta peptide. *J Am Chem Soc* **2009**, *131*, 1195-1207.
- (192) Atwood, C. S.; Moir, R. D.; Huang, X.; Scarpa, R. C.; Bacarra, N. M.; Romano, D. M.; Hartshorn, M. A.; Tanzi, R. E.; Bush, A. I. Dramatic aggregation of Alzheimer abeta by Cu(II) is induced by conditions representing physiological acidosis. *J Biol Chem* **1998**, *273*, 12817-12826.
- (193) Drew, S. C.; Masters, C. L.; Barnham, K. J. Alanine-2 carbonyl is an oxygen ligand in Cu²⁺ coordination of Alzheimer's disease amyloid-beta peptide--relevance to N-terminally truncated forms. *J Am Chem Soc* **2009**, *131*, 8760-8761.
- (194) Himes, R. A.; Park, G. Y.; Siluvai, G. S.; Blackburn, N. J.; Karlin, K. D. Structural studies of copper(I) complexes of amyloid-beta peptide fragments: formation of two-coordinate bis(histidine) complexes. *Angew Chem Int Ed Engl* **2008**, *47*, 9084-9087.
- (195) Hureau, C.; Faller, P. Abeta-mediated ROS production by Cu ions: structural insights, mechanisms and relevance to Alzheimer's disease. *Biochimie* **2009**, *91*, 1212-1217.
- (196) Hureau, C.; Balland, V.; Coppel, Y.; Solari, P. L.; Fonda, E.; Faller, P. Importance of dynamical processes in the coordination chemistry and redox conversion of copper amyloid-beta complexes. *J Biol Inorg Chem* **2009**, *14*, 995-1000.
- (197) Barth, A. Infrared spectroscopy of proteins. *Biochim Biophys Acta* **2007**, *1767*, 1073-1101.
- (198) Deacon, G. B.; Phillips, R. J. Relationships between the Carbon-Oxygen Stretching Frequencies of Carboxylate Complexes and the Type of Carboxylate Coordination. *Coordin Chem Rev* **1980**, *33*, 227-250.
- (199) Robert, V.; Lemercier, G. A combined experimental and theoretical study of carboxylate coordination modes: a structural probe. *J Am Chem Soc* **2006**, *128*, 1183-1187.
- (200) El Khoury, Y.; Hellwig, P. Infrared spectroscopic characterization of copper-polyhistidine from 1,800 to 50 cm⁻¹: model systems for copper coordination. *J Biol Inorg Chem* **2009**, *14*, 23-34.
- (201) Seddiki, N.; Meunier, B.; Lemesle-Meunier, D.; Brasseur, G. Is cytochrome b glutamic acid 272 a quinol binding residue in the bc(1) complex *Saccharomyces cerevisiae*? *Biochemistry* **2008**, *47*, 2357-2368.
- (202) Wenz, T.; Hellwig, P.; MacMillan, F.; Meunier, B.; Hunte, C. Probing the role of E272 in quinol oxidation of mitochondrial complex III. *Biochemistry* **2006**, *45*, 9042-9052.
- (203) Shinkarev, V. P.; Crofts, A. R.; Wraight, C. A. Spectral and kinetic resolution of the bc1 complex components in situ: a simple and robust alternative to the traditional difference wavelength approach. *Biochim Biophys Acta* **2006**, *1757*, 273-283.
- (204) Ritter, M.; Palsdottir, H.; Abe, M.; Mantele, W.; Hunte, C.; Miyoshi, H.; Hellwig, P. Direct evidence for the interaction of stigmatellin with a protonated acidic group in the bc(1) complex from *Saccharomyces cerevisiae* as monitored by FTIR difference spectroscopy and ¹³C specific labeling. *Biochemistry* **2004**, *43*, 8439-8446.

- (205) Hellwig, P.; Barquera, B.; Gennis, R. B. Direct evidence for the protonation of aspartate-75, proposed to be at a quinol binding site, upon reduction of cytochrome bo₃ from *Escherichia coli*. *Biochemistry* **2001**, *40*, 1077-1082.
- (206) Baymann, F.; Robertson, D. E.; Dutton, P. L.; Mantele, W. Electrochemical and spectroscopic investigations of the cytochrome bc₁ complex from *Rhodobacter capsulatus*. *Biochemistry* **1999**, *38*, 13188-13199.
- (207) Kleinschroth, T.; Anderka, O.; Ritter, M.; Stocker, A.; Link, T. A.; Ludwig, B.; Hellwig, P. Characterization of mutations in crucial residues around the Q(o) binding site of the cytochrome bc complex from *Paracoccus denitrificans*. *FEBS J* **2008**, *275*, 4773-4785.
- (208) Ritter, M.; Anderka, O.; Ludwig, B.; Mantele, W.; Hellwig, P. Electrochemical and FTIR spectroscopic characterization of the cytochrome bc₁ complex from *Paracoccus denitrificans*: evidence for protonation reactions coupled to quinone binding. *Biochemistry* **2003**, *42*, 12391-12399.
- (209) Dorr, S.; Wolpert, M.; Hellwig, P. Study on the redox state dependent gamma(CH) vibrational modes of the c-type heme. *Biopolymers* **2006**, *82*, 349-352.
- (210) Dorr, S.; Schade, U.; Hellwig, P. Far infrared spectroscopy on hemoproteins: A model compound study from 1800-100 cm⁻¹. *Vib Spectrosc* **2008**, *47*, 59-65.
- (211) Widger, W. R.; Cramer, W. A.; Herrmann, R. G.; Trebst, A. Sequence homology and structural similarity between cytochrome b of mitochondrial complex III and the chloroplast b_{6-f} complex: position of the cytochrome b hemes in the membrane. *Proc Natl Acad Sci U S A* **1984**, *81*, 674-678.
- (212) Hacker, B.; Barquera, B.; Gennis, R. B.; Crofts, A. R. Site-directed mutagenesis of arginine-114 and tryptophan-129 in the cytochrome b subunit of the bc₁ complex of *Rhodobacter sphaeroides*: two highly conserved residues predicted to be near the cytoplasmic surface of putative transmembrane helices B and C. *Biochemistry* **1994**, *33*, 13022-13031.
- (213) Richter, O. M.; Durr, K. L.; Kannt, A.; Ludwig, B.; Scandurra, F. M.; Giuffre, A.; Sarti, P.; Hellwig, P. Probing the access of protons to the K pathway in the *Paracoccus denitrificans* cytochrome c oxidase. *FEBS J* **2005**, *272*, 404-412.
- (214) Olkhova, E.; Hutter, M. C.; Lill, M. A.; Helms, V.; Michel, H. Dynamic water networks in cytochrome C oxidase from *Paracoccus denitrificans* investigated by molecular dynamics simulations. *Biophys J* **2004**, *86*, 1873-1889.
- (215) Pfitzner, U.; Odenwald, A.; Ostermann, T.; Weingard, L.; Ludwig, B.; Richter, O. M. Cytochrome c oxidase (heme aa₃) from *Paracoccus denitrificans*: analysis of mutations in putative proton channels of subunit I. *J Bioenerg Biomembr* **1998**, *30*, 89-97.
- (216) Qian, J.; Mills, D. A.; Geren, L.; Wang, K.; Hoganson, C. W.; Schmidt, B.; Hiser, C.; Babcock, G. T.; Durham, B.; Millett, F.; Ferguson-Miller, S. Role of the conserved arginine pair in proton and electron transfer in cytochrome C oxidase. *Biochemistry* **2004**, *43*, 5748-5756.
- (217) Puustinen, A.; Wikstrom, M. Proton exit from the heme-copper oxidase of *Escherichia coli*. *Proc Natl Acad Sci U S A* **1999**, *96*, 35-37.
- (218) Wikstrom, M.; Ribacka, C.; Molin, M.; Laakkonen, L.; Verkhovskiy, M.; Puustinen, A. Gating of proton and water transfer in the respiratory enzyme cytochrome c oxidase. *Proc Natl Acad Sci U S A* **2005**, *102*, 10478-10481.
- (219) Muramoto, K.; Hirata, K.; Shinzawa-Itoh, K.; Yoko-o, S.; Yamashita, E.; Aoyama, H.; Tsukihara, T.; Yoshikawa, S. A histidine residue acting as a controlling site for dioxygen reduction and proton pumping by cytochrome c oxidase. *Proc Natl Acad Sci U S A* **2007**, *104*, 7881-7886.
- (220) Kuznetsova, S. S.; Azarkina, N. V.; Vygodina, T. V.; Siletsky, S. A.; Konstantinov, A. A. Zinc ions as cytochrome C oxidase inhibitors: two sites of action. *Biochemistry (Mosc)* **2005**, *70*, 128-136.

- (221) Aagaard, A.; Brzezinski, P. Zinc ions inhibit oxidation of cytochrome c oxidase by oxygen. *FEBS lett* **2001**, *494*, 157-160.
- (222) Mills, D. A.; Schmidt, B.; Hiser, C.; Westley, E.; Ferguson-Miller, S. Membrane potential-controlled inhibition of cytochrome c oxidase by zinc. *J Biol Chem* **2002**, *277*, 14894-14901.
- (223) Hellwig, P.; Grzybek, S.; Behr, J.; Ludwig, B.; Michel, H.; Mantele, W. Electrochemical and ultraviolet/visible/infrared spectroscopic analysis of heme a and a₃ redox reactions in the cytochrome c oxidase from *Paracoccus denitrificans*: separation of heme a and a₃ contributions and assignment of vibrational modes. *Biochemistry* **1999**, *38*, 1685-1694.
- (224) Hendler, R. W.; Westerhoff, H. V. Redox interactions in cytochrome c oxidase: from the "neoclassical" toward "modern" models. *Biophys J* **1992**, *63*, 1586-1604.
- (225) Hellwig, P.; Bohm, A.; Pfitzner, U.; Mantele, W.; Ludwig, B. Spectroscopic study on the communication between a heme a₃ propionate, Asp399 and the binuclear center of cytochrome c oxidase from *Paracoccus denitrificans*. *Biochim Biophys Acta* **2008**, *1777*, 220-226.
- (226) Miyazawa, T.; Shimanouchi, T.; Mizushima, S.-i. Normal Vibrations of N-Methylacetamide. *J Chem Phys* **1958**, *29*, 611-616.
- (227) Zundel, G. The far infrared vibration of hydrogen bonds with large proton polarizability. *J Mol Struct* **1996**, *381*, 23-37.
- (228) Xie, A. H.; van der Meer, A. F. G.; Austin, R. H. Excited-state lifetimes of far-infrared collective modes in proteins. *Phys Rev Lett* **2002**, *88*, -.
- (229) Ebbinghaus, S.; Kim, S. J.; Heyden, M.; Yu, X.; Heugen, U.; Gruebele, M.; Leitner, D. M.; Havenith, M. An extended dynamical hydration shell around proteins. *Proc Natl Acad Sci U S A* **2007**, *104*, 20749-20752.
- (230) Leitner, D. M.; Gruebele, M.; Havenith, M. Solvation dynamics of biomolecules: modeling and terahertz experiments. *Hfsp Journal* **2008**, *2*, 314-323.
- (231) Born, B.; Havenith, M. Terahertz Dance of Proteins and Sugars with Water. *J Infrared Millim Tera* **2009**, *30*, 1245-1254.
- (232) Eyster, J. M.; Prohofsky, E. W. Soft Modes and Structure of DNA Double Helix. *Phys Rev Lett* **1977**, *38*, 371-373.
- (233) Born, B.; Kim, S. J.; Ebbinghaus, S.; Gruebele, M.; Havenith, M. The terahertz dance of water with the proteins: the effect of protein flexibility on the dynamical hydration shell of ubiquitin. *Faraday Discuss* **2009**, *141*, 161-173; discussion 175-207.
- (234) Zundel, G. The far infrared vibration of hydrogen bonds with large proton polarizability. *J Mol Struct* **1996**, *381*, 23-37.
- (235) Kong, J.; Yu, S. Fourier transform infrared spectroscopic analysis of protein secondary structures. *Acta Biochim Biophys Sin* **2007**, *39*, 549-559.
- (236) Fändrich, M.; Dobson, C. M. The behaviour of polyamino acids reveals an inverse side chain effect in amyloid structure formation. *EMBO J* **2002**, *21*, 5682-5690.
- (237) Simonetti, M.; Di Bello, C. New Fourier transform infrared based computational method for peptide secondary structure determination. II. Application to study of peptide fragments reproducing processing site of ocytocin-neurophysin precursor. *Biopolymers* **2001**, *62*, 109-121.
- (238) Dong, A.; Huang, P.; Caughey, W. S. Protein secondary structures in water from second-derivative amide I infrared spectra. *Biochemistry* **1990**, *29*, 3303-3308.
- (239) Severcan, M.; Severcan, F.; Haris, P. I. Estimation of protein secondary structure from FTIR spectra using neural networks. *J Mol Struct* **2001**, *565-566*, 383-387.
- (240) Simonetti, M.; Di Bello, C. New Fourier transform infrared based computational method for peptide secondary structure determination. I. Description of method. *Biopolymers* **2001**, *62*, 95-108.

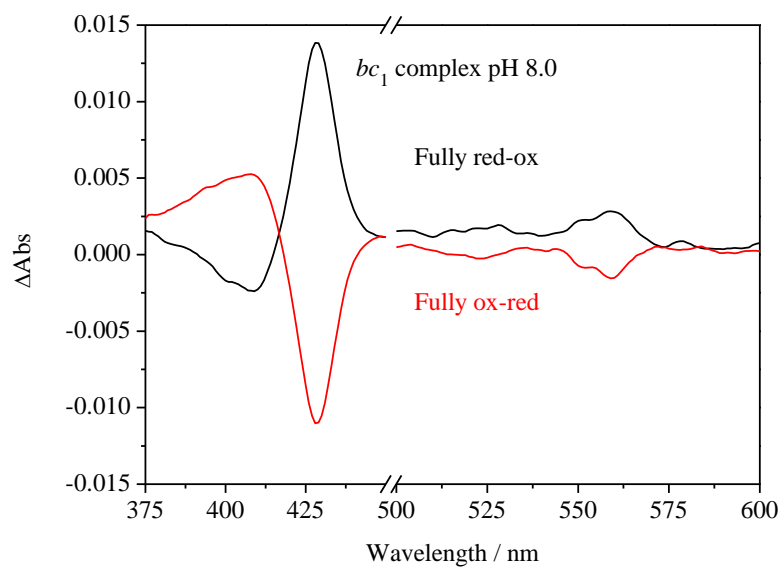
- (241) Oberg, K. A.; Ruyschaert, J. M.; Goormaghtigh, E. The optimization of protein secondary structure determination with infrared and circular dichroism spectra. *Eur J Biochem* **2004**, *271*, 2937-2948.
- (242) Overman, S. A.; Thomas, G. J., Jr. Amide modes of the alpha-helix: Raman spectroscopy of filamentous virus fd containing peptide ^{13}C and ^2H labels in coat protein subunits. *Biochemistry* **1998**, *37*, 5654-5665.
- (243) Dzwolak, W.; Muraki, T.; Kato, M.; Taniguchi, Y. Chain-Length Dependence of α -Helix to β -Sheet Transition in Polylysine: Model of Protein Aggregation Studied by Temperature-Tuned FTIR Spectroscopy. *Biopolymers* **2004**, *73*, 463-469.
- (244) Dzwolak, W.; Smirnovas, V. A conformational α -helix to β -sheet transition accompanies racemic self-assembly of polylysine: An FT-IR spectroscopic study. *Biophys Chem* **2005**, *115*, 49-54.
- (245) Lee, S. H.; Krimm, S. Ab initio-based vibrational analysis of α -poly(L-alanine). *Biopolymers* **1998**, *46*, 283-317.
- (246) Hunsicker-Wang, L. M.; Heine, A.; Chen, Y.; Luna, E. P.; Todaro, T.; Zhang, Y. M.; Williams, P. A.; McRee, D. E.; Hirst, J.; Stout, C. D.; Fee, J. A. High-resolution structure of the soluble, respiratory-type Rieske protein from *Thermus thermophilus*: analysis and comparison. *Biochemistry* **2003**, *42*, 7303-7317.
- (247) Allison, S. D.; Dong, A.; Carpenter, J. F. Counteracting effects of thiocyanate and sucrose on chymotrypsinogen secondary structure and aggregation during freezing, drying, and rehydration. *Biophys J* **1996**, *71*, 2022-2032.
- (248) Dong, A.; Prestrelski, S. J.; Allison, S. D.; Carpenter, J. F. Infrared spectroscopic studies of lyophilization- and temperature-induced protein aggregation. *J Pharm Sci* **1995**, *84*, 415-424.
- (249) van de Weert, M.; Haris, P. I.; Hennink, W. E.; Crommelin, D. J. Fourier transform infrared spectrometric analysis of protein conformation: effect of sampling method and stress factors. *Anal Biochem* **2001**, *297*, 160-169.
- (250) Dwivedi, A. M.; Krimm, S. Vibrational analysis of peptides, polypeptides, and proteins. XI. α -poly(L-alanine) and its N-deuterated derivative. *Macromolecules* **1982**, *15*, 186-193.
- (251) Han, S.; Czernuszewicz, R. S.; Spiro, T. G. Vibrational spectra and normal mode analysis for [2Fe-2S] protein analogues using ^{34}S , ^{54}Fe , and ^2H substitution: Coupling of Fe-S stretching and S-C-C bending modes. *J Am Chem Soc* **1989**, *111*, 3496-3504.
- (252) Min, T.; Ergenekan, C. E.; Eidsness, M. K.; Ichiye, T.; Kang, C. Leucine 41 is a gate for water entry in the reduction of *Clostridium pasteurianum* rubredoxin. *Protein Sci* **2001**, *10*, 613-621.
- (253) Lin, I. J.; Gebel, E. B.; Machonkin, T. E.; Westler, W. M.; Markley, J. L. Correlation between hydrogen bond lengths and reduction potentials in *Clostridium pasteurianum* rubredoxin. *J Am Chem Soc* **2003**, *125*, 1464-1465.
- (254) Xiao, Z.; Maher, M. J.; Cross, M.; Bond, C. S.; Guss, J. M.; Wedd, A. G. Mutation of the surface valine residues 8 and 44 in the rubredoxin from *Clostridium pasteurianum*: solvent access versus structural changes as determinants of reversible potential. *J Biol Inorg Chem* **2000**, *5*, 75-84.
- (255) Saito, H.; Imai, T.; Wakita, K.; Urushiyama, A.; Yagi, T. Resonance Raman Active Vibrations of Rubredoxin - Normal Coordinate Analysis of a 423-Atom Model. *Bull Chem Soc Jpn* **1991**, *64*, 829-836.
- (256) Czernuszewicz, R. S.; Kilpatrick, L. K.; Koch, S. A.; Spiro, T. G. Resonance Raman-Spectroscopy of Iron(III) Tetrathiolate Complexes - Implications for the Conformation and Force-Field of Rubredoxin. *J Am Chem Soc* **1994**, *116*, 7134-7141.

- (257) Tan, M. L.; Bizzarri, A. R.; Xiao, Y.; Cannistraro, S.; Ichiye, T.; Manzoni, C.; Cerullo, G.; Adams, M. W.; Jenney, F. E., Jr.; Cramer, S. P. Observation of terahertz vibrations in *Pyrococcus furiosus* rubredoxin via impulsive coherent vibrational spectroscopy and nuclear resonance vibrational spectroscopy--interpretation by molecular mechanics. *J Inorg Biochem* **2007**, *101*, 375-384.
- (258) Czernuszewicz, R. S.; Legall, J.; Moura, I.; Spiro, T. G. Resonance Raman-Spectra of Rubredoxin - New Assignments and Vibrational Coupling Mechanism from Fe-54 Fe-56 Isotope Shifts and Variable-Wavelength Excitation. *Inorg Chem* **1986**, *25*, 696-700.
- (259) Xiao, Y.; Wang, H.; George, S. J.; Smith, M. C.; Adams, M. W.; Jenney, F. E., Jr.; Sturhahn, W.; Alp, E. E.; Zhao, J.; Yoda, Y.; Dey, A.; Solomon, E. I.; Cramer, S. P. Normal mode analysis of *Pyrococcus furiosus* rubredoxin via nuclear resonance vibrational spectroscopy (NRVS) and resonance raman spectroscopy. *J Am Chem Soc* **2005**, *127*, 14596-14606.
- (260) Born, B.; Havenith, M. Terahertz Dance of Proteins and Sugars with Water. *J Infrared Millim Tera* **2009**, *30*, 1245-1254.
- (261) Vidakovic, M.; Fraczkiewicz, G.; Dave, B. C.; Czernuszewicz, R. S.; Germanas, J. P. The Environment of [2Fe-2S] Clusters in Ferredoxins - the Role of Residue-45 Probed by Site-Directed Mutagenesis. *Biochemistry* **1995**, *34*, 13906-13913.
- (262) Yachandra, V. K.; Hare, J.; Gewirth, A.; Czernuszewicz, R. S.; Kimura, T.; Holm, R. H.; Spiro, T. G. Resonance Raman-Spectra of Spinach Ferredoxin and Adrenodoxin and of Analog Complexes. *J Am Chem Soc* **1983**, *105*, 6462-6468.
- (263) Meyer, J.; Moulis, J. M.; Lutz, M. Structural Differences between [2Fe-2S] Clusters in Spinach Ferredoxin and in the Red Paramagnetic Protein from *Clostridium-Pasteurianum* - a Resonance Raman-Study. *Biochem Biophys Res Co* **1984**, *119*, 828-835.
- (264) Meyer, J.; Moulis, J. M.; Lutz, M. Resonance Raman-Spectroscopy of (2Fe-2S)₂⁺, (2Fe-Se)₂⁺ Clusters in Ferredoxins. *Biochim Biophys Acta* **1986**, *873*, 108-118.
- (265) Han, S.; Czernuszewicz, R. S.; Kimura, T.; Adams, M. W. W.; Spiro, T. G. Fe₂S₂ Protein Resonance Raman-Spectra Revisited - Structural Variations among Adrenodoxin, Ferredoxin, and Red Paramagnetic Protein. *J Am Chem Soc* **1989**, *111*, 3505-3511.
- (266) Fu, W.; Drozdowski, P. M.; Davies, M. D.; Sligar, S. G.; Johnson, M. K. Resonance Raman and magnetic circular dichroism studies of reduced [2Fe-2S] proteins. *J Biol Chem* **1992**, *267*, 15502-15510.
- (267) Rotsaert, F. J.; Pikus, J. D.; Fox, B. G.; Markley, J. L.; Sanders-Loehr, J. N-isotope effects on the Raman spectra of Fe(2)S(2) ferredoxin and Rieske ferredoxin: evidence for structural rigidity of metal sites. *J Biol Inorg Chem* **2003**, *8*, 318-326.
- (268) Xiao, Y.; Tan, M. L.; Ichiye, T.; Wang, H.; Guo, Y.; Smith, M. C.; Meyer, J.; Sturhahn, W.; Alp, E. E.; Zhao, J.; Yoda, Y.; Cramer, S. P. Dynamics of *Rhodobacter capsulatus* [2Fe-2S] ferredoxin VI and *Aquifex aeolicus* ferredoxin 5 via nuclear resonance vibrational spectroscopy (NRVS) and resonance Raman spectroscopy. *Biochemistry* **2008**, *47*, 6612-6627.
- (269) Bertini, I.; Donaire, A.; Feinberg, B. A.; Luchinat, C.; Piccioli, M.; Yuan, H. Solution structure of the oxidized 2[4Fe-4S] ferredoxin from *Clostridium pasteurianum*. *Eur J Biochem* **1995**, *232*, 192-205.
- (270) Prince, R. C.; Adams, M. W. Oxidation-reduction properties of the two Fe₄S₄ clusters in *Clostridium pasteurianum* ferredoxin. *J Biol Chem* **1987**, *262*, 5125-5128.
- (271) Backes, G.; Mino, Y.; Loehr, T. M.; Meyer, T. E.; Cusanovich, M. A.; Sweeney, W. V.; Adman, E. T.; Sandersloehr, J. The Environment of Fe₄S₄ Clusters in Ferredoxins and High-Potential Iron Proteins - New Information from X-Ray Crystallography and Resonance Raman-Spectroscopy. *J Am Chem Soc* **1991**, *113*, 2055-2064.

- (272) Czernuszewicz, R. S.; Macor, K. A.; Johnson, M. K.; Gewirth, A.; Spiro, T. G. Vibrational-Mode Structure and Symmetry in Proteins and Analogs Containing Fe₄S₄ Clusters - Resonance Raman Evidence for Different Degrees of Distortion in Hipip and Ferredoxin. *J Am Chem Soc* **1987**, *109*, 7178-7187.
- (273) Maes, E. M.; Knapp, H. J.; Czernuszewicz, R. S.; Hendrickson, D. N. Ligand conformational effects on the resonance Raman signature of [Fe₄S₄(SAryl)(4)](2-) clusters. *J Phys Chem B* **2000**, *104*, 10878-10884.
- (274) Mitchell, P. Possible molecular mechanisms of the protonmotive function of cytochrome systems. *J Theor Biol* **1976**, *62*, 327-367.
- (275) Berry, E. A.; Guergova-Kuras, M.; Huang, L. S.; Crofts, A. R. Structure and function of cytochrome bc complexes. *Annu Rev Biochem* **2000**, *69*, 1005-1075.
- (276) Iwata, S.; Saynovits, M.; Link, T. A.; Michel, H. Structure of a water soluble fragment of the 'Rieske' iron-sulfur protein of the bovine heart mitochondrial cytochrome bc₁ complex determined by MAD phasing at 1.5 Å resolution. *Structure* **1996**, *4*, 567-579.
- (277) Link, T. A.; Saynovits, M.; Assmann, C.; Iwata, S.; Ohnishi, T.; von Jagow, G. Isolation, characterisation and crystallisation of a water-soluble fragment of the Rieske iron-sulfur protein of bovine heart mitochondrial bc₁ complex. *Eur J Biochem* **1996**, *237*, 71-75.
- (278) Konkle, M. E.; Muellner, S. K.; Schwander, A. L.; Dicus, M. M.; Pokhrel, R.; Britt, R. D.; Taylor, A. B.; Hunsicker-Wang, L. M. Effects of pH on the Rieske protein from *Thermus thermophilus*: a spectroscopic and structural analysis. *Biochemistry* **2009**, *48*, 9848-9857.
- (279) Zu, Y.; Couture, M. M.; Kolling, D. R.; Crofts, A. R.; Eltis, L. D.; Fee, J. A.; Hirst, J. Reduction potentials of Rieske clusters: importance of the coupling between oxidation state and histidine protonation state. *Biochemistry* **2003**, *42*, 12400-12408.
- (280) Denke, E.; Merbitz-Zahradnik, T.; Hatzfeld, O. M.; Snyder, C. H.; Link, T. A.; Trumpower, B. L. Alteration of the midpoint potential and catalytic activity of the rieske iron-sulfur protein by changes of amino acids forming hydrogen bonds to the iron-sulfur cluster. *J Biol Chem* **1998**, *273*, 9085-9093.
- (281) Guergova-Kuras, M.; Kuras, R.; Ugulava, N.; Hadad, I.; Crofts, A. R. Specific mutagenesis of the rieske iron-sulfur protein in *Rhodobacter sphaeroides* shows that both the thermodynamic gradient and the pK of the oxidized form determine the rate of quinol oxidation by the bc(1) complex. *Biochemistry* **2000**, *39*, 7436-7444.
- (282) Iwasaki, T.; Kounosu, A.; Kolling, D. R.; Lhee, S.; Crofts, A. R.; Dikanov, S. A.; Uchiyama, T.; Kumasaka, T.; Ishikawa, H.; Kono, M.; Imai, T.; Urushiyama, A. Resonance Raman characterization of archaeal and bacterial Rieske protein variants with modified hydrogen bond network around the [2Fe-2S] center. *Protein Sci* **2006**, *15*, 2019-2024.
- (283) Klingen, A. R.; Ullmann, G. M. Negatively charged residues and hydrogen bonds tune the ligand histidine pK_a values of Rieske iron-sulfur proteins. *Biochemistry* **2004**, *43*, 12383-12389.
- (284) Ullmann, G. M.; Noodleman, L.; Case, D. A. Density functional calculation of pK_a values and redox potentials in the bovine Rieske iron-sulfur protein. *J Biol Inorg Chem* **2002**, *7*, 632-639.
- (285) Madden, J. F.; Han, S. H.; Siegel, L. M.; Spiro, T. G. Resonance Raman studies of *Escherichia coli* sulfite reductase hemoprotein. 2. Fe₄S₄ cluster vibrational modes. *Biochemistry* **1989**, *28*, 5471-5477.
- (286) Kuila, D.; Schoonover, J. R.; Dyer, R. B.; Batie, C. J.; Ballou, D. P.; Fee, J. A.; Woodruff, W. H. Resonance Raman studies of Rieske-type proteins. *Biochim Biophys Acta* **1992**, *1140*, 175-183.
- (287) Iwasaki, T.; Kounosu, A.; Kolling, D. R.; Crofts, A. R.; Dikanov, S. A.; Jin, A.; Imai, T.; Urushiyama, A. Characterization of the pH-dependent resonance Raman transitions of archaeal and bacterial Rieske [2Fe-2S] proteins. *J Am Chem Soc* **2004**, *126*, 4788-4789.

- (288) Mitsuo, S.; Kenichi, K.; Takeshi, T.; Yasutaka, K.; Shusuke, Y.; Mitsutaka, O.; Kizashi, Y. Theory of chemical bonds in metalloenzymes III: Full geometry optimization and vibration analysis of ferredoxin-type [2Fe-2S] cluster. *Int J Quantum Chem* **2007**, *107*, 116-133.
- (289) Mitsuo, S.; Kenichi, K.; Yasutaka, K.; Shusuke, Y.; Mitsutaka, O.; Kizashi, Y. Theory of chemical bonds in metalloenzymes IV: Hybrid-DFT study of Rieske-type [2Fe-2S] clusters. *Int J Quantum Chem* **2007**, *107*, 609-627.
- (290) Vanderkooi, J. M.; Dashnau, J. L.; Zelent, B. Temperature excursion infrared (TEIR) spectroscopy used to study hydrogen bonding between water and biomolecules. *Biochim Biophys Acta* **2005**, *1749*, 214-233.
- (291) Schroter, T.; Hatzfeld, O. M.; Gemeinhardt, S.; Korn, M.; Friedrich, T.; Ludwig, B.; Link, T. A. Mutational analysis of residues forming hydrogen bonds in the Rieske [2Fe-2S] cluster of the cytochrome bc(1) complex in *Paracoccus denitrificans*. *Eur J Biochem* **1998**, *255*, 100-106.
- (292) Allerhand, A.; Schleyer, P. V. R. A survey of C-H groups as proton donors in hydrogen bonding. *J Am Chem Soc* **1963**, *85*, 1717-1723.
- (293) Jeffery, G. A. An Introduction to Hydrogen Bonding. *Oxford University Press, New York* **1997**.
- (294) Zaccai, G. How soft is a protein? A protein dynamics force constant measured by neutron scattering. *Science* **2000**, *288*, 1604-1607.
- (295) Wood, K.; Plazanet, M.; Gabel, F.; Kessler, B.; Oesterhelt, D.; Tobias, D. J.; Zaccai, G.; Weik, M. Coupling of protein and hydration-water dynamics in biological membranes. *Proc Natl Acad Sci U S A* **2007**, *104*, 18049-18054.
- (296) Dioumaev, A. K.; Lanyi, J. K. Bacteriorhodopsin photocycle at cryogenic temperatures reveals distributed barriers of conformational substates. *Proc Natl Acad Sci U S A* **2007**, *104*, 9621-9626.
- (297) Fenimore, P. W.; Frauenfelder, H.; McMahon, B. H.; Parak, F. G. Slaving: solvent fluctuations dominate protein dynamics and functions. *Proc Natl Acad Sci U S A* **2002**, *99*, 16047-16051.
- (298) Liddington, R. C. Will the real integrin please stand up? *Structure* **2002**, *10*, 605-607.
- (299) Hynes, R. O. Integrins: bidirectional, allosteric signaling machines. *Cell* **2002**, *110*, 673-687.

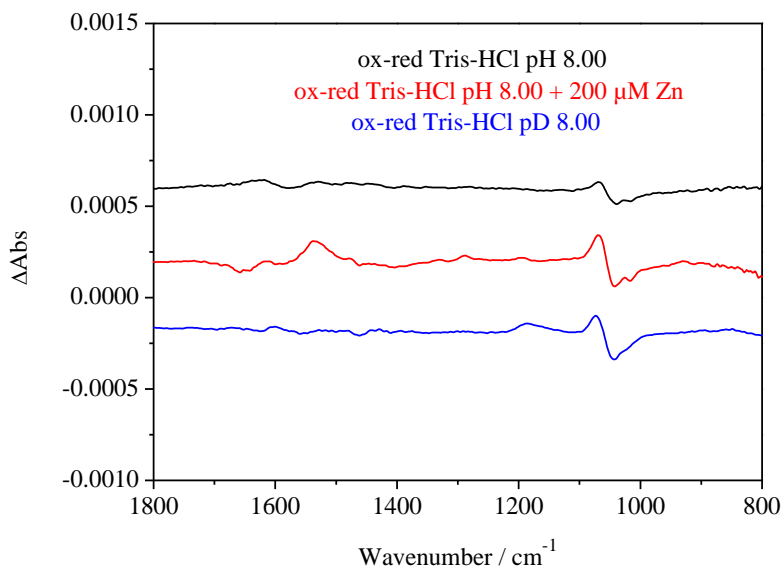
6. Appendix



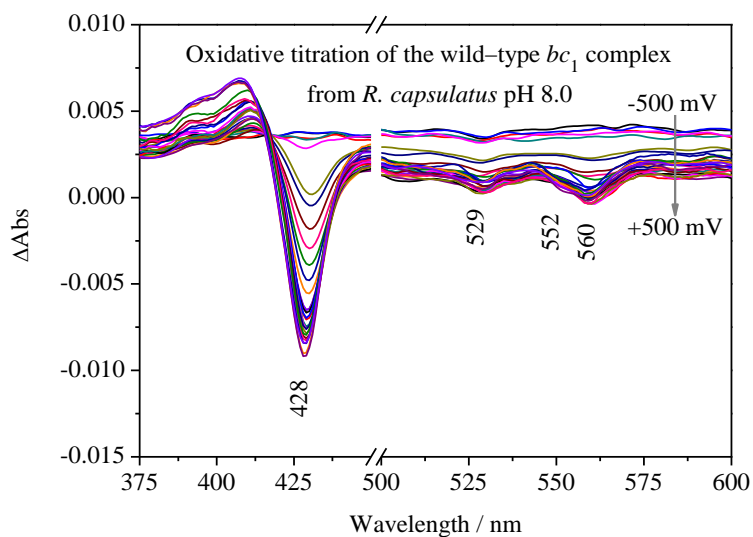
Appendix 1. Fully ox-red and fully red-ox UV-Vis difference spectra of the *bc*₁ complex.

Positions (cm ⁻¹)	Assignments ^{204,206-208}		Cofactor
1740(+)	$\nu(\text{C}=\text{O})$	Glu295	heme b_L
1720(-)			
1706(+)	$\nu(\text{C}=\text{O})$	Asp278	heme b_L
1694(+)	amide I	β -Sheet	Rieske protein
1684(-)	$\nu(\text{C}=\text{O})$	heme propionate	heme b_L heme b_H
1679(+)	$\nu(\text{C}=\text{O})$	heme propionate	heme b_L heme b_H
1672(-)	$\nu(\text{CN}_3\text{H}_5)^{\text{as}}$	Arg	heme b_L
1656(+)	amide I	β -Sheet	Rieske protein
1644(+)	amide I	α -Helix, random coils	
	$\nu(\text{C}=\text{O})$	quinone	free quinone
	$\nu(\text{C}=\text{O})$	quinone	free quinone
	ν_{37}		cy c_1
1625(-)	amide I	β -Sheet	Rieske protein
1612(+)	$\nu(\text{C}=\text{C})$	quinone	free or bound quinone
1594 (+) (sh)	$\nu(\text{C}=\text{C})$	quinone	free or bound quinone
1570(+ (sh)	amide II		
1559(-)	$\nu(\text{COO}^-)^{\text{as}}$	heme propionate	heme b_L heme b_H , heme c_1
		Asp/Glu	heme b
1547(+)	amide II		
	ν_{38}		heme b_L
1536(-)	amide II	heme propionate	heme b_L heme b_H , heme c_1
	$\nu(\text{COO}^-)^{\text{as}}$	Asp/Glu	heme b
1521(+w)	Amide II		
1516(-)	Tyr-OH		
1509(+)	Amide II		Rieske
1494(-)	$\nu(\text{CC})$	quinol ring	
1482(+)	$\nu(\text{CC})$	quinone ring	
1469(-)	$\nu(\text{CC})$	quinol ring	
1450(+)	ring vibration	Pro/Trp	
1430(-)	$\nu(\text{CC})$	quinol ring	
1421(+)	$\nu(\text{CC})$	quinone ring	
1407(-)	$\nu(\text{CC})$	quinol ring	
1385(-)	$\nu(\text{CC})$	quinol ring	
1368(+)	$\nu(\text{COO}^-)^{\text{s}}$	Asp/Glu	heme b_H
	C-CH ₃	isoprenoide	
1358(-)		heme propionate	heme b_L heme b_H , heme c_1
		Asp/Glu	heme b
1288 (+)	$\nu(\text{C}-\text{O})$	Methoxy group	quinone
		Methoxy group	quinone
1264(+)	$\nu(\text{C}-\text{O})$	heme c_1	heme c_1
	ν_{42}	heme b_H	heme b_H
1240(-)			
1220(+)	ν_{42}	heme b_H heme b_L heme c_1	heme b_H heme b_L heme c_1
1204(+)	$\nu(\text{C}-\text{O})$	quinone	heme b_H heme b_L heme c_1
	ν_{42}		
1177(+)			
1165(-)	$\nu(\text{C}\alpha\text{C}\beta)^{\text{s}}$	heme vinyl	heme b_H heme b_L heme c_1
1069(+)		C-N (CNH ₃ ⁺)	Tris- HCl buffer
1047(-)		C-N	Tris- HCl buffer
986(+)	$\delta(\text{ring})$	His	
964(-)	ring	porphyrin	heme b_H heme b_L heme c_1
952(+)	$\nu(\text{ring})$	deprotonated His	
946(-)			
930(+)	ring	porphyrin	heme b_H heme b_L heme c_1
836(+)			
827(-)	$\gamma(\text{C}_m\text{-H})$ vibration	porphyrin	heme b_H heme b_L heme c_1
815(+)			

Appendix 2. Complete assignments of the electrochemically induced difference spectrum of the wild-type bc_1 complex from *R. capsulatus*. The positive and negative signs indicate the positive and negative signals, respectively.



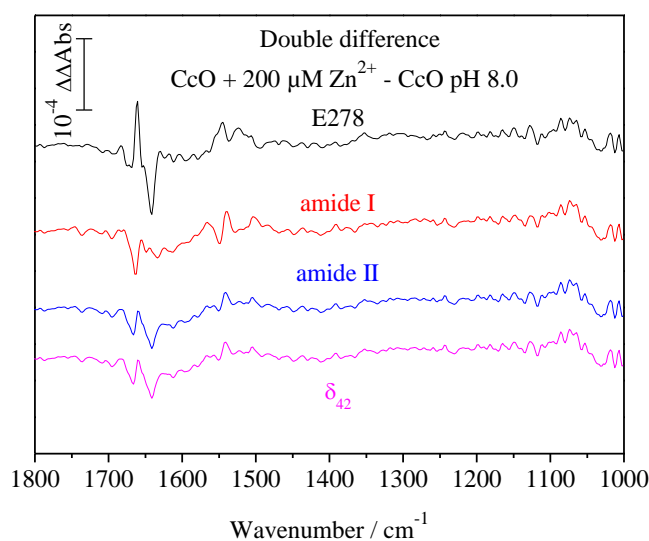
Appendix 3. Ox-red difference spectra of the Tris-HCl buffer at pH 8.0. Buffer alone (black), buffer + 200 μM Zn^{2+} (red) and buffer alone at pD 8.0 (blue). All the buffer samples contain 100 μM of KCl and the cocktail of mediators.



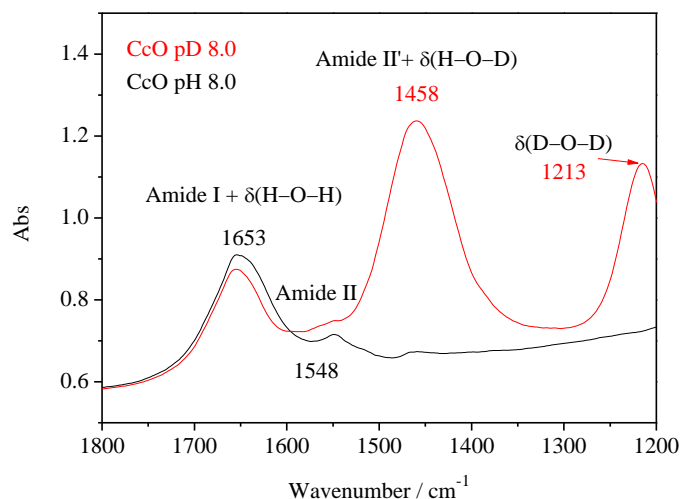
Appendix 4. Oxidative UV-Vis titration of the bc_1 complex at pH 8.0.

Frequency (cm ⁻¹)	Assignments ^{119,120,147,209,213,223}
1747(+)	$\nu(\text{C}=\text{O})$ Glu 278
1735(-)	$\nu(\text{C}=\text{O})$ Glu 278
1723(+)	$\nu(\text{C}=\text{O})$ Asp/Glu
1714(-)	$\nu(\text{C}=\text{O})$ Asp/ Glu
1705(+)	$\nu(\text{C}=\text{O})$ Asp/ Glu
1696(-)	$\nu(\text{C}=\text{O})$ Asp/ Glu
1688(+)	Amide I (β -sheet)
1682(-)	Amide I (β -sheet)
1676(+)	$\nu(\text{C}=\text{O})$ CHO heme a_3 $\nu(\text{C}=\text{O})$ heme propionates $\nu(\text{C}=\text{O})$ Asp/Gln $\nu(\text{CN}_3\text{H}_5)^{\text{as}}$ Arg
1662(-)	Amide I (α -helical) $\nu(\text{C}=\text{O})$ CHO heme a_3 $\nu(\text{CN}_3\text{H}_5)^{\text{as}}$ Arg
1655(+)	Amide I (α -helical)
1642(+)	$\nu(\text{C}=\text{O})$ CHO heme a
1632(-)	$\delta(\text{NH}_2)$ Asn/Gln $\nu(\text{CN}_3\text{H}_5)^{\text{s}}$ Arg Amide I (β -sheet)
1624(+)	$\delta(\text{NH}_2)$ Asn/Gln $\nu(\text{CN}_3\text{H}_5)^{\text{s}}$ Arg Amide I (β -sheet)
1617(-)	$\nu(\text{C}\alpha=\text{C}\beta)$ vinyl group (heme a/a_3)
1611(+)	ν_{37} heme c
1596(+)	ν_{37} heme c
1585(+)	$\nu(\text{COO}^-)^{\text{as}}$ heme propionates $\nu(\text{COO}^-)^{\text{as}}$ Asp/Glu
1566(+)	$\nu(\text{COO}^-)^{\text{as}}$ heme propionates $\nu(\text{COO}^-)^{\text{as}}$ Asp/Glu ring O ⁻ Tyr ν_{38} heme a/a_3
1549(-)	ν_{38} heme a
1538(+)	$\nu(\text{COO}^-)^{\text{as}}$ heme propionates
1525(-)	Amide II
1515(+)	$\nu(\text{CC})$ ring-OH Tyr
1510(-)	$\nu(\text{CC})$ ring-OH Tyr
1499(+)	$\nu(\text{CC})$ ring-O ⁻ Tyr
1463(-)	β -methylene Tyr280
1418(-)	$\nu(\text{COO}^-)^{\text{s}}$ Asp/Glu/heme propionates
1390(+)	ν_{41} heme a/a_3 $\nu(\text{COO}^-)^{\text{s}}$ heme propionates
1376(+)	ν_{41} heme a/a_3
1366(-)	ν_{41} heme a/a_3
1283(+)	$\nu(\text{CO})^{\text{s}}$ Tyr
1269(+)	δ_{42} heme a/a_3

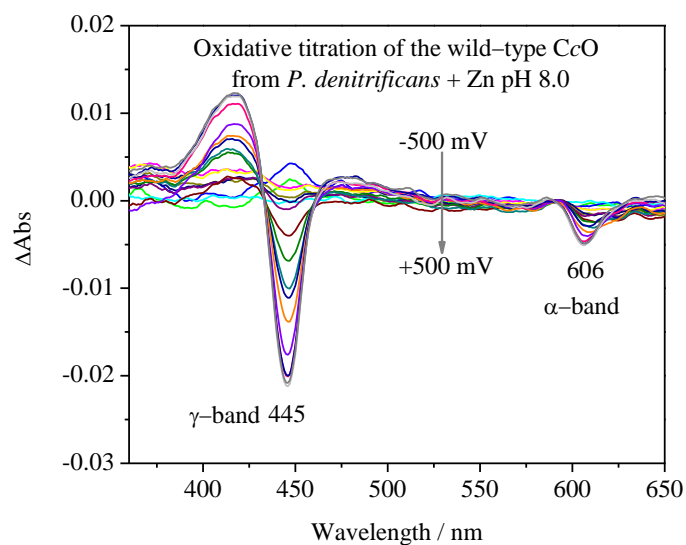
Appendix 5. Detailed band assignments of the FTIR electrochemically induced oxidized minus reduces difference spectrum of the wild-type CcO at pH 8.0.



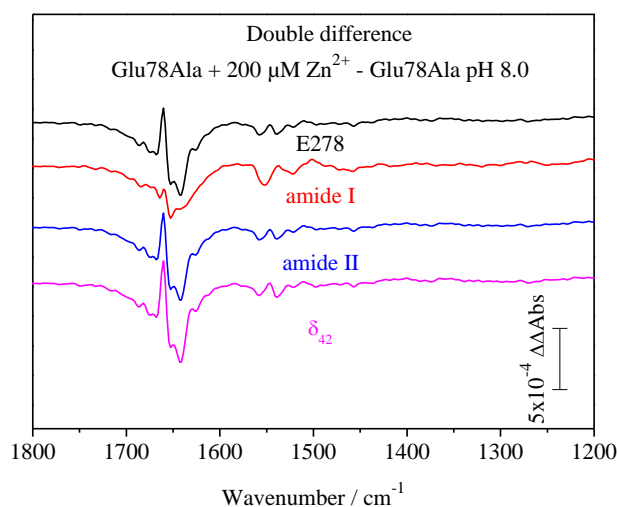
Appendix 6. Double difference spectra of the inhibited CcO minus the native CcO at pH 8.0. The difference spectra were normalized to the Glu278 absorption (black), to the amide I (red), to the amide II (blue), or to the δ_{42} vibration of the hemes.



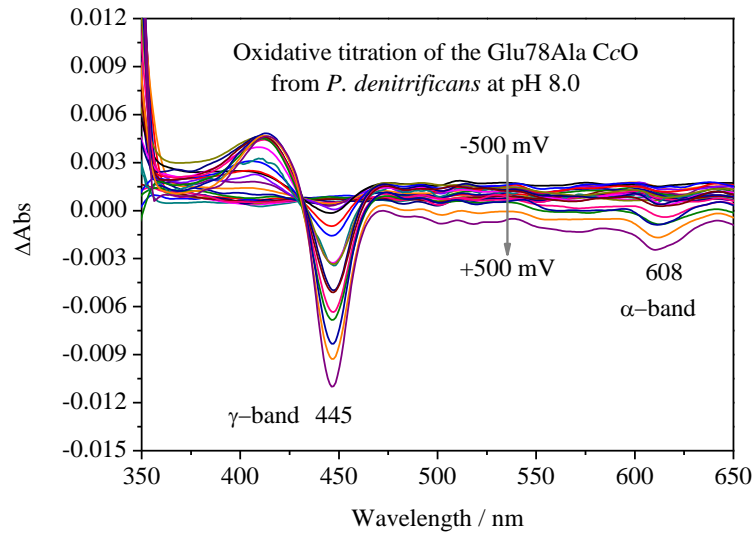
Appendix 7. Absorbance spectra of the wild-type CcO recorded at pH 8.0 (black) and pD 8.0 (red). The amide II contribution in the spectrum recorded at pD 8.0 is barely visible.



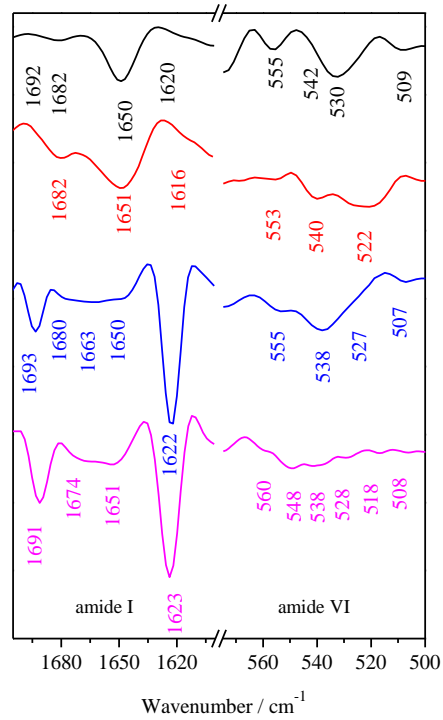
Appendix 8. Oxidative UV-Vis titration of the inhibited CcO at pH 8.0.



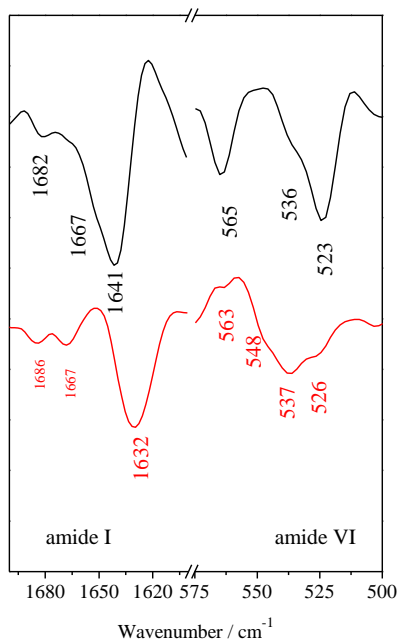
Appendix 9. Double difference spectra of the inhibited Glu78Ala CcO minus the native Glu78Ala at pH 8.0. The difference spectra were normalized to the Glu278 absorption (black), to the amide I (red), to the amide II (blue), or to the δ_{42} vibration of the hemes.



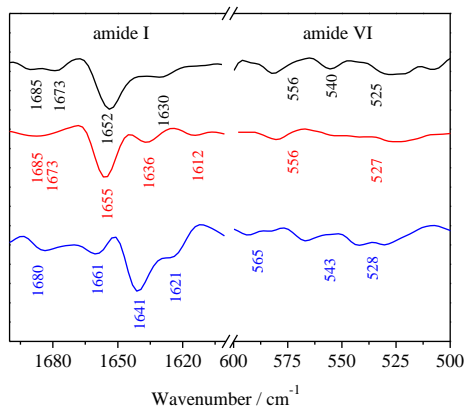
Appendix 10. Oxidative UV-Vis titration of the inhibited Glu78Ala CcO at pH 8.0.



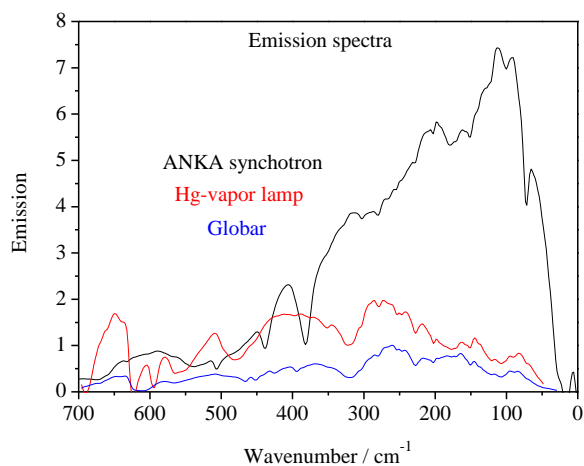
Appendix 11. Second derivatives of the amide I and amide VI bands of PLL samples. at neutral pH (black), at neutral pD (red), at pH 11.0 (blue) and at pD 11.0 (magenta).



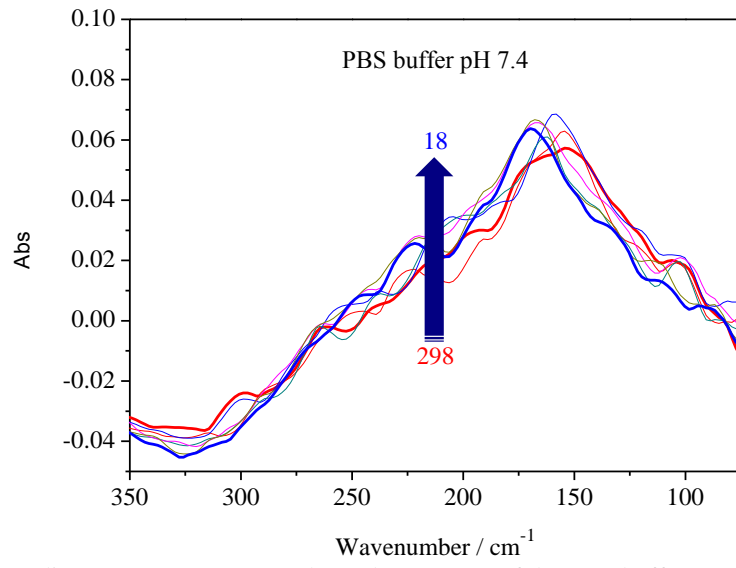
Appendix 12. Second derivatives of the amide I and amide VI bands of PLA at pD 7.0 (black) and PLH at pD 9.0 (red).



Appendix 13. Second derivatives of the amide I and amide VI bands of the *bc*₁ (black), of CcO (red) and Rieske (blue).



Appendix 14. Emission spectra of: ANKA synchrotron (black), Hg-vapor source (red) and globar source (blue).



Appendix 15. FIR temperature dependent spectra of the PBS buffer at pH 7.4.